Spin injection in III-V semiconductor-based systems for spintronic applications

Tiantian Zhang

Université de Toulouse

THÈSE

En vue de l'obtention du

DOCTORAT DE L'UNIVERSITÉ DE TOULOUSE

Délivré par : l'Institut National des Sciences Appliquées de Toulouse (INSA de Toulouse)

Présentée et soutenue le *09 avril 2014* **par :**

Tiantian ZHANG

Injection de spin dans des systèmes à base de semiconducteurs III-V en vue de nouveaux composants spintroniques

---

JURY

Rapporteur	Paul VOISIN	Directeur de Recherche, LPN-CNRS, Marcoussis
Rapporteur	Matthieu JAMET	Directeur de Recherche, CEA, Grenoble
Examinateur	Jacques PERETTI	Directeur de Recherche, LPMC-Polytechnique, Paris
Examinateur	Lionel CALMELS	Professeur, Université Paul Sabatier, Toulouse
Directeur de thèse	Pierre RENUCCI	Professeur, LPCNO-INSA, Toulouse
CoDirecteur de thèse	Hélène CARRERE	Maître de Conférence, LPCNO-INSA, Toulouse

---

École doctorale et spécialité :
Science de la matière: Nanophysique

Unité de Recherche :
Laboratoire de Physique et Chimie de Nano-Objets, INSA-CNRS-UPS (UMR 5215)

Directeur(s) de Thèse :
Pierre RENUCCI et **Hélène CARRERE**

Rapporteurs :
Paul VOISIN et **Matthieu JAMET**

Résumé de Thèse

Spécialité: Nanophysique

Nom: ZHANG

Prénom: Tiantian

Titre de la thèse en français: Injection de spin dans des systèmes à base de semiconducteurs III-V en vue de nouveaux composants spintroniques

Résumé de la thèse en français:

La spintronique dans les semiconducteurs vise à utiliser le spin de l'électron comme degré de liberté supplémentaire (en plus de la charge électrique) afin de véhiculer l'information, ce qui permettrait la mise au point de composants intégrant de nouvelles fonctionnalités. Ce travail de thèse porte sur deux étapes importantes qui doivent être maîtrisées : l'injection électrique de porteurs polarisés en spin dans les semiconducteurs III-V, et la manipulation du spin de l'électron (par champ magnétique) dans ces matériaux optimisés. Dans un premier temps, la grande efficacité des injecteurs de spin à base de CoFeB/MgO/GaAs est démontrée dans des dispositifs de type Diodes Electroluminescentes polarisées en spin (SpinLEDs). La comparaison entre des injecteurs comprenant une barrière tunnel fabriquée soit par pulvérisation cathodique, soit par épitaxie par jets moléculaires (MBE), permet de montrer que ces deux techniques donnent des résultats comparables. Dans les deux cas, l'efficacité de l'injection est améliorée par un recuit de l'échantillon autour de $300-350°C$. Le recuit induit une amélioration de la qualité de l'interface CoFeB/MgO. De plus, l'efficacité de l'injection de spin n'est stable en fonction du courant injecté que lorsque la barrière tunnel est fabriquée par pulvérisation cathodique. Ceci est dû aux caractéristiques de l'interface MgO/GaAs qui diffèrent selon la technique de croissance de la barrière. Dans un deuxième temps, l'injection de spin en l'absence de champ magnétique externe appliqué est réalisée grâce à un nouveau type d'injecteur constitué d'une électrode de CoFeB ultrafine présentant une aimantation rémanente de la couche le long de l'axe de croissance de l'échantillon. Pour la première fois des taux de polarisation circulaire de l'électroluminescence de l'ordre de 20% sont mesurés à 25 K à champ magnétique nul. Ensuite, la problématique de la relaxation de spin des porteurs injectés dans les vallées L de haute énergie dans GaAs (phénomène non négligeable sous injection électrique) est également traitée. Nous observons qu'une fraction de la mémoire du spin photogénéré en L est conservée lorsque les électrons sont diffusés vers la vallée Γ, malgré une relaxation d'énergie de plusieurs centaines de meV. Le temps de relaxation de spin dans les vallées L est estimé autour de 200 fs. Enfin, nous avons exploré le matériau GaAsBi dilué ($x \sim 2.2\%$) dont la perturbation de la matrice par l'élément Bi permet d'attendre des propriétés électroniques et de spin fortement modifiées. Des mesures de photoluminescence ont mis en évidence une diminution de l'énergie de bande interdite de l'ordre de 85meV/%Bi. De plus, par la mesure directe des battements quantiques de la polarisation de photoluminescence nous avons déterminé un facteur de Landé des électrons de conduction de l'ordre de deux fois supérieur à celui de GaAs. Ces résultats témoignent de la forte perturbation des états de valences et de l'augmentation de l'interaction spin-orbite.

Titre de la thèse en anglais: Spin injection in III-V semiconductor-based systems for spintronic applications

Résumé de la thèse en anglais:

Spintronics of semiconductors aims at using carrier spins as supplementary means of information transport. This would lead to components showing extended functionalities. This thesis work is dedicated to the study of injection and manipulation of electron spin in semiconductors, which are the basis of any spintronic application. In a first step we demonstrate the high efficiency of CoFeB/MgO/GaAs - based spin injectors. Circular polarization degrees of electroluminescence over 20% are measured on spin polarized LEDs (SpinLEDs) at 0.8 T and 25 K. Comparison between sputtering- and MBE- grown spin injectors has shown similar results. In both case, spin injection efficiency is increased by thermal annealing of the sample, in the range $300-350°C$. Indeed, annealing improves the quality of CoFeB/MgO interface, and induces the crystallization of CoFeB above $300°C$. A higher stability of spin injection with current injection is found when the tunnel barrier is grown by sputtering. This is due to the MgO/GaAs interface characteristics which is related to the growth technique. In a second step, we demonstrate spin injection without external applied magnetic field, through an ultra-thin (a few atomic layers) CoFeB electrode, taking advantage of the perpendicular magnetic anisotropy of the layer which leads to a remanant magnetization along the growth axis. For the first time in this configuration, circular polarization degrees of electroluminescence of about 20% are measured at 25 K at zero magnetic field. In a third step, due to the crucial role it may play in electrical injection, electron spin dynamics in high energy L-valleys is investigated. Using polarization resolved excitation photoluminescence in the range 2.8-3.4 eV, we observe that a fraction of photogenerated spin polarization is preserved when electrons are scattered hundreds of meV down to Γ valley. Spin relaxation time in L valleys is estimated to 200 fs. Finally we investigate electron and spin properties of GaAsBi dilute bismide alloy. We observe that the bandgap energy is reduced by 85meV/%Bi when Bi element is introduced into GaAs matrix. Moreover, the electron Landé factor is about twice the one in GaAs for a 2.2% Bi composition. These features are evidence of the strong perturbation of host states and spin-orbit interaction enhancement.

Remerciements

Avant d'exposer mon travail de thèse, je voudrais remercier toutes les personnes qui m'ont apporté, de près ou de loin, leur encouragement, leur soutient, leur aide, leur amitié ...

En premier lieu, je remercie P. Voisin et M. Jamet pour avoir accepté d'être rapporteurs de cette thèse. Je remercie également J. Peretti et L. Calmels pour leur participation à ce Jury en tant qu'examinateurs.

Merci à toute l'équipe d'optoélectronique quantique du LPCNO (Laboratoire de Physique et Chimie des Nano-Objets) pour m'avoir accueillie et guidée tout au long de ces trois années et demi :

Je voudrais tout d'abord dire un grand merci à mon superviseur Prof. Pierre Renucci, qui a été ,tout au long de cette thèse, très gentil et serviable. Merci de m'avoir aider lors de mon arrivé à Toulouse, de m'avoir présenté à toute l'équipe du LPCNO, de m'expliquer toutes les choses dans le laboratoire, de nous voir presque tous les soirs dans la salle de manip et de nous discuter avec nous des nouveaux résultats...

Je voudrais ensuite remercier à la co-directeur de thèse Hélène Carrère de m'avoir aidée rapidement a chaque fois que j'avais un problème, et d'avoir été aussi joilleuse et enthousiaste. Ce fut très agréable de travailler avec toi dans le même bureau durant ces 3 ans.

Un grand Merci à Thierry Amande et Xavier Marie, d'avoir pris le temps de m'expliquer les mécanismes de spintronique et pour lesquels j'ai pu bénéficier de conseils constructifs et d'explications lumineuses.

Merci à Andrea Balocchi et Délphine Lagarde de m'avoir aidé à régler des problèmes de réglage du laser lorsque je commencais à peine à travailler avec celui-ci.

Merci à Philippe Barate, Simone Mazzucato, Cong Tu Nguyen, Meal Vidal, pour toute l'aide que vous m'avez apporté lors des manipulations. Merci pour la bonne ambiance que vous avez su mettre dans la salle de manip. Merci aussi à Bernhard Urbaszek, Louis Bouet et Gang Wang.

Je remercie les secrétaires de notre laboratoire et Madame Fortuné, qui m'ont beaucoup aidé pour les dossiers administratifs.

Merci à Y. Lu, S. H. Liang, X. Devaux, C. Fontaine and A. Arnoult, J.-M. George, H. Jaffrès, J. Frougier, B. Xu, X. D. Qin d'avoir préparé les échantillons ainsi que pour

toutes les discutions que l'on a pu avoir.

Merci à tous mes amis en France: Shengnan, Hervé, Chaichai, Ran, Jian, Haoran, Juan, Hong, Lijian, Tao, Xiaojian, Wuwei, Hang, Wenjun, Chengcheng, Xu, Dongdong, Haojun, Xiaoxiao, Yanping, Rui, Yu, mes colocataires David et Juana... pour les conseils de vie dans un pays qui était pour moi totalement nouveaux, pour les voyages qui m'ont permise de visiter de nouveau pays et pour toutes ses soirées que l'on a passé ensemble. Merci à tous mes amis en chine: Yufei, Yuan, Yuzhou, Bingnan, Peng, Jinghua, Yue, Fang, Linlin, Yang... pour les encouragements et l'aide que vous m'avez apporté.

Je remercie les organisateurs du programme CSC/UT-INSA dont le financement a facilité ma venue en France pour réaliser ma thèse.

Un très grand Merci à mes parents pour m'avoir encouragé à partir faire mes études en France, merci à eux de toujours être présent pour moi.

Et enfin Merci pour cette rencontre inattendu, rencontre qui m'a permise de voir et faire des choses que je ne pouvais voir que dans les films. Merci à toi Emmanuel l'amour de ma vie.

Un grand MERCI à vous tous!

Contents

Abstract **i**

Remerciements **iii**

Introduction **1**

1 Introduction to the properties of zinc blende III-V semiconductors **7**

1.1 III-V semiconductors band structure 9

1.1.1 Bulk semiconductors 9

1.1.2 Semiconductor heterostructures 12

1.2 Optical orientation in zinc-blende semiconductors 17

1.2.1 Optical transitions 17

1.2.2 Optical selection rules 18

1.3 Main spin relaxation mechanisms 21

1.3.1 D'Yakonov-Perel Mechanism 21

1.3.2 Elliott-Yafet Mechanism 22

1.3.3 Bir-Aronov-Pikus Mechanism 23

1.3.4 Electron spin relaxation due to the Hyperfine-interaction 23

1.3.5 Exciton spin relaxation mechanism 24

1.4 Electrical spin injection into Spin-LEDs 24

1.4.1 Problem of impedance mismatch in the diffusive regime 25

1.4.2 Spin Light Emitting diodes as a tool to detect and quantify electrical spin injection 30

1.4.3 State of the art: breakthrough due to MgO tunnel barriers . . . 33

2 Experimental Set-ups **39**

2.1 Time-resolved Photoluminescence spectroscopy 41

2.1.1 Excitation laser source 41

2.1.2 Streak camera detection 42

2.1.3 Polarization resolution 45

2.2 Polarization-resolved Electroluminescence set-up 45

2.2.1 CCD camera detection 46

2.2.2 Electrical generator 47

2.3 Polarized Photoluminescence Excitation spectroscopy 47

2.4 Cryogenics and magnetic field 49

3 Electrical spin injection in Spin-LEDs **51**

3.1 Influence of the growth technique (Sputtering and Molecular Beam Epitaxy) 55

3.1.1 Spin-LEDs Samples 56

3.1.2 Electroluminescence measurements 57

3.1.3 Influence of the annealing process on the spin injection efficiency 58

3.1.4 Measurement of the electron lifetime and spin relaxation times in the InGaAs/GaAs quantum well by Time and Polarization-resolved Photoluminescence 59

3.1.5 Analysis of the influence of the annealing process on the hysteresis curves of the ferromagnetic layer by SQUID Measurements . 62

3.1.6 CoFeB/MgO and MgO/GaAs interfaces analysis by HRTEM and RHEED characterizations 64

3.2 Current dependence of the electrical spin injection 67

3.2.1 Current dependence of the Electroluminescence circular polarization 69

3.2.2 Voltage dependence of the Electroluminescence circular polarization 70

3.2.3 Discussion 71

3.3 Electrical injection at zero magnetic field up to room temperature . . . 76

3.3.1 Sample description 77

3.3.2 Microscopic origin of the Magnetic Perpendicular Anisotropy in the ultrathin CoFeB/MgO injector 78

3.3.3 Optimization of the CoFeB injector 80

3.3.4 Electrical spin injection without magnetic field at 25 K probed by Electroluminescence measurements 81

3.3.5 Electrical spin injection without magnetic field at room temperature 85

3.3.6 Dependence of the electrical spin injection as a function of temperature 87

3.3.7 Dependence of the electrical spin injection as a function of the applied bias 91

3.3.8 Conclusion 92

4 Spin Dynamics of L-valley Electrons in GaAs 95

4.1 Optical orientation in GaAs 97

4.1.1 Why analyzing the electron spin dynamics in satellite L-valleys in GaAs 97

4.1.2 GaAs band structure 98

4.1.3 Spin orbit splitting in the L-valley 100

4.1.4 Selection rules in the Γ-valley 103

4.2 Experimental results of Polarized Photoluminescence Excitation 103

4.2.1 Experimental setup and sample description 104

4.2.2 Photogenerated electron spin-polarization 104

4.2.3 Depolarization induced by the transverse magnetic field 109

4.3 Dynamics of spin relaxation in L-valley 110

4.3.1 Spin photogeneration and dynamics 111

4.3.2 Discussion 112

4.4 Conclusion 114

Calculation of the Photo-generated initial electron spin polarization in GaAs L-valleys 114

5 Spin Properties of GaAsBi 137

5.1 Introduction 139

5.2 TRPL characterization of GaAsBi epilayers 142

5.2.1 Bandgap energy variation and PL linewidth 143

5.2.2 Effect of Rapid Thermal Annealing on carrier lifetime 146

5.3 Spin properties of GaAsBi 148

5.3.1 Experimental determination of g-factor 149

5.3.2 Analysis of spin relaxation time 155

5.4 Conclusions and perspectives 156

Conclusion and Perspectives **157**

Bibliography **165**

Résume de la thèse en français **188**

List of Tables

1.1 Bloch eigenfunctions at the zone centre for a zinc-blende semiconductor 10

1.2 Selection rules for interband transitions [1] 20

2.1 Ti:Sa laser main characteristics 42

2.2 The characteristics of the Jobin-Yvon Triax 320 (for S1) and iHR320 (for S20) spectrometers. The spectral resolution values are given for a 200 μm width of the slit. 44

2.3 Temporal modes of streak camera 45

2.4 Characteristics of the Princeton Acton SP2500 spectrometer gratings. 46

2.5 Principle characteristics of the generator HP8160A 47

1 The L-valley electronic states representation in C_{3v} 132

2 The coupling tables of $\hat{p}_{\pm'}$ operators at L point. 132

3 The coupling tables for circularly polarized photons propagating along [001] at L point. 133

List of Figures

1.1 Schematic representation of the zinc blende structure. 9

1.2 Schematic representation of the zinc blende band structure near $\vec{k} = 0$. 11

1.3 Schematic of band energy structure of type I quantum well [2] 14

1.4 Hole relation dispersion in a $100\mathring{A}$ $GaAs/Al_{0.3}Ga_{0.7}As$ quantum well [3] 16

1.5 Optical selection rules from heavy-hole (HH), light-hole(LH) and split-off (SO) valence band (VB) to conduction band (CB) [4]. The relative oscilator strenth corresponding to each transition are indicated next to the colores arrows. 21

1.6 (a) energy band separates when $\vec{k} \neq 0$. (b) Spin relaxation process in D'Yakonov-Perel mechanism. 22

1.7 Schematics of the Elliott-Yafet mechanism : spin flip processes 23

1.8 (a) Spin up and spin down currents far from an interface between ferromagnetic and nonmagnetic materials (outside the spin accumulation zone). (b) Splitting of the chemical potentials $\mu \uparrow$ and $\mu \downarrow$ near the FM/N interface. The arrows symbolize the spin flips induced by the out of equilibrium spin-split distribution and governing the depolarization of the electron current between the left and the right. (c) Variation of the current spin polarization when there is an approximate balance between the spin flips on both sides (metal/metal) and when the spin flips on the left side are predominant (metal/ semiconductor for example). [5] . . . 26

1.9 Tunnel junction with different tunneling probabilities for the two spin species that can be modeled by a spin dependent interface resistance [6]. 29

1.10 Current spin polarization at an interface between a ferromagnetic metal FM and a semiconductor N. The calculation has been performed for F = Co with $r_F = \rho_F^* l_{sf}^F = 4.5 \times 10^{-15} \Omega m^2$, $\beta = 0.46$, $l_{sf}^F = 60$ nm from CPP-GMR data on Co, and for N=GaAs with $r_N = 4.5 \times 10^{-9} \Omega m^2$, $l_{sf}^N = 2$ μm derived from room temperature data on n-type GaAs (n = $10^{16} cm^{-3}$). The blue solid lines are calculated with a spin dependent interface resistance ($r_b^* = r_N = 4 \times 10^{-9} \Omega m^2$, $\gamma = 0.5$) and the red dashed lines without an interface resistance. [7]. 30

1.11 Left: Scheme of principle of a spin-LED. Right: Typical band diagram for a MgO-based spin-LED from 1D-Poisson-Schroedinger simulator [8]. 31

1.12 Typical electroluminescence spectra for a Spin-LED at 25K for I^+ and I^- components (here the QW embedded in the spin-LED is a 10 nm thick $In_{0.1}Ga_{0.9}As$/GaAs QW). 32

1.13 Magnetic field dependence of the EL circular polarization P_{EL} [(a) and (b)] (raw data) and P_C [(c) and (d)] (after substraction of the spurious signal increasing linearly with the applied magnetic field) for spin-LED I (8% of Al) at 100 K and spin-LED II (16% of Al) at 290 K (open circles). The crosses in (a) are the P_{EL} of a control sample with a Pt electrode. The solid lines in (c) and (d) show the field dependence of the CoFe moment measured with a SQUID magnetometer at 20 K, which has been scaled to allow comparison with P_C. [9] 34

1.14 Dispersion curves E(k^2) at $k_{\|} = 0$ for MgO (001). k and $k_{\|}$ are repectively the normal (z axis) and in-plane components (with respect to the MgO layer) of the vector k. k^2 is given in units of Δz^{-1}, with Δz corresponding to the interplanar spacing in MgO. The energy is given in Hartree (1 Hartree=27,2 eV). The region of interest is within the energy gap of MgO at the Fermi level E_F. The values of k^2 are negative ($k^2 = (i\lambda)^2$), corresponding to evanescent wavefunctions of the type $\Psi(z) = Aexp(-2\lambda z)$. [10] 35

2.1 Time Resolved Photoluminescence Spectroscopy Setup 41

2.2 (a) Operation principle of the streak camera; (b) Sketch of the sweeping mechanism responsible for the time resolution; (c) Spectral sensitivity of the photocathodes 43

2.3 An example of image obtained with a streak camera 43

2.4 Polarization Resolved Electroluminescence Spectroscopy Set-up 46

2.5 Polarized Photoluminescence Excitation Spectroscopy Set-up 48

3.1 Spin-LED structure with a single InGaAs/GaAs quantum well. The CoFeB/MgO/GaAs tri-layers is decomposed in terms of a top interface CoFeB/MgO and a bottom interface MgO/GaAs 56

3.2 Spin-LED (annealed at 350°C) with a sputtered tunnel barrier at T=25 K. EL Circular polarization as a function of the applied longitudinal magnetic field. Top inset: EL spectra at 25 K at zero magnetic field for $I^{\sigma+}$ (thick black line) and $I^{\sigma-}$ (thick red line) EL components. Bottom Inset: same quantities for B=0.8 T. 57

3.3 Electroluminescence circular polarization P_C as a function of the annealing temperature for sputtered (black squares) and MBE (red circles) grown MgO tunnel barriers. Inset: EL spectra of a Spin-LED (annealed at 350°C) with a MBE grown tunnel barrier at 25 K for B=0.8 T for $I^{\sigma+}$ (thick black line) and $I^{\sigma-}$ (thin red line) EL components. 59

3.4 PL and circular polarization measurements performed on bare $p \cdot i \cdot n$ sample annealed at 350°C at T=25 K. Top: Photoluminescence intensity components I^+ and I^- with respectively σ^+ polarization (black squares) and σ^- polarization (red squares) as a function of time after a 1.5 ps laser σ^+ pulsed excitation at 780 nm (above the GaAs bandgap). The sum of the two intensity components $I_{sum} = I^+ + I^-$ is displayed in pink opened circles. The decay is characterized by the electron lifetime τ. Bottom: time evolution of the circular polarization rate P_C of the photoluminescence at T=25 K (blue line). The decay is characterized by the electron spin relaxation time τ_s. 60

3.5 Relative variation of the circular polarization (black squares) and F factor (red circles) on bare $p \cdot i \cdot n$ samples annealed at different temperatures. 61

3.6 Electron spin relaxation time τ_s (red open circles), electron lifetime τ (black open squares) and F factor (blue open stars) as a function of the annealing temperature T_{AN}. 62

3.7 SQUID measurements. (a) Out-of-plane hysteresis curves (normalized magnetization as a function of the applied longitudinal magnetic field) for $T_{AN} = 25°C$ (black line), $T_{AN} = 275°C$ (red line) and $T_{AN} = 350°C$ (green line). (b) In-plane coercitive field H_c as a function of the annealing temperature T_{AN} for a spin-LED based on a sputtered tunnel barrier (red circles) and for a spin-LED based on a MBE grown tunnel barrier (black squares). (c) top: Spin-LED based on a MBE grown MgO tunnel barrier. In-plane hysteresis curves (normalized magnetization as a function of the applied magnetic field) for different annealing temperatures T_{AN}. Bottom: Same measurements for a Spin-LED based on a sputtered MgO tunnel barrier. 63

3.8 (a) HRTEM image of the sample with the MBE grown MgO tunnel barrier before annealing. Insets: RHEED images for [100] and [110] directions (left and right insets respectively). (b) HRTEM image of the sample with the MBE grown MgO tunnel barrier after annealing at $T_{AN} = 350°C$. Inset: TEM image at low magnification showing the good homogeneity of the layers. (c) HRTEM image of the sample with the sputtered MgO tunnel barrier before annealing. Upper insets: RHEED images for [100] and [110] directions (left and right insets respectively). (d) HRTEM image of the sample with the sputtered MgO tunnel barrier after annealing at $T_{AN} = 350°C$. Inset: TEM image at low magnification showing the good homogeneity of the layers. 66

3.9 Spin-LED with a sputtered tunnel barrier for $T_{AN} = 300°C$. Left panel: EL spectra at 25 K for B=0.8 T for I^+ (thick black line) and I^- (thin red line) EL components. Inset: EL Circular polarization as a function of the applied longitudinal magnetic field. Right panel.: EL spectra at 250 K for B=0.8 T for I^+ (thick black line) and I^- (thin red line) EL components. 68

3.10 (a) Spin-LED with a sputtered and a MBE grown tunnel barrier annealed at $300°C$. T=25 K. B=0.8 T : EL Circular polarization as a function of the current. Inset: P_C as a function of the current for sputtered samples at different annealing temperatures. (b) Spin-LED with a sputtered and a MBE grown tunnel barrier annealed at $300°C$. T=25 K. B=0.8 T : EL Circular polarization as a function of $\Delta V = V - V_{th}$. 69

3.11 Scheme of the principle of injection for Spin-LEDs with a sputtered (left) and MBE grown (right) MgO tunnel barrier 72

3.12 T=25 K. (a) EL intensity as a function of the current for spin-LEDs with a sputtered tunnel barrier (black squares) and a MBE grown tunnel barrier (red squares) for $T_{AN} = 300°C$ in the low current regime. (b) EL intensity (log scale) as a function of the current for spin-LEDs with a sputtered tunnel barrier (black squares) and a MBE grown tunnel barrier (red squares) for $T_{AN} = 300°C$. 73

3.13 Central wavelength of the EL emission as a function of the injected current for a sputtered sample (black squares) and a MBE sample (red squares) annealed at $300°C$. Top left inset: EL spectra as a function of the current for a spin-LED with a sputtered tunnel barrier annealed at $300°C$. Bottom right inset: EL spectra as a function of the current for a spin-LED with a MBE grown tunnel barrier annealed at $300°C$. . . . 74

3.14 T=25 K. Circular polarization as a function of the EL intensity for a spin-LED with a sputtered tunnel barrier (black squares) and a MBE grown tunnel barrier (red squares) for $T_{AN} = 300°C$. 75

3.15 Left: schematic device structure of a spin-LED. Right: HRTEM image of CoFeB/MgO PMA injector; Inset of HRTEM image: low magnification image showing the excellent homogeneity and the low roughness of the structures. 77

3.16 Left: layer-resolved orbital moment anisotropy ($\Delta\mu$). Middle: schematics of the calculated crystalline structures. Fe, Mg, and O are represented by blue, green, and red balls, respectively. Right: DOS with spin-orbit coupling for averaged Fe 3d out-of-plane ($3d_{z2} + 3d_{xz} + 3d_{yz}$) and in-plane orbitals ($3d_{x2-y2} + 3d_{xy}$) with Fe both at the interface (Fe5) and in the bulk (Fe3). Inset: a simple picture showing that the origin of PMA comes from the hybridization of Fe out-of-plane orbitals ($3d_{z2}, 3d_{xz}$ and $3d_{yz}$) and O $2p_z$ orbitals, which leads to an uncompensated charge occupation in Fe in-plane orbitals ($3d_{x2-y2}, 3d_{xy}$) and results in an enhanced out-of-plane orbital moment leading to PMA. 79

3.17 RT out-of-plane M-H curves for spin-injectors with different CoFeB thicknesses with $T_{AN} = 250°C$. 80

3.18 M-H curves at 30 K for a spin-injector with 1.2 nm of CoFeB and $T_{AN} = 250°C$ for in-plane and out-of-plane configurations. 81

3.19 EL spectra at 25 K with zero magnetic field for the optimized PMA conditions sample for σ^+ and σ^- polarizations when the field is swept from positive to negative values (curves on the top) and from negative to positive values (curves on the bottom) in the hysteresis loop 82

3.20 P_C as a function of the out-of-plane magnetic field measured at 25 K for a spin-LED with 1.2 nm CoFeB/MgO injectors, which is compared to the corresponding out-of-plane M-H hysteresis loop at 30 K by SQUID in PMA optimized conditions. 82

3.21 (a) P_C as a function of out-of-plane magnetic field measured at 25 K for the spin-LED with optimized PMA injector with a bias of 2.3 V. (b-i) EL spectra for σ^+ and σ^- components at different magnetic field, which are indicated in the hysteresis loop in (a). 83

3.22 MCD measurement from the PMA spin-LED as a function of magnetic field at 25 K. P_C of the EL for a reference sample without CoFeB layer as a function of magnetic field at 25 K. 84

3.23 In the as-grown injector (non annealed spin-LED), hysteresis loops from P_c (solid line) and corresponding SQUID data (dotted line) at 30 K . . 85

3.24 P_C as a function of the out-of-plane magnetic field measured at 300 K for the spin-LED with optimized PMA injector, which is compared to the out of plane M-H hysteresis loop at 300 K measured by SQUID. Inset: EL spectra at 300 K with zero magnetic field for σ^+ and σ^- polarizations. 86

3.25 (a) P_C as a function of the out-of-plane magnetic field measured at 300 K for the spin-LED with the optimized PMA injector at a bias of 2.3 V. (b-i) EL spectra for σ^+ and σ^- components at different magnetic fields, which are indicated in the hysteresis loop in (a). 86

3.26 Temperature dependence of P_C without magnetic field and with a 0.4 T field. The temperature dependence of P_s is calculated using: $P_s = P_C/F$ from the data without field. 87

3.27 Typical PL spectra after integration in time domain for $\sigma+$ and $\sigma-$ components. P_c is deduced from $(I^{\sigma+} - I^{\sigma-})/(I^{\sigma+} + I^{\sigma-})$. 88

3.28 Left: PL intensity (color code in arbitrary units) as a function of both time and photon wavelength. The white curve represents the PL intensity as a function of time when the emission is spectrally integrated. Right: PL circular polarization degree P_C (color code from $P_C = 0$ to $P_C = 44\%$) as a function of both time and photon wavelength. The white curve represents P_C as a function of time when the emission is spectrally integrated. 89

3.29 Determination of the carrier lifetime τ from an exponential fit of the decay time of the PL intensity $(I^{\sigma+} + I^{\sigma-})$. 89

3.30 Determination of the spin lifetime τ_s from an exponential fit of the decay time of the normalized P_C. 90

3.31 Temperature dependence of the electron lifetime τ, the electron spin relaxation time τ_s and the F factor in the QW. 90

3.32 P_C as a function of applied bias for the optimized PMA condition sample. Inset: EL spectra at 25 K with zero magnetic field for σ^+ and σ^- polarizations under a bias of 2.34 V. 91

4.1 Schematics of the GaAs band structure; the arrows present the optical excitations $E_{exc} = 2.987eV$ and detection energies used in the experiments of the following section. The high symmetry points in this figure are labelled according to [11]. 99

4.2 Reflectivity of etched GaAs at 80 K [12] 99

4.3 Spin relaxation time in the Γ valley and longitudinal spin relaxation time in the L valley as a function of temperature for a non-degenerate electron gas. The collision time is taken as $\tau_p = 200fs$. 102

4.4 Selection rules in the Γ valley 102

4.5 Dependence of the degree of circular polarization of the luminescence in GaAs on the exciting photon energy [13] 103

4.6 Time-integrated photoluminescence spectrum and the corresponding circular polarization following a σ^+-polarized laser excitation at an energy $E_{exc} = 2.987$ eV. 105

4.7 PL circular polarization as a function of the excitation energy at 10K. Inset: photogenerated electron spin polarization calculated using LDA and $k \cdot p$ band structures. 106

4.8 Photoemission spectrum of spin polarization from GaAs+CsOCs at low temperature. [14] 107

4.9 Selection rules in L-valleys 108

4.10 Sketch of the Brillouin zone of GaAs displaying the eight L valleys. Note that two L-valleys differing by a translation of the reciprocal lattice are equivalent. The blue arrows represent the photogenerated spins in L valleys. 108

4.11 Variation of the PL circular polarization degree as a function of the transverse magnetic field B. The full line is a Lorentzian curve with T_S = 140 ps. 110

4.12 Time evolution of the PL circular components I^+ and I^-, and the corresponding circular polarization P_c for a near band-gap excitation. . . . 112

4.13 Schematic representation of the two-level model including the spin relaxation times in both L and Γ valleys 113

5.1 Band gap energies and spin-orbit split-off energy calculated using the BAC model [15] 140

5.2 band gap energies and spin-orbit split-off energy calculated using tight-binding model [16] 141

5.3 PL peak emission energy (a) and FWHM (b) plotted as a function of temperature for the as-grown sample excited at 1 mW (filled squares) and 10 mW (filled triangles), and for the 750°C annealed sample at 1 mW (empty squares) and 10 mW (empty triangles). 144

5.4 Time integrated PL spectra for the as-grown and annealed samples at 750°C, taken at room temperature and 1 mw excitation power 145

5.5 Arrhenius plots for the as-grown sample (empty circles) and the annealed (crosses) sample at 1 mW. The dashed lines represent the fitting lines for the calculation of the defects' activation energies in the annealed sample. 146

5.6 TRPL curves for the as-grown sample (a) and the annealed sample (b), taken at 1 mW incident power for a series of increasing temperatures up to 300 K. (NB: The amplitudes of the signals in the two graphs are not comparable as data were taken under different acquisition conditions.) Spectra are shifted for presenting more clearly. 147

5.7 Decay time plot versus temperature for the as-grown (filled squares) and 750°C annealed samples (empty circles) at 1 mW incident power. The normalized TRPL curves taken at 10 K are shown in the inset (stacked for clarity), together with the exponential fit for the annealed sample. . 148

5.8 Co-polarized I^+ (black line) and counter-polarized I^- (red line) PL components, and related circular polarization degree (P_c) at room temperature under circular (black squares) or linear (hollow squares) excitation; dashed lines are guides to the eye. 150

5.9 Time dependence of the PL circular polarization degree for B=0T (black hollow squares) and B=0.73T (red hollow squares) at T=100 K, the black exponential decay line is a guide to the eye. The inset shows the measured Larmor precession frequency $\mu = \Omega/2\pi$ as a function of the applied magnetic field. 151

5.10 Measured electron g-factor in GaAsBi (black squares) as a function of lattice temperature with respective error bars, the line is a guide to the eye. The inset shows an example of acquired TRPL spectrum (I^+ component) with clear intensity oscillations appearing after the application of a transverse magnetic field of 0.73 T. 152

5.11 The principle of spin quantum-beat dephasing measurements. The sign of the dephasing between the +B and -B experiments allows one to determine the electron transverse Landé g factor sign. [17] 153

5.12 Luminescence polarization oscillations at T=100 K for the GaAsBi (main graph) and GaAs (inset) transitions, showing the temporal phase shift Δt between positive ($\mathbf{B}\overrightarrow{e_x}$, black hollow squares) and negative (-$\mathbf{B}\overrightarrow{e_x}$, red hollow circles) external magnetic field. 154

5.13 Experimentally measured electron spin relaxation time in intrinsic GaAsBi as a function of temperature (blue circles), plotted within the theoretically expected values calculated by Tong et. al. with a photo-electron density of $10^{17}cm^3$. 155

Introduction

The degree of freedom associated to the electron spin plays nowadays a key role in devices (e.g. Magnetic tunnel junctions) based on ferromagnetic metals, which is the crowning achievement of spin electronics or spintronics [18], a research field symbolized by the discovery of the Giant Magnetoresistance in 1988 [19,20] (by A Fert an P. Grünberg, Nobel Prize laureates in 2007). In parallel, the electron spin properties in semiconductors have been explored since the sixties [21,22], mainly by the orientated optical pumping technique. Since the middle of the nineties, the idea to use the electron spin in devices based on semiconductors (that will present the advantage of a very accurate control of the charge compared to metals) is the field of intense research in the United States [23], Europe [24] and Japan [25]. New components characterized by low power consumption and higher speed or new functionalities (Spin transistors [26], spin Light Emitting diodes (Spin-LEDs) [27], spinLasers [28]) have been proposed in the past decade. The semiconductor spintronics challenges are spin current generation [29] (and in particular electrical injection) and transport, spin storage and manipulation [26] (in view of the quantum treatment of information [30]), and spin current detection. A part of spintronic development in semiconductors is devoted to group IV semiconductors as Silicon and Germanium [31,32], but we concentrate in this thesis on spin injection into III-V semiconductors in view of spin-optoelectronics applications. This thesis is focused on two of the previous cited challenges: electrical spin injection into III-V semiconductors and exploration of spin properties of new materials as GaAsBi in view of manipulation of spin carriers.

The first axis of this work is devoted to electrical spin injection in hybrid Ferromagnetic Metal/Semiconductor nanostructures (FM/SC). Among all the methods considered in order to generate spin polarized currents in a semiconductor [29], the efficient

electrical injection of spin polarized electrons from a ferromagnetic metal towards a semiconductor could constitute a key step in view of realization of semiconductor devices with new functionalities based on the spin. In addition to the extrinsic spin relaxation processes due to the structural quality of the interfaces, the large difference of conductivity between these two materials has been identified as a fundamental obstacle to the spin injection, that can be overcome by the insertion of a thin tunnel barrier at the interface FM/SC. As injectors based on crystalline MgO tunnel barriers have exhibited up to now the highest spin injection efficiencies into III-V semiconductors, we have focused our work on CoFeB/MgO electrodes. A powerful way to study the processes that govern the spin injection and its efficiency through an interface is to probe the electron spin polarisation by analysing the circular polarization degree of the electroluminescence (EL) emitted in the semiconductor part of the Spin-LEDs [27,33,34]. This method relies on the exploitation of the optical selection rules that govern the radiative recombination of carriers in semiconductor heterostructures.

Using Spin-LEDs based on InGaAs quantum wells, we have analysed the influence of the growth technique (Molecular Beam Epitaxy or Sputtering) of the MgO layer on the efficiency of the spin injection process. Combined analysis of polarization-resolved electroluminescence with time-resolved photoluminescence (TRPL), transmission electron microscopy (TEM) and superconducting quantum interference device (SQUID) magnetometer measurements, lead to the conclusion that the control of the quality of the CoFeB/MgO interface is more important than the one of MgO/GaAs interface for an optimal spin injection. A systematic study of the impact of the post-annealing temperature of the injector is also performed for the two types of samples. Both show the same trend: an increase of the EL circular polarization (P_C) when the annealing temperature T_{AN} increases, with an optimized temperature in the range $300 - 350°C$. We attribute this behavior mainly to the improvement of the chemical structure at the top CoFeB/MgO interface. The current dependence of the electrical spin injection is also investigated for samples prepared by the two growth techniques. We demonstrate that the electroluminescence circular polarization is very stable as a function of the injected current for sputtered tunnel barriers, whereas this polarization decreases abruptly when the current increases for tunnel barriers grown by Molecular Beam Epitaxy. We attribute this behavior to the MgO/GaAs interface that presents specific

characteristics depending on the growth method. It appears that in view of future applications, spin-LEDs with sputtered tunnel barriers present the best compromise between high electroluminescence circular polarization and high electroluminescence intensity. Finally we have demonstrated a very efficient electrical spin injection without any external magnetic field using an ultrathin (a few monolayers thick) CoFeB injector that presents Perpendicular Magnetic Anisotropy (PMA). The EL circular polarization rate P_C can reach values as large as 20% at 25 K, which is more than six times the values obtained with usual multilayer PMA injectors [35] up to now. A significant P_C ($\sim$ 8%) is conserved at room temperature. A systematic study of P_C as a function of temperature leads to the conclusion that the injection is stable with temperature and that the variation of P_C are due to variation of the electron lifetime and spin relaxation times within the quantum well.

In a second part, we have explored the electron spin properties in the L valleys in GaAs, by polarisation-resolved Photoluminescence Excitation (PLE) spectroscopy in the blue range. These high energy electrons might play an important role in devices based on spin transport (as for example, if one wants to observe the recently predicted spin Gunn effect [36]) as well as in devices where electrical spin injection of high kinetic energy electrons occurs [37]. We demonstrate that a significant fraction of the electron spin memory can be conserved when the electron is scattered from the L to the Γ valley despite an energy relaxation of several hundreds of meV. The dependence of the circular polarization rate measured in Γ as a function of the laser energy is in good agreement with LDA and k.p calculations. Combining high energy photoexcitation experiments under transverse magnetic field (Hanle curves) with time-resolved photoluminescence spectroscopy of Γ valley spin-polarized photogenerated electrons allows us to deduce a typical L-valley electron spin relaxation time of 200 fs, in agreement with theoretical calculations where large spin splitting of conduction bands are expected for these valleys [38].

In the last part, the spin properties of GaAsBi as a potential new material for spintronics are explored. The electron spin relaxation time is measured by polarization-resolved TPRL and suggests a diminution of the effective mass of conduction electrons. The measurement of Landé g factors are performed by TRPL under transverse magnetic field by analysing the period of spin quantum beats as a function of the magnetic

field. A significant increase of the Landé g factor compared to the one of GaAs is observed, due to the decrease of the bandgap and the increase of the spin–orbit interaction in GaAsBi. Note that large g-factors and strong spin orbit coupling could present an interest for spin manipulation by external magnetic field and electric field respectively. The investigation of the spin properties of GaAsBi under circularly polarized light constitutes an interesting way to probe the electronic properties of this material. It appears that the introduction of Bismuth into GaAs strongly modifies the band structure, not only in the valence band, but also in the conduction band. Further investigations of the influence of the composition of Bi in GaAsBi should be led in order to have a deeper understanding of these modifications, and to be able to tune the optical properties of this material that could present also a potential interest for Photovoltaic and optical telecommunications applications.

This manuscript is divided into five chapters. In the first chapter we recall the main characteristics of the band structure of bulk III-V semiconductors. We briefly present the principle of the envelope function theory that allows to calculate the confined energy levels in heterostructures as quantum wells. Optical selections rules in the centre of the Brillouin zone, as well as the principle of spin relaxation mechanisms, are presented. A short introduction to the problematic of electrical spin injection is given, and the obstacle of "conductivity mismatch" between ferromagnetic metals and semiconductors is evoked. The principle of optical detection of electrical spin injection by the use of spin-LEDs is explained. The second chapter of the manuscript is devoted to the description of experimental set-ups of optical spectroscopy employed in this thesis (Electroluminescence and Ultra-fast Time-Resolved Photoluminescence at the picosecond timescale). A specific set-up of high sensitivity polarisation-resolved Photoluminescence Excitation (PLE) spectroscopy based on a double modulation technique has been developed in order to study electrons spin properties in the L valleys of GaAs. In chapter 3 we tackle the problem of electrical spin injection into GaAs with crystalline MgO tunnel barriers. We analyse the influence of the growth technique of the MgO layer as well as the influence of the current injected in the spin-LEDs on the spin injection efficiency. Finally, electrical spin injection without any external magnetic field using an ultrathin CoFeB layer is demonstrated up to room temperature. Chapter 4 is devoted to the electron spin properties in the L valleys (in particular the spin

relaxation time) of GaAs, studied by polarisation-resolved Photoluminescence Excitation (PLE) spectroscopy in the blue range. To finish with, in chapter 5 the potential of GaAsBi as a new material for spintronics, as well as its band structure modification due to Bi inclusion are explored by measuring spin relaxation times and Landé g-factors.

Chapter 1

Introduction to the electronic and optical properties of zinc blende III-V semiconductors

1.1 III-V semiconductors band structure 9

1.1.1 Bulk semiconductors 9

1.1.2 Semiconductor heterostructures 12

1.2 Optical orientation in zinc-blende semiconductors 17

1.2.1 Optical transitions 17

1.2.2 Optical selection rules 18

1.3 Main spin relaxation mechanisms 21

1.3.1 D'Yakonov-Perel Mechanism 21

1.3.2 Elliott-Yafet Mechanism 22

1.3.3 Bir-Aronov-Pikus Mechanism 23

1.3.4 Electron spin relaxation due to the Hyperfine-interaction . . 23

1.3.5 Exciton spin relaxation mechanism 24

1.4 Electrical spin injection into Spin-LEDs 24

1.4.1 Problem of impedance mismatch in the diffusive regime . . . 25

1.4.2 Spin Light Emitting diodes as a tool to detect and quantify electrical spin injection 30

1.4.3 State of the art: breakthrough due to MgO tunnel barriers . 33

In this chapter we present the basic physics in the bulk semiconductors and semiconductor heterostructures. In the first part, we discuss the electronic band structure at the center of the Brillouin zone of III-V semiconductors. We will present the electronic properties in quantum wells. Then, in the second part, we detail the fundamental principles of optical selection rules. The third section is devoted to spin relaxation mechanisms. After having presented the main electronic and spin properties of III-V semiconductors bulk and heterostructures, we give in the last section a short introduction to the problem of the electrical spin injection from a ferromagnetic electrode into a semiconductor through a tunnel barrier, a problem that will be at the heart of chapter 3. The principle of the optical detection of this spin injection process by the use of a Spin Light Emitting Diode is also presented.

1.1 III-V semiconductors band structure

1.1.1 Bulk semiconductors

In this section, we present the main characteristics of the band structure of zinc blende semiconductors. As shown in Figure 1.1, in zinc blende structure (like GaAs, InP, etc.) each atom's nearest neighbors consist of four atoms of the opposite type. The two types of atoms interpenetrate face-centered cubic lattices. The lattice parameter a is the edge length of the cube.

The Hamiltonian of an electron in a crystal periodic potential $V(r)$ can be described

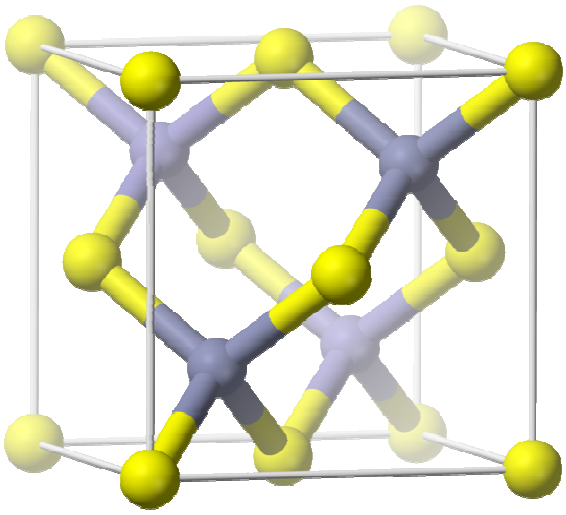

Figure 1.1: Schematic representation of the zinc blende structure.

as:

$$H = \frac{-\hbar^2}{2m_0}\Delta_r + V(\vec{r}) \tag{1.1}$$

m_0 is the electron mass in vacuum. The eigenstate ψ of Hamiltonian of equation 1.1 can be written as:

$$\psi(\vec{r}) = u(\vec{r})e^{i\vec{k}\vec{r}} \tag{1.2}$$

where $\vec{k}$ is the wave vector and $u(\vec{r})$ has the same periodicity as the crystal potential. The electron eigenenergies are divided into conduction band and valence band. The electronic state at $\vec{k} = 0$ corresponding to the conduction band is denoted $|S\rangle$ due to its spherical symmetry, while the degenerate solutions of the valence bands are noted $|X\rangle$, $|Y\rangle$, $|Z\rangle$ in analogy to the eigenfunctions of the Hydrogen atom p states.

Taking into account the electron spin and the orbital angular momentum interaction, we get a supplementary term W_{so} in the crystal Hamiltonian H_0,

$$H = H_0 + W_{so} = \frac{p^2}{2m_0} + V(\vec{r}) + \frac{\hbar}{4m_0^2c^2}\sigma \cdot (\Delta V(\vec{r}) \times p) \tag{1.3}$$

where σ is Pauli matrix. The third term in Equation 1.3 can be converted into the following form in spherical symmetry:

$$\frac{\hbar}{4m_0^2c^2}\sigma \cdot (\Delta V(\vec{r}) \times p) = \frac{\hbar}{2m_0^2c^2}\frac{1}{\vec{r}}\frac{dV}{dr}(\vec{L} \cdot \vec{S}) \tag{1.4}$$

where **L** is the orbital angular momentum, **S** is the spin angular momentum ($\pm 1/2$), **J** is the total angular momentum ($\mathbf{J} = \mathbf{L} + \mathbf{S}$). The conduction band is separated from the valence band (VB) by a bandgap energy E_g. (As shown in Figure 1.2). The valence band is then separated into a group of two double degenerate bands: heavy hole (HH) and light hole (LH), and a band called split-off (SO) which is separated from the two other bands by the spin-orbit coupling energy Δ_{so}. In GaAs, Δ_{so} is 341 meV at 300 K.

The conduction states at $k = 0$ can be described in the base $|S\uparrow\rangle$ and $|S\downarrow\rangle$ which correspond to the eigenvalue E_c. The valence bands' states at $k = 0$, which corresponds to the eigenvalue E_v, are described the bases $|X\uparrow\rangle$, $|X\downarrow\rangle$, $|Y\uparrow\rangle$, $|Y\downarrow\rangle$, $|Z\uparrow\rangle$, and $|Z\downarrow\rangle$ (here the sign $\uparrow$ and $\downarrow$ represent the spin angular momentum).

Table 1.1 summarized the eigenfunctions and eigenenergies in this base. Conduction

Eigenfunction u_i u_n	'Atomic' notations $\|J, m_j\rangle$	Eigenenergies
$u_1 = \|S,\uparrow\rangle$ $u_2 = \|S,\downarrow\rangle$	$\|\frac{1}{2},\frac{1}{2}\rangle$ $\|\frac{1}{2},-\frac{1}{2}\rangle$	$E_c = E_{HH} + E_G$
$u_3 = \frac{1}{\sqrt{2}}\|(X+iY),\uparrow\rangle$ $u_4 = \frac{1}{\sqrt{2}}\|(X-iY),\downarrow\rangle$	$\|\frac{3}{2},\frac{3}{2}\rangle$ $\|\frac{3}{2},-\frac{3}{2}\rangle$	$E_v = E_{HH}$
$u_5 = \frac{1}{\sqrt{6}}\|(X+iY),\downarrow\rangle - \sqrt{\frac{2}{3}}\|Z,\uparrow\rangle$ $u_6 = -\frac{1}{\sqrt{6}}\|(X-iY),\uparrow\rangle - \sqrt{\frac{2}{3}}\|Z,\downarrow\rangle$	$\|\frac{3}{2},\frac{1}{2}\rangle$ $\|\frac{3}{2},-\frac{1}{2}\rangle$	$E_v = E_{LH} = E_{HH}$
$u_7 = \frac{1}{\sqrt{3}}\|(X+iY),\downarrow\rangle + \sqrt{\frac{1}{3}}\|Z,\uparrow\rangle$ $u_8 = -\frac{1}{\sqrt{3}}\|(X-iY),\uparrow\rangle + \sqrt{\frac{1}{3}}\|Z,\uparrow\rangle$	$\|\frac{1}{2},\frac{1}{2}\rangle$ $\|\frac{1}{2},-\frac{1}{2}\rangle$	$E_{so} = E_{HH} - \Delta_{so}$

Table 1.1: Bloch eigenfunctions at the zone centre for a zinc-blende semiconductor

states are represented by u_1 and u_2. For the valence band, the eigenstates of heavy

holes and light holes are u_3, u_4 and u_5, u_6 respectively. u_7, u_8 are the split-off bands.

For calculating the band structure at $\vec{k} \neq 0$, the $k \cdot p$ method can be used. By substituting the Bloch function into Schrödinger equation, we obtain:

$$(\frac{p^2}{2m_0} + V(\vec{r}) + \frac{\hbar^2 k^2}{2m_0} + \frac{\hbar \boldsymbol{k} \cdot \boldsymbol{p}}{m_0}) u_{n,k}(\vec{r}) = E_{n,k} u_{n,k}(\vec{r}) \tag{1.5}$$

Where the energies $E_{n,k=0}$ are considered known. The $\boldsymbol{k} \cdot \boldsymbol{p}$ method consists in treating the $\hbar \boldsymbol{k} \cdot \boldsymbol{p}$ operator as a pertubation to the Hamiltonian and, by considering a small variation of the $\mathbf{k}$ vector from the central zone, the eigenenergies at $k \neq 0$ can be calculated as:

$$E_{n,k} = E_{n,0} + \frac{\hbar^2 k^2}{2m_0} + \frac{\hbar^2}{m_0^2} \sum_{m \neq n} \frac{|\langle u_{n,0} | k \cdot p | u_{m,0} \rangle|^2}{E_{n\mathbf{0}} - E_{m\mathbf{0}}} \tag{1.6}$$

The band structure of zinc blende semiconductors near the center of Brillouin zone calculated according to the $\boldsymbol{k} \cdot \boldsymbol{p}$ method in first approximation is presented in Figure 1.2, the energies show a parabolic dispersion.

In order to describe more precisely the degenerate valence bands, Luttinger-Kohn

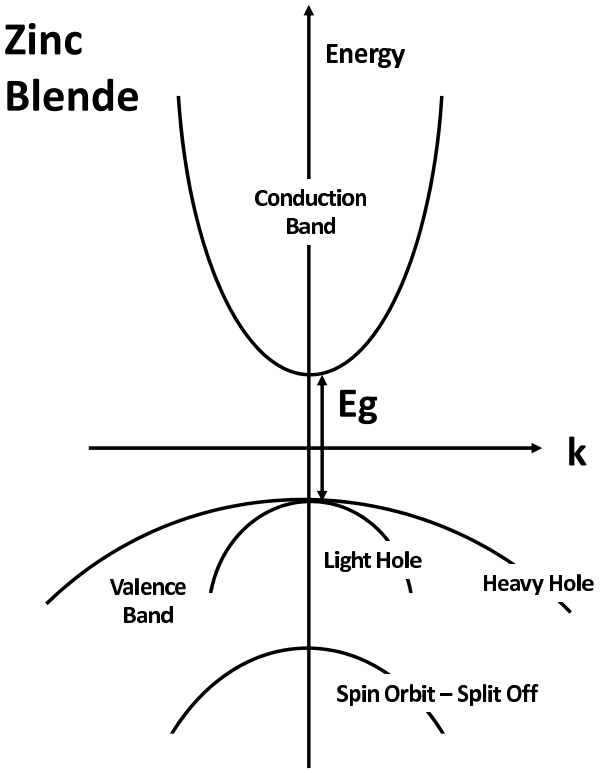

Figure 1.2: Schematic representation of the zinc blende band structure near $\vec{k} = 0$.

model [39,40] can be used in which the coupling between two degenerate conduction bands is neglected and the Löwdin partitioning method [41] is employed to treat the six degenerate valence bands. The general Hamiltonian for both cases of light and heavy holes are written as :

$$H_L = \frac{\hbar^2}{2m_0}[(\gamma_1 + \frac{5}{2}\gamma_2)\nabla^2 - 2\gamma_3(\nabla \cdot \boldsymbol{J})^2 + 2(\gamma_3 - \gamma_2)(\nabla_x^2 \boldsymbol{J}_x^2 + c.p.)] \tag{1.7}$$

where $\gamma_1, \gamma_2, \gamma_3$ are Luttinger parameters determined by experiments [42], $\boldsymbol{J} = (\boldsymbol{J_x}, \boldsymbol{J_y}, \boldsymbol{J_z})$ is total angular momentum operator, *c.p.* stands for cyclic permutation [43]. The eigenenergies of both light and heavy hole states are found in terms of Luttinger parameters,

$$E(k) = E_v(0) + \frac{\hbar^2}{m_0}[\gamma_1 k^2 \pm 2\sqrt{\gamma_2 \boldsymbol{k^4} + 3(\gamma_3^2 - \gamma_2^2)(k_x^2 k_y^2 + k_y^2 k_z^2 + k_z^2 k_x^2)}] \tag{1.8}$$

Intuitively, equation 1.8 shows that heavy holes (positive sign) and light holes (negative sign) are degenerated at $\vec{k} = 0$ and split for $\vec{k} \neq 0$ into two subbands with different characteristics presented by different effective masses. In fact, the relationship between the effective masses of heavy and light holes of (100) equivalent direction can be expressed in the forms related to Luttinger parameters :

$$\begin{aligned} \frac{m_{hh}^*}{m_0} &= \frac{1}{\gamma_1 - 2\gamma_2} \\ \frac{m_{lh}^*}{m_0} &= \frac{1}{\gamma_1 + 2\gamma_2} \end{aligned}$$

For GaAs, the values of the Luttinger parameters are $\gamma_1 = 7.0$, $\gamma_2 = 2.25$, $\gamma_3 = 2.9$ [43,44].

1.1.2 Semiconductor heterostructures

An heterostructure is composed of different layers of dissimilar crystalline semiconductors with unequal bandgap energies. In practice, advanced epitaxial techniques such as Molecular Beam Epitaxy (MBE) or Metal-Organic Chemical Vapor Deposition (MOCVD) allow us to grow layers as thin as a few atomic layers, in which the motion

of carriers is quantized. The heterostructural interfaces play a critical role in semiconductor heterostructure devices such as field-effect transistor (FET), bipolar transistor, light-emitting diode (LED), laser,... etc because they exhibit many interesting and useful electronic properties associated with their discontinuities of band structure at their interfaces [45]. This section recalls some basis on semiconductor heterostructures.

Envelope function approximation

As discussed before, the Bloch function only describes electron wavefunction under crystal periodic potential. However, in semiconductor heterostructure, the periodic condition is broken because of the interface between two different materials. In this situation, envelope function approximation (EFA) is implemented to find the wavefunction of electron in semiconductor heterostructures.

The Schrödinger equation for semiconductor heterostructures is written as [1]:

$$(\frac{-\hbar^2}{2m_0}\Delta_r + V_c(\vec{r}) + V_h(\vec{r}))\psi_{nk}(\vec{r}) = E_{nk}\psi_{nk}(\vec{r}) \tag{1.9}$$

where n is band index, m_0 is the free electron effective mass, $V_c(\vec{r})$ is the crystal potential, $V_h(\vec{r})$ is the heterojunction intefacial potential. In EFA method, the interfacial potential $V_h(\vec{r})$ is considered as a pertubative component. In fact, the EFA method is valid under two assumed conditions : the envelope wavefunction and the density of current probability are continuous through the interface. Now the wavefunction of an electron in semiconductor heterostructure is found in this form :

$$\psi_{n,k}(\vec{r}) = F_{nk}(\vec{r})u_{n0}(\vec{r})$$

where $F_{nk}(\vec{r})$ is the envelope function and $u_{n0}(\vec{r})$ is the Bloch wavefunction at $\boldsymbol{k} = 0$. The equation 1.9 becomes :

$$(\frac{-\hbar^2}{2m_c(\vec{r})}\Delta_r + V_h(\vec{r}))F_{nj}(\vec{r}) = (E_{ni} - E_{n0})F_{nj}(\vec{r}) \tag{1.10}$$

where $m_c(\vec{r})$ is the effective mass depending on semiconductor materials and $E_{nj} - E_{n0}$ is the confinement energy. In this approximation, the heterostructure is considered as a crystal with small pertubative potential $V_h(\vec{r})$.

Electronic properties of semiconductor quantum wells

A Quantum Well (QW) is a thin layer of semiconductor structure sandwiched between two layers of another semiconductor. Semiconductor quantum wells can be divided into two categories : type I and type II [46]. We only concentrate on studying type I quantum well (for instance AlGaAs/GaAs) in which, the material of barrier layers has wider bandgap than the quantum well layer as depicted in figure 1.3.

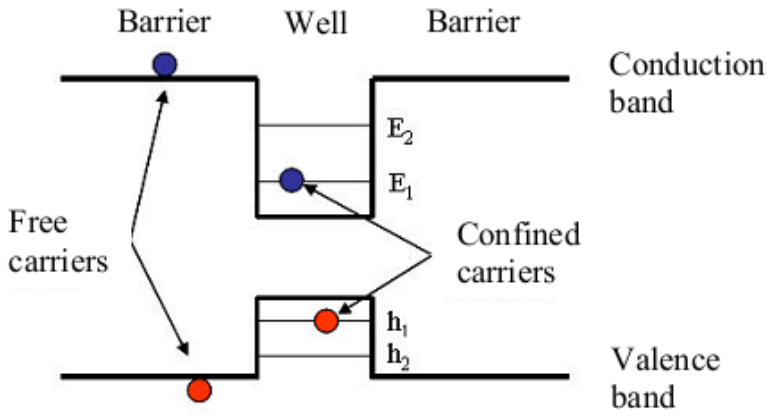

Figure 1.3: Schematic of band energy structure of type I quantum well [2]

Quantum well

For the band calculation, the potential for the finite quantum well is defined as :

$$V(z) = \begin{cases} 0 & \text{for } |z| \leq L/2 \\ V_0 & \text{for } |z| > L/2 \end{cases}$$

We denote material A for quantum well layer and material B for the barrier layers. Concerning the envelope wavefunction $\Phi(z)$, the Schrodinger equation can be written as :

$$[E_s + V_s(z) - \frac{\hbar^2}{2\mu(z)}(\frac{\partial^2}{\partial_{z^2}} + k_\perp^2)]\Phi(z) = E\Phi(z) \tag{1.11}$$

where E_s is the conduction band edge in the quantum well which can be set as zero for the sake of simplicity, $V_s(z)$ is zero in the quantum well and equals to V_0 in the barrier, $\mu(z)$ is the effective mass which is equal to m_A^* in the quantum well and m_B^*

in the barrier, $k_\perp$ is the in-plane wavevector ($k_\perp^2 = k_x^2 + k_y^2$), $\Phi(z)$ is the z-dependent part of the envelope function.

The boundary conditions are proposed in Ben Daniel-Duke model [1,47] as follow :

$$\Phi_A(\pm\frac{L}{2}) = \Phi_B(\pm\frac{L}{2}) \tag{1.12}$$

and :

$$\frac{1}{m_A^*}\frac{d\Phi(z)}{dz}\mid_{z=\pm L/2} = \frac{1}{m_B^*}\frac{d\Phi(z)}{dz}\mid_{z=\pm L/2} \tag{1.13}$$

Due to the potential symmetry, the wavefunction of a particle in this kind of quantum well can be expressed by even and odd functions. Solving the above Schrodinger equation 1.11, the envelope wavefunction is obtained :

$$\Phi(z) = \begin{cases} Ae^{\beta z} & \text{for } z < \text{-L/2} \\ B\cos(\alpha z) & \text{for } |z| \leq L/2 \text{ (even states)} \\ B\sin(\alpha z) & \text{for } |z| \leq L/2 \text{ (odd states)} \\ Ae^{-\beta z} & \text{for } z > L/2 \end{cases}$$

where :

$$\alpha = \sqrt{\frac{2m_A^*}{\hbar^2}E_n - k_\perp^2} \tag{1.14}$$

$$\beta = \sqrt{\frac{2m_B^*}{\hbar^2}(V_0 - E_n) + k_\perp^2} \tag{1.15}$$

and A, B are normalization constants. In the case of an infinite quantum well, the associated eigenenergies are of this form :

$$E_n(k_\perp) = \frac{\hbar^2}{m_A^*}((\frac{n\pi}{L})^2 + k_\perp^2) \tag{1.16}$$

As for the bulk materials, the valence band is of more complicated treatment than the conduction band. The approach is to add a confinement potential in Luttinger-Kohn Hamiltonian. We can rebuild the hole Hamiltonian in the QW by referring to equation 1.7 Firstly, the confinement potential term V(z) should be added into the Hamiltonian; then, the cubic term in equation 1.8 which is proportional to $(\gamma_3^2 - \gamma_2^2)$ is rather small in most zinc-blende semiconductors and we can omit it in a first approach. Finally, we assum that the Luttinger parameters are identical in the QW and the barriers. With

those simplifications, the Hamiltonian of holes in QW becomes :

$$H_{QW} = \frac{\hbar^2}{2m_0}[(\gamma_1 + \frac{5}{2}\gamma_2)\nabla^2 - 2\gamma_3(\nabla \cdot \boldsymbol{J})^2] + V(z)$$

With the assumption that Schrödinger function is separable in the direction of quantization from the in-plane movement, the Hamiltonian for the motion in z-direction can be simplified in this form :

$$H_z = \frac{\hbar^2}{2m_0}[(\gamma_1 + \frac{5}{2}\gamma_2) - 2\gamma_3\nabla J_z^2](\frac{\partial}{\partial z})^2 + V(z)$$

Figure 1.4 illustrates the schematic of hole dispersion relation in a typical 10 nm

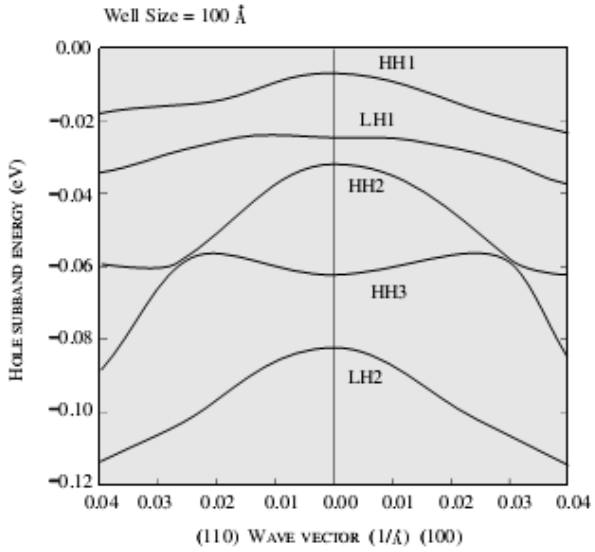

Figure 1.4: Hole relation dispersion in a 100$\mathring{A}$ $GaAs/Al_{0.3}Ga_{0.7}As$ quantum well [3]

thick GaAs/AlGaAs quantum well. As shown in this figure, the heavy hole (HH) subband is above the light hole (LH) subband at zone center because the confinement energy is inversely proportional to the effective mass (equation 1.16). As a result, the exciton E1-HH1 is dominant in the photoluminescence spectroscopy of type I quantum well.

1.2 Optical orientation in zinc-blende semiconductors

Optical properties provide an important tool for studying many inner physical phenomena in the solid. In fact, optical spectra reveal many information about electronic properties in a semiconductor such as the energy band diagram, the impurity level, the existance of localized states, the exciton energy, etc. Optics is also very useful to study the spin properties of carriers in semiconductors. This section mentions some background of optical orientation in zinc-blende semiconductors.

1.2.1 Optical transitions

When electromagnetic waves interact with a direct bandgap semiconductor that has a bandgap smaller than photon energy, electrons in the lower energy states are excited to higher energy states following the energy and momentum conservation laws and making an optical transition. There are different kinds of optical transitions in semiconductor. *Interband transitions* take place between the conduction band and the valence band, in which electrons in the occupied states of the valence band are excited in the empty states of the conduction band. *Intraband transitions* happen inside one band (the conduction band or the valence band) and involve only one type of carrier (electron or hole).

An electromagnetic radiation can be described by its electric field $E(\vec{r},t)$ and magnetic field $H(\vec{r},t)$ equivalent to a vector potential $\boldsymbol{A(\vec{r},t)}$ which is defined as:

$$\begin{aligned} E(\vec{r},t) &= -\frac{1}{c}\nabla \cdot \boldsymbol{A(\vec{r},t)} \\ H(\vec{r},t) &= \nabla \times \boldsymbol{A(\vec{r},t)} \end{aligned}$$

The Hamiltonian of an electron in the presence of an electromagnetic field is written as :

$$H = \frac{1}{2m_0}(\boldsymbol{p} - \frac{e\boldsymbol{A}}{c})^2 + V(\boldsymbol{r}) \tag{1.17}$$

This Hamiltonian can be developped as :

$$H = H_0 - \frac{e}{m_0}\vec{\boldsymbol{A}}.\vec{\boldsymbol{p}} + \frac{e^2}{2m_0c}A^2$$

where $H_0 = \frac{p^2}{2m_0} + V(r)$. If the term of A^2 is neglected in the first approximation, the interaction Hamiltonian between an electron and an electromagnetic field can be written as :

$$H_{int} = -\frac{e}{m_0c}\vec{\boldsymbol{A}}.\vec{\boldsymbol{p}} \tag{1.18}$$

where **e** is electron charge, m_0 is electron mass, c is the light velocity.

Using the first-order time-dependent pertubation theory, the Fermi Golden Rule states that the transition rate of an electron from an initial state $|i\rangle$ with an energy E_i to a final state $|f\rangle$ with an energy E_f by absorbing a photon with the energy $\hbar\omega$ is defined as :

$$W_{if} = \frac{2\pi}{\hbar}\left|\langle i|H_{int}|f\rangle\right|^2 \delta(E_f - E_i - \hbar\omega) \tag{1.19}$$

where $M_{if} = |\langle i|H_{int}|f\rangle|^2$ is denoted as the transition matrix element [48] whose values determine the allowed transitions and their relative intensities; this defines the optical selection rule. The Dirac function δ is responsible for energy conservation law in these transitions.

If the quantum states $|i\rangle$ and $|f\rangle$ are partially occupied, the transition probability is weighted by the occupancy factor given by the Fermi-Dirac distribution as follows:

$$R_{i\to f} = W_{if} f(E_i)[1 - f(E_f)] \tag{1.20}$$

where $f(E) = (1 + e^{\frac{1}{k_B T}(E-\mu)})^{-1}$ is the Fermi-Dirac distribution, in which k_B is the Boltzmann constant, T is the temperature and μ is the chemical potential of the electron.

1.2.2 Optical selection rules

For direct bandgap semiconductors such as GaAs and InAs, the lowest energy point in the conduction band and the highest energy point in the valence band have the same momentum at the Γ-point (k=0). Hence, interband transitions in these materials can occur without any contribution of phonons. Optical selection rules in this situation are presented as follows.

Let us consider a monochromatic electromagnetic wave :

$$\vec{E}(\vec{r},t) = F\vec{\epsilon}\cos(\omega t - \vec{k}\cdot\vec{r}) \tag{1.21}$$

where F is the electric field strength, $\vec{\epsilon}$ is a polarization vector. For circular polarized light, the right-hand and left-hand polarization vectors can be defined as $\vec{\epsilon} = \frac{1}{\sqrt{2}}(1,i,0)$ and $\vec{\epsilon} = \frac{1}{\sqrt{2}}(1,-i,0)$, respectively. For linear-polarized light, $\vec{\epsilon} = (1,0,0)$.

The potential vector is rewritten in this form :

$$A(\vec{r},t) = -\frac{cF\vec{\epsilon}}{2i\omega}[e^{i(\omega t-\vec{k}.\vec{r})} - e^{-i(\omega t-\vec{k}.\vec{r})}] \tag{1.22}$$

and the interaction Hamiltonian is :

$$H_{int} = \frac{ieF}{2m_0\omega}(e^{i\omega t} - e^{-i\omega t})\vec{\epsilon}.\vec{p} \tag{1.23}$$

under the dipole approximation $e^{i\vec{k}.\vec{r}} \approx 1$ which is valid for the studied wavelength. As a result, the transition rate is given by :

$$W_{if} = \frac{2\pi}{\hbar}(\frac{e}{m_0\omega})^2 \left|\frac{F(\omega)}{2}\right|^2 |\vec{\epsilon}.\vec{p_{if}}|^2 \,\delta(E_f - E_i - \hbar\omega) \tag{1.24}$$

in which $\vec{p_{if}} = \langle i|\vec{p}|f\rangle$ contains the selection rules information.

For quantum wells, the envelope functions for electrons in the conduction band and the valence band are taken into account in the matrix element $\langle i|\vec{p}|f\rangle$. We introduce the non-zero irreducible momentum matrix elements at Γ-point for zinc-blende structure calculated by group theory [49]:

$$\Pi = \frac{-i}{m_0}\langle S|p_x|X\rangle = \frac{-i}{m_0}\langle S|p_y|Y\rangle = \frac{-i}{m_0}\langle S|p_z|Z\rangle \tag{1.25}$$

Table 1.2 shows the selection rules for different polarizations of electromagnetic waves for interband transitions in a quantum well.

Owing to optical selection rules, it is well-known that spin-polarized carriers can be generated by the absorption of circular-polarized light and vice versa, the recombination of spin-polarized charges results in the emission of circular-polarized light [22]. Let $\sigma^{\pm}$ represent the helicity of the exciting light related to right and left-hand circular polarized light propagating along the z-direction, as shown in figure 1.5. In bulk zinc-blende semiconductors, the spin polarization of generated carriers are determined by the photon energy $\hbar\omega$. Under the condition $E_g < \hbar\omega < E_g + \Delta_{SO}$, the heavy and light

$Polarization$	$\vec{\epsilon} \parallel \vec{x}$	$\vec{\epsilon} \parallel \vec{y}$	$\vec{\epsilon} \parallel \vec{z}$	$Type\ of\ transitions$
$\vec{k} \parallel \vec{z}$	$\Pi/\sqrt{2}$	$\Pi/\sqrt{2}$	$Impossible$	$HH \rightarrow E$
$\vec{k} \parallel \vec{x}$	$Impossible$	$\Pi/\sqrt{2}$	0	$HH \rightarrow E$
$\vec{k} \parallel \vec{y}$	$\Pi/\sqrt{2}$	$Impossible$	0	$HH \rightarrow E$
$\vec{k} \parallel \vec{z}$	$\Pi/\sqrt{6}$	$\Pi/\sqrt{6}$	$Impossible$	$LH \rightarrow E$
$\vec{k} \parallel \vec{x}$	$Impossible$	$\Pi/\sqrt{6}$	$2\Pi/\sqrt{6}$	$LH \rightarrow E$
$\vec{k} \parallel \vec{y}$	$\Pi/\sqrt{6}$	$Impossible$	$2\Pi/\sqrt{6}$	$LH \rightarrow E$

Table 1.2: Selection rules for interband transitions [1]

hole subbands are excited simultaneously because they are degenerated at $\boldsymbol{k} = 0$ in the zinc-blende structure. Denoting n_+ and n_- as the density of spin-polarized electron with $S_z = +1/2$ and $-1/2$ respectively, the spin polarization is defined as [50]:

$$P_s = \frac{n_+ - n_-}{n_+ + n_-} \tag{1.26}$$

At the moment of photoexcitation, the spin carriers are oriented against the direction of exciting light since the probability of heavy-hole transitions (E-HH) is three times larger than that of light-hole transitions (E-LH) (see in table 1.2) in zinc-blende structure indicated by :

$$P_s = \frac{1-3}{1+3} = -\frac{1}{2} \tag{1.27}$$

The circular polarization of photoluminescence is :

$$P_{circ} = \frac{I_+ - I_-}{I_+ + I_-} = \frac{(n_+ + 3n_-) - (3n_+ + n_-)}{(n_+ + 3n_-) + (3n_+ + n_-)} = -\frac{P_s}{2} = \frac{1}{4} \tag{1.28}$$

where $I_\pm$ are defined as the radition intensities of corresponding helicity $\sigma_\pm$.

When the photon energy allows for the excitation of electrons from the split-off band ($\hbar\omega \geq E_g + \Delta_{SO}$), the carriers will not be spin-polarized because the numbers of spin-up and spin-down carriers are the same; which underlines the role of spin-orbit coupling in optical orientation.

For semiconductor quantum wells, depending on both hole and strain, the heavy and light hole subbands are splitted. It allows thus the selective excitation of only one conduction subband ($|+1/2\rangle$ or $|-1/2\rangle$). This selective excitation can improve the spin polarization P_s up to 100%; which offers a nice feature to observe the spin relaxation phenomena.

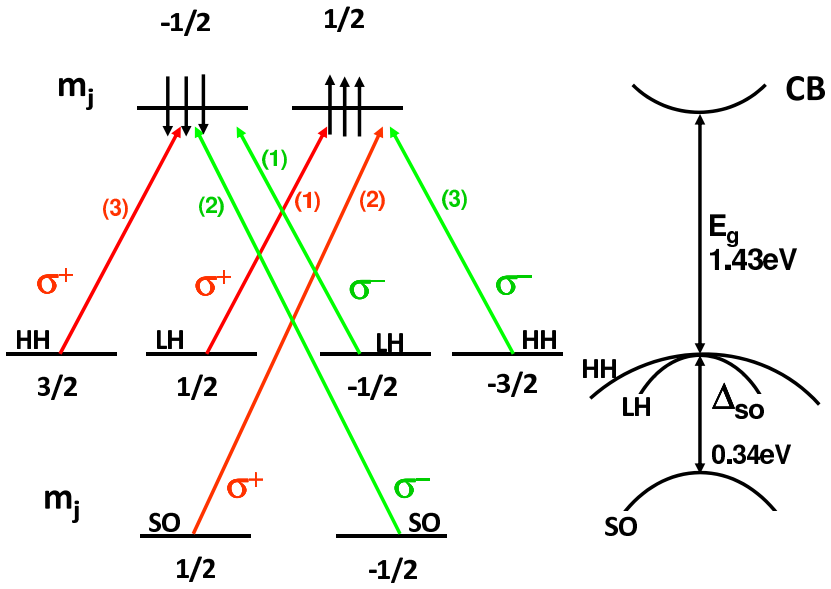

Figure 1.5: Optical selection rules from heavy-hole (HH), light-hole(LH) and split-off (SO) valence band (VB) to conduction band (CB) [4]. The relative oscilator strenth corresponding to each transition are indicated next to the colores arrows.

1.3 Main spin relaxation mechanisms

In this section, we synthetically present the main spin relaxation mechanisms of carriers in semiconductors. The spin relaxation is the process that brings back a non-equilibrium spin population to the initial equilibrium condition. It is the central issue in the spin physics of semiconductors.

1.3.1 D'Yakonov-Perel Mechanism

This mechanism manifests in semiconductors with non-inversion crystal symmetry and is related to the spin splitting of the conduction band due to spin-orbit interaction. When $\vec{k} \neq 0$, the spin orbit interaction lifts the spin degeneracy of the conduction band [51]: the electrons, which have the same vector $\vec{k} \neq 0$ but opposite spins, belong to different energy bands (see Figure 1.6 (a)). For bulk semiconductors, Dresselhaus [52] first pointed out this splitting. The Hamiltonian associated to the interaction writes:

$$\frac{\hbar}{2}\sigma\Omega(\vec{k}) \tag{1.29}$$

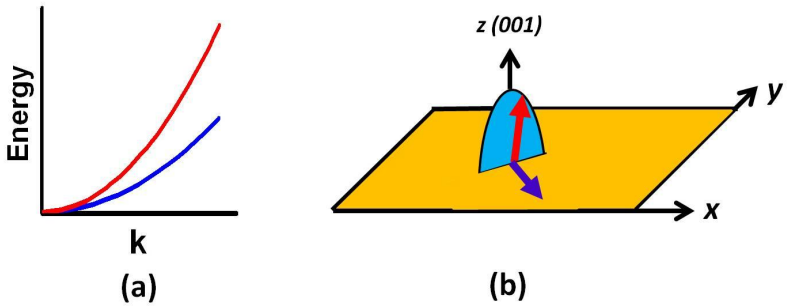

Figure 1.6: (a) energy band separates when $\vec{k} \neq 0$. (b) Spin relaxation process in D'Yakonov-Perel mechanism.

For a given $\vec{k}$, $\Omega(\vec{k})$ is the spin precession frequency in an effective magnetic field $B = \Omega\frac{m}{e}$.

However, the effective field direction changes after each collision process. So the spin relaxation time (τ_s) depends on the time between two collisions (τ_p). If this time is long, the spin will have enough time to precess between two collisions. The spin relaxation time τ_s is found to be [53]:

$$\frac{1}{\tau_s} \sim \Omega^2 \tau_p \tag{1.30}$$

This mechanism often dominates in III-V semiconductors and 2D structures. In chapter IV, we study the spin dynamics of in the L-valley of GaAs where a very efficient D'Yakonov-Perel mechanism is expected.

1.3.2 Elliott-Yafet Mechanism

The Elliott-Yafet mechanism was first proposed by Elliott [54], who realized that electron spins in the conduction band can relax via ordinary momentum scattering on phonons or impurities due to the spin-orbit coupling as shown in Figure 1.7.

The calculation of the spin relaxation time due to the EY mechanism for III-V semiconductors can be performed analytically in a simple approach. It can be written as [50]:

$$\frac{1}{T_{s1}(E_k)} = A(\frac{\Delta_{SO}}{E_g + \Delta_{SO}})^2(\frac{E_k}{E_g})^2\frac{1}{\tau_p(E_k)} \tag{1.31}$$

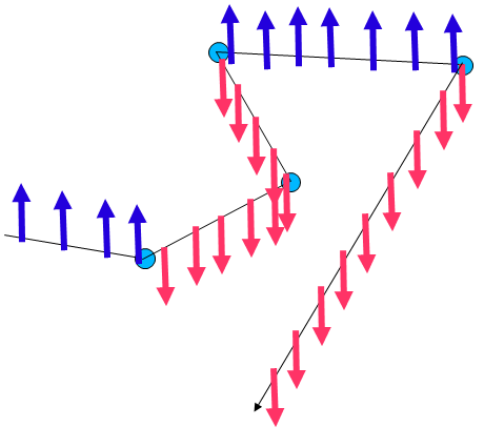

Figure 1.7: Schematics of the Elliott-Yafet mechanism : spin flip processes

where $\tau_p(E_k), T_{s1}(E_k)$ are the momentum scattering time and the spin relaxation time at energy E_k, respectively. E_g is the energy bandgap, Δ_{SO} is the spin-orbit splitting of the valence band. The numerical factor A depends on the dominant scattering mechanism (impurities at low temperatures and phonons at hight temperatures). Equation 1.31 shows that EY mechanism is important for narrow-gap semiconductors with large spin-orbit splitting.

1.3.3 Bir-Aronov-Pikus Mechanism

This mechanism is first proposed by Bir et al. [55]. They demonstrated that this spin relaxation mechanism mainly takes place in p-type semiconductors. It occurs during the diffusion process including an electron and a hole. Their spins relax simultaneously by the exchange interaction. Therefore, the probability of electron-hole scattering directly determines the efficiency of this mechanism. That's why at low temperature in heavily p-doped semiconductors, this mechanism is dominant.

1.3.4 Electron spin relaxation due to the Hyperfine-interaction

This mechanism finds its origin from the interaction between the magnetic momentum of nuclei and electrons. The electron spin can interact with the spins of the lattice nuclei, which being normally randomly oriented, provide a randomly varying effective

magnetic field acting on the electron spin. Usually the corresponding relaxation rate is rather weak compared to other mechanisms, but it may become important for localized electrons, when other mechanisms associated with the electron motion are quenched (as for example, for electrons in quantum dots).

1.3.5 Exciton spin relaxation mechanism

The exciton spin relaxation is another important process that gives a contribution to spin relaxation in semiconductor heterostructures at low temperature. The theory of exciton spin relaxation has been elaborated by Maialle et al. [56] and observed in GaAs quantum wells [57–60], in which the exciton spin relaxation mechanism is similar from a formal point of view to the BAP mechanism as the electron-hole Coulomb exchange interaction can be considered as an effective magnetic field. This process involves two components: spin flips through the exchange interaction and the "motional-narrowing" process through the scattering of the excitation center of mass.

1.4 Electrical spin injection into semiconductors probed by Spin Light Emitting diodes (Spin-LEDs)

Efficient generation of spin currents in semiconductors is the fundamental requirement of semiconductor-based spintronic devices. Different techniques can be used to create a spin accumulation and a spin current in a semiconductor. One can cite optical orientation by circularly polarized light [22], spin Hall effect [61], spin caloritronics [62], spin pumping [63], and electrical spin injection from a magnetic electrode [9,27,64–66]. In this section, we are going to concentrate on this last method that is well suited for electrical devices operating at room temperature.

In the field of electrical spin injection, spectacular results have been obtained using spin injectors based on dilute magnetic semiconductors [27], such as (Be)ZnMnSe. Unfortunately, Room Temperature (RT) operation has been impossible so far because of the very low Curie temperature of these compounds. High spin injection efficiencies

have also been reported by using GaMnAs as a spin injector [67], but still at relatively low temperature compared to 300 K. In contrast, electrical spin injection using FM metals as spin injectors has already been demonstrated at RT [9]. These injectors are the most efficient in view of operation at room temperature thanks to Curie temperature of FM metals well above 300 K. However, as presented in the following, a fundamental obstacle must be overcome in order to use such electrodes.

1.4.1 Problem of impedance mismatch in the diffusive regime

This section is devoted to the mechanism of spin injection at the interface between a ferromagnetic conductor (FM) (typically a 3d magnetic metal), and a semiconductor (SC) [68]. We will consider the specific problem of spin injection in a diffusive picture beyond a ballistic range. This approach is adapted from the Valet-Fert theory [69] of spin injection in metallic magnetic multilayers related to the Giant Magneto-Resistance (GMR) and extended to the case of a single FM/SC interface [7]. This is of a particular interest to understand the spin depolarization processes occurring at the FM side that prevent a massive injection of spins in the semiconductor part. This is known as the 'impedance mismatch' problem [70]. Nonetheless, we will show how the inclusion of a spin-dependent interfacial resistance e.g. a spin-conserving tunnel barrier (I) at the FM/SC interface to form a FM/I/SC system can solve such 'impedance mismatch' to restore a significant current spin-polarization in the semiconductor part.

Schmidt et al. [70] were the first authors to put forward the difficulty to inject, by electrical means, spins into a semiconductor from a ferromagnetic reservoir by taking benefit of the 'natural' spin-polarization of the current in a bulk FM material. This spin polarization of the current in the FM is due to different density of states at the Fermi level for the two spin species, leading to different momentum scattering times, and thus to different conductivities. In the Mott model [71], the two currents propagate in two parallel channels. The physical issues involved in the problem of spin injection are presented in Figure 1.8. As illustrated by Figure 1.8 (a), the flow of electrons is spin polarized far on the left in the ferromagnetic reservoir FM with a characteristic value β [69], equal to a fraction of unity, and non-polarized far on the right in the non-

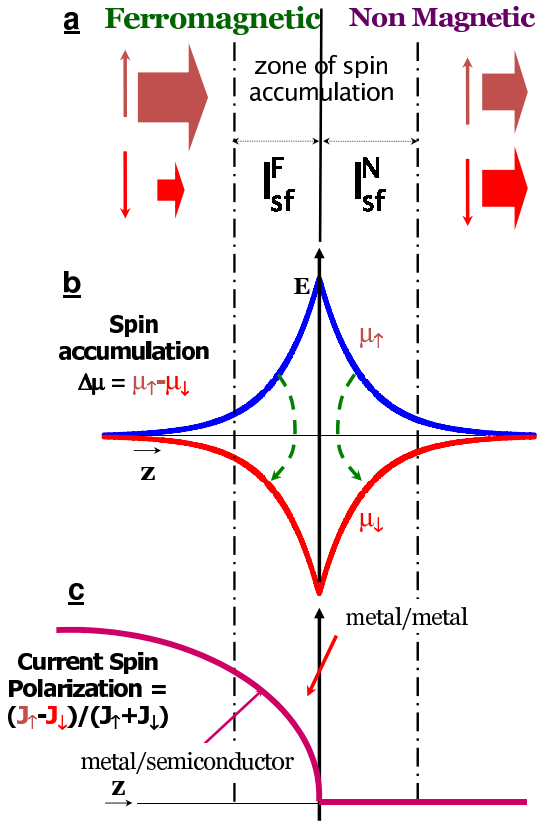

Figure 1.8: (a) Spin up and spin down currents far from an interface between ferromagnetic and nonmagnetic materials (outside the spin accumulation zone). (b) Splitting of the chemical potentials $\mu\uparrow$ and $\mu\downarrow$ near the FM/N interface. The arrows symbolize the spin flips induced by the out of equilibrium spin-split distribution and governing the depolarization of the electron current between the left and the right. (c) Variation of the current spin polarization when there is an approximate balance between the spin flips on both sides (metal/metal) and when the spin flips on the left side are predominant (metal/ semiconductor for example). [5]

magnetic conductor N. Near the interface over a region of a certain extension, there must be a transfer of current between one of the spin channel (spin ↑ channel on the figure) to the other one. A spin accumulation appears in the region of the interface, characterized by a splitting $\Delta\mu$ between the electro-chemical potentials of the spin ↑ and spin ↓ carriers, as shown in Figure 1.8 (b).

Such spin accumulation profile near the interface is characterized by a positive gradient in the FM region (left part) and a negative gradient in the non magnetic region (right part) giving rise to a respective negative diffusive spin-polarized current on the left and a positive spin-polarized current on the right. It results in a gradual drop of the spin-polarized current in the FM material when the electrons approach the interface and, inversely, an increase of the spin-polarization when the electrons approach the interface at the N side (from its zero value at infinity). Such diffusive spin-currents write simply as the product of the unpolarized diffusive constants times the gradient of the out-of equilibrium spin density (Δm) according to:

$$\vec{J_+} - \vec{J_-} = eDg\vec{r}ad(\Delta m)\delta(j_+ - j_-) = eDdiv(\Delta m) \tag{1.32}$$

The steady state is reached when the number of spin flips generated by this out of equilibrium distribution is just what is needed to balance the ingoing and outgoing spin fluxes as seen from the general law of spin conservation which yields to:

$$div(\vec{J_+} - \vec{J_-}) = div[\delta(j_+ - j_-)] = e\frac{\Delta m}{\tau_{sf}} \tag{1.33}$$

where j_+ and j_- are the respective + and - spin currents, Δm is the out-of-equilibrium spin density profile, e the electron charge and τ_{sf} the spin relaxation time. In that sense, due to spin diffusion, the spin accumulation is not localized just at the interface but extends over a distance of the order of the spin diffusion length, respectively l_{sf}^F on the left and l_{sf}^N on the right. The spin diffusion length l_{sf}^N in the nonmagnetic material can be expressed as a function of τ_{sf} and the diffusion constant D or equivalently the density of states $N(E_F)$ and the resistivity ρ_N by:

$$l_{sf}^N = \sqrt{\frac{D\tau_{sf}}{3}} = \sqrt{\frac{\tau_{sf}}{4e^2N(E_F)\rho_N}} \tag{1.34}$$

in a metal or a degenerate semiconductor and by:

$$l_{sf}^{N} = \sqrt{\frac{k_B T \tau_{sf}}{2ne^2\rho_N}} \tag{1.35}$$

in the non-degenerate regime of a semiconductor [68]. The resolution of the standard equation for diffusive spin dependent transport found by merging equation 1.32 and 1.33 leads to an exponential decrease of the spin accumulation splitting $\Delta\mu$ as well as out-of-equilibrium spin densities on both sides of the interface, respectively as $exp(\frac{z}{l_{sf}^{F}})$ and $exp(-\frac{z}{l_{sf}^{N}})$ as shown in Figure 1.8 (b), with continuity at the interface of $\Delta\mu$.

From an alternative point of view, the progressive depolarization of the spin current at the FM side is due to the spin flips related to this spin accumulation. When the FM is a metal and N a semiconductor the density of states (DOS) is much higher in the FM and similar spin accumulation splittings on both sides correspond to a much higher spin accumulation density (number of accumulated spins) in the FM. For similar spin relaxation times in the the FM and N, this leads to a much higher number of spin flips in the FM, so that the depolarization of the spin current occurs in the FM before the interface (see curve Figure 1.8 (c)). The same depolarization also occurs if the DOS are similar but the spin lifetime is much shorter in the ferromagnet. Quantitatively, it can be shown that the polarization of the current just at the interface is [7,72,73]:

$$(SP)_I = \frac{j_+ - j_-}{j_+ + j_-} = \frac{\beta}{1 + r_N/r_F} \tag{1.36}$$

where, in the notation of ref. [7], the specific resistances r_i are the product of the corresponding resistivity $\rho_i \propto N(E_F)^{-1}$ and the spin diffusion length l_{sf}^{i} according to $r_N = \rho_N l_{sf}^{N}$ and $r_F = \rho_F^* l_{sf}^{N}$. The resistivities of the majority spin (+) and minority spin (-) channels in the FM are written as: $\rho_{\pm}^{N} = 2\rho_N$ and $\rho_{\pm}^{F} = 2[1 \mp \beta]\rho_F^*$. From Eq. 1.36 above, the current is almost completely depolarized when it enters the semiconductor as $r_N \gg r_F$ that is, for example, if the resistivity is much smaller, we will say that this is in the condition of "conductivity mismatch".

To restore the spin polarization of the current inside the semiconductor, it is then necessary to increase the proportion of spin flips on the N side by increasing the spin accumulation on the N side with respect to its value on the FM side. Such a discontinuity of the spin splitting can be brought by a spin-dependent interface resistance of the form $r_{+(-)} = 2r_b^*[1 - (+)\gamma]$ (typically a tunnel junction resistance (see Figure 1.9);

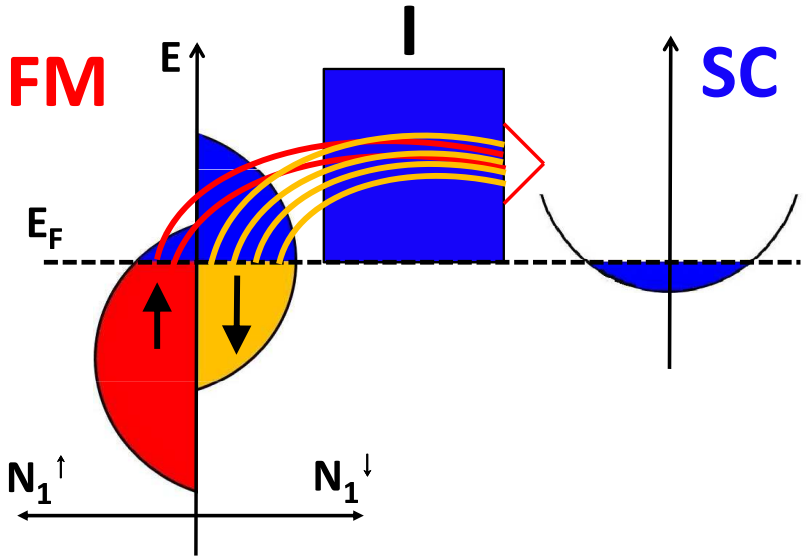

Figure 1.9: Tunnel junction with different tunneling probabilities for the two spin species that can be modeled by a spin dependent interface resistance [6].

note that γ is the usual notation for the interface spin asymmetry in CPP-GMR, the notation being rather P in tunneling).

This interface resistance introduces, in general, a sufficiently large spin-dependent discontinuity of the electro-chemical potentials at the interface according to the following equations:

$$\mu_{+(-)}(z=0^+) - \mu_{+(-)}(z=0^-) = r_{+(-)} j_{+(-)}(z=0) \tag{1.37}$$

and an enhancement of the spin accumulation in N which increases the proportion of spin flips on the N side and restores the current polarization in N. With such a spin-dependent interface resistance, the spin polarization of the current at the interface (in the limit of low currents) equals [7,72,73]:

$$(SP)_I = \left(\frac{j_+ - j_-}{j_+ + j_-}\right)_I = \frac{\beta r_F + \gamma r_b^*}{r_F + r_N + r_b^*} \tag{1.38}$$

and then decreases exponentially as $exp(-z/l_{sf}^N)$ on the nonmagnetic side. Eq. 1.38 expresses the gradual rise of the current spin-polarization as the interfacial resistance r_b^* increases. We see from Eq. 1.38 that an intermediate value of the current spin polarization is partly restored for $r_b^* \simeq r_N$, as illustrated by the example of Fig.3 and that the polarization reaches the spin asymmetry coefficient γ of the interface resistance for

$r_b^* \gg r_N + r_F$.

As presented in the previous paragraph, an efficient electrical spin injection from

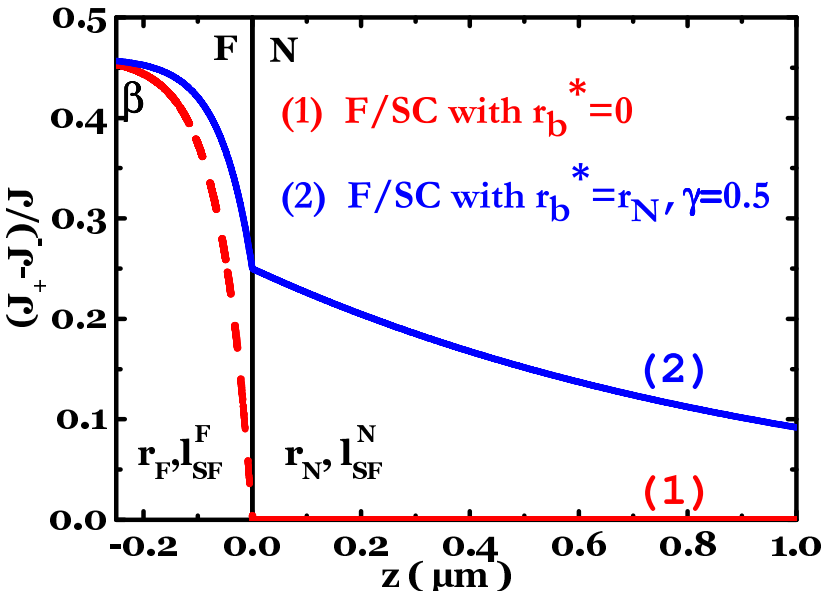

Figure 1.10: Current spin polarization at an interface between a ferromagnetic metal FM and a semiconductor N. The calculation has been performed for F = Co with $r_F = \rho_F^* l_{sf}^F = 4.5 \times 10^{-15} \Omega m^2$, $\beta = 0.46$, $l_{sf}^F = 60$ nm from CPP-GMR data on Co, and for N=GaAs with $r_N = 4.5 \times 10^{-9} \Omega m^2$, $l_{sf}^N = 2$ μm derived from room temperature data on n-type GaAs (n = $10^{16} cm^{-3}$). The blue solid lines are calculated with a spin dependent interface resistance ($r_b^* = r_N = 4 \times 10^{-9} \Omega m^2$, $\gamma = 0.5$) and the red dashed lines without an interface resistance. [7].

a FM metal into a semiconductor can only be achieved in the presence of a tunnel barrier between them. Two kinds of tunnel barriers have been successfully used. The first one consists in a Schottky barrier obtained through the engineering of the doping concentration of the semiconductor at the interface with the metal [33,65]. The second type of tunnel barrier is composed of a thin insulator layer (Al_2O_3, SiO_2, GaO, or MgO) inserted between the FM layer and the semiconductor [66,74–76].

1.4.2 Spin Light Emitting diodes as a tool to detect and quantify electrical spin injection

Several methods have been used to evidence electrical spin injection into semiconductors. Spatially resolved Kerr rotation technique has been employed to image spin

injection into lateral semiconductor channels [77]. Non-local full electrical measurements are also employed in a lateral geometry [78], as for example in the three-terminal geometry [32,79]. In this case the spin injection is probed by a voltage measured between the injector and a reference contact placed at a distance much larger than the spin diffusion length in the semiconductor channel. The Hanle effect is used to destroy the spin accumulation generated in the semiconductor part below the electrode. In this part, we are going to describe the optical technique used in this thesis. The efficiency of the electrical spin injection is measured thanks to an hybrid FM/tunnel barrier/SC device called a Spin Light Emitting diode (Spin-LED), where the circular polarization of the electroluminescence probes the electron spin polarization degree in the semiconductor. This concept of combining electrical spin injection and optical detection was originally proposed by G. Aronov and E. Pikus [80]. This technique allows to quantify the spin polarization of the injected carriers in absolute value. It is well suited in the case of spin injection into III-V semiconductors and takes benefit from their direct bandgap. A typical Spin-LED device structure (with a InGaAs/GaAs QW) with a MgO tunnel barrier is shown in Figure 1.11 (left panel). An example of the band diagram for a MgO based Spin-LED is also shown in the right panel.

The operation principle of a Spin-LED is the following: spin polarized electrons

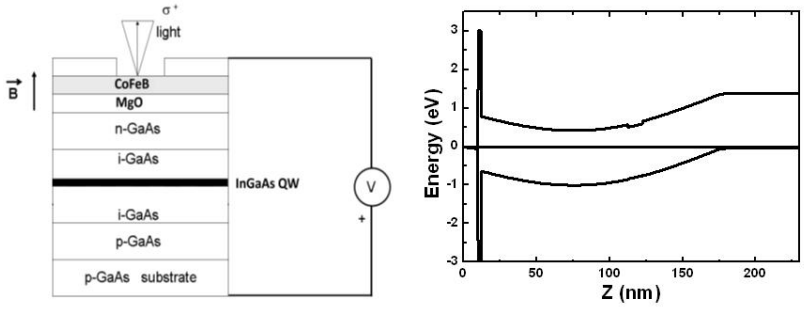

Figure 1.11: Left: Scheme of principle of a spin-LED. Right: Typical band diagram for a MgO-based spin-LED from 1D-Poisson-Schroedinger simulator [8].

from the FM metal electrode will be injected electrically into the SC by applying a forward bias (with respect to the P-I-N junction) to the device. These electrons have a spin polarization along the growth axis of the structure (Oz) thanks to the application of an external magnetic field B along this axis. Once these electrons are captured by the Quantum Well (QW), they recombine radiatively with the unpolarized holes coming from the substrate. The corresponding electroluminescence (EL) will be circularly

polarized if the electrons have kept their spin orientation after the injection, capture and recombination processes.

If electrons with a spin polarization aligned in the FM along Oz are injected into the semiconductor, the polarization of the electroluminescence of the Spin-LED detected along (Oz) will be easily related to the spin polarization degree of the electrons P_s ($P_s = (N_n^+ - N_n^-)/(N_n^+ + N_n^-)$ where N_n^+ and N_n^- are the spin up and down populations respectively) in the QW thanks to the optical selection rules [81]. If one considers the electron-heavy hole transition, the circular polarization of the light P_c ($P_c = (I^+ - I^-)/(I^+ + I^-)$ where where I^+ (I^-) is the right (left) circularly-polarized EL component) is directly equal to the electron spin polarization P_s (an absolute value). Note that if the luminescence is detected perpendicular to the growth axis, the electroluminescence corresponding to the recombination in the QW of electron and heavy-hole should not be circularly polarized due to the symmetry of the heavy-hole wavefunction [1]; this makes the interpretation of the experiments performed with this geometry very difficult [64]. A typical EL spectrum of the Spin-LED at 25 K is shown in Figure 1.12. The EL peak corresponds to the radiative recombination of excitons involving electrons and heavy-holes.

Due to the shape anisotropy of the thin magnetic electrode, the spontaneous magne-

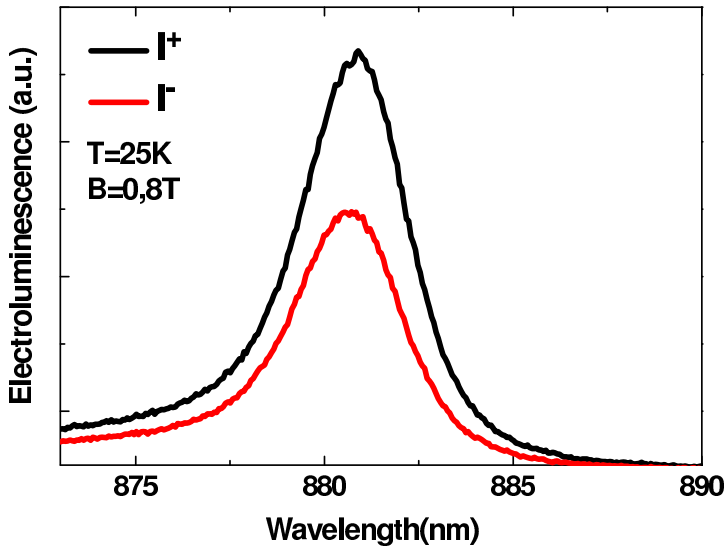

Figure 1.12: Typical electroluminescence spectra for a Spin-LED at 25K for I^+ and I^- components (here the QW embedded in the spin-LED is a 10 nm thick $In_{0.1}Ga_{0.9}As$/GaAs QW).

tization stays within the plane. An external magnetic field is thus necessary to rotate it along (Oz). This magnetic field can induce spurious effects: Magnetic Circular Dichroism (MCD), leading to different absorption for the two circularly polarized components of the light, as well as a thermal spin polarization of carriers due to Zeeman splitting. Usually in the range of temperature explored, for a magnetic field of 0.8 T along (Oz), both the circular polarization due to Magnetic Circular Dichroism (MCD) [74] through the FM layer and spurious effect of electron Zeeman splitting in the QW [33] can be estimated to be inferior to 1% in our samples.

Up to now, we have considered that the circular polarization degree of the luminescence is identical to the spin polarization of the electrically injected carriers in the semiconductor QW structure according to the quantum selection rules. In fact, this description is oversimplified because the measured Continuous Wave (CW) electroluminescence polarization depends on the electrical spin injection efficiency at the FM/oxide/SC and also on all the spin relaxation mechanisms which occur in the SC part in particular in the QW. Taking into account the electron lifetime τ and the spin relaxation time τ_s in the quantum well, the circular polarization measured in CW electroluminescence experiments writes [82]:

$$P_C = FP_s, F = \frac{1}{1+\frac{\tau}{\tau_s}} \tag{1.39}$$

where P_s is the spin polarization of the electrons injected in the quantum well. The electron lifetime τ and the spin relaxation time τ_s in the quantum well have to be determined separately by complementary measurements as for example by time and polarization-resolved photoluminescence as we will see in chapter 3.

1.4.3 State of the art: breakthrough due to MgO tunnel barriers

The first spinLEDs with FM injectors were taking benefit from the natural Schottky barrier that forms between the FM and the n-doped SC. The measured EL polarization were about a few percent [33]. Thanks to the optimization of the Schottky barrier by a gradual doping increasing close to the interface, the group of Jonker in the Naval

Research Laboratory (Washington, the USA) managed to measure a maximum EL circular polarization degree of $P_{CExp.}$=32% for B=4 T at a temperature of 4 K with a Fe ferromagnetic spin injector [34]. Several groups have then successfully injected spin-polarized electrons by using this method [83–85]. An alternative way to achieve an efficient electrical spin injection is to insert between the ferromagnetic metal and the semiconductor an amorphous insulating layer as aluminium oxide which acts as a tunnel barrier. This technique has been first demonstrated by V. F. Motsny et al. [74]. The results in terms of spin injection efficiency are comparable with the best ones obtained with a Schottky barrier, even if the charge injection efficiency is lower [75].

In 2005 a spectacular breakthrough was realized by Jiang et al. [9] in the group of

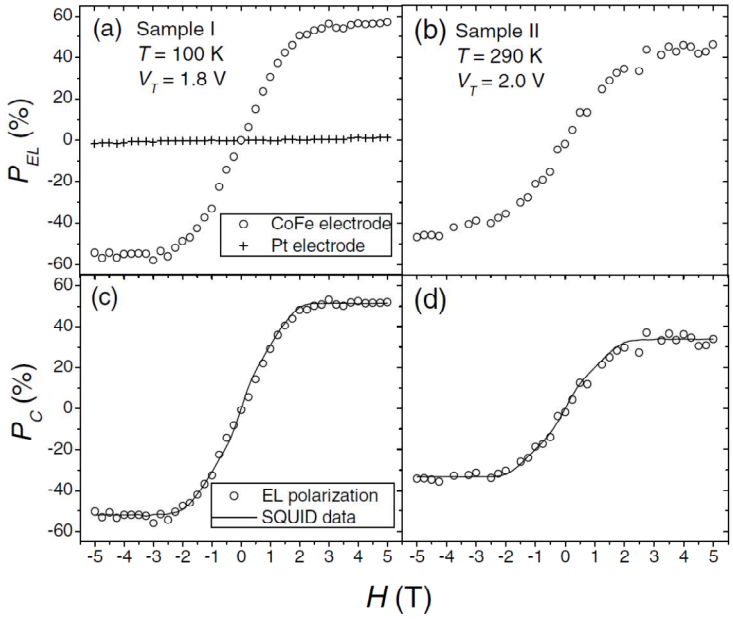

Figure 1.13: Magnetic field dependence of the EL circular polarization P_{EL} [(a) and (b)] (raw data) and P_C [(c) and (d)] (after substraction of the spurious signal increasing linearly with the applied magnetic field) for spin-LED I (8% of Al) at 100 K and spin-LED II (16% of Al) at 290 K (open circles). The crosses in (a) are the P_{EL} of a control sample with a Pt electrode. The solid lines in (c) and (d) show the field dependence of the CoFe moment measured with a SQUID magnetometer at 20 K, which has been scaled to allow comparison with P_C. [9]

S.S. Parkin at IBM San Jose (the USA). They have demonstrated that polycrystalline MgO tunnel barriers, already widely used in Tunnel Magnet Resistance based devices, yield very efficient spin injection into AlGaAs. This effect might be attributed to the symmetry-based spin selection rules during the tunneling transfer of carriers [10]. An EL circular polarization as high as 52% is evidenced at 100 K and is still around 32%

at room temperature (Figure 1.13) [9].

Let us precise some important theoretical features concerning Ferromagnetic

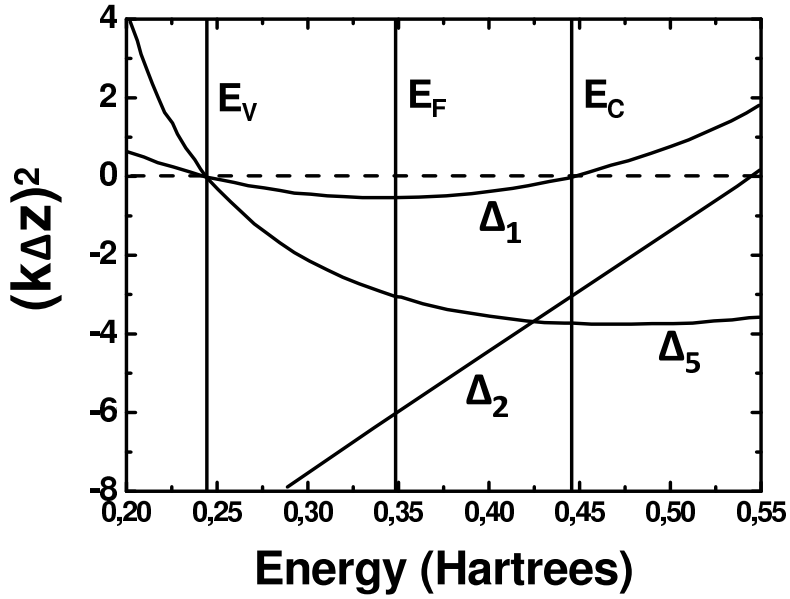

Figure 1.14: Dispersion curves E(k^2) at $k_{\|} = 0$ for MgO (001). k and $k_{\|}$ are repectively the normal (z axis) and in-plane components (with respect to the MgO layer) of the vector k. k^2 is given in units of Δz^{-1}, with Δz corresponding to the interplanar spacing in MgO. The energy is given in Hartree (1 Hartree=27,2 eV). The region of interest is within the energy gap of MgO at the Fermi level E_F. The values of k^2 are negative ($k^2 = (i\lambda)^2$), corresponding to evanescent wavefunctions of the type $\Psi(z) = Aexp(-2\lambda z)$. [10]

metal/MgO interfaces. Butler et al. [10] have predicted in 2001 a strong tunnel magnetoresistance for Fe(100)/MgO(100)/Fe(100) tunnel junctions. Their calculations included the role of the symmetries of both the conduction states in the electrodes and the evanescent states in the barrier. At the Fermi level, majority spin conduction states in Fe exhibit Δ_1 (spd hybridization), $\Delta_{2'}$ and Δ_5 symmetries. On the contrary, minority spin conduction states in Fe present Δ_2, $\Delta_{2'}$ and Δ_5 symmetries. In MgO, the attenuation of the evanescent wavefunction will be much less important for Δ_1 states than for all the others. As we can see in Figure 1.14, the imaginary part of the wavevector (that is related to the exponential attenuation of the wavefunction) at the Fermi level is smaller in absolute values than for the other symmetries. In consequence, the tunneling probability will be more probable for electrons with a Δ_1 character, this character being only present for majority spin electrons. This is the origin of the spin filtering effect, that should increase with the thickness of the MgO tunnel barrier (provided

that the direct tunnel regime is the dominant process). Identical calculations have been performed for CoFe/MgO/CoFe (bcc(100)) tunnel junctions, and the effect was predicted to be even stronger in this case [86]. Experimentally, a 220% Tunnel magnetoresistance [87] (and more recently 300% [88]) was observed in CoFe/MgO/CoFe junctions at room temperature. This effect is even better in CoFeB/MgO/CoFeB junctions (TMR of 600% [89]) that presents the advantages (compared to CoFe) to be grown in a full bcc crystalline lattice afer post growth annealing. This has triggered the interest for CoFeB/MgO as a very promising injector even if no calculations are availaible up to now for the CoFeB/MgO/GaAs interface. Note that the growth of a MgO layer on GaAs is possible due to their lattice parameters: a_{MgO}=0,421 nm and a_{GaAs}=0,565 nm, giving the relationship $4a_{GaAs} = 3a_{MgO}$ with a mismatch of less than 1%. The efficiency of CoFeB/MgO/AlGaAs as a spin-LED injector was demonstrated [90] and the influence on the spin injection efficiency of (i) the crystalline or amorphous nature of the MgO tunnel barrier, (ii) the MgO thickness and (iii) the system temperature has been investigated (the CoFeB was mainly amorphous in this case).

From a more general point of view, let us mention the different evolutions that have appeared in the field of electrical spin injection probed by the spin-LED technique in the past years. Guided by the fact that the achievement of spintronic devices necessitates sufficiently long spin relaxation times to manipulate or store the spin orientation of the injected carriers, electrical spin injection has been implemented in semiconductor quantum dots [91,92]. In addition, the optical readout has been performed on a single quantum dot [93]. The production of coherent circularly polarized light by Spin Vertical Cavity Surface Emitting Lasers (spin VCSEL) was demonstrated (a reduction of the threshold current was observed in these systems) [28]. Electrical spin injection in the pulsed regime (in the GHz range) has been investigated [94,95]. In order to perform electrical spin injection in vertical geometry without the need for an external magnetic field, injectors with Perpendicular Magnetic Anisotropy (PMA) have been tested. EL circular polarization of a few percent have been measured up to now [35,96,97]. Finally, the electrical spin injection into Silicium (recently the use of a graphene layer as a tunnel barrier to inject spin polarized electrons into Si was proposed [98]) and Germanium, materials widely used in the conventional microelectronics, was also intensively explored [31,32,66,97,99].

Chapter 2

Experimental Set-ups

2.1 Time-resolved Photoluminescence spectroscopy 41
2.1.1 Excitation laser source 41
2.1.2 Streak camera detection 42
2.1.3 Polarization resolution 45
2.2 Polarization-resolved Electroluminescence set-up 45
2.2.1 CCD camera detection 46
2.2.2 Electrical generator 47
2.3 Polarized Photoluminescence Excitation spectroscopy . . 47
2.4 Cryogenics and magnetic field 49

This chapter deals with the description of three experimental set-ups dedicated to optical spectroscopy: time-resolved photoluminescence, electroluminescence and polarized photoluminescence excitation.

First we present the time-resolved photoluminescence (TRPL) experimental set-up, including the excitation laser and detection devices. This set-up plays a key role in analyzing the spin relaxation mechanisms in each chapter.

Then in the following part, we present the polarization-resolved electroluminescence (EL) measurement bench. The analysis of the electrical spin injection in the hybrid metal/semiconductor heterostructures which are described in chapter 3 is based on this experimental set-up.

The description of the polarized photoluminescence excitation (PLE) measurement is reported in the third section. A double-modulation lock-in technique is introduced in this section as well. This set-up was mainly used for the study of the L-valley electron spin dynamics presented in chapter 4.

2.1 Time-resolved Photoluminescence spectroscopy

The principle of the time-resolved photoluminescence (TRPL) experimental set-up is shown in Figure 2.1. A pulsed laser beam is focused onto the analyzed sample and its helicity can be modulated by optical waveplate elements. The photoluminescence from the sample is first collimated to analyze the corresponding polarization, then focused onto the entrance slit of a spectrometer. The luminescence, spectrally dispersed by this spectrometer, is then detected by an ultrafast detector (streak camera) which is synchronised with the laser pulses. The different elements composing the experimental set-up will be described in this section.

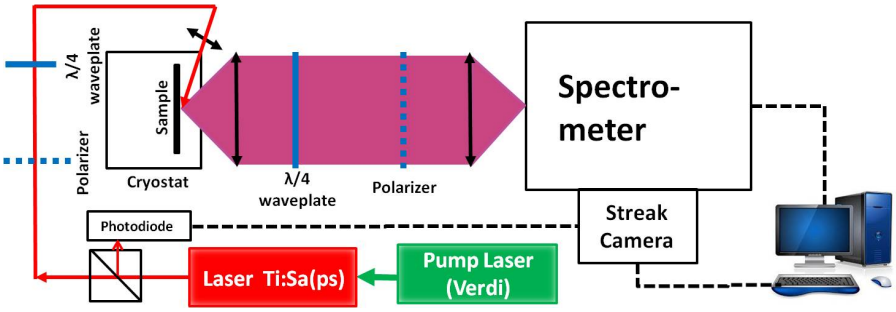

Figure 2.1: Time Resolved Photoluminescence Spectroscopy Setup

2.1.1 Excitation laser source

The principal excitation source is a mode-locked Titanium-Sapphire(Ti:Sa) laser pumped by a continuous wave Coherent laser(VERDI-V10). The VERDI source is an all-solid-state, single-frequency 532nm laser generating power up to 10W. This pump laser uses a $Nd : YVO_4$ (Neodymium Doped Yttrium Orthovanadate) crystal as the amplifying medium, that has an absorption wavelength around 809 nm and an emission wavelength around 1064 nm. This crystal is pumped by two laser diodes and placed into a mono-mode cavity. The emission wavelength 532 nm is achieved by doubling the fundamental frequency (1064 nm) with a LBO crystal. This VERDI laser output power is very stable thanks to a temperature cooling loop and a delivery power.

The output of VERDI then pumps the Tsunami Ti:Sa laser in which the active material is a sapphire crystal doped with titanium ions (Ti:Al_2O_3). This Ti:Sa laser

can operate in a pulsed regime with a repetition rate of 80 MHz in two modes : femtosecond mode (temporal pulse width: 100 fs) and picosecond mode (pulse duration of about 1.5 ps). In our experiment, we use the picosecond mode that corresponds to the best balance between spectral width and pulse time duration.

To achieve the pulsed operation mode, this Ti:Sa laser utilizes a mode-locking technique which combines self-phase modulation and Kerr effects in the crystal [100]. The longitudinal optical modes in the laser cavity are synchronized by optical Kerr effect. Due to the power density distribution of the laser beam characterized by a Gaussian shape, the crystal acts as a converging lens. This refractive index variation is responsible for the nonlinear optical effects of self-focusing and self-phase modulation. The result is a "locking" of the modes of the cavity which favours the pulsed operation. However, the mode-locked regime cannot start automatically, it requires an acoustic-optical modulator to initialize the temporal regime. At the end, a dispersion compensation of the group velocity is employed. It is realized by a Gires-Tournois Interferometer (GTI).

The advantage of such an oscillator is its tunable wavelength, thanks to an interference Lyot filter. The main characteristics of the picosecond laser system are given in Table 2.1.

Repetition Frequency	Spectral Range	Average Power	Pulse Energy	Pulse Duration	Spectral Width
80 MHz	680-990 nm	0.4-2 W	5-25 nJ	1.2-1.8 ps	$\approx$ 1.2 meV

Table 2.1: Ti:Sa laser main characteristics

2.1.2 Streak camera detection

The principle of a streak camera is shown in Figure 2.2. The PL signal from the spectrometer is focused on a photocathode. Depending on the wavelength range of the detected light, we have used a S1 or a S20 photocathode (for the spectral sensitivity see the inset (c) of Figure 2.2). The tube will then generate photo-electrons in proportion of the incident signal intensity. The electrons are accelerated and multiplied by a MCP (micro-channel plate) before being collected by a phosphorous screen, the signal is then

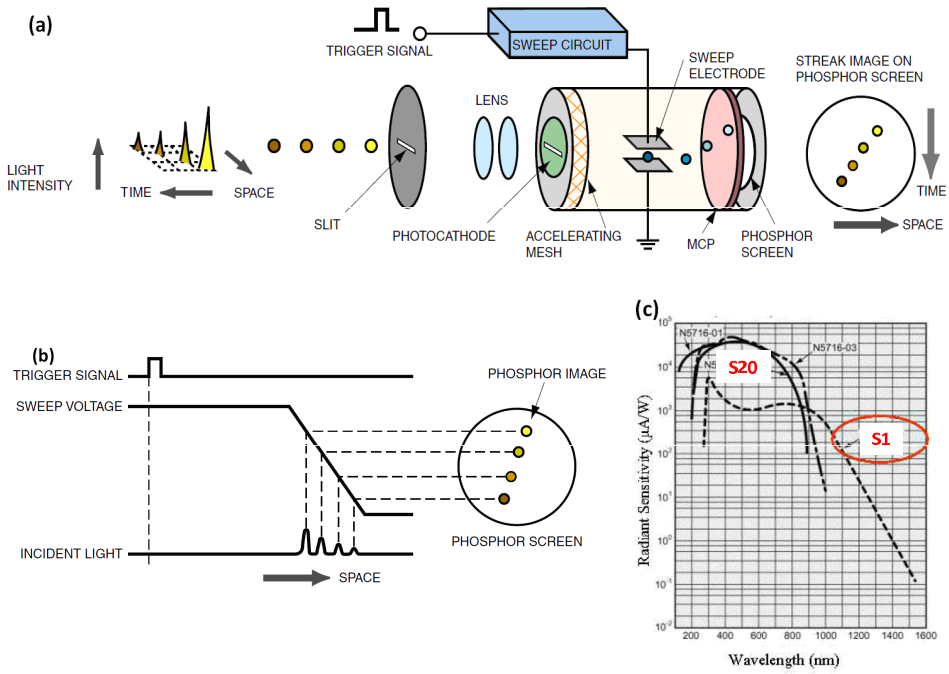

Figure 2.2: (a) Operation principle of the streak camera; (b) Sketch of the sweeping mechanism responsible for the time resolution; (c) Spectral sensitivity of the photocathodes

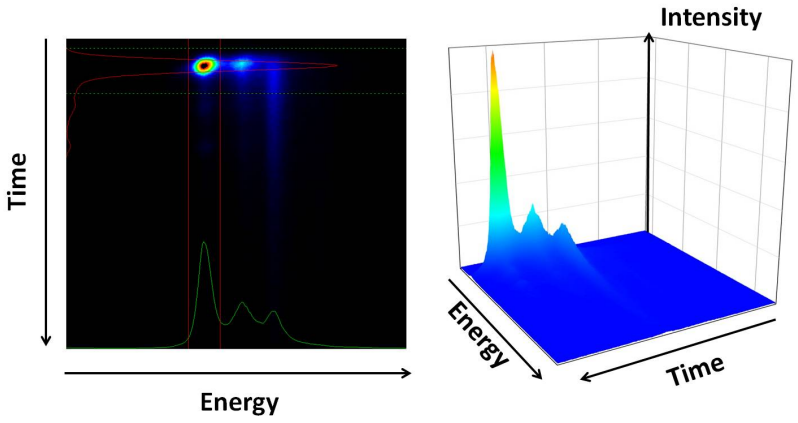

Figure 2.3: An example of image obtained with a streak camera

recorded by a CCD (Charged Coupled Device) camera. An ultrafast voltage slope is applied to deviation electrodes, synchronised with the laser pulses thanks to the ultrafast photodiode. We thus obtain a three dimensional image as shown in Figure 2.3: the photon energy dispersion (or wavelength) is given by the x-axis, the time dependence is given along the y-axis and the signal intensity is represented by colors.

Spectral resolution

The spectral resolution is dictated by the spectrometer (Jobin-Yvon Triax 320 or iHR320) placed before the streak camera (S1 or S20) and equipped with three gratings. The characteristics are presented in table 2.2.

	Grating (grooves/mm)	Blaze wavelength (nm)	Spectral range (nm)	Dispersion (nm/mm)	Resolution (nm)
Triax	100	450	140	28.2	0.7
	300	250	46	9.4	0.3
	600	300	23	4.7	0.1
iHR	100	450	170	28.2	0.7
	600	300	28	4.7	0.12
	1200	330	14	2.35	0.06

Table 2.2: The characteristics of the Jobin-Yvon Triax 320 (for S1) and iHR320 (for S20) spectrometers. The spectral resolution values are given for a 200 μm width of the slit.

Temporal resolution

The intrinsic time resolution of the streak camera depends on the time range (see table 2.3). However, the effective time resolution depends on the wavelength dispersion of the spectrometer. A larger dispersion produces a larger optical path between the portion of light traveling on the side and on the central optical axis of the grating. Therefore, this difference generates a temporal dispersion which can be minimized by placing a vertical slit inside the spectrometer to reduce the lateral dimension of the beam. The streak camera can operate in 4 different time ranges.

Time range index	Temporal span (ps)	Time resolution (ps) using the 100 grooves/mm grating
1	157	5
2	809	8
3	1542	12
4	2263	17

Table 2.3: Temporal modes of streak camera

2.1.3 Polarization resolution

In optical orientation experiments, the analysis of PL polarization components allows the study of the spin dynamics of photo-generated carriers after excitation of the sample by polarized light. The polarization of the exciting laser is modified from linear (Σ^X) to circular polarization (σ^+ or σ^-) by a Glan-Taylor polarizing cube together with a quarter-wave plate whose neutral axis can be rotated (see Figure 2.1). The photoluminescence of the sample contains both counter-polarized (I^-) and co-polarized (I^+) light with respect to the laser excitation (σ^+). The PL polarization analysis is performed by a quarter-wave plate followed by the Glan-Taylor cube on the collimated beam before focusing onto the spectrometer. The images corresponding the two PL components are stored and analyzed separately.

The circular polarization degree is defined as :

$$P_{circ} = \frac{I^+ - I^-}{I^+ + I^-} \tag{2.1}$$

The linear polarization degree of the PL is likewise defined using the linearly polarized components.

2.2 Polarization-resolved Electroluminescence set-up

The principle of electroluminescence (EL) measurements is presented in Figure 2.4. The spin-LED is placed in a magnetic field which will be presented in last section of this chapter. The EL signal is detected in the Faraday geometry. The circular polarization P_c is analyzed similarly as in the time-resolved PL experiments. The tested mesa is excited by square voltage pulses (pulse width=5 μs, repetition rate=50 kHz) to avoid

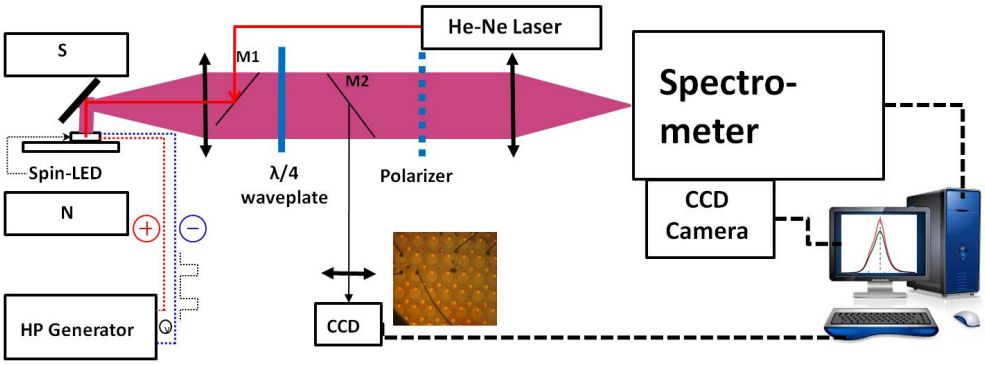

Figure 2.4: Polarization Resolved Electroluminescence Spectroscopy Set-up

spurious effects due to heating. Due to the small size of the mesa (diameter 300 μm) compared to the sample size (2-3 mm^2) and in order to make the optical alignment easier, we first excite the spin-LED with an He-Ne laser source and collect the PL. Once this pre-alignment is made, the EL signal can then be detected and measured. Mirror M2 and a CCD camera following M2 in the set-up are placed in order to make an optical image of the mesa.

2.2.1 CCD camera detection

Spectral resolution

The spectrometer (Princeton Acton SP2500) placed before the CCD camera is equipped with three gratings. Its characteristics are presented in the table 2.4. In the experiments we used the 600 grooves/mm grating to analyze the EL signal.

We usually use a slit of 500 μm corresponding to a resolution of 0.062nm.

Grating (grooves/mm)	Blaze wavelength (μm)	Dispersion (nm/mm)
300	1	6.5
600	1	3.2
1200	0.75	1.52

Table 2.4: Characteristics of the Princeton Acton SP2500 spectrometer gratings.

CCD camera

The camera Spec-10: 100 series from Princeton Instruments is designed with extremely low noise electronics and can measure the EL signal in the near infrared wavelength range. Cooling the CCD down to -120°C effectively strongly reduces dark noise and provides an excellent signal to noise ratio.

2.2.2 Electrical generator

The generator we used in EL experiments to generate electrical pulses is a HP8160A, its characteristics are presented in table 2.5.

Typically, we used 5 μs duration pulses separated by 15 μs. The voltage output

Voltage range(V)	Pulse width	Repetition period
0.1∼9.99	6.0ns∼9.99ms	20ns∼999ms

Table 2.5: Principle characteristics of the generator HP8160A

is tunable. In order to detect the luminescence, the applied voltage must be higher than the threshold voltage of each sample and lower than the voltage corresponding to the damage current density of about 4 mA for a mesa diameter of 300 μm. As the duration of the pulse is very long compared to the different characteristic relaxation times of the system, we can consider that we work in a quasi-stationary regime.

2.3 Polarized Photoluminescence Excitation spectroscopy

In order to measure the electron spin relaxation time in the L-valleys (see chapter 4), we have developed a very specific set-up. First the wavelength of excitation must be extended to the blue region to reach the range of 2.8-3.2 eV to be able to photogenerate electrons in L-valleys. We have thus used a Ti:Sa laser which frequency is doubled by a Spectra Physics GWU system with a LBO non-linear crystal. Second, we need to detect circular polarization rates of a few percent at maximum. In order to get a very high sensitivity in the detection of the luminescence circular polarization (sensitivity of about 0.1 %), we have used a double modulation technique.

The scheme of principle of the polarized Photoluminescence Excitation (PLE) ex-

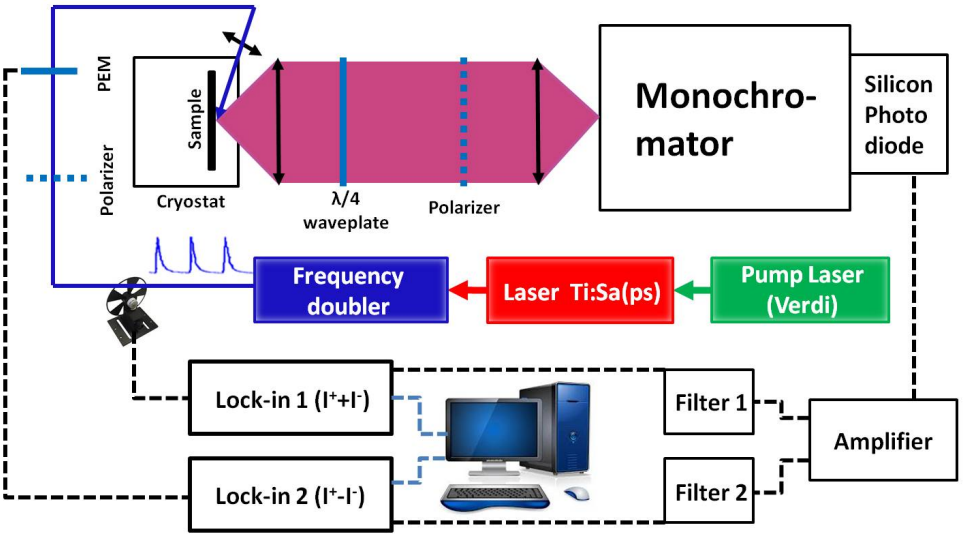

Figure 2.5: Polarized Photoluminescence Excitation Spectroscopy Set-up

perimental set-up is shown in Figure 2.5. The excitation laser passes through a chopper working at $f \simeq 220Hz$, and its helicity is modulated σ^+/σ^- with a photo-elastic modulator (PEM) at a frequency of 50 kHz. In addition to an increased measurement accuracy, this avoids the buildup of a dynamic nuclear polarization [22]. The laser beam propagating perpendicular to the sample surface is focused to a 100 μm diameter spot with an average power of P_{exc}= 15 mW. The photoluminescence is dispersed by a monochromator and then detected by a silicon photodiode. The output of the photodiode is sent on a transimpedance amplifier, followed by two filters and to lock-in amplifiers. In the following, we describe the double modulation technique.

The intensity of the laser after the PEM modulator can be written for the two circularly components:

$$I^+_{laser} = \frac{I_{laser}}{2}(1 + sin(\varphi(t))), I^-_{laser} = \frac{I_{laser}}{2}(1 - sin(\varphi(t))) \tag{2.2}$$

where $\varphi(t) = \frac{\pi}{2} sin(\omega_2 t)$.

The circular polarization of the laser is $P_{claser} = \frac{I^{+laser} - I^{-laser}}{I^{+laser} + I^{-laser}} = sin(\varphi(t))$. The circular polarization of the PL emitted by the sample is $P_C = \frac{I^{+lum} - I^{-lum}}{I^{+lum} + I^{-lum}} = \gamma sin(\varphi(t))$. γ is the circular polarization of the PL emitted by the sample if it is excited

by a 100% σ^+ polarized laser.

Let us consider that the chopper creates a modulation of the PL intensity between zero and I_0. If one takes into account the first harmonic only, the corresponding signal writes: $\frac{I_0}{2}\left(\frac{1}{2}+\frac{2}{\pi}sin(\omega_1 t)\right)$. Let us also develop $sin(\varphi(t)) = sin\left(\frac{\pi}{2}sin(\omega_2 t)\right)$ in $2J_1(\frac{\pi}{2}sin(\omega_2 t))$ (here also only the first harmonic has been taken into account, J_1 is the first order Bessel function). The signal measured by the silicon photodiode then writes (after the $\lambda/4$ plate and the analysis in the detection time):

$$S(t) = \frac{I_0}{2}\left(\frac{1}{2}+\frac{2}{\pi}sin(\omega_1 t)\right)\left(1+2\gamma J_1(\frac{\pi}{2})sin(\omega_2 t)\right) \tag{2.3}$$

that can be developed in:

$$S(t) = \frac{I_0}{4}+\frac{I_0}{\pi}sin(\omega_1 t)+\frac{I_0}{2}\gamma J_1(\frac{\pi}{2})sin(\omega_2 t)+\frac{2}{\pi}\gamma J_1(\frac{\pi}{2})cos((\omega_2+\omega_1)t)+\frac{2}{\pi}\gamma J_1(\frac{\pi}{2})cos((\omega_2-\omega_1)t) \tag{2.4}$$

The first demodulation is performed at low frequency at the pulsation ω_1. The obtained voltage V_{low} is proportional to the PL intensity. The second demodulation is performed at high frequency at the pulsation ω_2. The obtained voltage V_{high} is proportional to the PL intensity multiplied by γ.

The circular polarization P_C of the luminescence is thus proportional to V_{high}/V_{low}. The calibration factor can be found by comparing V_{high}/V_{low} to the circular polarization P_C measured with the usual technique ($\lambda/4$ rotating waveplate) in a case where the detected P_C corresponding to the luminescence detected at the Γ valley is large (for example, by exciting at a photon energy just above the bandgap of GaAs).

The sensitivity obtained with this technique ($\sim 0.1\%$) is much better then the one ($\sim 1\%$) obtained by rotating a $\lambda/4$ plate in front of an analyzer (as in the time-resolved and electroluminescence set-ups presented before).

All the measurements in this part were finished in a low temperature.

2.4 Cryogenics and magnetic field

In PL and EL measurements, samples were placed on the cold finger of a closed cycle helium cryogenerator, allowing operating temperatures in the range 10 K- 300 K. Unless specified in the text, the experiments in this thesis were performed at very

low temperature. In order to generate a magnetic field parallel to the sample plane, we used two permanent magnet cubes. By changing the distance between this two magnets, we can get a magnetic field from 0 to 750 mT.

In EL experiments, Spin-LED samples were placed into a Helmoltz-split magnetic coil providing a maximum magnetic field (B) of 0.8 T normal to the sample plane. The B field is controlled by the power supply. Each current in the coils corresponds to a value of the magnetic field, which is calibrated by a teslameter.

Chapter 3

Electrical spin injection in GaAs-based Spin Light Emitting Diodes (Spin-LEDs) through MgO tunnel barriers

3.1 Influence of the growth technique (Sputtering and Molecular Beam Epitaxy) 55

3.1.1 Spin-LEDs Samples 56

3.1.2 Electroluminescence measurements 57

3.1.3 Influence of the annealing process on the spin injection efficiency 58

3.1.4 Measurement of the electron lifetime and spin relaxation times in the InGaAs/GaAs quantum well by Time and Polarization-resolved Photoluminescence 59

3.1.5 Analysis of the influence of the annealing process on the hysteresis curves of the ferromagnetic layer by SQUID Measurements 62

3.1.6 CoFeB/MgO and MgO/GaAs interfaces analysis by HRTEM and RHEED characterizations 64

3.2 Current dependence of the electrical spin injection 67

3.2.1 Current dependence of the Electroluminescence circular polarization 69

3.2.2 Voltage dependence of the Electroluminescence circular polarization 70

3.2.3 Discussion 71

3.3 Electrical injection at zero magnetic field up to room temperature 76

3.3.1 Sample description 77

3.3.2 Microscopic origin of the Magnetic Perpendicular Anisotropy in the ultrathin CoFeB/MgO injector 78

3.3.3 Optimization of the CoFeB injector 80
3.3.4 Electrical spin injection without magnetic field at 25 K probed by Electroluminescence measurements 81
3.3.5 Electrical spin injection without magnetic field at room temperature 85
3.3.6 Dependence of the electrical spin injection as a function of temperature 87
3.3.7 Dependence of the electrical spin injection as a function of the applied bias 91
3.3.8 Conclusion 92

This chapter is focused on the problem of the electrical spin injection into GaAs. A large number of new semiconductor spintronic devices including spin-transistors [26], Spin Light Emitting diodes (spin-LEDs) [9,34,64,85,101,102] and spin-lasers [28] have been proposed in the past decade. All these systems require a generation of spin currents into the semiconductor material. Among all the methods proposed up to now to generate these spin polarized currents [51,61–63], an efficient way consists in injecting spin polarized electrons from a ferromagnetic injector through a tunnel barrier (to overcome the problem of conductivity mismatch between the metal and the semiconductor [7,9,34,70,85,102]). As explained in chapter I, the quantitative estimation of the spin polarization of the injected carriers is usually performed through polarization resolved electroluminescence in Spin-LEDs. Up to now, CoFe/MgO injectors have exhibited the highest spin injection yield into AlGaAs at low temperature and room temperature (the electroluminescence polarization can reach in these systems up to 50% at 100 K and 32% at 300 K) [9,103]. This high polarization could be due to the non equivalent attenuation of the evanescent wavefunctions during the tunneling process depending on their symmetries and resulting in a spin filtering effect [10,86]. In this chapter, we are going to concentrate on injectors based on this type of MgO tunnel barriers. We first dicuss the influence of the growth method (Molecular beam epitaxy and sputtering) of the MgO tunnel barrier on the spin injection efficiency in order to establish which interface (Ferromagnetic metal/MgO or MgO/GaAs) is crucial for an efficient spin injection. We then analyse the behavior of our injectors as a function of the current injected in the spin-LEDs. Finally, we demonstrate a very efficient electrical spin injection at zero magnetic field that persists at room temperature thanks to a perpendicular injector based on an ultrathin CoFeB layer on MgO.

The results presented in the following are the fruit of a collective work between different laboratories that are involved in the French-Chinese project ANR-NSFC SISTER (electrical control of Spin Injection in Spin-LEDs via spin TransfER effect without magnetic field). The Magnetic/Insulator bilayers have been grown by Y. Lu and S. Liang at the Institut Jean Lamour (IJL) in Nancy in the group of M. Hehn, whereas the semiconductor part of the structures was grown by Molecular Epitaxy at the Institute of Semiconductors (IOS) in Beijing in the group of B. Xu. Lithography processes are

performed by J. Frougier at UMP CNRS Thalès in the group of H. Jaffrès and J.M. George. The superconducting quantum interference device (SQUID), high-resolution transmission electron microscopy (HRTEM) and reflection high-energy electron diffraction (RHEED) characterizations (by X. Devaux) were performed at the IJL .

3.1 Influence of the growth technique (Sputtering and Molecular Beam Epitaxy) of the MgO tunnel barrier on the electrical spin injection efficiency in spin-LEDs

The injector is constituted by two interfaces: the Ferromagnetic Metal (FM)/MgO and the MgO/Semiconductor interfaces. It is still an open question to determine which interface is crucial for an optimal spin injection. We propose to tackle this point by studying CoFeB/MgO/GaAs injectors, where the MgO barrier is grown by two different techniques: Sputtering and Molecular Beam Epitaxy (MBE). CoFeB is a promising candidate as a ferromagnetic layer for Spin-LEDs, because it is easier to obtain a grain-to-grain epitaxial bcc crystalline phase on MgO after the crystallization of CoFeB by annealing, and it could lead to even more efficient electrical spin injection due to the improved spin filtering effect of MgO. This improvement has been in particular observed in Magnetic Tunnel Junctions, where a 600% TMR [89] was measured at room temperature on CoFeB/MgO/CoFeB junctions instead of 220% [87] (and more recently 300% [88]) observed on CoFe/MgO/CoFe junctions. Another advantage of CoFeB is its lower saturation field necessary for rotating the magnetization along the growth axis of the structure (about 1.3 T instead of about 2.2 T for CoFe). On the other hand, successful injection through the MgO/GaAs interface has not been widely explored up-to now [104]. Most of the works concerning MgO tunnel barriers, have investigated the MgO/AlGaAs interface in order to inject spin polarized electrons into AlGaAs/GaAs quantum wells [9,35,90,94,96,103,105–107]. A slight change at the MgO/Semiconductor interface (such as the aluminium content) could have drastic effects on the spin injection yield and a full measurement proving an efficient ($> 10\%$) spin injection through MgO into GaAs has to be done. Finally, the use of light emitters such as InGaAs/GaAs quantum wells [33,84,108] for which GaAs substrates are optically transparent could be a key point in order to build a device working without any external magnetic field with a thick light absorbing perpendicularly remanent injector [96] or for more complex and thicker injectors allowing the electrical switching of the magnetization of the ferromagnetic contact for example by the spin torque effect [109]. In this situation, the collection of light should be optimal through the substrate.

3.1.1 Spin-LEDs Samples

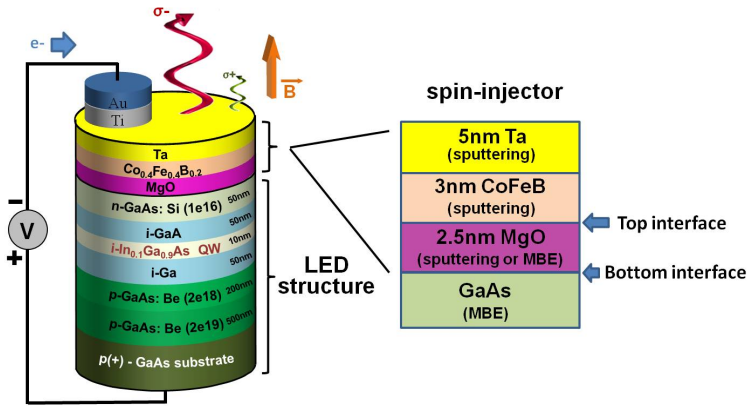

Figure 3.1: Spin-LED structure with a single InGaAs/GaAs quantum well. The CoFeB/MgO/GaAs tri-layers is decomposed in terms of a top interface CoFeB/MgO and a bottom interface MgO/GaAs

The spin polarized light emitting diodes (Spin-LED) structures (Figure 3.1) were grown by molecular beam epitaxy (MBE) for the semiconductor part before depositing the tunnel barrier either by sputtering or by MBE. The ferromagnetic contact is grown by sputtering in both cases. The p-i-n LED device has the following structure: p^+-GaAs (001) substrate /500 nm p-GaAs ($p = 2 \times 10^{19} cm^{-3}$) /200 nm GaAs ($p = 2 \times 10^{18} cm^{-3}$)/50 nm undoped GaAs /10 nm undoped $In_{0.1}Ga_{0.9}As$ quantum well/50 nm undoped GaAs/ 50 nm n-GaAs ($n = 1 \times 10^{16} cm^{-3}$). The LEDs were passivated with amorphous arsenic in the MBE chamber. The sample was then transferred through air into a MBE-sputtering interconnected system. The As capping layer was firstly desorbed at $300°C$ in the MBE chamber. Two methods were used to grow the MgO layer. Either we can grow MgO by MBE after As desorption at $250°C$, either we transfer the sample through UHV in a sputtering chamber to grow the MgO layer. In both cases, the MgO layer has the same thickness of 2.5 nm. Finally, the 3 nm thick $Co_{0.4}Fe_{0.4}B_{0.2}$ spin injector and a 5nm thick Ta protection layer were deposited by sputtering (directly after the sample transfer in case of the MBE grown tunnel barrier). Hereafter, we call MBE and sputtering samples the spin-LEDs with MgO prepared by the two different methods. These two different ways to prepare the MgO barrier lead to different interfaces qualities. During the sample transfer from the MBE

to the sputtering (several minutes in a pressure of 10^{-7} torr) chamber, the sample surface could suffer from contamination. For sputtered MgO spin-LEDs, the quality of the CoFeB/MgO interface named hereafter "top interface" (see Figure 3.1) should in principle be better than for MBE grown samples. On the contrary, the quality of the MgO/GaAs interface called hereafter "bottom interface" (see Figure 3.1) should be better for MBE grown MgO sample. It will allow us in the following to determine which interface (top or bottom one) is crucial for the efficient electrical spin injection, knowing that all the layers involved in the injector have the same thicknesses for both kinds of samples (see TEM observations in the following). 300 μm-diameter circular mesas were then processed using standard UV photolithography and etching techniques. Finally, the processed wafers were cut into small pieces to perform rapid temperature annealing (RTA) at different temperatures during 3 minutes. Bare PIN samples are used for TRPL measurements.

3.1.2 Electroluminescence measurements

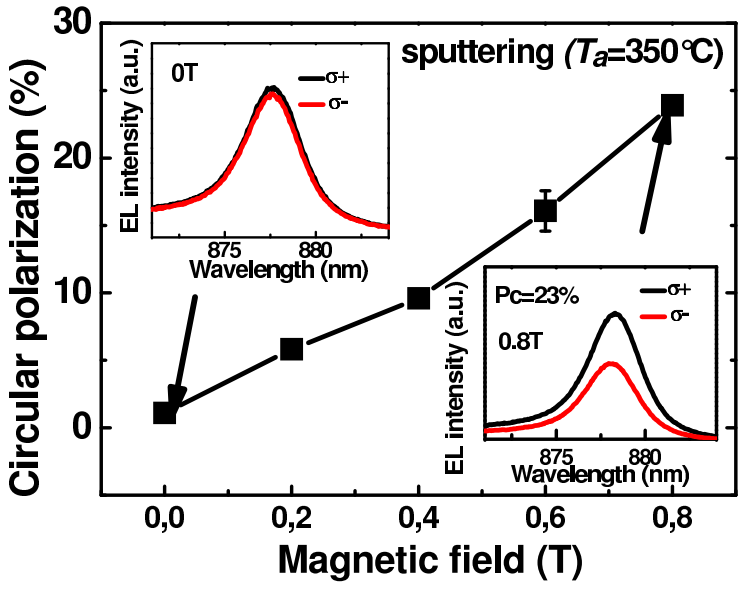

Figure 3.2: Spin-LED (annealed at 350°C) with a sputtered tunnel barrier at T=25 K. EL Circular polarization as a function of the applied longitudinal magnetic field. Top inset: EL spectra at 25 K at zero magnetic field for $I^{\sigma+}$ (thick black line) and $I^{\sigma-}$ (thick red line) EL components. Bottom Inset: same quantities for B=0.8 T.

For the polarization resolved electroluminescence (EL) measurements, the Spin-

LEDs were placed into a Helmoltz-split magnetic coil providing a maximum magnetic field (B) of 0.8T normal to the sample plane. The EL signal was detected in the Faraday geometry. The EL circular polarization P_C was analyzed through a $\lambda/4$ wave plate and a linear analyzer. P_c is defined as $P_c = (I^{\sigma+}–I^{\sigma-})/(I^{\sigma+} + I^{\sigma-})$ where $I^{\sigma+}$ and $I^{\sigma-}$ are the intensities of the right and left circularly polarized components of the luminescence, respectively. The insets of Figure 3.2 show typical CW EL spectra from a spin-LED with a sputtered tunnel barrier acquired at 25 K under a bias of V=1.7 V for B = 0 T (top inset) and B= 0.8 T (bottom inset). The heavy-hole exciton (XH) EL peak observed at 878 nm does not show any circular polarization at zero magnetic field (top inset), the EL circular polarization reaches $23.0\% \pm 1.5\%$ under B= 0.8 T (bottom inset). According to the optical selection rules applied to the quantum well (QW) [81], the EL circular polarization P_C mimics the electron spin polarization P_s injected in the quantum well, proving that an efficient spin injection process occurs. We have checked that the Magnetic Circular Dichroism is less than 1% at 0.8 T thanks to a measurement based on a linearly polarized He-Ne laser [65]. As expected, the measured EL P_C increases with the applied longitudinal magnetic field (Figure 3.2), due to the progressive increase of the projection of the magnetization along the growth axis (at zero magnetic field, the magnetization is within the plane of the thin CoFeB layer due to shape anisotropy).

3.1.3 Influence of the annealing process on the spin injection efficiency

In previous works, the influence on the spin injection efficiency of (i) the crystalline or amorphous nature of the MgO tunnel barrier, (ii) the MgO thickness and (iii) the system temperature has been investigated in CoFeB/MgO/AlGaAs multilayers where the CoFeB layer was mainly amorphous [90]. We present here in Figure 3.3 a systematic study of the influence of the post-annealing temperature on the EL circular polarization for our two kinds of CoFeB/MgO/GaAs samples. For sputtered tunnel barriers, we observe a clear improvement of the measured EL circular polarization rate from $13.5 \pm 1.5\%$ for $T_{NoAN} = 25°C$ up to $23.0 \pm 1.5\%$ for the optimal $T_{AN} = 350°C$. This trend is very similar for the sample with a MBE grown barrier, with a slightly

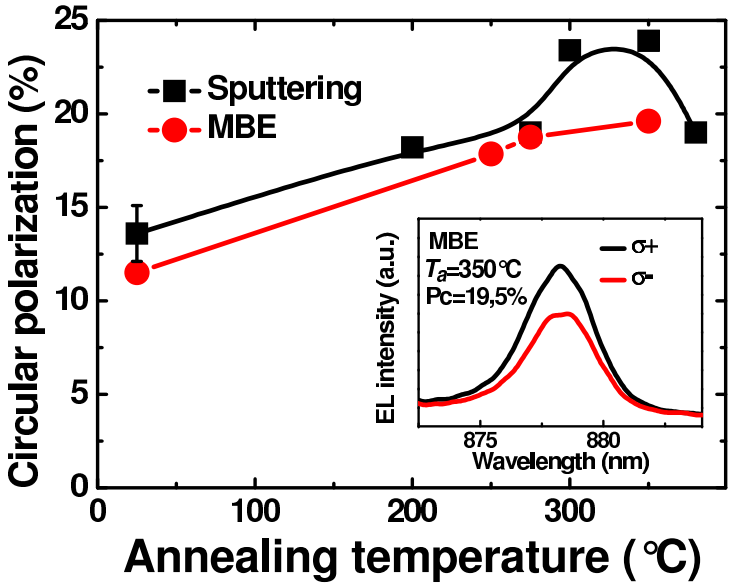

Figure 3.3: Electroluminescence circular polarization P_C as a function of the annealing temperature for sputtered (black squares) and MBE (red circles) grown MgO tunnel barriers. Inset: EL spectra of a Spin-LED (annealed at 350°C) with a MBE grown tunnel barrier at 25 K for B=0.8 T for $I^{\sigma+}$ (thick black line) and $I^{\sigma-}$ (thin red line) EL components.

lower optimal polarization of $19.5 \pm 1.5\%$ (the corresponding spectra are shown in the inset of Figure 3.3). The behavior is similar to the one observed by Wang et al. [103] for CoFe/MgO/AlGaAs samples.

3.1.4 Measurement of the electron lifetime and spin relaxation times in the InGaAs/GaAs quantum well by Time and Polarization-resolved Photoluminescence

It is of importance to discriminate if the observed large improvement of the EL circular polarization rate P_C as a function of the annealing temperature displayed in Figure 3.3 is due to a real improvement of the electrical injection P_s, or only due to the impact of the annealing process on the quantum well properties. The use of spin-LEDs as an optical means to quantify the electrical spin injection in GaAs is based on a quite straightforward relation between the electron spin polarization P_s injected in the quantum well and the measured EL circular polarization P_C : $P_C = P_s * F$. The F factor takes into account the electron spin relaxation in the quantum well during the

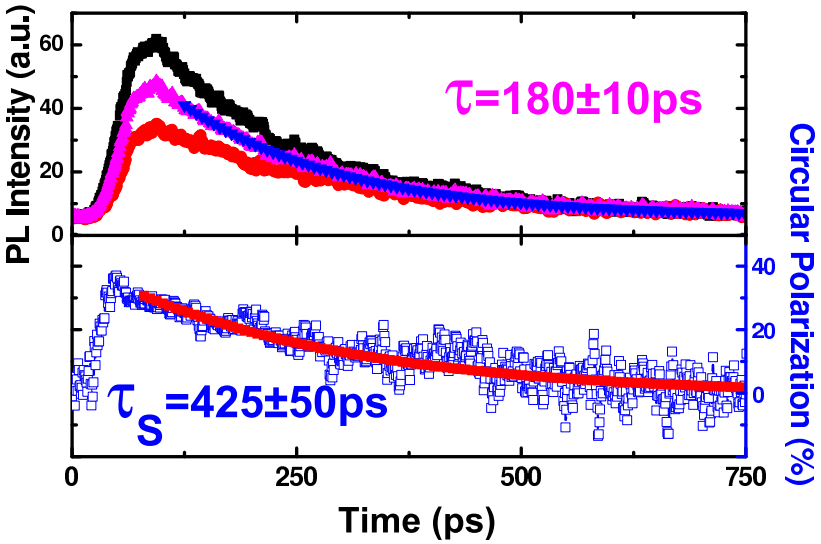

Figure 3.4: PL and circular polarization measurements performed on bare $p{\cdot}i{\cdot}n$ sample annealed at 350°C at T=25 K. Top: Photoluminescence intensity components I^+ and I^- with respectively σ^+ polarization (black squares) and σ^- polarization (red squares) as a function of time after a 1.5 ps laser σ^+ pulsed excitation at 780 nm (above the GaAs bandgap). The sum of the two intensity components $I_{sum} = I^+ + I^-$ is displayed in pink opened circles. The decay is characterized by the electron lifetime τ. Bottom: time evolution of the circular polarization rate P_C of the photoluminescence at T=25 K (blue line). The decay is characterized by the electron spin relaxation time τ_s.

electron lifetime: $F = 1/(1+\tau/\tau_s)$ where τ_s is the spin relaxation time and τ the electron lifetime in the QW [82]. To rule out the possibility that the increase of P_C could be due to an increase of the F factor, we have performed a systematic measurement of this factor as a function of the annealing temperature by measuring the spin relaxation time τ_s and the electron lifetime τ (see Figure 3.5) by time and polarization resolved photoluminescence. We have studied bare p-i-n samples annealed at different temperatures. The samples were excited by 1.5 ps pulses generated by a mode-locked Ti-doped sapphire laser with a repetition rate of 80 MHz. The time resolved photoluminescence (PL) is then recorded using a S20 photocathode Hamamatsu Streak Camera with an overall time-resolution of 8 ps. The laser excitation wavelength is 780 nm, above the GaAs bandgap. The laser power was 1 μW, focused on a 50 μm diameter spot. The luminescence intensity components co-polarized (I^+) and counter-polarized (I^-) with the excitation laser are recorded. Since the spin relaxation time of the photogenerated holes is less than 1 ps [110], the circular polarization degree P_C of the detected luminescence associated to the E1-HH1 exciton QW transition (XH) corresponds directly to the electron spin polarization degree. Our systematic measurement of the F factor

as a function of the annealing temperature as well as the spin relaxation time τ_s and the electron lifetime τ are displayed in Figure 3.6.

For example, F is estimated around 0.70 ± 0.15 for $T_{AN} = 350°C$ (for $T_{AN} = 350°C$,

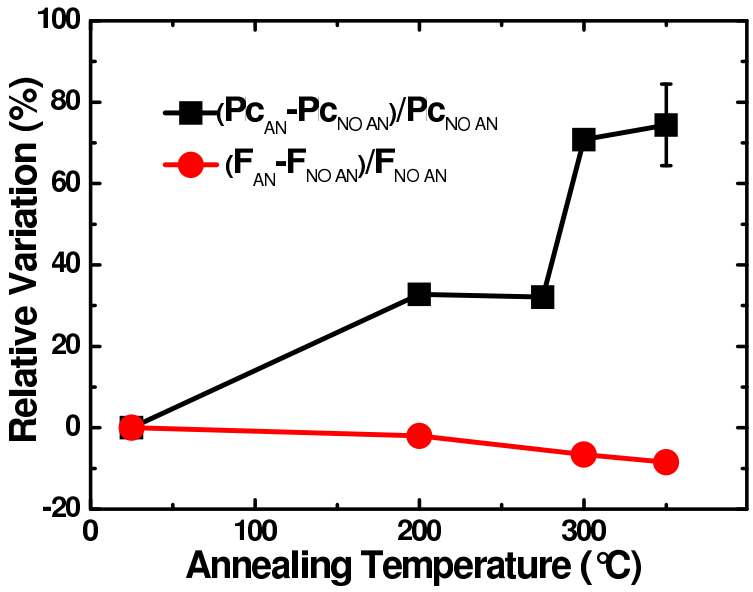

Figure 3.5: Relative variation of the circular polarization (black squares) and F factor (red circles) on bare $p \cdot i \cdot n$ samples annealed at different temperatures.

$\tau_s \simeq 425 \pm 50$ ps at 1/e and $\tau \simeq 180 \pm 10$ ps at 1/e). So the electron spin polarization P_s in the semiconductor part just before electrons are trapped in the QW is estimated to be about P_s=34% for B=0.8 T in this case. We have measured the relative change of the F factor amplitude with the annealing temperature. The results are summarized in Figure 3.5 and Figure 3.6. The relative improvement of the EL circular polarization $(P_{cAN} - P_{cNoAN})/P_{cNoAN}$ is plotted as a function of the annealing temperature and reaches about 80% between $T_{NoAN} = 25°C$ and $T_{AN} = 350°C$. In the same time, the relative variation of the F factor $(F_{AN} - F_{NoAN})/F_{NoAN}$ as a function of T_{AN} is small (less than 10% between $T_{NoAN} = 25°C$ and $T_{AN} = 350°C$) and is moreover negative, so it cannot be responsible for the large improvement of the EL circular polarization rate P_C as a function of the annealing temperature observed in Figure 3.3. Therefore, one can conclude that this increase is due to a real improvement of spin injector part.

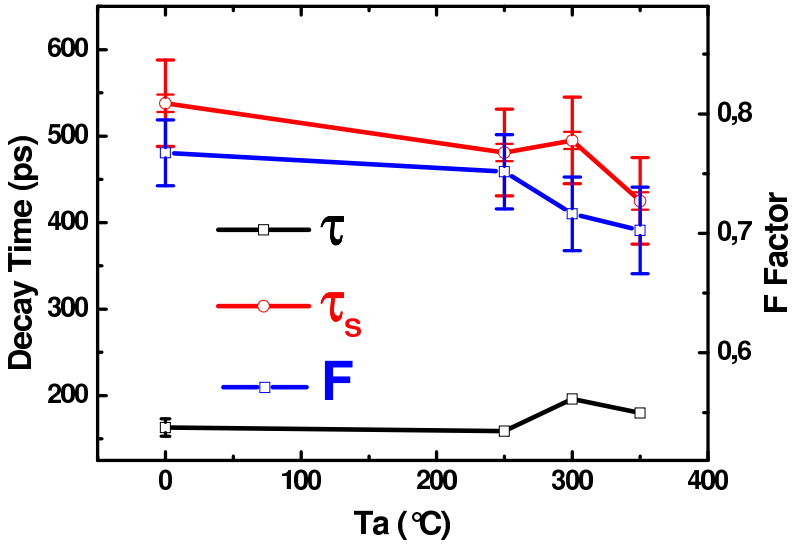

Figure 3.6: Electron spin relaxation time τ_s (red open circles), electron lifetime τ (black open squares) and F factor (blue open stars) as a function of the annealing temperature T_{AN}.

3.1.5 Analysis of the influence of the annealing process on the hysteresis curves of the ferromagnetic layer by SQUID Measurements

In EL measurements, the maximum out-of-plane field is 0.8 T, which cannot fully saturate the CoFeB magnetization. To check if the increase of P_C is not due to a change of the saturation field, we have used a SQUID to measure the magnetization of the film sample in out-of-plane configuration. As shown in Fig 4a, the magnetization is quasi linear between -1.3 T and 1.3 T as a function of the magnetic field for $T_{NoAN} = 25°C$ and $T_{AN} = 275°C$ and becomes non-linear for an annealing temperature above $300°C$. Let's note that the saturation field for CoFeB measured by SQUID is $\sim 1.3T$ for annealing temperatures below $300°C$ and $\sim 1,75T$ for $350°C$. In order to extrapolate P_C at saturation, we multiply P_C (0.8 T) by a factor $M_{saturation}$/M (0.8 T) based on the results obtained by SQUID. This extrapolation leads to a rough estimation of P_C at saturation of about $40.0 \pm 1.5\%$ at 25 K for $T_{AN} = 350°C$, proving the efficiency of CoFeB/MgO injector. This result that is close to the best one obtained by Parkin and co-workers (P_C =50% at low temperature with CoFe/MgO/AlGaAs [9]) attests of the high quality of the device. Moreover, this high circular polarization of the XH

transition in the InGaAs/GaAs quantum well, obtained using a textured MgO tunnel barrier, is larger than the values reported previously with the use of a Schottky barrier [33,35,90,94,96,104–107]. Note that the factor $M_{saturation}$/M (0.8 T) is almost constant for different annealing temperatures: it cannot explain the increase of P_C with T_{AN} and it validates the direct comparison of the circular polarization rates measured in Figure 3.3.

To further clarify the role of the annealing process on the crystallization of CoFeB

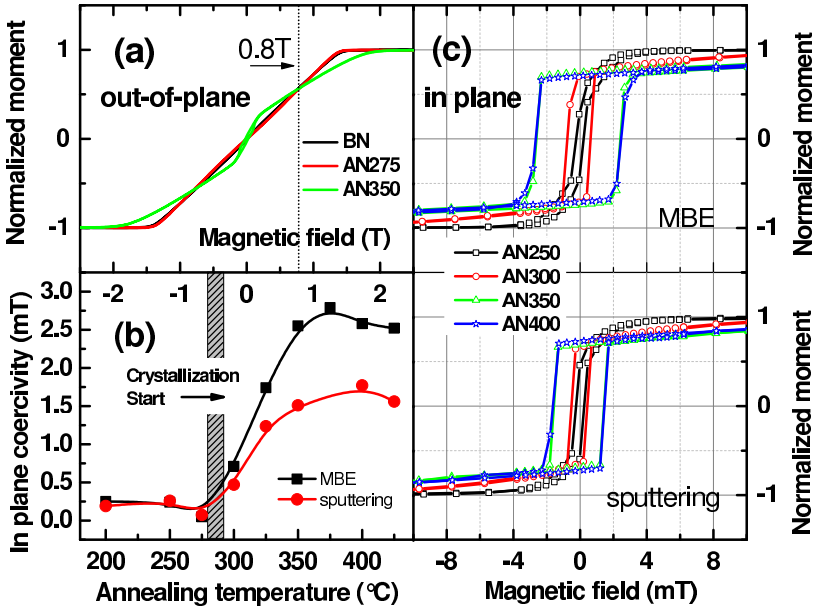

Figure 3.7: SQUID measurements. (a) Out-of-plane hysteresis curves (normalized magnetization as a function of the applied longitudinal magnetic field) for $T_{AN} = 25°C$ (black line), $T_{AN} = 275°C$ (red line) and $T_{AN} = 350°C$ (green line). (b) In-plane coercitive field H_c as a function of the annealing temperature T_{AN} for a spin-LED based on a sputtered tunnel barrier (red circles) and for a spin-LED based on a MBE grown tunnel barrier (black squares). (c) top: Spin-LED based on a MBE grown MgO tunnel barrier. In-plane hysteresis curves (normalized magnetization as a function of the applied magnetic field) for different annealing temperatures T_{AN}. Bottom: Same measurements for a Spin-LED based on a sputtered MgO tunnel barrier.

layers, we have performed SQUID measurements in in-plane configuration to check the coercitivity of CoFeB layers. Figure 3.7(c) (top and bottom) shows the hysteresis curves of two different spin-LEDs annealed at different temperatures. In Figure 3.7(b) we have summarized the evolution the coercitive field H_c as a function of T_{AN}. When the annealing temperature is above $300°C$, H_C increases in both types of samples. This is a strong indication of the beginning of the CoFeB layer crystallisation. The increase of the coercitive field with T_{AN} saturates around $350°C$, which indicates the

full crystallization of the CoFeB layer. Let us note that the MBE sample has a relative larger coercitive field than the sputtered sample. However, the EL measurement in Figure 3.3 indicates that P_C increases far below $300°C$, and saturates at $300°C$ when the crystallization is just starting. We can infer that the increase of P_C is not due to the full crystallization of the CoFeB layer.

3.1.6 CoFeB/MgO and MgO/GaAs interfaces analysis by HRTEM and RHEED characterizations

To well understand the effect of annealing, HRTEM characterizations are necessary to examine the crystal structure and interfaces. HRTEM studies were done using a JEOL ARM200 cold FEG gun working at 200 kV The good homogeneity of the structures is checked on the low magnification images in the insets of Figure 3.8(b) and (d) (for samples annealed at $350°C$). Note also that the MgO thicknesses are identical for the two types of samples validating the direct comparison of the measured circular polarization from the two kinds of spin-LEDs in Figure 3.3. First, we compare the HRTEM images for MBE samples before annealing (Figure 3.8(a)) and after annealing at $350°C$ (Figure 3.8(b)). In both cases, the MgO/GaAs interface is very sharp. The CoFeB layer is amorphous before annealing and fully crystallized after annealing at $350°C$. It confirms the increase of H_c measured by SQUID. As P_C clearly increases with T_{AN} for the MBE sample (Figure 3.3) whereas no change is observed at the MgO/GaAs interface and while a drastic change occurs at the CoFeB/MgO interface (evidenced by the CoFeB crystallization at $350°C$), one can infer that the CoFeB/MgO interface is the crucial one for an optimal spin injection. A second observation reinforces this conclusion: if we compare the HRTEM images for the MBE (Figure 3.8(a)) and sputtering (Figure 3.8(c)) samples before annealing, a presence of a thin amorphous layer (~ 0.5 nm) is detected (Figure 3.8(c)) at the MgO/GaAs interface (bottom interface) for the sputtered sample. The same interface is much sharper (Figure 3.8(a)) for the MBE sample. The fact that P_C is comparable (Figure 3.3) before annealing for both samples (and even slightly better for a sputtered MgO barrier) whereas the quality of the MgO/GaAs interface is much better by MBE also indicates that the influence of the MgO/GaAs interface is weak and that the CoFeB/MgO interface is the most im-

portant one for an efficient electrical spin injection. Finally, for the sputtered samples, a trend comparable to the one observed for MBE samples is observed: P_C increases with T_{AN} while the CoFeB layer initially amorphous becomes fully crystallized after a $350°C$ annealing process. Let us note that the amorphous layer at the MgO/GaAs interface is much reduced after annealing.

To summarize, the quality of the CoFeB/MgO interface seems to be crucial for an efficient electrical spin injection. As a large increase of the spin injection efficiency takes place before $300°C$, that is to say before the crystallization of the whole CoFeB layer, we attribute this trend to an improvement of chemical bounds at the CoFeB/MgO interface, as it was also observed for TMR values after annealing of magnetic tunnel junctions with MgO tunnel barriers [111]. Here, we cannot totally exclude the possibility that a partial crystallization of CoFeB on a few atomic layers at the CoFeB/MgO interface occurs which is not detectable by SQUID. The saturation of P_C above $300°C$ (clearly observed for sputtered samples) indicates that the full crystallization of CoFeB layer is not a critical factor.

Finally RHEED measurements have been performed on MgO surfaces (top interface) prepared by different methods to check the surface crystalline structure. The insets of Figure 3.8(a) show the RHEED patterns along GaAs[100] and [110] directions for the 2.5 nm thick MgO larger grown by MBE on GaAs. The RHEED images from the two directions exhibit a monocrystalline spotty diffraction pattern, which allows to identify the in-plane epitaxial relationship of the structure as GaAs[100](100)//MgO[100](100). On the contrary, the RHEED images of the sputtered MgO surface (insets of Figure 3.8(c)) indicate a worse crystalline quality since some polycrystalline rings appear in the two directions. The TEM images (Figure 3.8(a) and (c)) for these two kinds of samples further reinforce the conclusions from RHEED. Compared with a more uniform MBE grown MgO film, the sputtered MgO layer contains many small grains with different orientations. As we know, during annealing, the Ta layer can absorb B atoms which results in the crystallization of CoFeB from the MgO/CoFeB interface [112]. The polycrystalline MgO grains observed before annealing will certainly induce more grains in the crystallized CoFeB layer due to the grain to grain epitaxial relationship. This could explain the smaller coercivity we have observed in SQUID measurements (Figure 3.7(b)) for the sputtered sample.

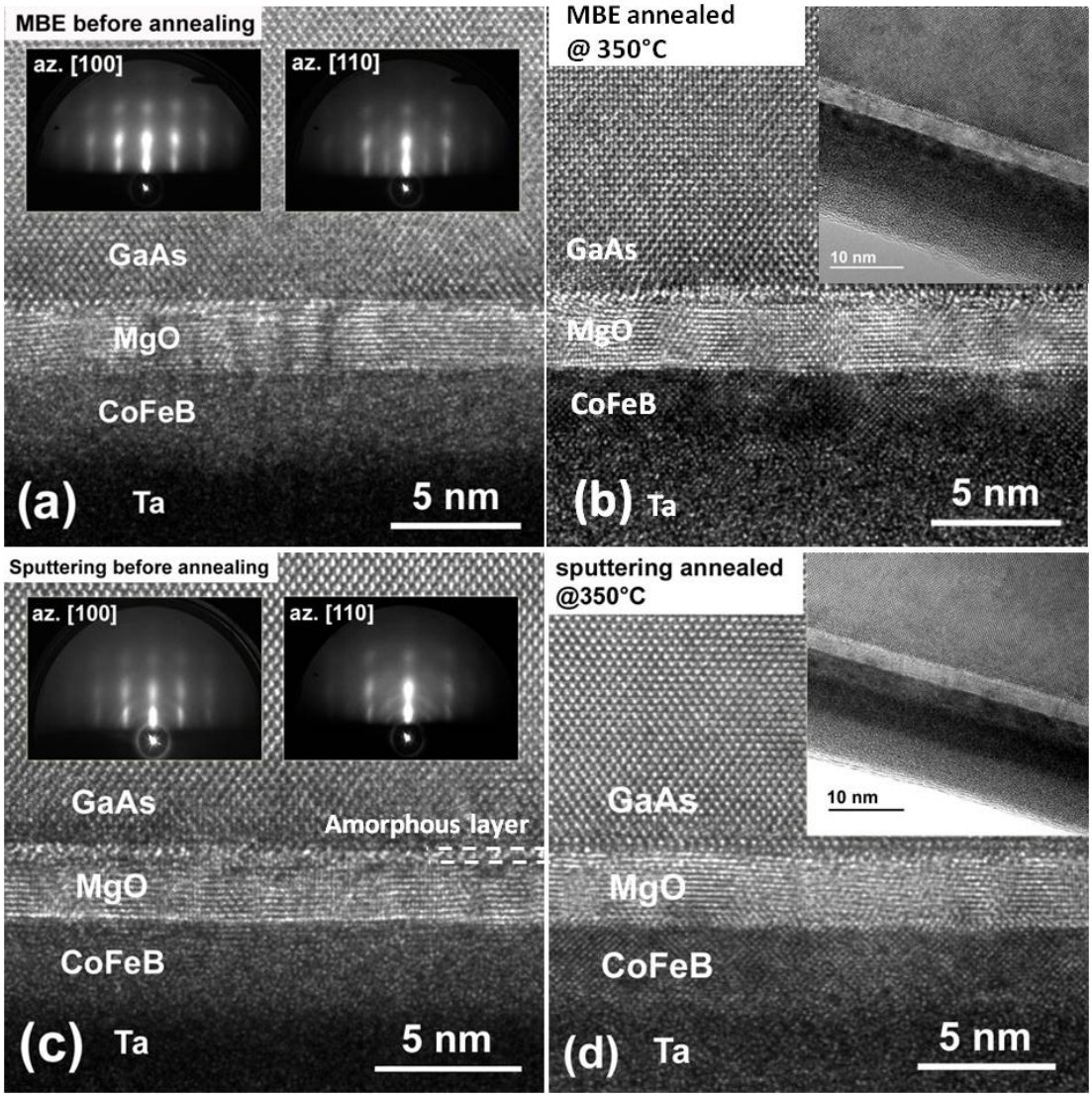

Figure 3.8: (a) HRTEM image of the sample with the MBE grown MgO tunnel barrier before annealing. Insets: RHEED images for [100] and [110] directions (left and right insets respectively). (b) HRTEM image of the sample with the MBE grown MgO tunnel barrier after annealing at $T_{AN} = 350°C$. Inset: TEM image at low magnification showing the good homogeneity of the layers. (c) HRTEM image of the sample with the sputtered MgO tunnel barrier before annealing. Upper insets: RHEED images for [100] and [110] directions (left and right insets respectively). (d) HRTEM image of the sample with the sputtered MgO tunnel barrier after annealing at $T_{AN} = 350°C$. Inset: TEM image at low magnification showing the good homogeneity of the layers.

Conclusion

In this section, an efficient electrical spin injection from CoFeB into InGaAs/GaAs quantum well through textured MgO tunnel barriers is demonstrated. By comparing Electroluminescence circular polarizations (P_C) obtained on spin-LEDs with MgO tunnel barriers fabricated by two different techniques (Sputtering and MBE), and after combined analysis with time-resolved photoluminescence (TRPL), transmission electron microscopy (TEM) and superconducting quantum interference device (SQUID) measurements, we show that the optimized electrical spin injection efficiency is comparable for both methods: $P_C \sim 23.0 \pm 1.5\%$ (for a tunnel barrier grown by sputtering) and $P_C \sim 19.5 \pm 1.5\%$ (for a tunnel barrier grown by MBE) at 25 K under 0.8T for an annealing temperature T_{AN} of $350°C$. These results together with the structural analysis of the interfaces lead to the conclusion that the control of the quality of the CoFeB/MgO interface is more important than the one of the MgO/GaAs interface for an optimal spin injection. A systematic study of the impact of the post-annealing temperature of the injector is also performed for the two types of samples. Both show the same trend: an increase of the EL circular polarization (P_C) when the annealing temperature T_{AN} increases, with an optimized temperature in the range $300 - 350°C$. We attribute this behavior mainly to the improvement of the chemical structure at the top CoFeB/MgO interface.

3.2 Current dependence of the electrical spin injection

For practical applications, it is of major importance to understand the influence of the voltage or current on the electrical spin injection efficiency in our devices. The bias or current dependence has been investigated in several types of hybrid Ferromagnetic Metal/Semiconductor systems: unipolar devices studied by Kerr rotation technique [77], non local 3-terminal full-electrical devices [31,78,113] or bipolar devices

such as spin-LEDs [9,83,90,102,114–120]. Several investigations have been performed on spin-LEDs based on Schottky barriers [83,102,116,118–120], Al_20_3 [114,115,117] or MgO barriers [9,90,103]. To explain the behavior of the electroluminescence polarization as a function of bias, the complex behavior of the electron lifetime and its spin relaxation time as a function of the applied voltage [83,102,118–120] in the semiconductor part of the device, as well as the D'Yakonov-Perel mechanism [121,122] for electrons injected at the interface with a given kinetic energy are usually evoked [9,114,115,117].

In this section we have focused our attention on optimized samples annealed at

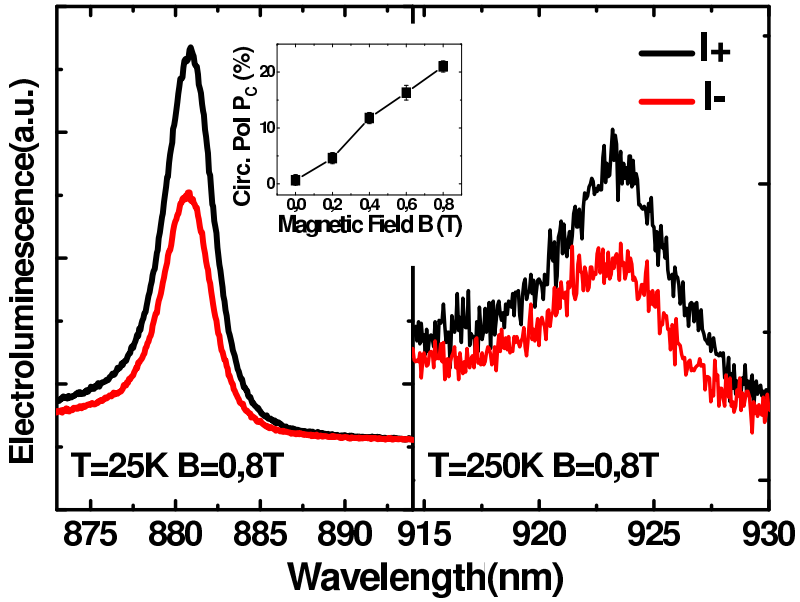

Figure 3.9: Spin-LED with a sputtered tunnel barrier for $T_{AN} = 300°C$. Left panel: EL spectra at 25 K for B=0.8 T for I^+ (thick black line) and I^- (thin red line) EL components. Inset: EL Circular polarization as a function of the applied longitudinal magnetic field. Right panel.: EL spectra at 250 K for B=0.8 T for I^+ (thick black line) and I^- (thin red line) EL components.

$300°C$, but the presented trends are verified for all the annealing temperatures. Figure 3.9 shows typical CW EL spectra for a spin-LED annealed at $300°C$ (for a sample with a sputtered tunnel barrier) acquired under a bias of V=2.4V for B= 0.8T (left panel) at 25 K (left) and 250 K (right panel). The EL polarization reaches 21.0% ± 1.5% under B= 0.8 T at 25 K and is still about 20.0 ± 1.5% at 250 K. As expected, the measured EL P_C increases with the applied longitudinal magnetic field (Figure 3.9 inset), due to the progressive increase of the projection of the magnetization along the growth axis. In order to extrapolate P_C at saturation, we multiply P_C (0.8 T) by a factor $M_{saturation}$/M(0.8 T) ∼ 0,57 based on the results obtained by SQUID on this

sample. This extrapolation leads to a rough estimation of P_C at saturation of about $37.0 \pm 1.5\%$ at 25 K and $35.0 \pm 1.5\%$ at 250 K.

3.2.1 Current dependence of the Electroluminescence circular polarization

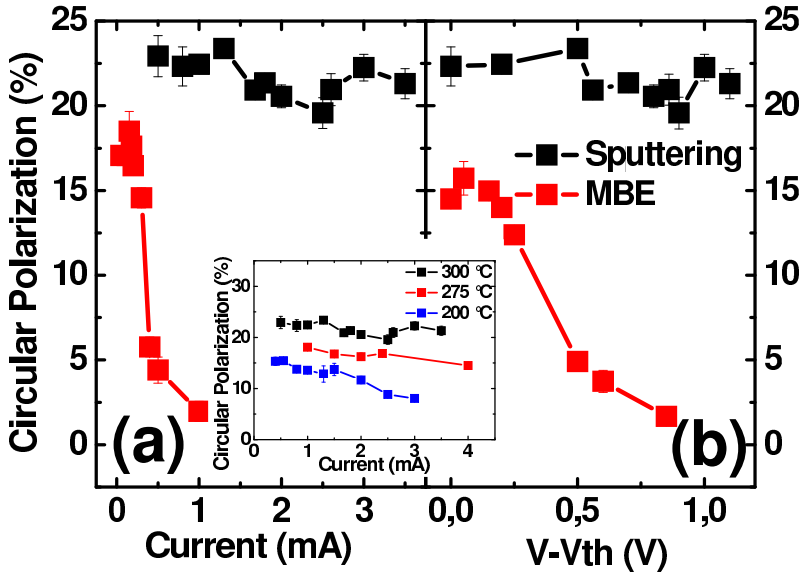

Figure 3.10: (a) Spin-LED with a sputtered and a MBE grown tunnel barrier annealed at 300°C. T=25 K. B=0.8 T : EL Circular polarization as a function of the current. Inset: P_C as a function of the current for sputtered samples at different annealing temperatures. (b) Spin-LED with a sputtered and a MBE grown tunnel barrier annealed at 300°C. T=25 K. B=0.8 T : EL Circular polarization as a function of $\Delta V = V - V_{th}$.

Figure 3.10(a) shows the study of the electroluminescence polarization rates P_C measured as a function of the current injected in the spin-LEDs annealed at 300°C for the sputtered sample and for the MBE sample. It appears clearly that the electroluminescence circular polarization is quite stable (slightly decreasing) as a function of the injected current in the former case, whereas this polarization decreases abruptly when the current increases in the latter case. We have checked that this trend does not depend on the annealing temperature in the range 200°C-350°C (the inset of Figure 3.10 shows for example very similar dependences of P_C as a function of the current for sputtered samples annealed at 200°C, 270°C and 300°C). However, in the annealing temperature range 200°C-350°C, the CoFeB/MgO interface is strongly changed with

annealing due to the crystallization of the CoFeB layer and the improvement of the chemical quality of this interface, as demonstrated by TEM and SQUID measurements in the previous section. Thus we believe that the CoFeB/MgO interface is not responsible for these two striking different current dependences.

On the other hand, the MgO/GaAs interface is very different for the two kinds of samples: (i) due to the two growth techniques used to elaborate the MgO tunnel barrier on GaAs; (ii) due to the existence of a transfer step from the MBE chamber to the sputtering chamber that occurs for the sputtered sample, and that can induce a contamination of the GaAs surface (this is not the case for the MBE sample). This MgO/GaAs interface which is different for the two growth techniques could thus be at the origin of the observed different behaviors of P_C as a function of the injected current.

3.2.2 Voltage dependence of the Electroluminescence circular polarization

Concerning the dependence of the EL circular polarization as a function of the applied voltage or current, several investigations have been performed on spin-LEDs based on Schottky barriers [83,102,116,118–120], or Oxide barriers [9,90,114,115,117]. For a thin Schottky barrier formed in a highly n-doped semiconductor layer at the interface, it has been demonstrated that a very significant part of the voltage drops in the semiconductor emitting zone even in the regime of photon emission. In this case, the dependence of the electroluminescence circular polarization on bias is usually explained by the dependence on the applied voltage of the ratio between the electron lifetime and the electron spin relaxation time in the emitting zone (bulk or quantum well) [83,102]. For oxide tunnel barriers, the applied voltage initially drops in the $p{\cdot}i{\cdot}n$ part of the device during a first step. Once enough holes are accumulated at the oxide/semiconductor interface [117], the voltage drops also in the oxide barrier, allowing the bending of the tunnel barrier and the alignment of the semiconductor conduction band on the ferromagnetic metal Fermi level. Then electrons start to be efficiently injected from the FM to the SC and electroluminescence appears. The carriers are injected with increasing kinetic energy for increasing biases. Thus these electrons can experience spin relaxation due to the D'Yakonov-Perel mechanism, leading to the de-

creasing behavior of the electroluminescence circular polarization as a function of the applied voltage [9,114,115,117].

To further investigate the different trends observed in the samples, we have displayed in Figure 3.10(b) the behavior of the electroluminescence polarization rates measured as a function of the voltage ΔV applied on the spin-LEDs for the sputtered sample and for the MBE sample annealed at $300°C$. The voltage ΔV is defined as $\Delta V = V - V_{threshold}$ where V is the voltage applied to the structure and $V_{threshold}$ is the voltage required to obtain the first photons in the electroluminescence process. $V_{threshold}$ may have several contributions: the voltage required to make the band flater in the $p \cdot i \cdot n$ region, the voltage required to bend the MgO tunnel barrier in order to align the conduction band of GaAs with the Fermi level of the CoFeB and to allow an efficient injection of electrons into the conduction band of GaAs, as well as an additional voltage due to a parasitic Schottky bottom contact on the p-doped part of the structure. Working with ΔV instead of V allows to rule out in particular this parasitic voltage that can fluctuate from a mesa to another one. As can be seen in Figure 3.10, the circular polarization rate decreases faster as a function of ΔV for spin-LEDs with a tunnel barrier grown by MBE.

3.2.3 Discussion

From a general point of view, the electroluminescence circular polarization rate detected in the quantum well can be written as $P_0(E_k)/[(1+\tau^{GaAs}/\tau_s^{GaAs})(1+\tau^{QW}/\tau_s^{QW})]$. τ^{GaAs} and τ_s^{GaAs} are respectively the electron lifetime and the electron spin relaxation time during the transit time in the bulk GaAs layer before being trapped in the well. τ^{QW} and τ_s^{QW} are the electron lifetime and the electron spin relaxation time [82] in the InGaAs/GaAs QW. $P_0(E_k)$ is the electron spin polarization in the bottom of the conduction band just after the MgO/GaAs interface when the electrons have been injected with a kinetic energy E_k. The discrepancy between the measured variation of P_C as a function of current or voltage for the two samples could originate from a non equivalent balance of the voltages that drop respectively on the tunnel barrier and on the semiconductor part of the device. The characteristics of the MgO/GaAs interface

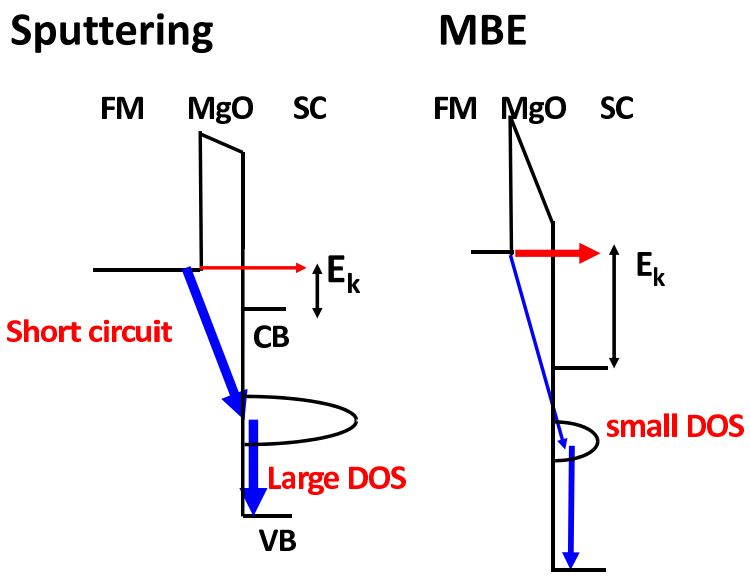

Figure 3.11: Scheme of the principle of injection for Spin-LEDs with a sputtered (left) and MBE grown (right) MgO tunnel barrier

should be different for the two growth methods. A smaller density of interface states can be supposed for samples with a MBE grown tunnel barrier due to the full MBE grown GaAs/MgO interface compared to the one obtained by a mixed growth method (MBE/Sputtering) where a transfer step from the MBE chamber to the sputtering chamber occurs. For the MBE sample, the parasitic current from electrons that cross the tunnel barrier from the CoFeB Fermi level to the valence band of GaAs (or in an equivalent picture the parasitic hole current crossing the MgO from the GaAs valence band to the CoFeB Fermi level [117]) through the interface states will be smaller (see Figure 3.11).

This parasitic current channel can be seen as a leakage resistor in parallel to the tunnel barrier. Due to this weaker leakage resistance, the voltage drop on the tunnel barrier will be larger, whereas the voltage drop in the $p \cdot i \cdot n$ junction is thus smaller in this case [123]. The consequence of a smaller leakage current from the CoFeB Fermi level to the valence band of GaAs through the tunnel barrier is the existence of a lower current threshold to get electroluminescence. We have indeed observed this phenomenon. Figure 3.12(a) and Figure 3.12(b) show the EL intensity as a function of the current through the device for both kinds of samples (sputtered tunnel barrier and MBE grown tunnel barrier).

We observe that the EL threshold is smaller for the Spin-LED with the MBE grown

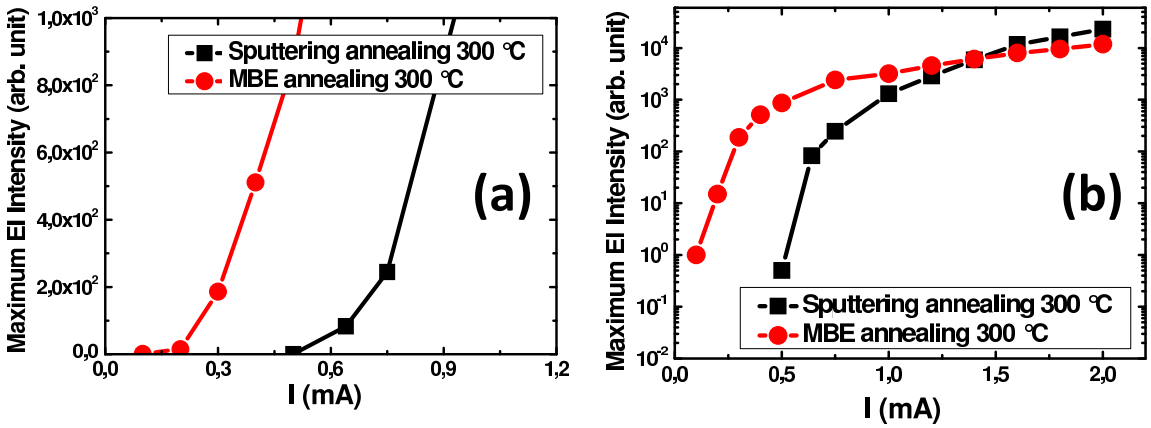

Figure 3.12: T=25 K. (a) EL intensity as a function of the current for spin-LEDs with a sputtered tunnel barrier (black squares) and a MBE grown tunnel barrier (red squares) for $T_{AN} = 300°C$ in the low current regime. (b) EL intensity (log scale) as a function of the current for spin-LEDs with a sputtered tunnel barrier (black squares) and a MBE grown tunnel barrier (red squares) for $T_{AN} = 300°C$.

barrier (Figure 3.12(a)). In the low current regime, the EL intensity is larger for MBE grown samples due to this threshold behavior. As the voltage drop on the tunnel barrier is larger for these samples, the initial kinetic energy E_k is larger (see Figure 3.11) for a given ΔV (compared to samples with a sputtered tunnel barrier). Let us consider the relaxation of these electrons towards the bottom of the conduction band. In bulk III-V semiconductors, the spin relaxation time associated to the D'Yakonov-Perel mechanism is inversely proportional to an effective precession vector related to the Dresselhaus spin orbit term that is cubic in k, k being the modulus of the electron wavevector [121,122]. As k is itself proportional to $E_k^{1/2}$ the spin relaxation time is finally decreasing when E_k increases due to equation 1.30 in Chapter 1. For the sample with the MBE grown oxide, the efficiency of the D'Yakonov-Perel mechanism is thus stronger and it leads to a $P_0(E_k)$ strongly decreasing when the applied bias increases. It could explain the observed clear decay of the EL circular polarization as a function of the applied bias or current (Figure 3.10). On the contrary for the sample with the sputtered oxide, the efficiency of the D'Yakonov-Perel mechanism is weaker and it leads to a $P_0(E_k)$ slightly decreasing when the applied bias increases. It could explain the relatively stable EL circular polarization observed as a function of the applied bias or current (Figure 3.10). A significant part of the current in this case may be due to a leakage through the MgO barrier.

Note that in a complementary way, the voltage drop in the semiconductor part

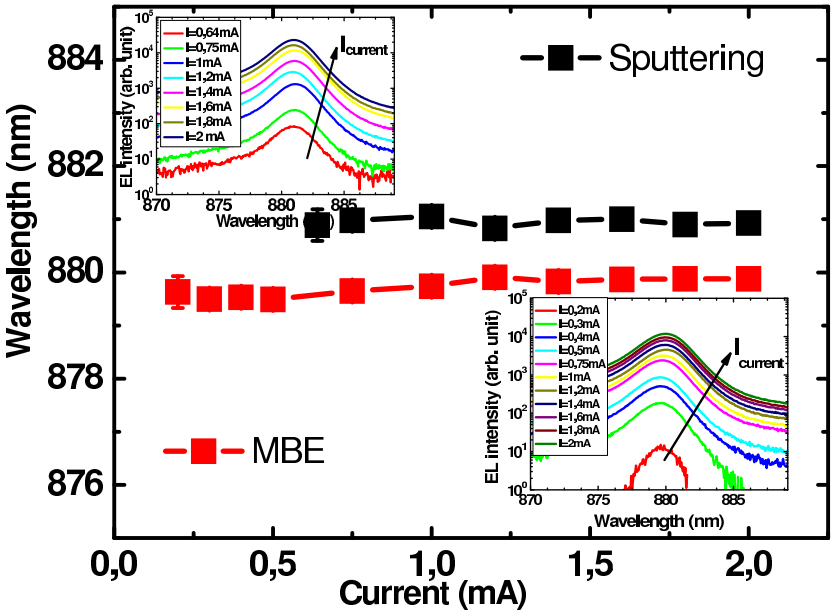

Figure 3.13: Central wavelength of the EL emission as a function of the injected current for a sputtered sample (black squares) and a MBE sample (red squares) annealed at $300°C$. Top left inset: EL spectra as a function of the current for a spin-LED with a sputtered tunnel barrier annealed at $300°C$. Bottom right inset: EL spectra as a function of the current for a spin-LED with a MBE grown tunnel barrier annealed at $300°C$.

should be more efficient for the sputtered sample. As we observe no clear stark shift on the XH transition of the quantum well as a function of the applied voltage (see Figure 3.13), one can consider that the variation of the ratio τ^{QW}/τ_s^{QW} due to the variation of the electric field in the QW is not of key importance in our case.

Anyway, one cannot exclude that the voltage drop in the semiconductor part may have an influence near the interface in the GaAs region located before the quantum well because the band bending in the semiconductor part could be more favorable for the electrons to reach the quantum well in case of sputtered samples. That could explain why, at higher currents, the intensity of the light becomes as large as the one of samples with the MBE grown tunnel barrier, and even slightly larger, as seen in Figure 3.12(b). Finally, we have plotted the figure of merit of the circular polarization as a function of the EL intensity in Figure 3.14. It appears clearly that the sample with a sputtered tunnel barrier exhibits the best compromise between high circular polarization rate and high electroluminescence intensity. This point can be of importance in view of future devices.

To conclude, the current dependence of the electrical spin injection into an In-

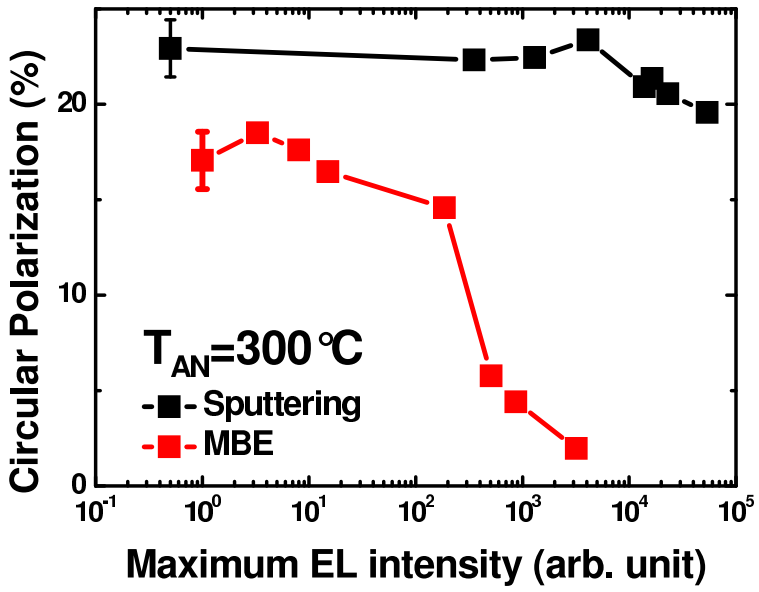

Figure 3.14: T=25 K. Circular polarization as a function of the EL intensity for a spin-LED with a sputtered tunnel barrier (black squares) and a MBE grown tunnel barrier (red squares) for $T_{AN} = 300°C$.

GaAs/GaAs quantum well light emitting diode is investigated for textured MgO tunnel barriers fabricated either by Sputtering or Molecular Beam Epitaxy. We demonstrate that the electroluminescence circular polarization is very stable as a function of the injected current for sputtered tunnel barriers, whereas this polarization decreases abruptly when the current increases for tunnel barriers grown by Molecular Beam Epitaxy. We attribute this behavior to the MgO/GaAs interface that presents specific characteristics depending on the growth method. It appears that in view of future applications, spin-LEDs with sputtered tunnel barriers present the best compromise between high electroluminescence circular polarization and high electroluminescence intensity. Finally, a deeper understanding of the dependence of the spin injection efficiency as a function of the applied voltage would require a 3-terminal device [124] in order to apply or measure independently the voltage drops in the tunnel barrier and in the semiconductor part of the device.

3.3 Electrical injection at zero magnetic field up to room temperature: Spin-LED with an ultra-thin CoFeB perpendicular injector

As seen in the previous sections, spin-LEDs are very powerful tools to quantify the electron spin polarization that has been successfully injected through the ferromagnetic/tunnel barrier/semiconductor interface. These spin-LEDs constitute also by themselves new optoelectronic devices with spin functionalities. Potential devices ranging from optical transport of spin information [125], memory elements with optical readout, advanced optical switches [126] and quantum cryptography concepts [127] to chiral analysis [128] and 3-dimensional display screens [129] have been anticipated. According to the optical selection rules [22,81], conventional spin-injector with in-plane magnetization [9,34,65,66,83,85,92,120,130–132] cannot satisfy the practical application because a strong external magnetic field up to a few Tesla is required to rotate the magnetization into the perpendicular direction. A prerequisite to obtain optimized device functionalities is to promote a robust perpendicular magnetic anisotropy (PMA) medium [102] up to room temperature (RT) to be used as a solid-state ferromagnetic (FM) injector electrode. Good candidates are systems including alternated planes of 3d/4f (like Fe/Tb [96,133]), 3d/5d (like Co/Pt [35,97]), or 3d/3d (like Co/Ni multilayers [134]). However, these systems generally suffer from the requirement of a minimum thickness (generally several units of bilayers) grown on a thin oxide layer, which is used as a tunneling barrier to circumvent the conductivity mismatch between the metal and the semiconductor [7]. The large thickness of the injector results in a large absorption of light in the near infrared region, e.g. 95% of the light is absorbed for 40 nm thick Fe/Tb multilayers [96,133]. Moreover, in the case of spin-LEDs, there is also a requirement that the first FM atomic plane grown at the interface must possess a robust spin-polarization for an efficient spin-injection, which is hardly attainable due to the chemical inter-diffusion or intermixing in the multilayer systems [35]. Therefore, up to now, the circular polarization (P_C) of emitted light was still limited to 3% at remanence [35,96].

A series of recent theoretical investigations have proposed that the Fe(Co)/MgO interface itself could provide PMA in the range of magnitude of $1 mJ/m^2$, sufficient

to reorient the magnetization along the out-of-plane direction [135,136]. This PMA property has been put forward in the case of CoFeB/MgO/CoFeB p-MTJs grown on SiO_2 substrates used for spin transfer torque (STT) operations in MRAM technologies (STT-MRAM) [109,137]. These STT devices display high tunneling magnetoresistance (TMR) ratios, good thermal stability together with low switching current densities.

In this work, we demonstrate, the occurrence of such PMA functionality in semiconducting heterostructures with III-V based spin-LEDs by integrating CoFeB/MgO perpendicular spin-injectors. For the first time, large values of the electroluminescence circular polarization (20% at 25 K and 8% at 300 K) are measured under zero magnetic field.

3.3.1 Sample description

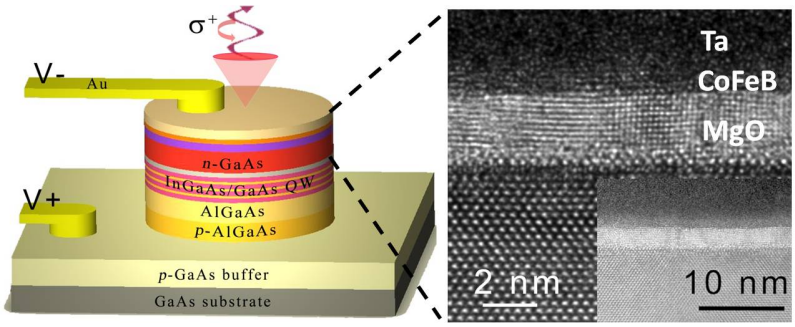

Figure 3.15: Left: schematic device structure of a spin-LED. Right: HRTEM image of CoFeB/MgO PMA injector; Inset of HRTEM image: low magnification image showing the excellent homogeneity and the low roughness of the structures.

The p-i-n semiconducting part of the spin-LED was grown by molecular beam epitaxy (MBE), while the tunnel barrier/ferromagnet contacts were deposited by sputtering. The whole structure of the sample is schematically shown in the left part of Figure 3.15. The p-i-n LED device has the following structure sequence: p-GaAs:Zn (001) substrate ($p = 2\times10^{19}cm^{-3}$) /500 nm p- GaAs:Be ($p = 2\times10^{19}cm^{-3}$) /100 nm p-$Al_{0.3}Ga_{0.7}As$:Be ($p = 2\times10^{19}cm^{-3}$)/ 100 nm p- $Al_{0.3}Ga_{0.7}As$:Be ($p = 2\times10^{18}cm-3$)/ 50 nm undoped $Al_{0.3}Ga_{0.7}As$ / [15 nm undoped GaAs/ 8 nm undoped $In_{0.1}Ga_{0.9}As$] $\times$3/ 15 nm undoped GaAs/ 5 nm undoped $Al_{0.3}Ga_{0.7}As$ / 30 nm undoped GaAs/ 50 nm n-GaAs:Si ($n = 1\times10^{16}cm^{-3}$). The surface was passivated with arsenic in the III-V MBE chamber. The intended design of the 3 QWs structure for the LED is to obtain a stronger electroluminescence intensity especially at room temperature. An-

other important reason is that the surface roughness of the 3 QWs-LED is found to be much better than the single QW-LED, which is also a critical factor to obtain a continuous ultrathin CoFeB layer. The sample was then transferred through air into a magnetron sputtering-MBE interconnected system to grow the CoFeB/MgO spin-injector. The arsenic capping layer was firstly desorbed at 300 $°C$ by monitoring insitu reflection high energy electron diffraction (RHEED) patterns in the MBE chamber, and then the sample was transferred into the sputtering chamber to grow the spin-injector. The spin-injector grown at room temperature consists in a 2.5 nm thick MgO tunnel barrier and a thin $Co_{40}Fe_{40}B_{20}$ ferromagnetic layer (1.1-1.7 nm). Finally, 5 nm of Ta was deposited to prevent oxidation. 300 μm diameter circular mesas were then processed using standard UV photolithography and etching techniques. In the end, the processed wafers were cut into small pieces to perform rapid thermal annealing (RTA) at different temperatures for 3 minutes. The RTA procedure is a good way to promote PMA of CoFeB [138] while almost keeping no change to the LED optical characteristics.The right part of Figure 3.15 is a high-resolution transmission electron microscopy (HRTEM) image of the injector. The low magnification image (inset of the HRTEM image) reveals a good homogeneity and a very low roughness of MgO on GaAs.

3.3.2 Microscopic origin of the Magnetic Perpendicular Anisotropy in the ultrathin CoFeB/MgO injector

The origin of PMA in our system can be understood with the model system Fe/MgO. Using calculations based on the Vienna Ab initio Simulation Package (VASP) [139–141] with the generalized gradient approximation [142], and projector augmented wave potentials [143,144], H. Yang, A.Hallal, M. Chshiev from SPINTEC, CEA-INAC/CNRS/UJF at Grenoble and H. Jaffrès from UMP CNRS-Thalès have developed the following interpretation.

In bulk Fe with a bcc structure, the charge distribution in the 3d shell is almost isotropic as well as the resulting average orbital moment. The orbital moment acquired in the plane of the layer exactly compensates that acquired along the out-of-plane direction by equal filling of the corresponding orbitals. This produces zero orbital moment anisotropy ($\Delta\mu$) as shown in Figure 3.16 (left) for the bulk atom Fe3. In contrast to bulk Fe films, the Fe/MgO interface exhibits a strong uniaxial character. The out-of-

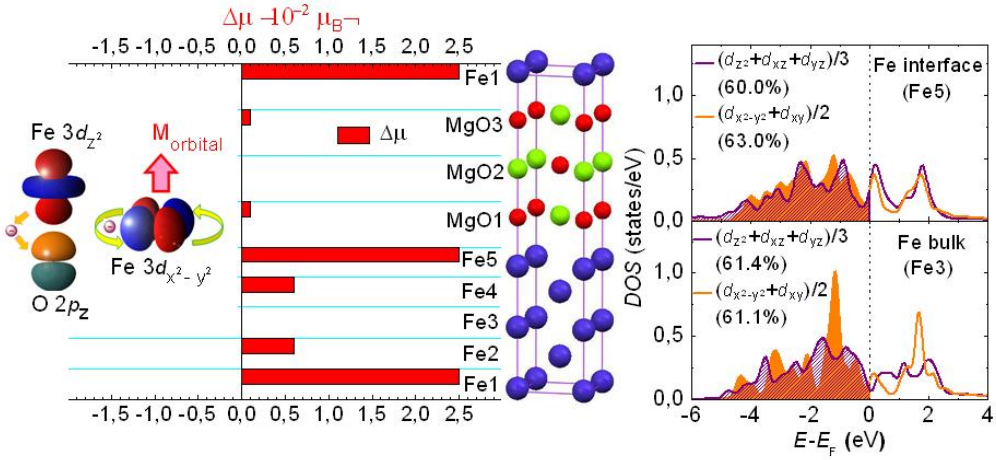

Figure 3.16: Left: layer-resolved orbital moment anisotropy ($\Delta\mu$). Middle: schematics of the calculated crystalline structures. Fe, Mg, and O are represented by blue, green, and red balls, respectively. Right: DOS with spin-orbit coupling for averaged Fe 3d out-of-plane ($3d_{z2} + 3d_{xz} + 3d_{yz}$) and in-plane orbitals ($3d_{x2-y2} + 3d_{xy}$) with Fe both at the interface (Fe5) and in the bulk (Fe3). Inset: a simple picture showing that the origin of PMA comes from the hybridization of Fe out-of-plane orbitals ($3d_{z2}, 3d_{xz}$ and $3d_{yz}$) and O $2p_z$ orbitals, which leads to an uncompensated charge occupation in Fe in-plane orbitals ($3d_{x2-y2}, 3d_{xy}$) and results in an enhanced out-of-plane orbital moment leading to PMA.

plane Fe $3d_{z^2}$ orbital strongly bonds to the O $2p_z$ orbital and it introduces a significant charge transfer from Fe to O orbitals (Inset of Figure 3.16 (left)). This results in a lack of electrons within the Fe $3d_{z^2}$, $3d_{xz}$ and $3d_{yz}$ out-of-plane orbitals compared to the Fe in-plane orbitals ($3d_{x2-y2}$ and $3d_{xy}$). As a consequence, an enhanced out-of-plane orbital moment occurs from the uncompensated in-plane orbitals and generates a sizable PMA once the spin-orbit coupling (SOC) is introduced. To better understand this simple explanation of PMA, we show in Figure 3.16 (right) the density of states (DOS) with spin-orbit coupling of averaged Fe 3d out-of-plane ($d_{z2} + d_{xz} + d_{yz}$) and in-plane orbitals ($d_{x2-y2} + d_{xy}$) for Fe both at the interface and in the bulk (spin up and down are mixed due to SOC). From the integration of the occupied states below the Fermi level (E_F), we found an occupation difference of about 3% between respective out-of-plane and in-plane orbitals for an Fe atom bound to O at the interface (Fe5), while almost no difference appears for Fe atoms in the bulk (Fe3). This gives an unbalanced orbital moment anisotropy ($\Delta\mu \simeq 0.03\mu B$) associated with the magnetization out-of-plane direction for the interfacial atom Fe5 (and Fe1).

3.3.3 Optimization of the CoFeB injector

To obtain an ultrathin CoFeB layer with PMA on GaAs, we have optimized the CoFeB annealing temperature (T_a) and thickness by superconducting quantum interference device (SQUID) measurements. The optimized annealing temperature is found to be in the range $250°C - 300°C$. Below or above these temperatures, PMA is much reduced and the magnetization rotates back along the in-plane direction. As already investigated theoretically by Yang et al. [135], the PMA is very sensitive to the Fe(Co)/MgO interface chemical structure. The improvement of PMA at T_{AN} up to $250°C$ could be attributed to an optimization of the chemical structure at CoFeB/MgO interface [111] (the PMA is very sensitive in particular to an under or over oxidized CoFeB/MgO interface). When T_{AN} is too large, Ta atoms start to diffuse through the ultrathin CoFeB to the MgO surface and significantly damage PMA [145].

Figure 3.17 displays the out-of-plane magnetization vs external magnetic field (M-

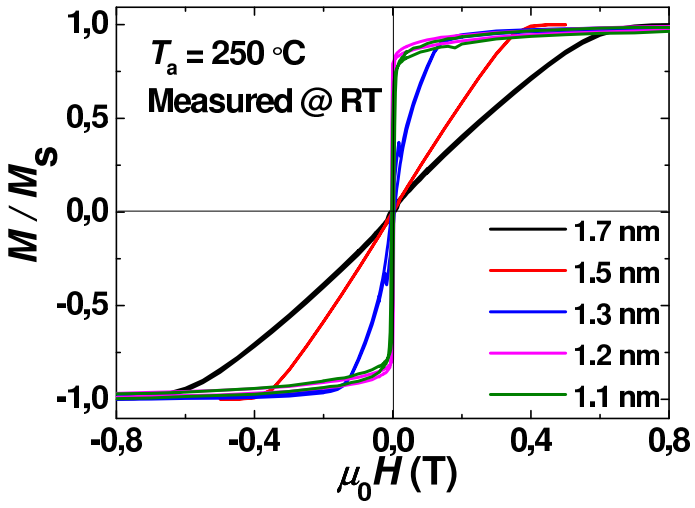

Figure 3.17: RT out-of-plane M-H curves for spin-injectors with different CoFeB thicknesses with $T_{AN} = 250°C$.

H) curves for annealed spin-injectors ($T_{AN} = 250°C$) with different CoFeB thicknesses. The saturation field is found to rapidly decrease on reducing the CoFeB thickness. When the thickness is lower than 1.2 nm, the CoFeB layer possesses a remanent out-of-plane magnetization signifying the occurrence of PMA. This behavior can be easily understood from the competition between the bulk in-plane shape anisotropy and the interface anisotropy.

Figure 3.18 shows the in-plane and out-of-plane M-H curves at 30 K for the perpen-

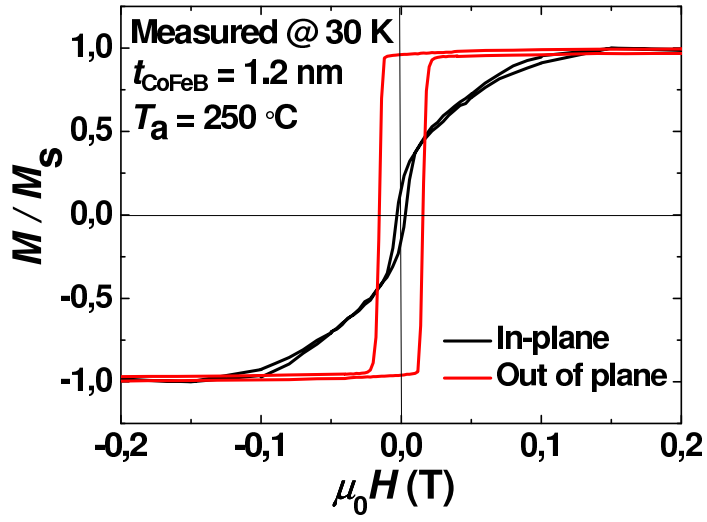

Figure 3.18: M-H curves at 30 K for a spin-injector with 1.2 nm of CoFeB and $T_{AN} = 250°C$ for in-plane and out-of-plane configurations.

dicular injector with optimized conditions: t_{CoFeB}=1.2 nm and T_{AN}=250°C. We can observe a clear perpendicular easy axis with an out-of-plane coercivity of $\mu_0 H_C = 20mT$ and an in-plane saturation field of $\mu_0 H_K = 150mT$.

3.3.4 Electrical spin injection without magnetic field at 25 K probed by Electroluminescence measurements

In this section, we will present the results of EL at low temperature on a spin-LED sample where both the thickness (1.2 nm) and the annealing temperature ($T_{AN} = 300°C$) of the CoFeB injector have been optimized.

A typical EL spectrum acquired at 25 K under a bias of 2.3 V is shown in the top of Figure 3.19 for $\mu_0 H = 0T$. In this spectrum, we can observe a main peak located at about 873 nm corresponding to the heavy exciton line, with a small shoulder at about 870 nm. The multi-peak feature could be attributed to a slightly different indium concentration for the three InGaAs QWs as well as the possible bound exciton at low temperature [119,146,147]. The striking feature is that we can get a large difference of the EL intensities for right (I^+) and left (I^-) circularly polarized components at zero field. The EL circular polarization (P_C) can be determined from the main peak differ-

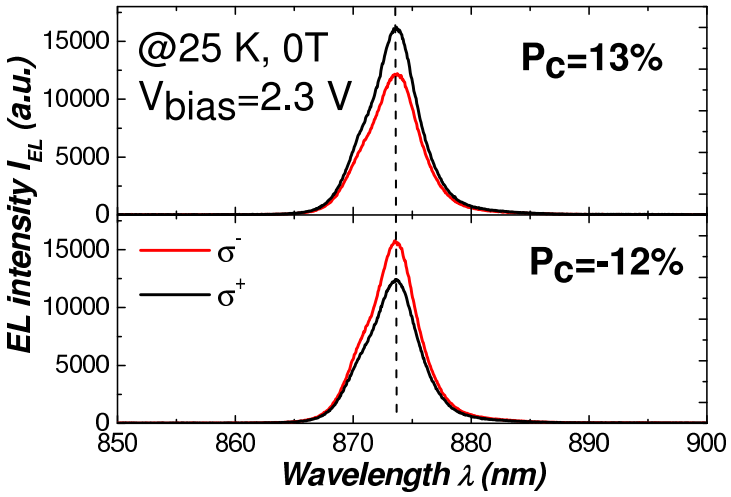

Figure 3.19: EL spectra at 25 K with zero magnetic field for the optimized PMA conditions sample for σ^+ and σ^- polarizations when the field is swept from positive to negative values (curves on the top) and from negative to positive values (curves on the bottom) in the hysteresis loop

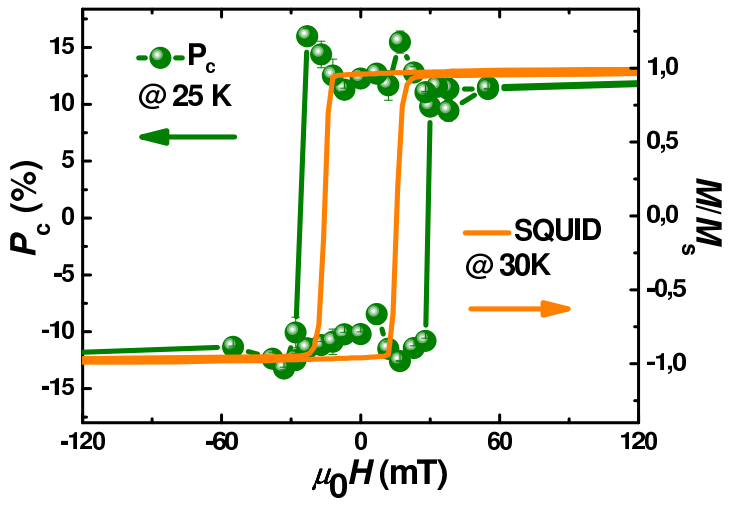

Figure 3.20: P_C as a function of the out-of-plane magnetic field measured at 25 K for a spin-LED with 1.2 nm CoFeB/MgO injectors, which is compared to the corresponding out-of-plane M-H hysteresis loop at 30 K by SQUID in PMA optimized conditions.

ence for I^+ and I^- to be about 13%. To further confirm that this feature originates from the perpendicular spin-injector, we have measured the P_C variation at different magnetic fields. As shown in Figure 3.20, P_C exhibits a clear hysteresis loop feature with almost constant value around 13% at saturation and changing its sign rapidly at $\mu_0 H = \pm 30mT$. The bottom of Figure 3.19 displays the spectrum at $\mu_0 H = 0T$ when the field is swept from negative to positive direction. The hysteresis loop of P_C fairly matches the SQUID hysteresis loop acquired at 30 K on an unpatterned sample (Figure 3.20). The slight difference in the coercivity could be due to a different measuring temperature in the two systems or a slight different effective RTA annealing temperature for the two measured samples.

In Figure 3.21 we show more details about the hysteresis loop measurements of the

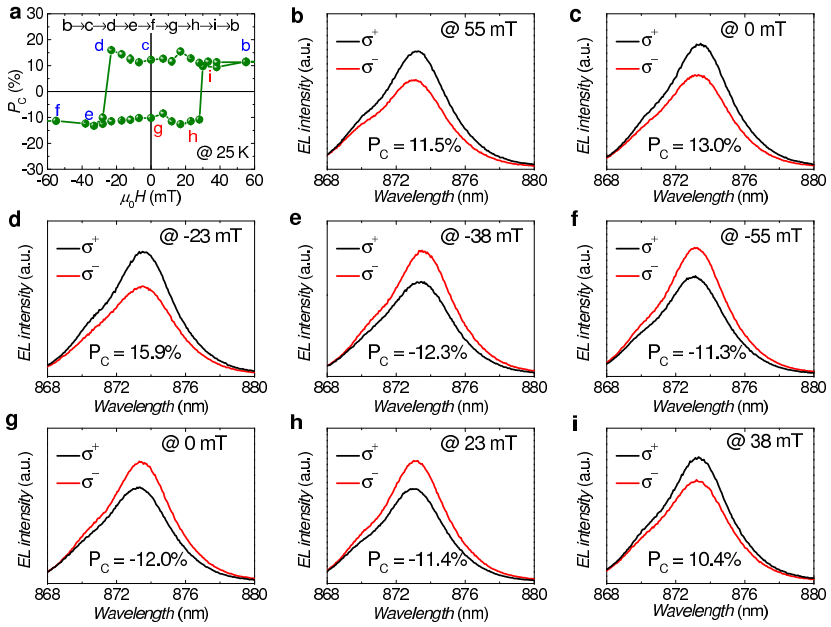

Figure 3.21: (a) P_C as a function of out-of-plane magnetic field measured at 25 K for the spin-LED with optimized PMA injector with a bias of 2.3 V. (b-i) EL spectra for σ^+ and σ^- components at different magnetic field, which are indicated in the hysteresis loop in (a).

circular polarization P_C at 25K. When we sweep the magnetic field between 55 mT to -55 mT, the circular polarization exhibits a sharp jump at $\pm 30mT$, and P_C keeps almost constant around $\pm 13\%$, which is directly related to the ferromagnetic properties of the PMA injector.

To exclude any artificial effect for the measured circular polarization at remanence (zero magnetic field), we have performed two complementary measurements. One is the

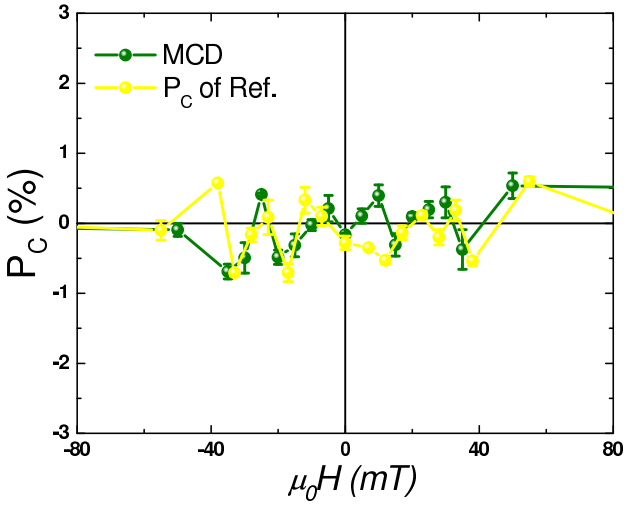

Figure 3.22: MCD measurement from the PMA spin-LED as a function of magnetic field at 25 K. P_C of the EL for a reference sample without CoFeB layer as a function of magnetic field at 25 K.

evaluation of the magnetic circular dichroism (MCD) effect in order to check the differential absorption of respective left and right circularly polarized light [148], through the CoFeB ferromagnetic layer in our sample. With linearly polarized excitation light, we have recorded the MCD signal by photoluminescence (PL) with different magnetic fields. As shown in Figure 3.22, the MCD effect from the PMA spin-LED sample is lower than 1% in all the investigated field range, and this means that the large P_C is really due to the circularly polarized light emitted from the radiative recombination of the spin-polarized electron with unpolarized holes in the QW. The other measurement is to exclude artificial effects such as Zeeman splitting in the QW [149] by EL characterization of a reference sample without CoFeB layer, which can allow us to verify the origin of this spin-polarized injection of electrons. The reference sample has almost the same structure except that the ultrathin CoFeB layer is now replaced by a non-magnetic Ta layer in contact with MgO. As shown in Figure 3.22, the P_C from the reference sample is also less than 1% in all the investigated field range. This gives a strong argument that the large P_C we have observed is really due to the spin-polarized electrons injected from the ultrathin CoFeB layer with PMA.

As a comparison, we display now the signature of the polarization-resolved EL for an in-plane magnetization injector such as CoFeB/MgO before annealing (Figure 3.23). P_C increases linearly with the field before reaching its saturation value (10%) at about 0.4 T. The variation of P_C vs. field pretty matches the corresponding variation of the

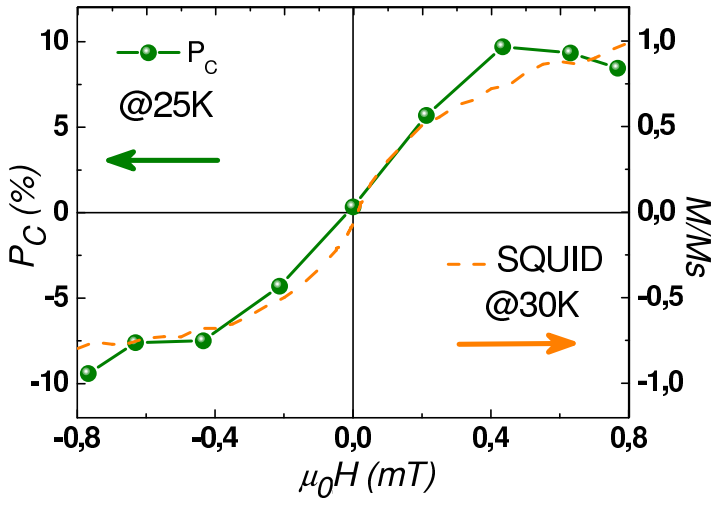

Figure 3.23: In the as-grown injector (non annealed spin-LED), hysteresis loops from P_c (solid line) and corresponding SQUID data (dotted line) at 30 K

out-of-plane magnetization from SQUID measurements. Indeed, in this configuration, P_C tracks the continuous rotation of the magnetization direction from in-plane to out-of-plane, as expected from the optical selection rules [22,81].

3.3.5 Electrical spin injection without magnetic field at room temperature

Another very interesting behavior is that the PMA property of our spin-injector can even persist up to room temperature with almost the same quality. The inset of Figure 3.24 shows the EL spectra with different circular polarizations at 300 K under zero field. The RT coercivity is much reduced compared to low temperature and the transition of P_C around ± 10 mT is also less sharp. This could be due to the domain wall formation at high temperature [150]. A clear difference of $I^{\sigma+}$ and $I^{\sigma-}$ components allows us to obtain $P_C = 8\%$ at RT. The P_C hysteresis loop is also in good agreement with the RT M-H hysteresis loop (Figure 3.24) from SQUID measurements. Although the out-of-plane coercivity $\mu_0 H_C$ is reduced to about 5 mT, it is sufficient to obtain an almost 100% remanent magnetization. In Figure 3.25 we have shown more details about the hysteresis loop measurement of the circular polarization P_C at 300 K.

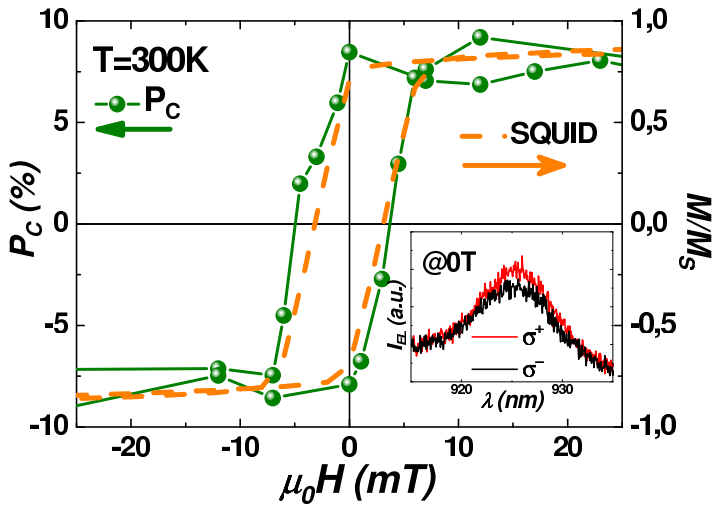

Figure 3.24: P_C as a function of the out-of-plane magnetic field measured at 300 K for the spin-LED with optimized PMA injector, which is compared to the out of plane M-H hysteresis loop at 300 K measured by SQUID. Inset: EL spectra at 300 K with zero magnetic field for σ^+ and σ^- polarizations.

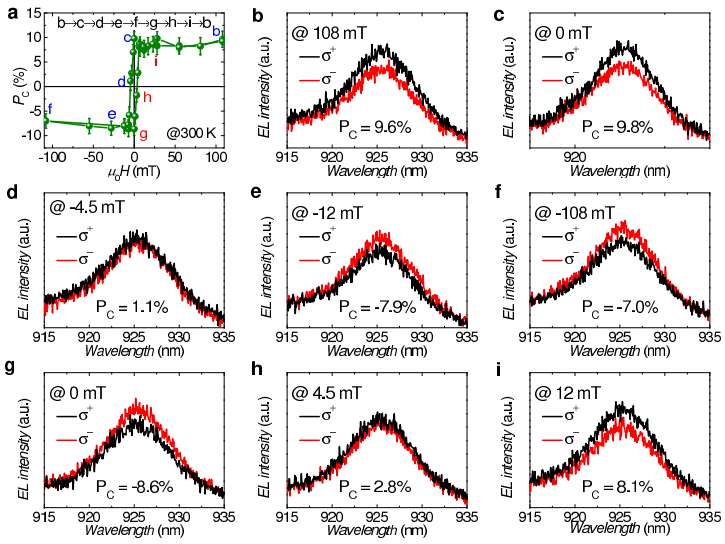

Figure 3.25: (a) P_C as a function of the out-of-plane magnetic field measured at 300 K for the spin-LED with the optimized PMA injector at a bias of 2.3 V. (b-i) EL spectra for σ^+ and σ^- components at different magnetic fields, which are indicated in the hysteresis loop in (a).

3.3.6 Dependence of the electrical spin injection as a function of temperature

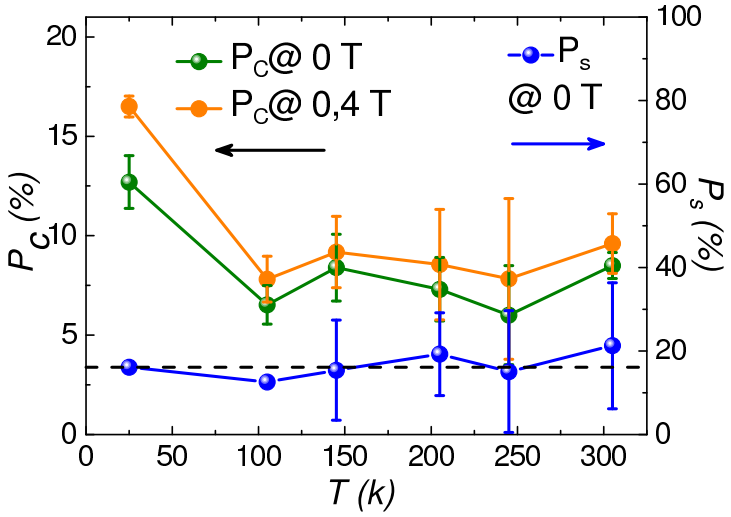

Figure 3.26: Temperature dependence of P_C without magnetic field and with a 0.4 T field. The temperature dependence of P_s is calculated using: $P_s = P_C/F$ from the data without field.

To further investigate the temperature dependence of the spin-injection efficiency with PMA injectors, we have plotted in Figure 3.26 the temperature dependence of P_C without field and with a 0.4T field which is sufficient large to insure an out-of-plane magnetization. We have observed a non-monotonic variation of P_C as a function of the temperature: first a decrease of P_C, followed by a low varying regime above 100 K. A remarkable feature is the very similar evolution for P_C at both $\mu_0 H = 0T$ and $\mu_0 H = 0.4T$. This behavior confirms that the PMA is strong enough to persist up to room temperature. The non-monotonic evolution of P_C likely reflects physical effects inherent to the semiconductor heterostructures rather than to the property of CoFeB/MgO injector itself. In order to check this assumption, we have performed time-resolved photoluminescence (TRPL) measurements [90] on an identical bare p-i-n LED.

As explained in section 3.1.3, the optical circular polarization P_C directly equals the injected electron spin polarization P_s except for a renormalization factor ($F = 1/(1 + \tau/\tau_s)$, where τ is the electron lifetime and τ_s is the spin relaxation time in the QW) which takes into account possible electron spin relaxation mechanisms during its lifetime in the QW. In order to estimate this F factor, we have measured τ and τ_s as

a function of temperature by TRPL.

Figure 3.27 shows typical PL spectra after integration in time domain. Here we

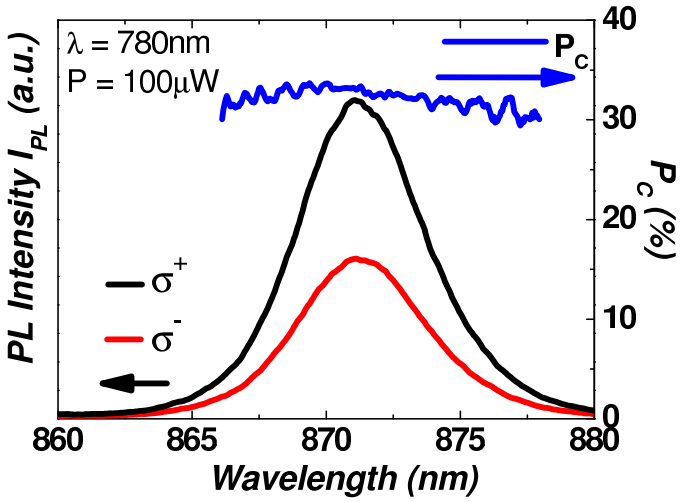

Figure 3.27: Typical PL spectra after integration in time domain for $\sigma+$ and $\sigma-$ components. P_c is deduced from $(I^{\sigma+} - I^{\sigma-})/(I^{\sigma+} + I^{\sigma-})$.

cannot distinguish the multi-peak feature as we have observed in EL spectra because the spectra resolution is lower for TRPL (5.2 nm instead 1.3 nm). With 50% spin polarized photogenerated electrons in the GaAs barrier, we can get about 33% of P_C for the PL. P_C is almost constant around the maximum of the PL spectra. Then we record the time-resolved information through integrating spectrally around the peak maximum with a window of 4-6 nm depending on the spectral width. In fact, the dynamic parameters (τ and τ_s) are not sensitive to the width of this window.

The left picture in Figure 3.28 shows the PL intensity (color code in arbitrary units) as a function of both time and photon wavelength. The white curve represents the PL intensity $(I^+ + I^-)$ as a function of time when the emission is spectrally integrated. The decay time of this PL intensity corresponds to the carrier lifetime τ. As an example shown in Figure 3.29, we perform the exponential fitting of the PL dynamic curve to obtain τ to be about $80 \pm 15ps$. To extract the spin lifetime τ_s, we have studied time-resolved PL circular polarization P_C dynamics. The right picture in Figure 3.28 shows P_C (color code from P_C=0 to 44%) as a function of both time and photon wavelength. The white curve represents P_C as a function of time. The decay time of this P_C dynamics which corresponds to the spin relaxation time τ_s can be extracted by exponential fitting of the curve. As an example shown in Figure 3.30,

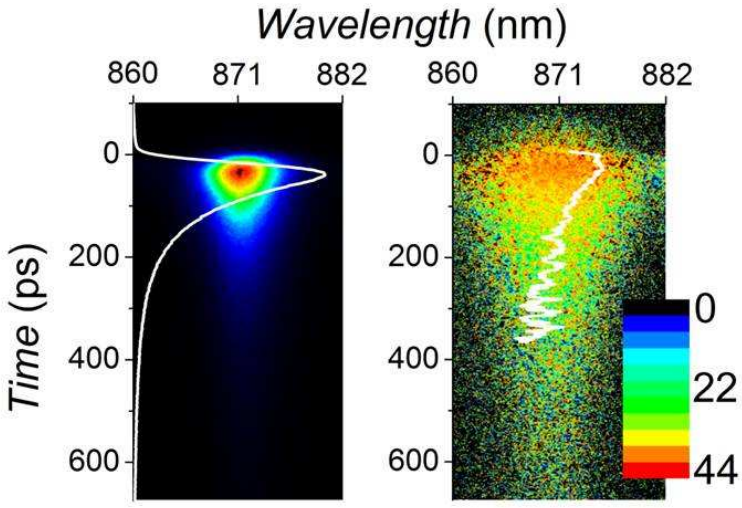

Figure 3.28: Left: PL intensity (color code in arbitrary units) as a function of both time and photon wavelength. The white curve represents the PL intensity as a function of time when the emission is spectrally integrated. Right: PL circular polarization degree P_C (color code from $P_C = 0$ to $P_C = 44\%$) as a function of both time and photon wavelength. The white curve represents P_C as a function of time when the emission is spectrally integrated.

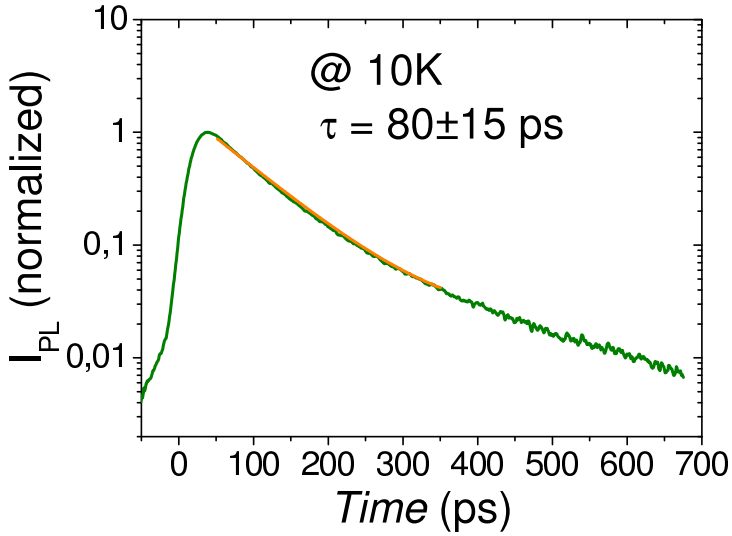

Figure 3.29: Determination of the carrier lifetime τ from an exponential fit of the decay time of the PL intensity ($I^{\sigma+} + I^{\sigma-}$).

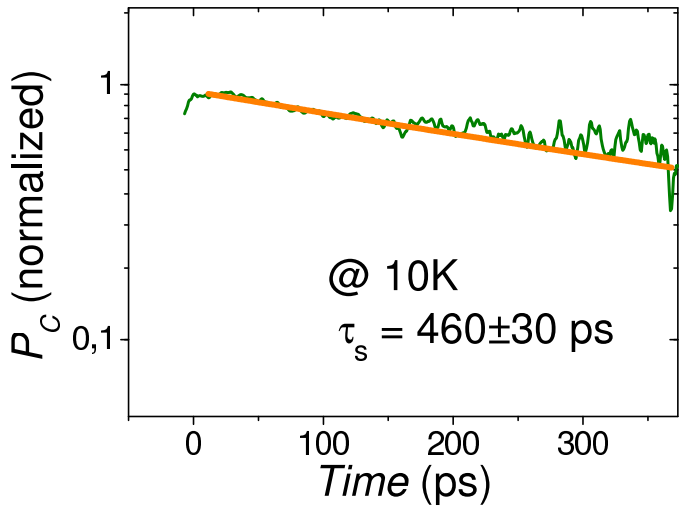

Figure 3.30: Determination of the spin lifetime τ_s from an exponential fit of the decay time of the normalized P_C.

the τ_s can be determined to be about $460 \pm 30ps$.

The spin relaxation time τ_s, as well as the carrier lifetime τ, extracted from the

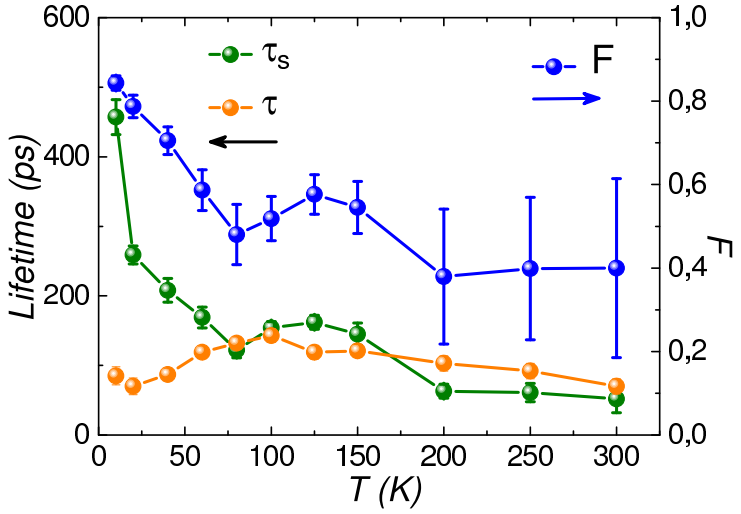

Figure 3.31: Temperature dependence of the electron lifetime τ, the electron spin relaxation time τ_s and the F factor in the QW.

TRPL measurements, are presented in Figure 3.31. A relatively weak variation of the carrier lifetime τ (of the order of 100 ps) vs. temperature can be highlighted, whereas a strong thermal variation of the spin lifetime τ_s is evidenced with an initially fast fall-off followed by a lower decline. The large increase of the spin lifetime at low temperature could be attributed to the spatial localization of excitons due to the inhomogeneity of the QWs. When the temperature increases, the spin relaxation is dominated by the

D'Yakonov-Perel (DP) mechanism which gives a small variation of τ_s up to RT [81]. We have also plotted in Figure 3.31 the temperature dependence of the F factor The F factor vs. temperature behavior mimics the variation of P_C vs. temperature, which results in an overall small variation of P_s vs. temperature. P_s is found to be almost constant with temperature at about $16 \pm 4\%$ (Figure 3.26). This also confirms the thermal stability of our PMA spin-injectors with a high Curie temperature of the FM layer.

3.3.7 Dependence of the electrical spin injection as a function of the applied bias

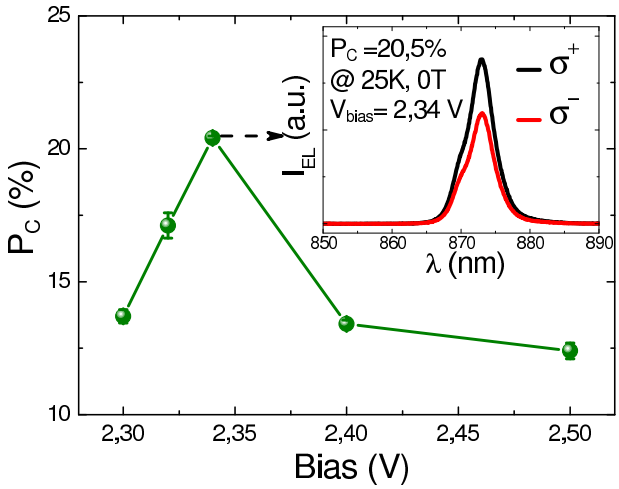

Figure 3.32: P_C as a function of applied bias for the optimized PMA condition sample. Inset: EL spectra at 25 K with zero magnetic field for σ^+ and σ^- polarizations under a bias of 2.34 V.

Finally, we have measured P_C as a function of the applied bias at 25 K under zero field. As shown in Figure 3.32, P_C is found to be strongly dependent on the bias. Our maximum P_C in remanence can even reach 20.5% at the optimal bias of 2.34 V. The corresponding polarization-resolved EL spectra are shown in the inset of Figure 3.32. P_C decreases below and above this optimized bias. The best remanent P_C we obtained is already six times larger than the published results using any other PMA injectors [35,96,97,102,133]. Although the electrical spin-injection efficiency is still lower than the one for the best in-plane injector [9], which could be related to some particular effect rising from the ultrathin CoFeB layer during annealing, we believe that a detailed interfacial investigation and a further optimization of the annealing effect

could certainly lead to even larger values.

3.3.8 Conclusion

In this part, we have demonstrated a large EL P_C in GaAs-based spin-LEDs at zero magnetic field using a CoFeB/MgO perpendicular spin-injector. The value of P_C at remanence is measured as large as 20% at 25 K and still 8% at 300 K.

The potential impact of such an ultrathin injector should be stronger than the one of thick PMA multi-layers injectors for two main reasons:

- For monolithic Spin Vertical Cavity Lasers (Spin VCSELs) or Spin Vertical External Cavity Lasers (Spin VECSELs) where the magnetic injector has to be embedded inside the optical cavity. The light absorption by the injector becomes a critical point because the corresponding intracavity loss can easily prevent the laser regime. Only an ultrathin injector as we proposed here should be employed, ruling out the use of thick multilayers PMA injectors. In this purpose, let's note that the typical absorption coefficient of Co/Pt (7 nm) multilayers integrated in spin-LEDs is about 30% in the infrared spectra [151] which clearly prevents, for instance, any laser operation in cavity VECSELs. On the other hand, the absorption at the same wavelength within a 1.2 nm CoFeB layer has been measured to be less than 3% [151] which is compatible with VECSELs operation.

- For the electrical control of circularly polarized light via Spin Transfer Torque (STT). The ultrathin CoFeB PMA layers are now considered as the most promising electrodes for STT operations in MRAM technology, because they satisfy (i) high thermal stability at reduced dimension, (ii) low current induced magnetization switching and (iii) high spin polarization at the same time. Obviously, this type of injector is also the best candidate for electrical control of circularly polarized light via STT for devices operating at room temperature without magnetic field which will be one of the main concerns in some future technological

developments.

Chapter 4

Spin Dynamics of L-valley Electrons in GaAs

4.1 Optical orientation in GaAs 97

4.1.1 Why analyzing the electron spin dynamics in satellite L-valleys in GaAs 97

4.1.2 GaAs band structure 98

4.1.3 Spin orbit splitting in the L-valley 100

4.1.4 Selection rules in the Γ-valley 103

4.2 Experimental results of Polarized Photoluminescence Excitation 103

4.2.1 Experimental setup and sample description 104

4.2.2 Photogenerated electron spin-polarization 104

4.2.3 Depolarization induced by the transverse magnetic field . . . 109

4.3 Dynamics of spin relaxation in L-valley 110

4.3.1 Spin photogeneration and dynamics 111

4.3.2 Discussion 112

4.4 Conclusion 114

In this chapter, optical orientation experiments have been performed in GaAs epilayers with photoexcitation energies in the 3 eV region yielding the photogeneration of spin-polarized electrons in the satellite L-valley. We demonstrate that a significant fraction of the electron spin memory can be conserved when the electron is scattered from the L to the Γ valley following an energy relaxation of several hundreds of meV. Combining these high energy photo-excitation experiments with time-resolved photoluminescence spectroscopy of Γ valley spin-polarized photogenerated electrons allows us to deduce a typical L valley electron spin relaxation time of 200 fs, in agreement with theoretical calculations.

4.1 Optical orientation in GaAs

4.1.1 Why analyzing the electron spin dynamics in satellite L-valleys in GaAs

During the past 50 years, electron spin dynamics in III-V semiconductors has been studied in great detail using optical orientation technique. GaAs is one of the most studied systems due to its wide use in optoelectronics. However all optical orientation experiments in GaAs were performed with optical excitation energies close to the band gap (typically 1.5 - 2 eV), yielding the photogeneration of spin-polarized electrons in the Γ valley. In addition to its fundamental aspect, the understanding of the electron spin dynamics of electrons in the upper valleys is crucial for devices based on electrical injection such as spin light-emitting diodes(LEDs) [37,101,152] and spin lasers [6,153], where electrons populate not only the Γ valley but also the satellite L and X valleys (at large bias). The spin polarization dynamics of the L and X electrons will therefore make an important contribution to the overall spin injection efficiency in spin LEDs based on a ferromagnetic layer (FM) and a Schottky or MgO barrier (at large bias) and is also vital for the observation of the recently predicted spin Gunn effect, i.e., the spontaneous generation of a spin-polarized current [36].

Despite their importance, the experimental determination of the spin relaxation times in the L and X valleys, which have been predicted to be much shorter than in the Γ valleys, is lacking [37,154–156]. The interplay between Γ and L electrons in GaAs has been studied in detail both experimentally and theoretically in the context of the classic, spin-independent Gunn effect [157–159]. Apart from their different energies, Γ and L electrons experience a Dresselhaus intrinsic spin splitting of a very different amplitude, which is a key parameter for the spin polarization. The spin-orbit coupling parameters in the upper valleys, for $k_0 = k_L$ or $k_0 = k_X$, have been calculated recently by different groups [38,160,161]. Compared to the Γ valley of III-V semiconductors, larger k-dependent spin splittings in the surrounding of the L point were predicted: as a fact, (as will be shown later) for k momentum close to the Γ or L points, the spin splitting is cubic in k in the former while it is linear in k in the latter. As an important consequence, the Dyakonov-Perel spin relaxation mechanism in the L valleys is expected to be very efficient.

The few experimental investigations of the L-valley electron spin polarization were performed by photoemission spectroscopy in GaAs [11,14]. In these experiments the GaAs surface is treated with Cs and O to obtain a negative electron affinity close to the surface. The spin polarization of electrons photoemitted from (110) GaAs following the excitation with circularly polarized light (∼3 eV) measured by means of a Mott polarimeter was 8% at low temperature. However, L-valley electron spin relaxation times are difficult to extract from these photoemission experiments [14] since:

- The kinetic energy of electrons was not measured simultaneously with their spin so that it is impossible to assign this polarization to L electrons only or to an admixture of L and Γ electrons.
- Depolarization can occur when the electrons photoemitted from GaAs pass through the Cs-O layer.

In this chapter, we report the first PL experiments showing that a significant electron spin memory can be conserved when electrons are scattered from the L to the Γ valley. A typical L-valley spin relaxation time of about 200 fs is measured experimentally for the first time.

4.1.2 GaAs band structure

Figure 4.1 displays a simplified scheme of the GaAs band structure, including Γ and L valleys. When carriers are photogenerated with an excitation energy $E_{exc} = 2.987eV$, four types of optical transitions are allowed. Three of them (dotted lines) will photogenerate electrons in the conduction band (CB) near the Γ valley through respectively the heavy-hole band→ CB ($\Gamma_8 \rightarrow \Gamma_6$ close to Γ point), light-hole band → CB ($\Gamma_8 \rightarrow \Gamma_6$) and the spin-orbit split-off band → CB ($\Gamma_7 \rightarrow \Gamma_6$) transitions. In the effective mass approximation, this yields the photogeneration of electrons with kinetic energy of 1310 meV, 830 meV and 800 meV respectively. The overall initial polarization involves the joint density of states for all these transitions. Note however that the spin density generated by these transitions should be weak due to partial cancellation of

the contribution of the three valence bands (HH, LH and SO). As will be seen in the next section 4.1.4. (Figure 4.5)

In addition to these three optical transitions leading to the photogeneration of Γ_6

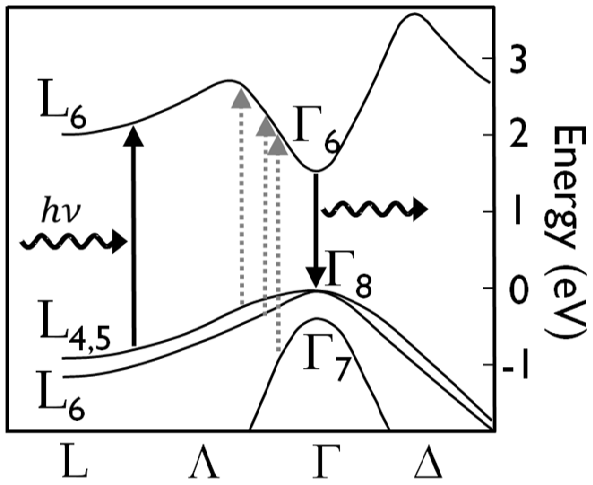

Figure 4.1: Schematics of the GaAs band structure; the arrows present the optical excitations $E_{exc} = 2.987eV$ and detection energies used in the experiments of the following section. The high symmetry points in this figure are labelled according to [11].

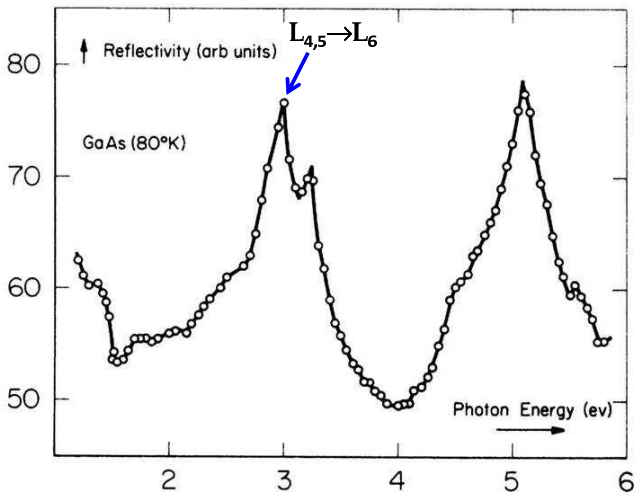

Figure 4.2: Reflectivity of etched GaAs at 80 K [12]

electrons, a strong absorption occurs due to the allowed $L_{4,5} \rightarrow L_6$ transitions in the vicinity of the L valley. Note that the CB in the L valley minimum lies 296 meV above the Γ one. As depicted in Figure 4.1, there is a large region in k space where the L_6 and valence $L_{4,5}$ bands are nearly parallel; this feature together with the fact that the corresponding masses are larger than the ones in Γ make these L-valley transitions

dominant in this spectral region [12]. For an excitation energy ∼200 meV larger, the reflectivity peak associated to the $L_{4,5} \rightarrow L_6$ transitions vanishes and is replaced by a second peak with a similar amplitude corresponding to the $L_6 \rightarrow L_6$ transitions (see Figure 4.2).

4.1.3 Spin orbit splitting in the L-valley

Besides the non k-dependent spin-orbit term described in equation 1.3 of chapter 1, there is an additional k-dependent spin-orbit term. We recall that in the Γ-valley, due to symmetry arguments, this spin-orbit Hamiltonian in the conduction band takes the form:

$$H_D = \gamma_D \left(k_x(k_y^2 - k_z^2)\omega_x + k_y(k_z^2 - k_x^2)\omega_y + k_z(k_x^2 - k_y^2)\omega_z \right) = \Omega_D \cdot S \tag{4.1}$$

where: $\Omega_D \equiv \frac{2\gamma_D}{\hbar}(k_x(k_y^2 - k_z^2), k_y(k_z^2 - k_x^2), k_z(k_x^2 - k_y^2))$, $S = \frac{\hbar}{2}\sigma$, and σ_j (j=x, y, z) are the Pauli matrixes ((x, y, z) directions correspond to the ones of the cubic cell). This leads to the k-dependent spin spliting:

$$\Delta E(k) = 2\gamma_D \sqrt{k_x^2(k_y^2 - k_z^2)^2 + k_y^2(k_z^2 - k_x^2)^2 + k_z^2(k_x^2 - k_y^2)^2} \tag{4.2}$$

where γ_D is the Dresselhaus spin-orbit coefficient. Note that this expression is valid in any non centro-symmetric cubic crystal with point group of T_d symmetry. The value of γ_D was calculated by using $k \cdot p$ and tight binding approaches yielding in :$\gamma_D \approx 23.7eV \cdot \mathring{A}^3$. This description is valid when $|k| < 2.5 \times 10^7 cm^{-1}$ [162]. For $\langle 110 \rangle$ directions, $\Delta E(\vec{k})$ is maximum and takes the value: $\Delta E_{\langle 110 \rangle} = \gamma_D k^3$.

In the L-valleys, the symmetry is C_{3v}. So the Dresselhaus spin-orbit Hamiltonian in the conduction band takes the form:

$$H_D^L = \beta_D^L(k_{y'}\sigma_{x'} - k_{x'}\sigma_{z'}) = \Omega_D^L \cdot S \tag{4.3}$$

where the unit vectors are $\vec{e}_{x'} = \frac{1}{\sqrt{6}}(-2, 1, 1)$, $\vec{e}_{y'} = \frac{1}{\sqrt{2}}(-1, 1, 0)$, $\vec{e}_{z'} = \frac{1}{\sqrt{3}}(1, 1, 1)$ [163], and the coefficient $\beta_D^L = 0.26eV\dot{A}$ is given in [164]. Similar expressions are

obtained for other L-valleys. The associated peudo-vector Ω_D^L is:

$$\Omega_D^L = \frac{2\beta_D^L}{\hbar}(k_{y'}, -k_{x'}, 0) \tag{4.4}$$

The spin splitting in the L-valleys is given by:

$$\Delta E^L(k) = 2\beta_D^L \cdot k_\perp^L = 2\beta_D^L \sqrt{k_{x'}^2 + k_{y'}^2} \tag{4.5}$$

It is maximal in the plane orthogonal to the considered L-valley axis. So we can deduce from the expression 4.4 that the spin relaxation tensor due to the D'Yakonov-Perel mechanism is anisotropic. In that case the spin relaxation rates are given by:

$$\frac{1}{\tau_{z'z'}} = \langle (\Omega_D^L)^2 \tau_p \rangle = \frac{2}{\tau_{x'x'}} = \frac{2}{\tau_{y'y'}} \tag{4.6}$$

where τ_p is the linear momentum relaxation time due to electron collisions. So we observe now that the spin splitting in the L valley is k linear while in the Γ-valley it is cubic in k.

To give a feeling of the relative spin relaxation efficiencies in L and Γ valleys with the D'Yakonov-Perel mechanism, we present a simple estimation of the spin relaxation time in the case of a non-degenerate electron gas taking a fixed collision time.

In the Γ valley, we get the expression

$$\frac{1}{\tau_s^\Gamma} = \left(\frac{2\gamma_D^\Gamma}{\hbar}\right)^2 \left(\frac{2m^\Gamma kT}{\hbar^2}\right)^3 \tau_p \tag{4.7}$$

For the L valley, we obtain:

$$\frac{1}{\tau_{s,\parallel}^L} = 2\left(\frac{2\beta_D^L}{\hbar}\right)^L \frac{m_\perp^L kT}{\hbar^2} = \frac{2}{\tau_{s,\perp}^L} \tag{4.8}$$

where $m^\Gamma = 0.0665 m_0$ and $m_\perp^L = 0.0754 m_0$.

The Figure 4.3 presents the results for a typical value of $\tau_p = 200 fs$.

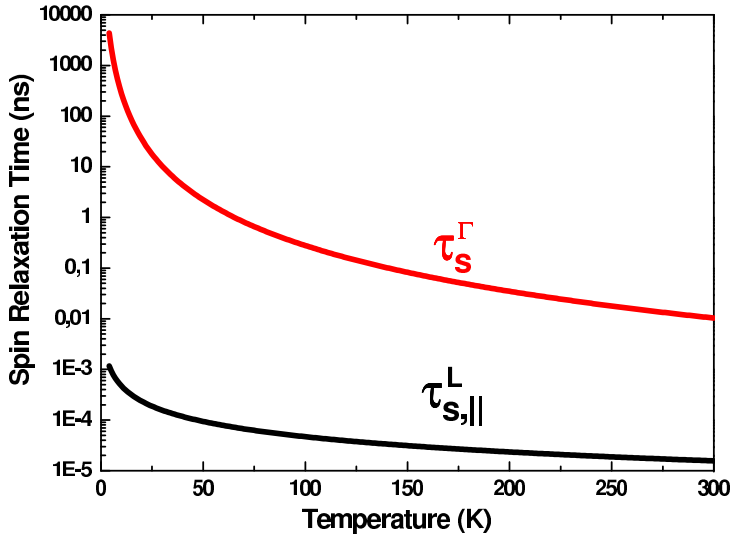

Figure 4.3: Spin relaxation time in the Γ valley and longitudinal spin relaxation time in the L valley as a function of temperature for a non-degenerate electron gas. The collision time is taken as $\tau_p = 200 fs$.

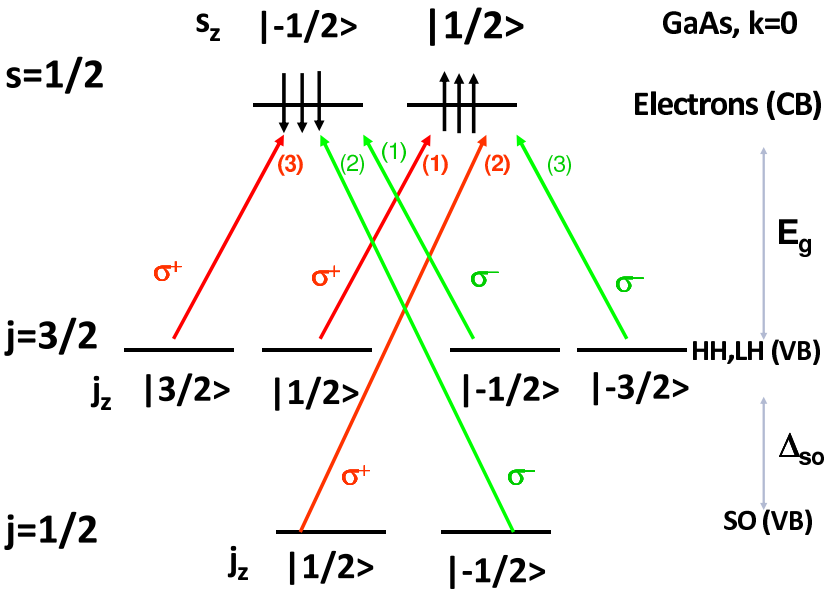

Figure 4.4: Selection rules in the Γ valley

4.1.4 Selection rules in the Γ-valley

We recall here the usual selection rules in the Γ valley (see Figure 4.4). Due to the degeneracy of heavy and light holes in Γ, exciting at the gap with fully circularly polarized light ($P_c = 100\%$) leads to the photo-generation of a population of electrons with a spin polarization $P_s = 50\%$, and to the circular polarization of corresponding emited photons $P_c = 25\%$ [22]. The exploration of optical orientation in the Γ valley has already been performed extensively (see Figure 4.5).

The goal of the work presented in the following is to extend these previous studies

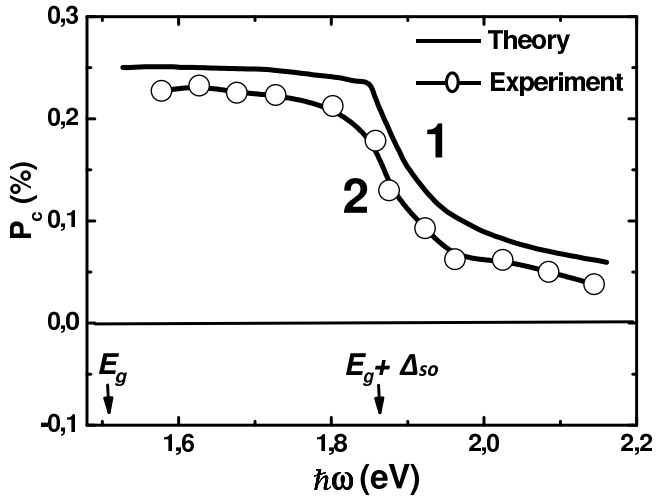

Figure 4.5: Dependence of the degree of circular polarization of the luminescence in GaAs on the exciting photon energy [13]

in the Γ-valley to the L-valleys in the photon energy range $h\nu = 2.8 \sim 3.2$ eV.

4.2 Experimental results of Polarized Photoluminescence Excitation

In order to access the spin polarization of L-valley electrons in an all optical experiment, we have performed optical orientation experiments with laser excitation energies in the range $h\nu = 2.8$–3.2 eV and detected the variation of the luminescence polarization at the fundamental gap transition (Eg $\sim$ 1.5 eV) as a function of $h\nu$ (Figure 4.1) by using the set-up which has been introduced in the third section of Chapter 2 (see

Figure 2.5). These measurements allow us to precisely quantify the energy-dependent optical orientation of L electrons and the significant, remaining polarization of electrons that have relaxed from the L to the bottom of the Γ valley. These experiments, combined with classical time-resolved optical orientation experiments performed with an excitation energy close to 1.5 eV, allowed us to measure a typical L-valley electron spin relaxation time τ_S^L= 200 fs, in good agreement with theoretical predictions.

4.2.1 Experimental setup and sample description

In order to measure the electron spin relaxation time in the L-valleys, we have developed a very specific detection set-up. First the wavelength of excitation must be extended to the blue to reach the range 2.8-3.2 eV to be able to photogenerate electrons in L-valleys. We have thus used a Ti:Sa laser which frequency is doubled by a spectra GWU system with a LBO non-linear crystal. Second, we will have to detect circular polarization rates of a few percent at maximum. In order to get a very high sensitivity in the detection of luminescence circular polarization (required sensitivity of about 0.1%), we have used a double modulation technique. (see Chapter 2 for more details)

The investigated sample has been grown by molecular beam epitaxy on nominally undoped (001) GaAs substrates. It consists of 1 μm Beryllium p-doped epilayer with $p_0 = 10^{18}$ cm^{-3}. The sample was grown by C. Fontaine (LAAS-CNRS Toulouse). This allows us to increase the detected PL circular polarization by decreasing the carrier life time in the Γ conduction band.

The PL peak position ($\sim$1.494 eV) we observed is consistent with the band-gap shrinkage induced by the high p doping [165]. Figure 4.6 presents the time-integrated PL spectrum for an excitation energy $E_{exc} = 2.987eV$.

4.2.2 Photogenerated electron spin-polarization

Figure 4.7 displays the PL circular polarization detected at the fundamental gap (E_{det}=1.494 eV) as a function of the excitation energy. The regions (b) and (c) indicate regions where the absorption is associated to the $L_{4,5} \rightarrow L_6$ and $L_6 \rightarrow L_6$

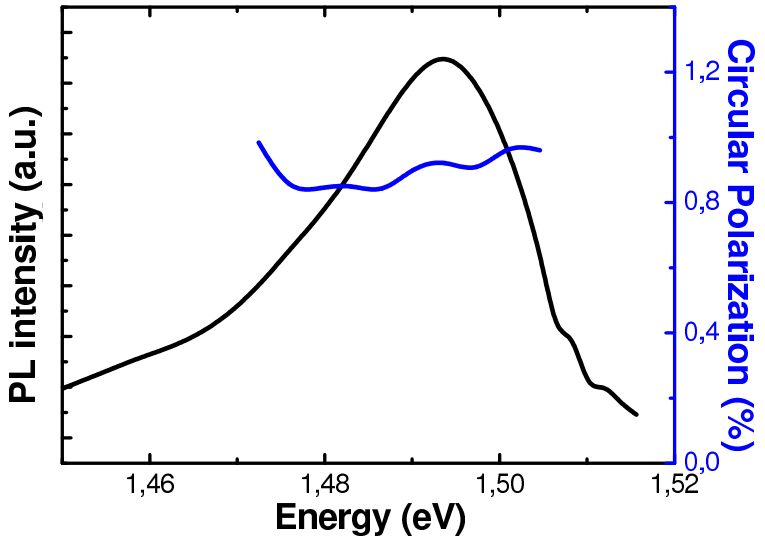

Figure 4.6: Time-integrated photoluminescence spectrum and the corresponding circular polarization following a σ^+-polarized laser excitation at an energy $E_{exc} = 2.987$ eV.

transitions respectively [12]. Remarkably we observe a significant polarization though the photogenerated spin-polarized electrons have experienced a very large energy loss before radiative recombination at the bottom of Γ_6 valley. Let us remind that the PL circular polarization P_c detected at the fundamental gap tracks directly the electron spin polarization P_s: $P_s = 2P_c$ according to the well known optical selection rules [22] and the fact that the hole spin relaxation time is of the order of 1 ps or less [81]. For E_{exc}=2.987 eV (labeled (b) position in Figure 4.7), we observe a peak in the PL circular polarization at $P_c \sim 0.9\%$. This peak coincides unambiguously with the absorption peak corresponding to the $L_{4,5} \rightarrow L_6$ transition [12] ; its position is also close to the one observed in photo-emission experiments [11]. This demonstrates that the electrons photogenerated in the L valley preserve a fraction of the initial spin polarization after the scattering in the Γ valley and subsequent radiative recombination.

The detected electron spin polarization depends both on (i) the maximum photogenerated spin polarization P_0 related to the optical selection rules imposed by the symmetry of the carrier wave functions and (ii) the ratio between the electron spin relaxation time and electron lifetime. The inset graph of Figure 4.7 displays the photogenerated electron spin polarization P_0 as a function of the optical excitation energy deduced from pseudo potential band structure calculations based on local density approximation (LDA) or 30 bands $\mathbf{k} \cdot \mathbf{p}$ calculations [166]. We observe a good qualitative agreement between the excitation energy dependences in the 3 eV region of the mea-

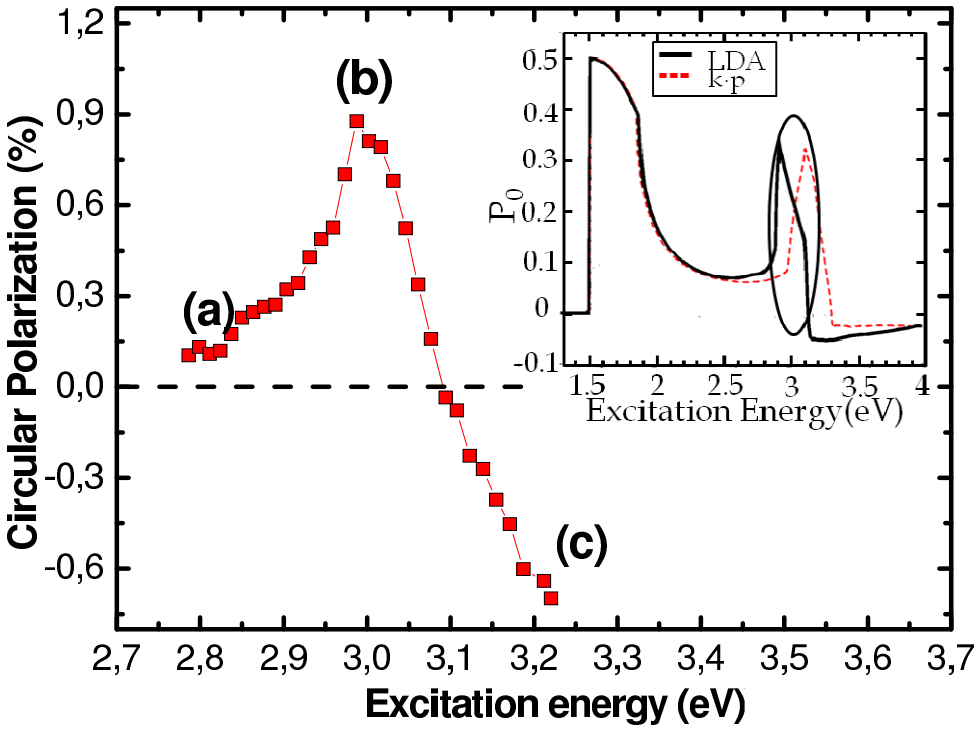

Figure 4.7: PL circular polarization as a function of the excitation energy at 10K. Inset: photogenerated electron spin polarization calculated using LDA and $k \cdot p$ band structures.

sured PL circular polarization and the calculated maximum spin polarization despite the great complexity inherent to the calculation of high energy electron wave functions. The energy of the measured circular polarization peak (2.987 eV) is closer to the one calculated with LDA (2.90 eV) than with the $\mathbf{k} \cdot \mathbf{p}$ method (3.15 eV).

When the excitation energy increases further we observe that the measured circular polarization decreases and becomes negative ($h\nu \simeq$3.1 eV, (c) in Figure 4.7) in the excitation energy (c) region. Again, the measured position of P_C is closer to the LDA calculation than the $k \cdot p$ one ($\sim$3.3 eV).

Note that the sign reversal of the spin polarization that we observe in the lumines-

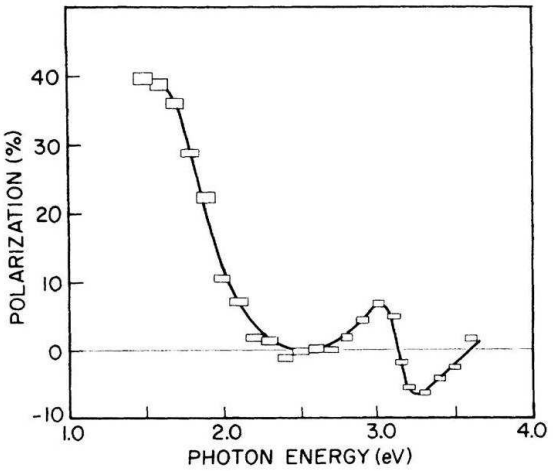

Figure 4.8: Photoemission spectrum of spin polarization from GaAs+CsOCs at low temperature. [14]

cence is in very good agreement with the one observed previously in photo-emission experiments (see Figure 4.8) [14].

This is in full agreement with the expected reversed spin polarization when the transition $L_6 \rightarrow L_6$ is excited; indeed, the spin-orbit splitting energy between the $L_{4,5}$ and L_6 bands is $\sim$220 meV [167]. Note that Nastos *et al.* calculated a photogenerated spin polarization in this region of $P_0 \sim -5\%$ (inset of Figure 4.7 [166]). The reversal of the spin polarization sign for the two types of L valley transitions can be explained qualitatively as follows. For σ^+ polarized light propagating along the valley axis (*e.g.* [111]), the photogenerated electron spin polarization would be 100% for transitions from $L_{4,5}$ with a wave function $|(X - iY)\downarrow\rangle/\sqrt{2}$ to $|S\downarrow\rangle$ in L_6 and -100% for transitions from L_6 with a wave function $|(X - iY)\uparrow\rangle/\sqrt{2}$ to $|S\uparrow\rangle$ in L_6, if we consider the excitation of states in a single L valley [11,168]. Without taking into account the joint density of

states, the optical selection rules for electrons photo-generated in a single L-valley for a light propagating along the valley axis ($\langle 111 \rangle$ directions) are demonstrated in appendix A. These rules are summerized in Figure 4.9.

Taking into account the 8 different L valleys orientations (Figure 4.10), the re-

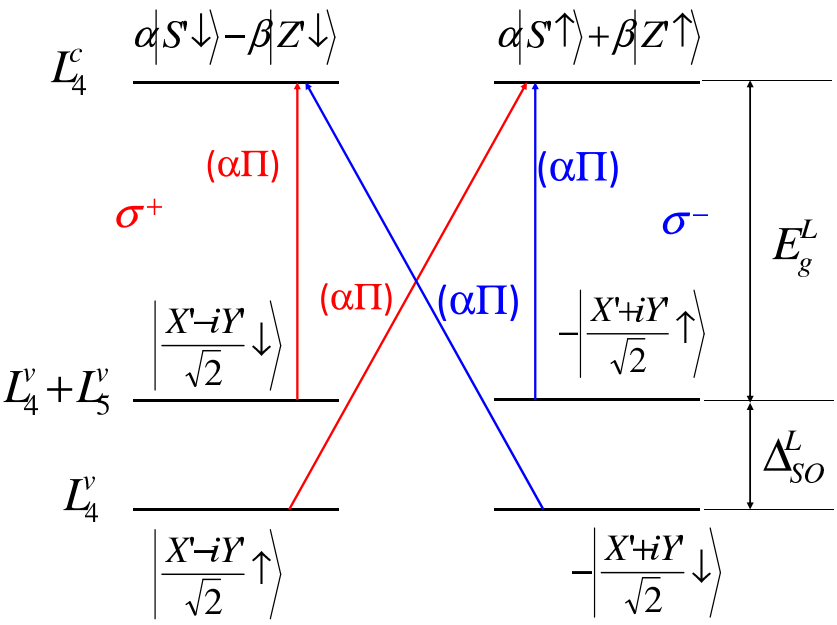

Figure 4.9: Selection rules in L-valleys

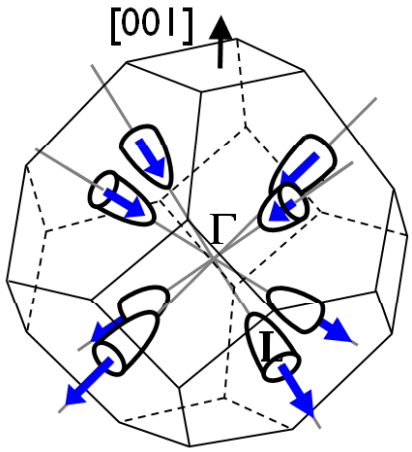

Figure 4.10: Sketch of the Brillouin zone of GaAs displaying the eight L valleys. Note that two L-valleys differing by a translation of the reciprocal lattice are equivalent. The blue arrows represent the photogenerated spins in L valleys.

spective joint densities of states for each transition and a light propagation along the [001] direction (as in the experiments presented here) this yields the calculated value P_0 ∼30% for a resonant excitation of the $L_{4,5} \rightarrow L_6$ transition and $P_0 \sim -5\%$ for

exciting both$L_{4,5} \rightarrow L_6$ and $L_6 \rightarrow L_6$ transitions (inset of Figure 4.7). We give the following qualitative explanation for this negative polarization.

Since the conduction electron mass becomes lighter when k goes from L to Γ point, while the valence band mass remains similar, the joint density of states of $L_6 \rightarrow L_6$ is lightly stronger than the $L_{4,5} \rightarrow L_6$ bands transition, leading to some imbalance between the photon generated spin-down population $L_{4,5} \rightarrow L_6$ and spin-up populations $L_6 \rightarrow L_6$. This leads to a reverse of the P_c sign.

Finally let us emphasize that for excitation energies less than 2.8 eV (i.e. smaller than the L valley absorption), we measure in the region (a) in Figure 4.7 a circular polarization close to zero. The calculations predict in this energy region a maximum photogenerated spin polarization P_0 ∼10%. Thus our results indicate that the total contribution of the spin-polarized hot electrons photogenerated in the Γ_6 conduction band (dotted arrows in Figure 4.1) to the PL circular polarization detected at the bottom of the Γ_6 band is very weak in this excitation energy range. The spin relaxation time for these high energy electrons in the Γ_6 CB might be short as a result of the large electron k vector values and the k^3 splitting of the Γ valley Dresselhaus spin-orbit coupling in bulk GaAs [156]. However, this effect is partly concerned due to the very short life time of this highly excited states. As a consequence, the detected P_c ∼0.9% measured for an excitation energy of 2.987 eV can undoubtedly be assigned to the spin-polarized electrons photogenerated in the L valley. Moreover, the contribution of the L valley transitions to the absorption in this energy range is much larger than the Γ valley ones [12,166] where the electron mass is much lower, leading to a smaller joint density of states for transition $\Gamma_8 \rightarrow \Gamma_6$ than for $L_{4,5(6)} \rightarrow L_6$ transitions. For the sake of simplicity we will neglect in the following the small contribution of these photogenerated Γ_6 hot electrons.

4.2.3 Depolarization induced by the transverse magnetic field

To confirm that the measured circular polarization of the luminescence is the result of the optical orientation of electron spins, we have observed depolarization induced by an externally applied transverse magnetic field (Hanle effect). We measured the dependence of the circular polarization degree on a variable transverse magnetic field

(Voigt configuration) when the spin polarized electrons are photogenerated in the L valley. Figure 4.11 presents the corresponding Hanle curve for E_{exc}=2.987 eV (this corresponds to the peak of zone b in Figure 4.7) and a detection energy of E_{det}=1.494 eV.

Because of the fast $L \rightarrow \Gamma$ scattering time, the Hanle curve can be well described by

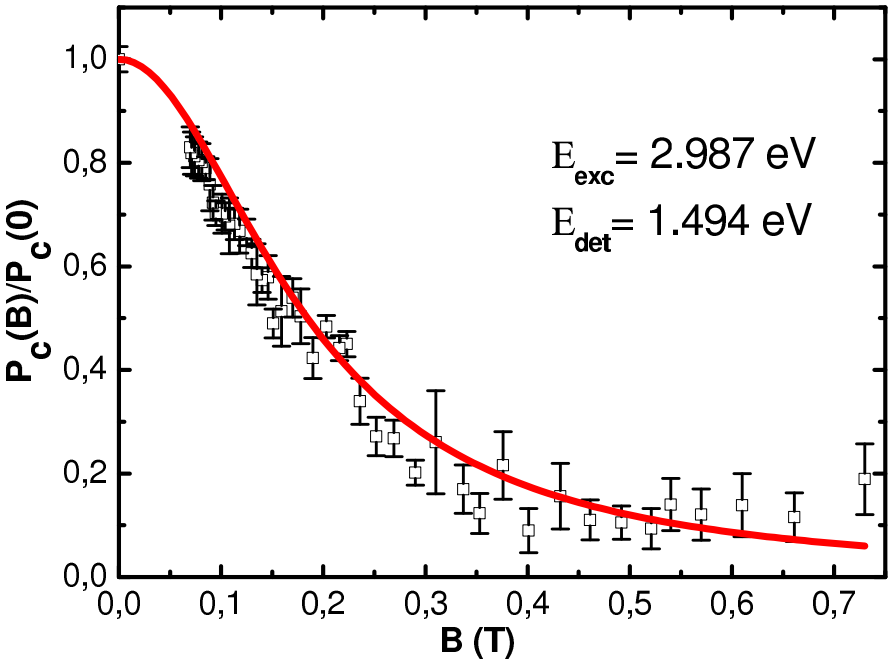

Figure 4.11: Variation of the PL circular polarization degree as a function of the transverse magnetic field B. The full line is a Lorentzian curve with T_S = 140 ps.

a simple Lorentzian function which takes into account only the electron spin relaxation time τ_S^Γ and the electron lifetime τ^Γ in the Γ valley: $P(B)/P(0) = [1 + (\Omega \cdot T_S)^2]^{-1}$ where $\Omega = g\mu_B B/\hbar$, $g = -0.44$ is the Γ electron g factor and μ_B the Bohr magneton. The Γ electron spin lifetime T_S writes simply $(T_S)^{-1} = (\tau_S^\Gamma)^{-1} + (\tau^\Gamma)^{-1}$. The full line in Figure 4.11 is the result of a fit with T_S=140 ps in satisfactory agreement with the direct measurement by time-resolved photoluminescence spectroscopy presented in the next section.

4.3 Dynamics of spin relaxation in L-valley

In order to extract some quantitative information on the electron spin dynamics in the L valley from the measured polarization of the luminescence displayed in Figure

4.7, one has to take into account the optical selection rules in the L valley and the electron spin relaxation time which can occur both in the Γ and L valleys.

4.3.1 Spin photogeneration and dynamics

As said previously in section 4.2.2, optical selection rules have to be re-calculated for electrons photo-generated in the L-valleys (see Appendix A). In contrast to the well-known optical selection rules related to the photogeneration of spin-polarized electrons in the isotropic conduction band Γ_6 valley, the calculated photogenerated spin polarization in the L valley requires to consider the 4 unequivalent $\langle 111 \rangle$ valleys whose orientations are different from the [001] σ^+ polarized light propagation axis (Figure 4.10). For the $L_{4,5} \rightarrow L_6$ optical transition, it can be shown that the corresponding spin polarization in the L valley is $P_0^L = 50\%$ considering a quantization axis along [001] (appendix A); this value is consistent with P_0 ∼30% calculated by Nastos *et al.* (inset of Figure 4.7) for an optical excitation energy resonant with $L_{4,5} \rightarrow L_6$, but which also includes a weak contribution of the hot photogenerated electrons in the Γ_6 valley characterized by a smaller spin polarization [166]. The maximum circular polarization of the luminescence which could be detected at the fundamental gap ($\Gamma_8 \rightarrow \Gamma_6$) is thus $P_0^L/2$ =25%, or $P_0/2$ =15% according to Nastos *et al.* (the factor 2 is due to the transitions involving both heavy holes and light holes in the Γ valley [22]). We emphasize that this "loss"of spin polarization arises from symmetry considerations and not from any spin relaxation mechanisms which have been so far neglected.

We have independently measured the spin relaxation time of the electrons in the Γ valley by recording the time- and polarization-resolved photoluminescence spectrum following a direct photogeneration of Γ electrons. Figure 4.12 presents the time evolution of the luminescence copolarized I^+ and counterpolarized I^- with the σ^+ excitation laser; the excitation energy is $E_{exc} = 1.590$ eV, yielding a photogeneration of spin-polarized electrons in the Γ_6 conduction band only. The measured initial circular polarization of luminescence is $\sim$ 25%, in very good agreement with the optical selection rules in bulk GaAs [22]. From these kinetics we measure τ_S^Γ ∼200 ps and τ^Γ ∼105 ps. These values are consistent with previous measurements performed in p-doped GaAs epilayers with similar doping values, where it was demonstrated that

the spin relaxation of thermalized electrons in the Γ valley is mainly due to the Bir-Aronov-Pikus mechanism [22,161,169–172].

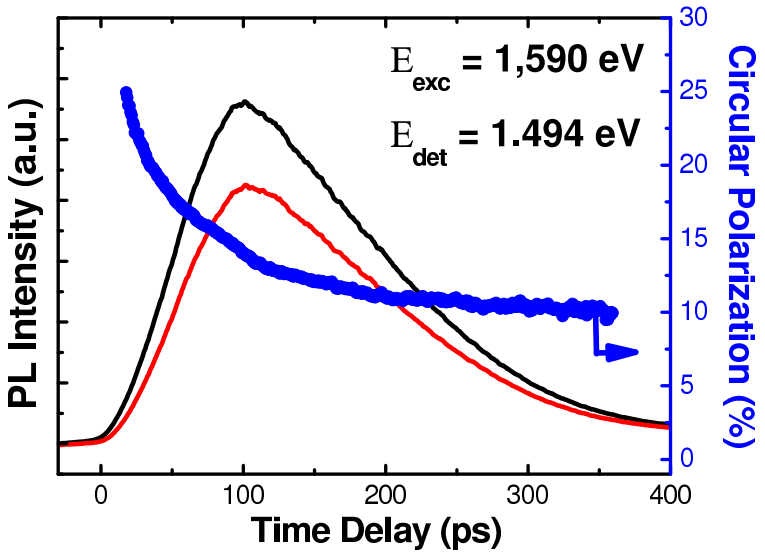

Figure 4.12: Time evolution of the PL circular components I^+ and I^-, and the corresponding circular polarization P_c for a near band-gap excitation.

4.3.2 Discussion

We have interpreted the experimental results of Figure 4.7 in the framework of the following simple two levels rate equation system :

$$\begin{cases} \dfrac{dn^L_{+(-)}}{dt} &= -\dfrac{n^L_{+(-)} - n^L_{-(+)}}{2\tau^L_S} - \dfrac{n^L_{+(-)}}{\tau^{L\Gamma}} - \dfrac{n^L_{+(-)}}{\tau^{L\Gamma}_S} \\ \dfrac{dn^\Gamma_{+(-)}}{dt} &= \dfrac{n^\Gamma_{+(-)} - n^\Gamma_{-(+)}}{2\tau^\Gamma_S} - \dfrac{n^\Gamma_{+(-)}}{\tau^\Gamma} + \dfrac{n^L_{+(-)}}{\tau^{L\Gamma}} + \dfrac{n^L_{-(+)}}{\tau^{L\Gamma}_S} \end{cases} \tag{4.9}$$

where $n^L_{+(-)}$ and $n^\Gamma_{+(-)}$ are the electrons' density with spin up and spin down in the L and Γ valleys respectively, τ^L_S and τ^Γ_S the electron spin relaxation times in the L and Γ valleys; $\tau^{L\Gamma}$ is the spin conserving $L \rightarrow \Gamma$ relaxation time and $\tau^{L\Gamma}_S$ is the spin flip $L \rightarrow \Gamma$ relaxation time, τ^Γ is the electron lifetime in Γ (Figure 4.13).

The resolution of equations (4.1) in steady state conditions leads to the calculated circular polarization of the photoluminescence detected on the fundamental gap

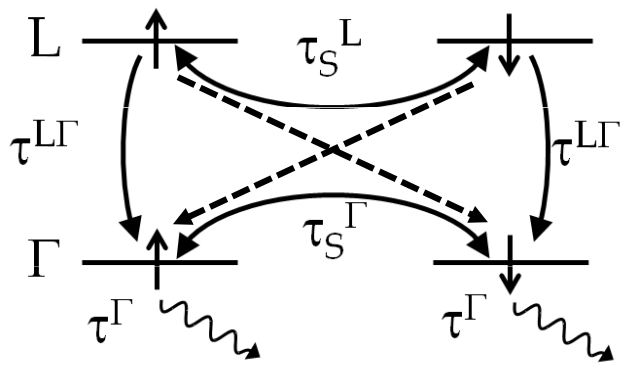

Figure 4.13: Schematic representation of the two-level model including the spin relaxation times in both L and Γ valleys

following a photogeneration of electrons in the L valley :

$$P_C^{\Gamma} \simeq \frac{P_0^L}{2} \frac{1}{\left(1+\frac{\tau^{\Gamma}}{\tau_S^{\Gamma}}\right)\left(\frac{\frac{1}{\tau^{L\Gamma}}-\frac{1}{\tau_s^{L\Gamma}}}{\frac{1}{\tau_s^L}+\frac{1}{\tau^{L\Gamma}}+\frac{1}{\tau_s^{L\Gamma}}}\right)} \tag{4.10}$$

As we measured some positive circular polarization with $\sigma+$ excitation, this means that $\tau_s^{L\Gamma} > \tau^{L\Gamma}$. In order to get a lower estimation of τ_s^L, we will neglect in the following the spin flip relaxation process. We get the expression:

$$P_C^{\Gamma,0} = \frac{P_0^L}{2} \frac{1}{\left(1+\frac{\tau^{\Gamma}}{\tau_S^{\Gamma}}\right)\left(1+\frac{\tau^{L\Gamma}}{\tau_S^{L}}\right)} \tag{4.11}$$

Then we have $P_C^{\Gamma} < P_C^{\Gamma,0}$. In the following calculations, we will use the value P_C^{Γ} that we have measured in the experiments, instead of $P_C^{\Gamma,0}$. So we use an underestimated circular polarization in our calculations.

For an excitation energy of E_{exc}=2.987 eV yielding the photogeneration of L_6 electrons, the inset graph of Figure 4.7 shows that the measured PL circular polarization is P_C^{Γ}=0.9% and the calculated photogenerated electron spin polarization P_0^L= 30% (inset of Figure 4.7) [166]. Assuming a $L \rightarrow \Gamma$ transfer time $\tau^{L\Gamma}$=2 ps as measured by ultrafast spectroscopy [173–175], we deduce from equation (4.2) that the electron spin relaxation time in the L valley is τ_S^L=200 fs. This measured value is in quite good agreement with recent calculations predicting a spin relaxation time of $\tau_S^L \sim$ 100 fs in GaAs at room temperature as a result of the strong spin-orbit splitting of conduction

electrons in the L valley [156]. As said before, in this very simple model we have neglected the possible electron spin relaxation which might occur during the $L \rightarrow \Gamma$ scattering and during the energy relaxation process in the Γ valley; our measured spin relaxation time thus includes the "intrinsic"spin relaxation time in the L valley, a possible Elliot-Yafet type spin relaxation may occur during the valley transfer and during the energy relaxation. As expected, the L valley spin lifetime in GaAs is much shorter than the L valley electron spin relaxation time in centro-symmetric materials with weaker spin-orbit interaction such as Silicon or Germanium [176].

4.4 Conclusion

In conclusion we have measured the electron spin relaxation time in satellite L valleys in GaAs. In addition to the well documented spin dynamics in the Γ valley, it is a key parameter to develop and optimize spin-optronic and spin transport devices where spin-polarized electrons are redistributed among several valleys. Our measured L electrons spin relaxation time ($\sim$200 fs) does indeed confirm the enhanced efficiency of the D'Yakonov-Perel spin relaxation induced by the spin splitting of L valleys. This relaxation time looks at first sight shorter than what is required ($\sim$3 ps) for the spontaneous spin amplification to appear under electric field where the charge Gunn effect appears [36]. Nevertheless we believe that the enhanced electron-electron scattering in highly n-doped GaAs could yield longer spin relaxation times compared to the ones we have measured here where the electron population in L valley is small, which could allow the experimental demonstration of the Spin Gunn effect.

Appendix A: L-valley electron spin generation in GaAs

We develop here our method to determine the initial spin photo-generated in GaAs L-valleys. This appendix is divided in three parts: we first derive the evolution of the density matrix under the perturbation induced by an electromagnetic field, the crystal being initially in its ground state, and using the secular approximation. We then derive the population and spin density generation in the conduction's bands due to optical transitions, and evaluate it close to some high symmetry point of the semiconductor. We finally apply this formalism for transitions near the L point of the Brillouin zone, close to the L-gap of GaAs.

General Formalism: evolution equation of the density matrix

Assuming the laser excitation is slowly varying, the density matrix evolution of the conduction/valence electrons is given, in interaction representation by [177]:

$$\left(\frac{d\hat{\rho}^I}{dt}\right) = \frac{1}{i\hbar}[\hat{H}^I_{e-ph}(t), \hat{\rho}^I(t)] \tag{12}$$

where:

$$\hat{\rho}^I_{e-ph}(t) \equiv e^{i\frac{\hat{H}_0}{\hbar}t}\hat{\rho}_{e-ph}(t)e^{-i\frac{\hat{H}_0}{\hbar}t}\hat{H}^I_{e-ph}(t) \equiv e^{i\frac{\hat{H}_0}{\hbar}t}\hat{H}_{e-ph}(t)e^{-i\frac{\hat{H}_0}{\hbar}t} \tag{13}$$

and:

$$\hat{H}_0(t) = \sum_{\nu,k} E_{\nu,k}|\Psi_{\nu,k}\rangle\langle\Psi_{\nu,k}| \tag{14}$$

is the unperturbed electron hamiltonian for electron Bloch states $|\Psi_{\nu,k}\rangle$ of band ν and wave vector $\mathbf{k}$ with eigen-energy $E_{\nu,k} = \hbar\omega_{\nu,k}$ (here the summation is restricted to the

first Brillouin zone). Note that, in virtue of Kramers theorem, the bands are twice degenerated in energy, so that $\nu \in (\nu_+, \nu_-)$. Moreover, due to the fact that each state is populated by at most one fermion, the population terms of the density matrix must satisfy the condition:

$$\langle \Psi_{\nu,k} | \hat{\rho}^I_{e-ph}(t) | \Psi_{\nu,k} \rangle \leq 1 \tag{15}$$

The explicit expression for $\hat{H}_{e-ph}(t)$ is, in the semi-classical approach and taking the Coulomb gauge which ensures that $\mathbf{A}(t) \cdot \hat{\mathbf{p}} = \hat{\mathbf{p}} \cdot \mathbf{A}(t)$:

$$\hat{H}_{e-ph}(t) = \frac{e}{m_0 c} \mathbf{A}(t) \cdot \hat{\mathbf{p}} + \left(\frac{eA(t)}{2m_0 c} \right)^2 \tag{16}$$

In the weak perturbation regime, we neglect as usual the last term on the right hand side, so that the interaction representation of $\hat{H}_{e-ph}(t)$ is now:

$$\hat{H}_{e-ph}(t) \approx \frac{e}{m_0 c} \mathbf{A}(t) \cdot \hat{\mathbf{p}} \tag{17}$$

Integrating equation (12), we obtain the implicit integral equation for $\hat{\rho}^I(t)$:

$$\hat{\rho}^I(t) = \hat{\rho}^I(0) + \frac{1}{i\hbar} \int_0^t [\hat{H}^I_{e-ph}(t'), \hat{\rho}^I(t')] dt' \tag{18}$$

Inserting this expression in (12) yields:

$$\left(\frac{d\hat{\rho}^I}{dt} \right) = \frac{1}{i\hbar} [\hat{H}^I_{e-ph}(t), \hat{\rho}(0)] + \frac{1}{(i\hbar)^2} \int_0^t dt_1 [\hat{H}^I_{e-ph}(t), [\hat{H}^I_{e-ph}(t_1), \hat{\rho}^I(t_1)]]$$

Repeating this operation indefinitely, we finally obtain the series expansion:

$$\begin{aligned} \left(\frac{d\hat{\rho}^I}{dt} \right) = & \frac{1}{i\hbar} [\hat{H}^I_{e-ph}(t), \hat{\rho}(0)] \\ & + \sum_{n=1}^{\infty} \frac{1}{(i\hbar)^n} \int_0^t dt_1 \int_0^{t_1} dt_2 \cdots \int_0^{t_{n-1}} dt_n [\hat{H}^I_{e-ph}(t_1), [\hat{H}^I_{e-ph}(t_2) \cdots, [\hat{H}^I_{e-ph}(t_n), \hat{\rho}^I(0)]]] \end{aligned}$$

which, in the weak perturbation regime, is assumed to be convergent. We further assume that truncating this series at second order approximately describes the evolution of $\hat{\rho}^I(t)$:

$$\left(\frac{d\hat{\rho}^I}{dt} \right) \approx \frac{1}{i\hbar} [\hat{H}^I_{e-ph}(t), \hat{\rho}(0)] - \frac{1}{\hbar^2} \int_0^t [\hat{H}^I_{e-ph}(t), [\hat{H}^I_{e-ph}(t_1), \hat{\rho}(0)]] dt_1 \tag{19}$$

Letting: $\tau = t - t_1$, we get the equivalent expression:

$$\left(\frac{d\hat{\rho}^I}{dt} \right) \approx \frac{1}{i\hbar} [\hat{H}^I_{e-ph}(t), \hat{\rho}(0)] - \frac{1}{\hbar^2} \int_0^t [\hat{H}^I_{e-ph}(t), [\hat{H}^I_{e-ph}(t-\tau), \hat{\rho}(0)]] d\tau \tag{20}$$

For a monochromatic plane wave, the incident electromagnetic field is characterized by a vector potential $\mathbf{A}(t)$ which takes the form:

$$\mathbf{A}_{\mathbf{q},\omega}(t) = \frac{1}{2}[\mathcal{A}_{\mathbf{q},\omega}e^{i(\mathbf{q}.\mathbf{r}-\omega t)} + \mathcal{A}^*_{\mathbf{q},\omega}e^{-i(\mathbf{q}.\mathbf{r}-\omega t)})] \tag{21}$$

where $\omega = \frac{c}{n}|\mathbf{q}| > 0$, $\mathbf{q}$ and $\mathcal{A}_{\mathbf{q},\omega}$ characterise respectively the positive pulsation, wave vector, and complex vector potential amplitude of the single optical mode considered at this stage.

For a stationary optical excitation, we can then always define:

$$\hat{H}_{e-ph}(t) \equiv \hat{H}_+(t) + \hat{H}_-(t) \tag{22}$$

where $\hat{H}_+(t) = \frac{e}{2m_0c}e^{-i(\mathbf{q}.\mathbf{r}-\omega t)}\mathcal{A}^*_{\mathbf{q},\omega} \cdot \hat{\mathbf{p}}$ and $\hat{H}_-(t) = [\hat{H}_+(t)]^\dagger$. In the interaction representation:

$$\hat{H}^I_{e-ph}(t) \approx e^{i\frac{\hat{H}_0}{\hbar}t}\frac{e}{m_0c}\mathbf{A}(t) \cdot \hat{\mathbf{p}}e^{-i\frac{\hat{H}_0}{\hbar}t}$$

and, with the previous definition (22):

$$\begin{aligned} \hat{H}^I_-(t) &= \frac{e}{2m_0c}e^{-i\omega t}e^{i\frac{\hat{H}_0}{\hbar}t}\left(e^{i\mathbf{q}.\mathbf{r}}\mathcal{A}_{\mathbf{q},\omega} \cdot \hat{\mathbf{p}}\right)e^{-i\frac{\hat{H}_0}{\hbar}t} \\ \hat{H}^I_+(t) &= \frac{e}{2m_0c}e^{i\omega t}e^{i\frac{\hat{H}_0}{\hbar}t}\left(e^{-i\mathbf{q}.\mathbf{r}}\mathcal{A}^*_{\mathbf{q},\omega} \cdot \hat{\mathbf{p}}\right)e^{-i\frac{\hat{H}_0}{\hbar}t} \end{aligned} \tag{23}$$

Note the operators $\hat{H}^I_+(t)$ and $\hat{H}^I_-(t)$ are mutually conjugates:

$$\hat{H}^I_\pm(t) = \left(\hat{H}^I_\mp(t)\right)^\dagger \tag{24}$$

The initial electron density matrix at $t = 0$ is given at temperature $T = 0$ by:

$$\hat{\rho}(0) = \frac{1}{tr(\hat{\rho}(0))}\sum_{\substack{k \\ v\in\{valence\\ bands\}}}|\Psi_{\nu,k}\rangle\langle\Psi_{\nu,k}| = \frac{1}{2n_{val}N}\sum_{\substack{k \\ \nu\in\{v_+,v_-\}}}|u_{\nu,k}\rangle\langle u_{\nu,k}| = \hat{\rho}^I(0) \tag{25}$$

Here, $N = V/\Omega$ is the number of crystal unit cells, V and Ω are the volumes of the crystal and its unit cell respectively, $2n_{val}$ is the total number of valence bands (the factor 2 stands for their degeneracy) and $v \in (v_+, v_-)$ where $v_\pm$ denote bands with a given (pseudo-) spin state. Note the expression (25) is still approximately valid when $k_BT \ll E_g$. Due to Bloch theorem, we can write the electron states as: $\Psi_{\nu,k}(\mathbf{r}) = \frac{1}{\sqrt{V}}e^{i\mathbf{k}.\mathbf{r}}u_{\nu,k}(\mathbf{r})$, where $u_{\nu,k}(\mathbf{r}) = \langle\mathbf{r}|u_{\nu,k}\rangle$ is the periodic part of the Bloch function, satisfying the orthogonality criterion in the elementary Wigner unit cell:

$\langle u_{\nu,k}|u_{\nu',k}\rangle = \delta_{\nu,\nu'}$, so that $\langle \Psi_{\nu,k}|\Psi_{\nu',k'}\rangle = \delta_{\nu,\nu'}, \delta_{k,k'}$. We can then evaluate $\hat{H}_{\pm}(t)$ for interband transitions. For instance:

$$\hat{H}_{-}(t) = \frac{e}{2m_0 c} e^{-i\omega t} \sum_{\nu,\nu',k,k'} \langle \Psi_{\nu',k'}|e^{i\mathbf{q}.\mathbf{r}} \mathcal{A}_{\mathbf{q},\omega} \cdot \hat{\mathbf{p}}|\Psi_{\nu,k}\rangle |\Psi_{\nu',k'}\rangle\langle\Psi_{\nu,k}|$$

that is:

$$\hat{H_{-}}(t) = \frac{e}{2m_0 c} e^{-i\omega t} \sum_{\nu,\nu',k} \langle u_{\nu',k+q}|\mathcal{A}_{\mathbf{q},\omega} \cdot \hat{\mathbf{p}}|u_{\nu,k}\rangle |\Psi_{\nu',k+q}\rangle\langle\Psi_{\nu,k}| \tag{26}$$

which manifests the wave vector conservation in the matrix coupling elements. In interaction representation, we obtain, according to (13):

$$\hat{H}_{-}(t) = \frac{e}{2m_0 c} \sum_{\nu,\nu',k} e^{-i(\omega-\omega_{\nu',k+q}+\omega_{\nu,k})t} \langle u_{\nu',k+q}|\mathcal{A}_{\mathbf{q},\omega} \cdot \hat{\mathbf{p}}|u_{\nu,k}\rangle |\Psi_{\nu',k+q}\rangle\langle\Psi_{\nu,k}| \tag{27}$$

and similarly:

$$\hat{H}_{+}(t) = \frac{e}{2m_0 c} \sum_{\nu,\nu',k} e^{+i(\omega-\omega_{\nu',k-q}+\omega_{\nu,k})t} \langle u_{\nu',k-q}|\mathcal{A}^{*}_{\mathbf{q},\omega} \cdot \hat{\mathbf{p}}|u_{\nu,k}\rangle |\Psi_{\nu',k-q}\rangle\langle\Psi_{\nu,k}|$$

Substituting **k** with **-k** and ν with ν', we obtain:

$$\hat{H}_{+}(t) = \frac{e}{2m_0 c} \sum_{\nu,\nu',k} e^{+i(\omega-\omega_{\nu',k+q}+\omega_{\nu,k})t} \langle u_{\nu,k}|\mathcal{A}^{*}_{\mathbf{q},\omega} \cdot \hat{\mathbf{p}}|u_{\nu',k+q}\rangle |\Psi_{\nu,k}\rangle\langle\Psi_{\nu',k+q}| \tag{28}$$

expression which confirms, comparing expressions (27,28), that (24) is indeed satisfied. We will neglect in the following the excitonic effects, for the sake of simplicity.

We shall make at this point the secular approximation, dropping all the terms oscillating at the frequency $\pm\omega$ or $\pm 2\omega$ in the expression (20), in order to retain only the slow evolution part of the density matrix. It follows that the first order term, which characterize the linear polarisation oscillating at frequencies $\pm\omega$, and the second order terms containing two contributions $\hat{H}^{I}_{\pm}(t)$ of the same sign (see (21)) oscillating at frequency $\pm 2\omega$ are neglected.

The relation (30) yields then explicitly for the remaining second order contribution:

$$\left(\frac{d\hat{\rho}^I}{dt}\right) \approx \frac{1}{2n_{val}N} \int_0^t d\tau \times$$
$$[-H^I_{+}(t)H^I_{-}(t-\tau)\hat{\rho}(0) + H^I_{+}(t)\hat{\rho}(0)H^I_{-}(t-\tau) + H^I_{-}(t-\tau)\hat{\rho}(0)H^I_{+}(t) - \hat{\rho}(0)H^I_{-}(t-\tau)H^I_{+}(t)$$
$$- H^I_{-}(t)H^I_{+}(t-\tau)\hat{\rho}(0) + H^I_{-}(t)\hat{\rho}(0)H^I_{+}(t-\tau) + H^I_{+}(t-\tau)\hat{\rho}(0)H^I_{-}(t) - \hat{\rho}(0)H^I_{+}(t-\tau)H^I_{-}(t)] \tag{29}$$

As we shall see in the following, the dependence on time t of the integrand in (29) will cancel. We evaluate now successively the four remaining contributions and their hermitic conjugates, and start with the "positive" terms in (29) using (25,27,28).

$$\frac{1}{\hbar^2}\int_0^t H_-^I(t-\tau)\hat{\rho}(0)H_+^I(t)d\tau = \frac{1}{2n_{val}N}\left(\frac{e}{2\hbar m_0 c}\right)^2\int_0^t d\tau$$
$$\sum_{\nu,\nu',k} e^{i(\omega-\omega_{\nu',k+q}+\omega_{\nu,k})(t-\tau)}\langle u_{\nu',k+q}|\mathcal{A}_{\mathbf{q},\omega}\cdot\hat{\mathbf{p}}|u_{\nu,k}\rangle|\Psi_{\nu',k+q}\rangle\langle\Psi_{\nu,k}|\left(\sum_{\nu,k''}|\Psi_{\nu,k''}\rangle\langle\Psi_{\nu,k"}|\right)$$
$$\sum_{\nu_1,\nu_1',k_1} e^{i(\omega-\omega_{\nu_1',k_1+q}+\omega_{\nu_1,k_1})t}\langle u_{\nu_1,k_1}|\mathcal{A}^*_{\mathbf{q},\omega}\cdot\hat{\mathbf{p}}|u_{\nu_1',k_1+q}\rangle|\Psi_{\nu_1,k_1}\rangle\langle\Psi_{\nu_1',k_1+q}|$$
$$= \frac{1}{2n_{val}N}\left(\frac{e}{2\hbar m_0 c}\right)^2$$
$$\sum_{\substack{v,\nu,\nu'\\k}} e^{i(\omega_{\nu,k+q}-\omega_{\nu',k+q})t}\int_0^t e^{i(\omega-\omega_{\nu',k+q}+\omega_{v,k})\tau}d\tau\langle u_{\nu,k}|\mathcal{A}^*_{\mathbf{q},\omega}\cdot\hat{\mathbf{p}}|u_{v,k+q}\rangle\langle u_{v,k+q}|\mathcal{A}_{\mathbf{q},\omega}\cdot\hat{\mathbf{p}}|u_{v',k}\rangle|\Psi_{\nu,k}\rangle\langle\Psi_{\nu',k}|$$

Here, the summation on k runs over all the allowed states of the first Brillouin zone. Similarly, we obtain:

$$\frac{1}{\hbar^2}\int_0^t H_-^I(t)\hat{\rho}(0)H_+^I(t-\tau)d\tau = \frac{1}{2n_{val}N}\left(\frac{e}{2\hbar m_0 c}\right)^2\int_0^t d\tau$$
$$\sum_{\nu,\nu',k} e^{-i(\omega-\omega_{\nu',k+q}+\omega_{\nu,k})t}\langle u_{\nu',k+q}|\mathcal{A}_{\mathbf{q},\omega}\cdot\hat{\mathbf{p}}|u_{\nu,k}\rangle|\Psi_{\nu',k+q}\rangle\langle\Psi_{\nu,k}|\left(\sum_{\nu,k"}|\Psi_{v,k"}\rangle\langle\Psi_{v,k"}|\right)$$
$$\sum_{\nu_1,\nu_1',k_1} e^{i(\omega-\omega_{\nu_1',k_1+q}+\omega_{\nu_1,k_1})(t-\tau)}\langle u_{\nu_1,k_1}|\mathcal{A}^*_{\mathbf{q},\omega}\cdot\hat{\mathbf{p}}|u_{\nu_1',k_1+q}\rangle|\Psi_{\nu_1,k_1}\rangle\langle\Psi_{\nu_1',k_1+q}|$$
$$= \frac{1}{2n_{val}N}\left(\frac{e}{2\hbar m_0 c}\right)^2\sum_{\substack{v,\nu,\nu'\\k}} e^{i(\omega_{\nu,k+q}-\omega_{\nu',k+q})t}$$
$$\int_0^t e^{-i(\omega-\omega_{\nu',k+q}+\omega_{v,k})\tau}d\tau\langle u_{\nu,k}|\mathcal{A}^*_{\mathbf{q},\omega}\cdot\hat{\mathbf{p}}|u_{v,k+q}\rangle\langle u_{v,k+q}|\mathcal{A}_{\mathbf{q},\omega}\cdot\hat{\mathbf{p}}|u_{v',k}\rangle|\Psi_{\nu,k}\rangle\langle\Psi_{\nu',k}|$$
$$= \frac{1}{2n_{val}N}\left(\frac{e}{2\hbar m_0 c}\right)^2\sum_{\substack{v,\nu,\nu'\\k}} e^{i(\omega_{\nu,k+q}-\omega_{\nu',k+q})t}$$
$$\int_0^{-t} e^{i(\omega-\omega_{\nu',k+q}+\omega_{v,k})\tau}d\tau\langle u_{\nu,k}|\mathcal{A}^*_{\mathbf{q},\omega}\cdot\hat{\mathbf{p}}|u_{v,k+q}\rangle\langle u_{v,k+q}|\mathcal{A}_{\mathbf{q},\omega}\cdot\hat{\mathbf{p}}|u_{\nu',k}\rangle|\Psi_{\nu,k}\rangle\langle\Psi_{\nu',k}|$$

where we have replaced τ by $-\tau$ in the integral. Adding the two contributions together,

we obtain:

$$\frac{1}{\hbar^2}\int_0^t [H_-^I(t-\tau)\hat{\rho}(0)H_+^I(t)+H_-^I(t)\hat{\rho}(0)H_+^I(t-\tau)]d\tau =$$
$$= \frac{1}{2n_{val}N}\left(\frac{e}{2\hbar m_0 c}\right)^2 \sum_{\substack{v,\nu,\nu' \\ k}} e^{i(\omega_{\nu,k+q}-\omega_{\nu',k+q})t}$$
$$\int_{-t}^t e^{i(\omega-\omega_{\nu',k+q}+\omega_{v,k})\tau}d\tau\langle u_{\nu,k}|\mathcal{A}^*_{\mathbf{q},\omega}\cdot\hat{\mathbf{p}}|u_{v,k+q}\rangle\langle u_{v,k+q}|\mathcal{A}_{\mathbf{q},\omega}\cdot\hat{\mathbf{p}}|u_{v',k}\rangle|\Psi_{\nu,k}\rangle\langle\Psi_{\nu',k}|$$
$$= \frac{2}{2n_{val}N}\left(\frac{e}{2\hbar m_0 c}\right)^2 \sum_{\substack{v,\nu,\nu' \\ k}} e^{i(\omega_{\nu,k}-\omega_{\nu',k})t}$$
$$\frac{sin(\omega-\omega_{\nu',k+q}+\omega_{v,k})t}{\omega-\omega_{v,k+q}+\omega_{\nu',k}}\langle u_{\nu,k}|\mathcal{A}^*_{\mathbf{q},\omega}\cdot\hat{\mathbf{p}}|u_{v,k+q}\rangle\langle u_{v,k+q}|\mathcal{A}_{\mathbf{q},\omega}\cdot\hat{\mathbf{p}}|u_{\nu',k}\rangle|\Psi_{\nu,k}\rangle\langle\Psi_{\nu',k}|$$

The main contributions in the summations will be obtained for $(\omega-\omega_{\nu',k+q}+\omega_{v,k})t<\pi$. For an observation time of the order a few hundred of femtoseconds, defining $\Delta\omega = \omega-\omega_{\nu',k+q}+\omega_{v,k}$, this yields $\hbar\Delta\omega \leq$10 meV. Clearly, tuning the excitation laser in the region of valence to conduction bands leads to selecting only the conduction states $|\Psi_{\nu',k}\rangle$ with $\nu'\in\{c_+,c_-\}$ in the above summation. Using now the identity:

$$lim_{t\to\infty}\int_{-t}^t e^{i(\omega-\omega_0)\tau}d\tau = 2\pi\delta(\omega-\omega_0)$$

we get, for $t\geq 100$ fs typically, the approximation :

$$\frac{1}{\hbar^2}\int_0^t [H_-^I(t-\tau)\hat{\rho}(0)H_+^I(t)+H_-^I(t)\hat{\rho}(0)H_+^I(t-\tau)]d\tau$$
$$\approx \frac{2}{2n_{val}N}\left(\frac{e}{2\hbar m_0 c}\right)^2 \sum_{\substack{v,\nu,\nu' \\ k}} e^{i(\omega_{\nu,k+q}-\omega_{\nu',k+q})t}$$
$$\delta(\omega-\omega_{\nu',k+q}+\omega_{v,k})\langle u_{\nu,k+q}|\mathcal{A}_{\mathbf{q},\omega}\cdot\hat{\mathbf{p}}|u_{v,k}\rangle\langle u_{v,k}|\mathcal{A}^*_{\mathbf{q},\omega}\cdot\hat{\mathbf{p}}|u_{\nu',k+q}\rangle|\Psi_{\nu,k+q}\rangle\langle\Psi_{\nu',k+q}|$$

Finally, since we retain only the slowly varying in time terms, we are led to select only the conduction states $|\Psi_{\nu,k}\rangle$ with $\nu\in\{c_+,c_-\}$ (this means that the inter-band coherences time evolution are fast oscillating terms which quickly average to zero, and that we retain only intra-band spin coherences). In that case, the energy difference $\hbar(\omega_{\nu,k}-\omega_{\nu',k})$ is either strictly zero or equal to , which is of the order of a few tens of μeV. Since the excitation pulse is of the order of a few picoseconds, we see that we can safely make the approximation: $e^{i(\omega_{\nu,k}-\omega_{\nu',k})t}\approx 1$ valid for $t\leq|\omega_{c_+,k}-\omega_{c_-,k}|\sim 70$ ps.

We obtain finally:

$$\begin{aligned}
&\frac{1}{\hbar^2}\int_0^t [H_-^I(t-\tau)\hat{\rho}(0)H_+^I(t) + H_-^I(t)\hat{\rho}(0)H_+^I(t-\tau)]d\tau \\
&\approx \frac{2\pi}{2n_{val}N}\left(\frac{e}{2\hbar m_0 c}\right)^2 \\
&\sum_{\substack{v;\nu,\nu'\in\{c_+,c_-\}\\ \mathbf{k}}} \delta(\omega-\omega_{\nu',k+q}+\omega_{v,k})\langle u_{\nu,k+q}|\mathcal{A}_{\mathbf{q},\omega}\cdot\hat{\mathbf{p}}|u_{v,k}\rangle\langle u_{v,k}|\mathcal{A}^*_{\mathbf{q},\omega}\cdot\hat{\mathbf{p}}|u_{\nu',k+q}\rangle|\Psi_{\nu,k+q}\rangle\langle\Psi_{\nu',k+q}|
\end{aligned} \tag{30}$$

expression in which the Dirac distribution express the energy conservation in the process.

We turn now to the evaluation of the two similar remaining terms in expression (28). Using a similar protocol, we obtain:

$$\begin{aligned}
&\frac{1}{\hbar^2}\int_0^t [H_+^I(t)\hat{\rho}(0)H_-^I(t-\tau) + H_+^I(t-\tau)\hat{\rho}(0)H_-^I(t)]d\tau \\
&= \frac{2}{2n_{val}N}\left(\frac{e}{2\hbar m_0 c}\right)^2 \sum_{\substack{v,\nu,\nu'\\ k}} e^{i(\omega_{\nu,k+q}-\omega_{\nu',k+q})t} \\
&\frac{sin(\omega-\omega_{v,k+q}+\omega_{\nu',k})t}{\omega-\omega_{v,k+q}+\omega_{\nu',k}}\langle u_{\nu,k}|\mathcal{A}^*_{\mathbf{q},\omega}\cdot\hat{\mathbf{p}}|u_{v,k+q}\rangle\langle u_{v,k+q}|\mathcal{A}_{\mathbf{q},\omega}\cdot\hat{\mathbf{p}}|u_{v',k}\rangle|\Psi_{\nu,k}\rangle\langle\Psi_{\nu',k}| \\
&\approx \frac{2\pi}{2n_{val}N}\left(\frac{e}{2\hbar m_0 c}\right)^2 \\
&\sum_{\substack{v;\nu,\nu'\in\{c_+,c_-\}\\ \mathbf{k}}} \delta(\omega-\omega_{v,k+q}+\omega_{\nu',k})\langle u_{\nu,k}|\mathcal{A}^*_{\mathbf{q},\omega}\cdot\hat{\mathbf{p}}|u_{v,k+q}\rangle\langle u_{v,k+q}|\mathcal{A}_{\mathbf{q},\omega}\cdot\hat{\mathbf{p}}|u_{\nu',k}\rangle|\Psi_{\nu,k}\rangle\langle\Psi_{\nu',k}|
\end{aligned}$$

where the same approximations have been done as above. However, since the frequency ω has been defined as positive, the transitions towards conduction states are strongly non resonant, so their contributions are vanishingly small. The remaining possible transitions should occur towards valence bands lower in energy than $\hbar\omega_{v,k+q}$. Since the valence bands are initially fully populated, this is not possible due to Pauli Exclusion Principle (c.f. condition (15)). However, when time increases during excitation pulse, valence band depletion occurs, but it turns that in GaAs the resonance condition between valence bands is not generally fulfilled for photons in the visible range. We can thus simply drop these contributions.

We turn now to the evaluation of the four remaining terms in (29). As we shall

see, they describe the depletion of the valence bands. These contributions are obtained using the same procedure, so that under the same assumptions, we obtain for two of them, as previously:

$$
\begin{aligned}
&-\frac{1}{\hbar^2}\int_0^t [H_+^I(t)H_-^I(t-\tau)\hat{\rho}(0)+\hat{\rho}(0)H_+^I(t-\tau)H_+^I(t)]d\tau \\
&\approx -\frac{2}{2n_{val}N}\left(\frac{e}{2\hbar m_0 c}\right)^2 \\
&\sum_{\substack{v,\nu\in\{v_+,v_-\};\nu'\in\{c_+,c_-\}\\ \mathbf{k}}} \delta(\omega-\omega_{\nu',k+q}+\omega_{v,k})\langle u_{\nu,k+q}|\mathcal{A}^*_{\mathbf{q},\omega}\cdot\hat{\mathbf{p}}|u_{\nu',k+q}\rangle\langle u_{\nu',k+q}|\mathcal{A}_{\mathbf{q},\omega}\cdot\hat{\mathbf{p}}|u_{v,k}\rangle|\Psi_{\nu,k}\rangle\langle\Psi_{v,k}|
\end{aligned}
\tag{31}
$$

where the state ν has to be taken in the valence bands v_+ or v_- close to v, and ν' is a conduction state c_+ or c_-. The last two contributions are:

$$
\begin{aligned}
&-\frac{1}{\hbar^2}\int_0^t [H_-^I(t)H_+^I(t-\tau)\hat{\rho}(0)+\hat{\rho}(0)H_-^I(t-\tau)H_+^I(t)]d\tau \\
&\approx -\frac{2\pi}{2n_{val}N}\left(\frac{e}{2\hbar m_0 c}\right)^2 \\
&\sum_{\substack{v,\nu;\nu'\in\{v_+,v_-\}\\ \mathbf{k}}} \delta(\omega-\omega_{v,k+q}+\omega_{\nu,k})\langle u_{v,k+q}|\mathcal{A}_{\mathbf{q},\omega}\cdot\hat{\mathbf{p}}|u_{\nu',k}\rangle\langle u_{\nu,k}|\mathcal{A}^*_{\mathbf{q},\omega}\cdot\hat{\mathbf{p}}|u_{\nu',k+q}\rangle|\Psi_{v,k+q}\rangle\langle\Psi_{\nu',k+q}|
\end{aligned}
$$

The main contributions in the summations will be obtained for $\omega_{v,k+q}-\omega_{\nu,k}\approx\omega$, which implies that for the generated states, we have $\omega_{\nu,k}<\omega_{v,k+q}$, so that again we have to discard these contributions as previously. Finally, gathering (30) and (31) we end with the expression:

$$
\begin{aligned}
&\left(\frac{d\hat{\rho}^I}{dt}\right)=\frac{2\pi}{2n_{val}N}\left(\frac{e}{2\hbar m_0 c}\right)^2 \\
&\times\{\sum_{\substack{v;\nu,\nu'\in\{c_+,c_-\}\\ \mathbf{k}}} \delta(\omega-\omega_{\nu',k+q}+\omega_{v,k})\langle u_{\nu,k+q}|\mathcal{A}_{\mathbf{q},\omega}\cdot\hat{\mathbf{p}}|u_{v,k}\rangle\langle u_{v,k}|\mathcal{A}^*_{\mathbf{q},\omega}\cdot\hat{\mathbf{p}}|u_{\nu',k+q}\rangle|\Psi_{\nu,k+q}\rangle\langle\Psi_{\nu',k+q}| \\
&-\sum_{\substack{v,\nu\in\{v_+,v_-\},\nu'\in\{c_+,c_-\}\\ \mathbf{k}}} \delta(\omega-\omega_{\nu',k+q}+\omega_{v,k})\langle u_{\nu,k}|\mathcal{A}^*_{\mathbf{q},\omega}\cdot\hat{\mathbf{p}}|u_{\nu',k+q}\rangle\langle u_{\nu',k+q}|\mathcal{A}_{\mathbf{q},\omega}\cdot\hat{\mathbf{p}}|u_{v,k}\rangle|\Psi_{\nu,k}\rangle\langle\Psi_{v,k}|\}
\end{aligned}
\tag{32}
$$

The positive term express the creation of conduction states under the action of the electromagnetic wave, while the negative term expresses the depletion of the valence

states. The energy conservation ensured by the Dirac factors implies that the optical transition can be simultaneously resonant only with the states of a Kramers doublet of a given conduction band ν, so that spin coherences can be generated in the conduction band.

Populations and spin density photo-generation in the conduction bands

The population generation rate in a given conduction band $c_j (j = +, -)$ is given by:

$$\frac{dN_{cj}}{dt} \equiv tr_{cj}\left(\frac{d\hat{p}^I}{dt}\right) = \sum_{v,k} \langle \Psi_{v,k}| \left(\frac{d\hat{p}^I}{dt}\right) |\Psi_{v,k}\rangle \tag{33}$$

From (31) we get straightforwardly:

$$\begin{aligned} \frac{dN_{cj}}{dt} &= \frac{2\pi}{2n_{val}N}\left(\frac{e}{2\hbar m_0 c}\right)^2 \times \\ &\sum_{\substack{v\in\{v_+,v_-\} \\ \mathbf{k}}} \delta(\omega - \omega_{c_j,k+q} + \omega_{v,k}) |\langle u_{c_j,k+q}|\mathcal{A}_{\mathbf{q},\omega}\cdot\hat{\mathbf{p}}|u_{v,k}\rangle|^2 \end{aligned} \tag{34}$$

Similarly, we get for a given valence band v_j:

$$\frac{dN_{vj}}{dt} \equiv tr_{vj}\left(\frac{d\hat{p}^I}{dt}\right) = \sum_{c,k} \langle \Psi_{c,k}| \left(\frac{d\hat{p}^I}{dt}\right) |\Psi_{c,k}\rangle \tag{35}$$

$$\begin{aligned} \frac{dN_{vj}}{dt} &= -\frac{2\pi}{2n_{val}N}\left(\frac{e}{2\hbar m_0 c}\right)^2 \\ &\times \sum_{\substack{c\in\{c_+,c_-\} \\ \mathbf{k}}} \delta(\omega - \omega_{c_j,k+q} + \omega_{v,k}) |\langle u_{c_j,k+q}|\mathcal{A}_{\mathbf{q},\omega}\cdot\hat{\mathbf{p}}|u_{v,k}\rangle|^2 \end{aligned} \tag{36}$$

Note that taking into account all the conduction and valence bands, the total population variation is exactly zero, since these terms compensate the increase of the conduction band population. Thus the expected relation: $\frac{dN}{dt} = tr\left(\frac{d\hat{p}^I}{dt}\right) = \sum_{\nu,k}\langle \Psi_{\nu,k}| \left(\frac{d\hat{\rho}^I}{dt}\right) |\Psi_{\nu,k}\rangle = 0$ is satisfied, which corresponds to the electron number conservation during the perturbation process by the electromagnetic wave (no photo-emission is possible in the visible range used here for the excitation laser).

For a pair of Kramers conjugate conduction band, we obtain thus:

$$\begin{aligned}\frac{dN_c}{dt} &= \frac{\hbar}{2}\frac{2\pi}{2n_{val}N}\left(\frac{e}{2\hbar m_0 c}\right)^2 \times \\ &\{\sum_{\substack{v\in\{v_+,v_-\}\\ \mathbf{k}}} \delta(\omega-\omega_{c_+,k+q}+\omega_{v,k})|\langle u_{c_+,k+q}|\mathcal{A}_{\mathbf{q},\omega}\cdot\hat{\mathbf{p}}|u_{v,k}\rangle|^2 \\ &+ \sum_{\substack{v\in\{v_+,v_-\}\\ \mathbf{k}}} \delta(\omega-\omega_{c_-,k+q}+\omega_{v,k})|\langle u_{c_-,k+q}|\mathcal{A}_{\mathbf{q},\omega}\cdot\hat{\mathbf{p}}|u_{v,k}\rangle|^2\}\end{aligned} \tag{37}$$

We turn now to the spin density generation in the conduction bands. For a given conduction band c_j, it is given generally by:

$$\frac{dS_c}{dt} \equiv tr_c\left(\frac{d\hat{p}^I}{dt}\hat{\mathbf{S}}\right) = \sum_{v,k}\langle\Psi_{v,k}|\left(\frac{d\hat{\rho}^I}{dt}\right)|\Psi_{v,k}\rangle \tag{38}$$

where the $\hat{\mathbf{S}} = \frac{\hbar}{2}\hat{\sigma}$ is the total spin operator acting in any (pseudo-)spin subspace $\left\{|\Psi_{\nu_+,k}\rangle, |\Psi_{\nu_-,k}\rangle\right\}$ and $\hat{\sigma} = (\sigma_x, \sigma_y, \sigma_z)$ are the set of Pauli matrixes. Note the vector-operator $\hat{\mathbf{S}}$ is time independent. Since we measure in this work the electron average spin polarisation along the quantization axis Oz, we will only calculate here the generation of the $S_z \equiv \langle\hat{S}_z\rangle$ component. We first write the operator in our electronic states basis:

$$\hat{S}_z = \frac{\hbar}{2}\sum_{\nu,k}(|\Psi_{v_+,k}\rangle\langle\Psi_{v_+,k}| - |\Psi_{v_-,k}\rangle\langle\Psi_{v_-,k}|) \tag{39}$$

where the summation is performed on Kramers conjugated band pairs. From expression (32), we get now:

$$\begin{aligned}\frac{dS_c}{dt} &= \frac{\hbar}{2}\frac{2\pi}{2n_{val}N}\left(\frac{e}{2\hbar m_0 c}\right)^2 \times \\ &\{\sum_{\substack{v\in\{v_+,v_-\}\\ \mathbf{k}}} \delta(\omega-\omega_{c_+,k+q}+\omega_{v,k})|\langle u_{c_+,k+q}|\mathcal{A}_{\mathbf{q},\omega}\cdot\hat{p}|u_{v,k}\rangle|^2 \\ &- \sum_{\substack{v\in\{v_+,v_-\}\\ \mathbf{k}}} \delta(\omega-\omega_{c_-,k+q}+\omega_{v,k})|\langle u_{c_-,k+q}|\mathcal{A}_{\mathbf{q},\omega}\cdot\hat{p}|u_{v,k}\rangle|^2\}\end{aligned} \tag{40}$$

We will make from now on the usual approximations. First, since the light wave vector q is much smaller than the size of the first Brillouin zone, we can safely make the approximation $|u_{c_j,k+q}\rangle \approx |u_{c_j,k}\rangle$ and $\omega_{c_j,k+q} \approx \omega_{c_j,k}$. Second, since the energy selection rule is only approximate due the finite state lifetimes, and the k-dependent spin splitting in any given band is quite small with respect to this state broadening, we

can make the further approximation: $\omega_{v_+,k} \approx \omega_{v_-,k}$. We get the simplified expressions:

$$\frac{dN_c}{dt} = \frac{\hbar}{2}\frac{2\pi}{2n_{val}N}\left(\frac{e}{2\hbar m_0 c}\right)^2 \times \left(\sum_{\substack{v\in\{v_+,v_-\}\\ \mathbf{k}}} |\langle u_{c_+,k}|\mathcal{A}_{\mathbf{q},\omega}\cdot\hat{\mathbf{p}}|u_{v,k}\rangle|^2 + |\langle u_{c_-,k}|\mathcal{A}_{\mathbf{q},\omega}\cdot\hat{\mathbf{p}}|u_{v,k}\rangle|^2\right)\delta(\omega-\omega_{c,k}+\omega_{v,k})$$

$$\frac{dS_{c,z}}{dt} = \frac{\hbar}{2}\frac{2\pi}{2n_{val}N}\left(\frac{e}{2\hbar m_0 c}\right)^2 \times \left(\sum_{\substack{v\in\{v_+,v_-\}\\ \mathbf{k}}} |\langle u_{c_+,k}|\mathcal{A}_{\mathbf{q},\omega}\cdot\hat{\mathbf{p}}|u_{v,k}\rangle|^2 - |\langle u_{c_-,k}|\mathcal{A}_{\mathbf{q},\omega}\cdot\hat{\mathbf{p}}|u_{v,k}\rangle|^2\right)\delta(\omega-\omega_{c,k}+\omega_{v,k})$$

where $E_{c,k} = \hbar\omega_{c,k}$ represents the approximate energy of the $|\Psi_{c\pm,k}\rangle$ without spin-dependent spin-orbit interaction.

Finally, when the excitation energy is close to a high symmetry point gap, we can make the further approximation: $u_{\nu,k}(\mathbf{r}) \approx u_{\nu,k_0}(\mathbf{r})$, with $\mathbf{k}_0 \in \{\mathbf{k}_\Gamma, \mathbf{k}_L, \mathbf{k}_X\}$. We end in this case with:

$$\frac{dN_c}{dt} \approx \frac{2\pi}{2n_{val}N}\left(\frac{e}{2\hbar m_0 c}\right)^2 \left(|\langle u_{c_+,k_0}|\mathcal{A}_{\mathbf{q},\omega}\cdot\hat{\mathbf{p}}|u_{v,k_0}\rangle|^2 + |\langle u_{c_-,k_0}|\mathcal{A}_{\mathbf{q},\omega}\cdot\hat{\mathbf{p}}|u_{v,k_0}\rangle|^2\right)\sum_{\substack{v\in\{v_+,v_-\}\\ \mathbf{k}}}\delta(\omega-\omega_{c,k}+\omega_{v,k}) \tag{41}$$

$$\frac{dS_{c,z}}{dt} \approx \frac{\hbar}{2}\frac{2\pi}{2n_{val}N}\left(\frac{e}{2\hbar m_0 c}\right)^2 \left(|\langle u_{c_+,k_0}|\mathcal{A}_{\mathbf{q},\omega}\cdot\hat{\mathbf{p}}|u_{v,k_0}\rangle|^2 - |\langle u_{c_-,k_0}|\mathcal{A}_{\mathbf{q},\omega}\cdot\hat{\mathbf{p}}|u_{v,k_0}\rangle|^2\right)\sum_{\substack{v\in\{v_+,v_-\}\\ \mathbf{k}}}\delta(\omega-\omega_{c,k}+\omega_{v,k}) \tag{42}$$

From these expressions the average generated electron spin z-component during the laser pulse of duration Δt is simply, if only two bands are coupled by optical transitions, and neglecting all spin relaxation processes during the excitation pulse:

$$\langle\hat{S}_{c,z}\rangle(\Delta t) = \frac{S_{c,z}(\Delta t)}{N_c(\Delta t)} \approx \frac{dS_{c,z}/dt}{dN_c/dt} \approx \frac{\hbar}{2}\frac{|\langle u_{c_+,k_0}|\mathcal{A}_{\mathbf{q},\omega}\cdot\hat{\mathbf{p}}|u_{v,k_0}\rangle|^2 - |\langle u_{c_-,k_0}|\mathcal{A}_{\mathbf{q},\omega}\cdot\hat{\mathbf{p}}|u_{v,k_0}\rangle|^2}{|\langle u_{c_+,k_0}|\mathcal{A}_{\mathbf{q},\omega}\cdot\hat{\mathbf{p}}|u_{v,k_0}\rangle|^2 + |\langle u_{c_-,k_0}|\mathcal{A}_{\mathbf{q},\omega}\cdot\hat{\mathbf{p}}|u_{v,k_0}\rangle|^2}$$

which can be evaluated from symmetry considerations on the states $|u_{\nu_\pm,k_0}\rangle$. The measured circular polarisation of the light emitted by the generated electron, defined as $P_{circ} = (I^{\sigma^+} - I^{\sigma^-})/(I^{\sigma^+} + I^{\sigma^-})$, would be initially, ignoring any relaxation process:

$P_{circ}(\Delta t) = -\frac{2}{\hbar}\langle \hat{S}_{c,z}\rangle(\Delta t)$. The calculation of $\langle \hat{S}_{c,x}\rangle(\Delta t)$ and $\langle \hat{S}_{c,y}\rangle(\Delta t)$ proceeds by the same method.

Finally, when departing from a high symmetry point, two aspects have to be taken into consideration:

- The optical selection rules are modified due the mixing of the Bloch states (when $\mathbf{k}_0 \neq \mathbf{k}_\Gamma, \mathbf{k}_L$, or $\mathbf{k}_X$ for instance).

- The bands dispersion has to be taken into account, so that the joint density of states has to be taken into account.

- If photon energy is sufficient, more than two bands may be coupled by optical transitions, so that the spin densities generated from each valence band add.

The first point can be worked out on the ground of a multiband **k.p** calculation [166]. We will not develop this aspect here, but only the two last points.

In order to generalize the formula (32) in a convenient way, we introduce now the joint energy density of state of a couple of interacting bands. Noticing that: $\frac{1}{\hbar}\sum_{v,k}\delta(\omega - \omega_{c,k} + \omega_{v,k}) = \delta(\hbar\omega - E_{c,k} + E_{v,k})$, the conduction band contribution to the density matrix time evolution is evaluated as:

$$\left(\frac{d\hat{\rho}^I}{dt}\right)_{cond} = \frac{2\pi}{2n_{val}N\hbar}\left(\frac{e}{2m_0c}\right)^2$$
$$\times\left\{\sum_{\substack{v;\nu,\nu'\in\{c_+,c_-\}\\ \mathbf{k}}} \delta(\hbar\omega - E_{\nu,k+q} + E_{v,k})\langle u_{\nu',k+q}|\mathcal{A}_{\mathbf{q},\omega}\cdot\hat{\mathbf{p}}|u_{v,k}\rangle\langle u_{v,k}|\mathcal{A}^*_{\mathbf{q},\omega}\cdot\hat{\mathbf{p}}|u_{\nu,k+q}\rangle|\Psi_{\nu',k+q}\rangle\langle\Psi_{\nu,k+q}|\right\}$$

$$\left(\frac{d\hat{\rho}^I}{dt}\right)_{cond} \approx \frac{2\pi}{2n_{val}N\hbar}\left(\frac{e}{2m_0c}\right)^2$$
$$\times\left\{\sum_{\substack{v;\nu,\nu'\in\{c_+,c_-\}\\ \mathbf{k}}} \delta(\hbar\omega - E_{\nu,k+q} + E_{v,k})\right\}$$
$$\langle u_{\nu',k_0}|\mathcal{A}_{\mathbf{q},\omega}\cdot\hat{\mathbf{p}}|u_{v,k_0}\rangle\langle u_{v,k_0}|\mathcal{A}^*_{\mathbf{q},\omega}\cdot\hat{\mathbf{p}}|u_{\nu,k_0}\rangle|\Psi_{\nu',k_0}\rangle\langle\Psi_{\nu,k_0}|$$

$$\left(\frac{d\hat{\rho}^I}{dt}\right)_{cond} \approx \frac{2\pi}{2n_{val}N\hbar}\left(\frac{e}{2m_0c}\right)^2 \times \left\{\sum_{\substack{v;\nu,\nu'\in\{c_+,c_-\}\\ \mathbf{k}}} \delta(\hbar\omega - E_{\nu,k} + E_{v,k})\right\} \langle u_{\nu',k_0}|\mathcal{A}_{\mathbf{q},\omega}\cdot\hat{\mathbf{p}}|u_{v,k_0}\rangle\langle u_{v,k_0}|\mathcal{A}^*_{\mathbf{q},\omega}\cdot\hat{\mathbf{p}}|u_{\nu,k_0}\rangle|\Psi_{\nu',k_0}\rangle\langle\Psi_{\nu,k_0}| \tag{43}$$

We evaluate the sum within brackets by introducing the density of state $\mathcal{D}_k = V/(2\pi)^3$ in the reciprocal space. Letting $E_{v,\nu}(\mathbf{k}) \equiv E_\nu(\mathbf{k}) - E_v(\mathbf{k})$, and since

$$\delta E_{v,\nu}(\mathbf{k}) = \bigtriangledown_k(E_{v,\nu}(\mathbf{k}))\cdot\delta\mathbf{k} = |\bigtriangledown_k(E_{v,\nu}(k_\parallel)|\delta k_\parallel$$

where $k_\parallel$ is the local coordinate along the normal to the iso-energy surface $S_{v,\nu}(E)$ in the reciprocal space such that $E_{v,\nu}(\mathbf{k}) = E$, and $d^3\mathbf{k} = dk_\parallel d^2k_\perp$, where $d^2k_\perp$ is the elementary surface on $S_{v,\nu}(E)$, we have, for each valence-conduction band pairs (v,ν):

$$\sum_k \delta(\hbar\omega - E_{\nu,k+q} + E_{v,k}) \approx \frac{V}{(2\pi)^3}\int d^3k\delta(\hbar\omega - E_{v,k} + E_{\nu,k})$$

and:

$$\begin{aligned}&\frac{V}{(2\pi)^3}\int d^3k\delta(\hbar\omega - E_{v,k+q} + E_{\nu,k})\\ &= \frac{V}{(2\pi)^3}\int\frac{\delta(\hbar\omega - E_{v,\nu})}{|\bigtriangledown_k(E_{v,\nu}(k_\parallel)|}dE_{v,\nu}\int d^2\mathbf{k}_\perp\\ &= \frac{V}{(2\pi)^3}\frac{1}{|\bigtriangledown_k(E_{v,\nu}(k_\parallel)|_{E_{v,\nu}(k)=\hbar\omega}}\int_{S_{v,\nu}(E)} d^2\mathbf{k}_\perp\end{aligned}$$

Finally:

$$\sum_k \delta(\hbar\omega - E_{\nu,k} + E_{v,k}) \approx \frac{V}{(2\pi)^3}\frac{S_{v,\nu}(\hbar\omega)}{|\bigtriangledown_k(E_{v,\nu}(\mathbf{k})|_{E_{v,\nu}(k)=\hbar\omega}}$$

We introduce the energy joint density of states $\mathcal{D}_{v,\nu}(E)$ for a transition from band v to ν:

$$\mathcal{D}_{v,\nu}(E) = \frac{V}{(2\pi)^3}\frac{S_{v,\nu}(E)}{|\bigtriangledown_k(E_{v,\nu}(\mathbf{k})|_{E_{v,\nu}(k)=\hbar\omega}} \tag{44}$$

where $S_{v,\nu}(E)$ is the surface in $\mathbf{k}$-space defined by the equation $E_{v,\nu}(\mathbf{k}) = E$. Finally, from (43), we get:

$$\left(\frac{d\hat{\rho}^I}{dt}\right)_{cond} \approx \frac{2\pi}{2n_{val}N\hbar}\left(\frac{e}{2m_0c}\right)^2 \sum_{v;\nu,\nu'\in\{c_+,c_-\}} \mathcal{D}_{v,\nu}(\hbar\omega)\langle u_{\nu',k_0}|\mathcal{A}_{\mathbf{q},\omega}\cdot\hat{\mathbf{p}}|u_{v,k_0}\rangle\langle u_{v,k_0}|\mathcal{A}^*_{\mathbf{q},\omega}\cdot\hat{\mathbf{p}}|u_{\nu,k_0}\rangle|\Psi_{\nu',k_0}\rangle\langle\Psi_{\nu,k_0}| \tag{45}$$

The generated population and spin densities generation rates are thus :

$$\frac{dN_c}{dt} = \frac{2\pi}{\hbar}\frac{1}{2n_{val}N}\left(\frac{e}{2m_0c}\right)^2 \sum_{v;c}\mathcal{D}_{v,c}(\hbar\omega)\left(|\langle u_{c_+,k}|\mathcal{A}_{\mathbf{q},\omega}\cdot\hat{\mathbf{p}}|u_{v,k}\rangle|^2 + |\langle u_{c_-,k}|\mathcal{A}_{\mathbf{q},\omega}\cdot\hat{\mathbf{p}}|u_{v,k}\rangle|^2\right) \tag{46}$$

$$\frac{dS_{c,z}}{dt} = \frac{\pi}{2n_{val}N}\left(\frac{e}{2m_0c}\right)^2 \sum_{v;c}\mathcal{D}_{v,c}(\hbar\omega)\left(|\langle u_{c_+,k}|\mathcal{A}_{\mathbf{q},\omega}\cdot\hat{\mathbf{p}}|u_{v,k}\rangle|^2 - |\langle u_{c_-,k}|\mathcal{A}_{\mathbf{q},\omega}\cdot\hat{\mathbf{p}}|u_{v,k}\rangle|^2\right) \tag{47}$$

where the summation extends over all valence-conduction bands couples coupled by the optical Hamiltonian. Note we have taken into account the approximation, legitimate here:

$$\mathcal{D}_{v,c_+}(E) \approx \mathcal{D}_{v,c_-}(E) \cong \mathcal{D}_{v,c}(E)$$

If only one conduction band c is accessible by optical transitions, the initial electron spin polarisation generated in this band is, neglecting all spin relaxation processes during the laser pulse duration:

$$\langle\hat{S}_{c,z}\rangle(\Delta t) \approx \frac{\hbar}{2}\frac{\sum_v \mathcal{D}_{v,c}(\hbar\omega)\left(|\langle u_{c_+,k_0}|\mathcal{A}_{\mathbf{q},\omega}\cdot\hat{\mathbf{p}}|u_{v,k_0}\rangle|^2 - |\langle u_{c_-,k_0}|\mathcal{A}_{\mathbf{q},\omega}\cdot\hat{\mathbf{p}}|u_{v,k_0}\rangle|^2\right)}{\sum_v \mathcal{D}_{v,c}(\hbar\omega)\left(|\langle u_{c_+,k_0}|\mathcal{A}_{\mathbf{q},\omega}\cdot\hat{\mathbf{p}}|u_{v,k_0}\rangle|^2 + |\langle u_{c_-,k_0}|\mathcal{A}_{\mathbf{q},\omega}\cdot\hat{\mathbf{p}}|u_{v,k_0}\rangle|^2\right)} \tag{48}$$

expression which shows how the energy dispersion of the coupled valence-conduction bands, through the corresponding joint density of states, impact the initially generated conduction electron spin.

Photogenerated Electron Spin Polarization in L-valleys

We turn now to the specific problem of optical pumping of spin oriented electrons in the GaAs L-valleys. Here, the excitation is provided by a laser beam assumed to propagate along the [001] direction with σ^+ polarisation.

Lets us define the laboratory frame $\mathcal{B} = \{\mathbf{e}_x, \mathbf{e}_y, \mathbf{e}_z\}$ with unit vectors oriented respectively along the [100], [010] and [001] crystallographic directions. To deal with circularly polarised light, it is convenient to introduce the spinorial basis [178] as $\mathcal{B}_S = \{\mathbf{e}_+, \mathbf{e}_-, \mathbf{e}_0\}$ with:

$$\mathbf{e}_+ = -\frac{1}{\sqrt{2}}(\mathbf{e}_x + i\mathbf{e}_y), \mathbf{e}_- = \frac{1}{\sqrt{2}}(\mathbf{e}_x - i\mathbf{e}_y), \mathbf{e}_0 = \mathbf{e}_z \tag{49}$$

The spinorial components of any vector $\mathbf{A}$ in this complex orthonormal basis write :

$$\mathbf{A}_+ = -\frac{1}{\sqrt{2}}(\mathbf{A}_x - i\mathbf{A}_y), \mathbf{A}_- = \frac{1}{\sqrt{2}}(\mathbf{A}_x + i\mathbf{A}_y), \mathbf{A}_0 = \mathbf{A}_z$$

Note that with these definitions: $\mathbf{e}_\mp = -\mathbf{e}^*_\mp$, and $\mathbf{A}_\mp = \mathbf{A}^*_\mp$. Taking

$$\mathbf{A}(\mathbf{r}, t) = A_0[cos(\mathbf{q}\cdot\mathbf{r} - \omega t)\mathbf{e}_x + sin(\mathbf{q}\cdot\mathbf{r} - \omega t)\mathbf{e}_y]$$

as the vector potential of a σ^+ polarised laser beam propagating along the [001] direction with, its expression in $\mathcal{B}_S$ frame is:

$$\mathbf{A}(\mathbf{r}, t) = \frac{A_0}{\sqrt{2}}[-e^{i(\mathbf{q}\cdot\mathbf{r}-\omega t)}\mathbf{e}_+ + e^{-i(\mathbf{q}\cdot\mathbf{r}-\omega t)}\mathbf{e}_-]$$

This description, suitable for optical transitions close to Γ point where the symmetry of the crystal is T_d , is not convenient for the transitions close to the L point. As a fact, the local symmetry at $\mathbf{k}_L$ point is C_{3v}, with the quantification axis z' along a $\langle 111\rangle$ direction, and the electronic states symmetry and the coupling tables by operators can be deduced simply within this new frame. We are thus led to define a new basis $\mathcal{B}'$. Among the 8 different possible choices for the L_i (i =1,...,8) valleys, we select the one oriented along [111], labelled L_1, and define the corresponding frame as :

$$\mathbf{e}_{x'} = -\frac{1}{\sqrt{6}}(\mathbf{e}_x + \mathbf{e}_y - 2\mathbf{e}_z), \mathbf{e}_{y'} = -\frac{1}{\sqrt{6}}(\mathbf{e}_x - \mathbf{e}_y), \mathbf{e}_{z'} = -\frac{1}{\sqrt{6}}(\mathbf{e}_x + \mathbf{e}_y + \mathbf{e}_z)$$

The corresponding spinorial basis is $\mathcal{B}'_S$ defined by:

$$\mathbf{e}_{+'} = -\frac{1}{\sqrt{2}}(\mathbf{e}_{x'} + i\mathbf{e}_{y'}), \mathbf{e}_{-'} = -\frac{1}{\sqrt{2}}(\mathbf{e}_{x'} + i\mathbf{e}_{y'}), \mathbf{e}_{0'} = \mathbf{e}_{z'} \tag{50}$$

The spinorial components of any vector $[\mathbf{r}]_{\mathcal{B}_S} = [r_+, r_-, r_0]$, $[\mathbf{r}]_{\mathcal{B}'_S} = [r'_+, r'_-, r'_0]$ transform as: $[\mathbf{r}]_{\mathcal{B}_S} = [P]_{\mathcal{B}_S,\mathcal{B}'_S}[\mathbf{r}]_{\mathcal{B}'_S}$, so that: $[\mathbf{r}]_{\mathcal{B}'_S} = [P]^{\dagger}_{\mathcal{B}_S,\mathcal{B}'_S}[\mathbf{r}]_{\mathcal{B}_S} = [P]_{\mathcal{B}'_S,\mathcal{B}_S}[\mathbf{r}]_{\mathcal{B}_S}$.

The passage matrix $[P]_{\mathcal{B}_S,\mathcal{B}'_S}$ from the basis $\mathcal{B}_S$ to the basis $\mathcal{B}'_S$ can be thoroughly deduced as:

$$[P]_{\mathcal{B}_S,\mathcal{B}'_S} = [P]_{\mathcal{B}_S,\mathcal{B}}[P]_{\mathcal{B},\mathcal{B}'}[P]_{\mathcal{B},\mathcal{B}'_S} \tag{51}$$

We deduce:

$$[P]_{\mathcal{B}_S,\mathcal{B}'_S} = \begin{bmatrix} \frac{e^{-i\frac{\pi}{4}}}{2}\left(1+\frac{1}{\sqrt{3}}\right) & \frac{e^{-i\frac{\pi}{4}}}{2}\left(1-\frac{1}{\sqrt{3}}\right) & -\frac{e^{-i\frac{\pi}{4}}}{\sqrt{3}} \\ \frac{e^{+i\frac{\pi}{4}}}{2}\left(1-\frac{1}{\sqrt{3}}\right) & \frac{e^{+i\frac{\pi}{4}}}{2}\left(1+\frac{1}{\sqrt{3}}\right) & \frac{e^{i\frac{\pi}{4}}}{\sqrt{3}} \\ \frac{1}{\sqrt{3}} & -\frac{1}{\sqrt{3}} & \frac{1}{\sqrt{3}} \end{bmatrix} \tag{52}$$

$$[P]^{-1}_{\mathcal{B}_S,\mathcal{B}'_S} = [P]^{\dagger}_{\mathcal{B}_S,\mathcal{B}'_S} = \begin{bmatrix} \frac{e^{+i\frac{\pi}{4}}}{2}\left(1+\frac{1}{\sqrt{3}}\right) & \frac{e^{-i\frac{\pi}{4}}}{2}\left(1-\frac{1}{\sqrt{3}}\right) & +\frac{1}{\sqrt{3}} \\ \frac{e^{+i\frac{\pi}{4}}}{2}\left(1-\frac{1}{\sqrt{3}}\right) & \frac{e^{-i\frac{\pi}{4}}}{2}\left(1+\frac{1}{\sqrt{3}}\right) & -\frac{1}{\sqrt{3}} \\ -\frac{e^{+i\frac{\pi}{4}}}{\sqrt{3}} & \frac{e^{-i\frac{\pi}{4}}}{\sqrt{3}} & +\frac{1}{\sqrt{3}} \end{bmatrix}$$

which is unitary, since the two complex basis are orthonormal. Note that these transformation laws apply to any vectorial operator as well. For circularly polarized excitation propagating in the [001] direction, we have in general:

$$\mathcal{A}_{\mathbf{q},\omega} = A_0 \begin{bmatrix} \varepsilon_x \\ \varepsilon_y \\ \varepsilon_z \end{bmatrix}, \mathcal{A}^*_{\mathbf{q},\omega} = A_0 \begin{bmatrix} \varepsilon^*_x \\ \varepsilon^*_y \\ \varepsilon^*_z \end{bmatrix}$$

$$\mathcal{A}_{\mathbf{q},\omega} = A_0 \begin{bmatrix} \varepsilon_+ = -\frac{\varepsilon_x - i\varepsilon_y}{\sqrt{2}} \\ \varepsilon_- = \frac{\varepsilon_x + i\varepsilon_y}{\sqrt{2}} \\ \varepsilon_0 = \varepsilon_z \end{bmatrix}_{\mathcal{B}_S}, \mathcal{A}^*_{\mathbf{q},\omega} = A_0 \begin{bmatrix} \varepsilon^*_+ = -\frac{\varepsilon_x + i\varepsilon_y}{\sqrt{2}} \\ \varepsilon^*_- = \frac{\varepsilon_x - i\varepsilon_y}{\sqrt{2}} \\ \varepsilon_0 = \varepsilon_z \end{bmatrix}_{\mathcal{B}_S}$$

$$[\mathcal{A}_{\mathbf{q},\omega}]_{\mathcal{B}'_S} = [P]^{-1}_{\mathcal{B}_S,\mathcal{B}'_S}[\mathcal{A}_{\mathbf{q},\omega}]_{\mathcal{B}_S} = \begin{bmatrix} \frac{e^{+i\frac{\pi}{4}}}{2}\left(1+\frac{1}{\sqrt{3}}\right)\varepsilon_+ + \frac{e^{-i\frac{\pi}{4}}}{2}\left(1-\frac{1}{\sqrt{3}}\right)\varepsilon_- + \frac{1}{\sqrt{3}}\varepsilon_0 \\ \frac{e^{+i\frac{\pi}{4}}}{2}\left(1-\frac{1}{\sqrt{3}}\right)\varepsilon_+ + \frac{e^{-i\frac{\pi}{4}}}{2}\left(1+\frac{1}{\sqrt{3}}\right)\varepsilon_- - \frac{1}{\sqrt{3}}\varepsilon_0 \\ -\frac{e^{+i\frac{\pi}{4}}}{\sqrt{3}}\varepsilon_+ + \frac{e^{-i\frac{\pi}{4}}}{\sqrt{3}}\varepsilon_- + \frac{1}{\sqrt{3}}\varepsilon_0 \end{bmatrix}_{\mathcal{B}'_S}$$

For instance, for circularly polarized excitation $\sigma^+_{[001]}$ propagating in the [001] direction, we have in general:

$$\mathcal{A}_{\mathbf{q},\omega} = A_0 \begin{bmatrix} 1 \\ i \\ 0 \end{bmatrix}, \mathcal{A}^*_{\mathbf{q},\omega} = A_0 \begin{bmatrix} 1 \\ -i \\ 0 \end{bmatrix}$$

The components in the basis $\mathcal{B}_S$ are:

$$\mathcal{A}_{\mathbf{q},\omega} = A_0\sqrt{2} \begin{bmatrix} -1 \\ 0 \\ 0 \end{bmatrix}_{\mathcal{B}_S}, \mathcal{A}^*_{\mathbf{q},\omega} = A_0\sqrt{2} \begin{bmatrix} 0 \\ 1 \\ 0 \end{bmatrix}_{\mathcal{B}_S}$$

In the basis $\mathcal{B}'_S$, we have thus:

$$\mathcal{A}_{\mathbf{q},\omega} = A_0\sqrt{2} \begin{bmatrix} -\frac{e^{+i\frac{\pi}{4}}}{2}\left(1+\frac{1}{\sqrt{3}}\right) \\ -\frac{e^{+i\frac{\pi}{4}}}{2}\left(1-\frac{1}{\sqrt{3}}\right) \\ \frac{e^{+i\frac{\pi}{4}}}{\sqrt{3}} \end{bmatrix}_{\mathcal{B}'_S}, \mathcal{A}^*_{\mathbf{q},\omega} = A_0\sqrt{2} \begin{bmatrix} \frac{e^{-i\frac{\pi}{4}}}{2}\left(1-\frac{1}{\sqrt{3}}\right) \\ \frac{e^{-i\frac{\pi}{4}}}{2}\left(1+\frac{1}{\sqrt{3}}\right) \\ \frac{e^{-i\frac{\pi}{4}}}{\sqrt{3}} \end{bmatrix}_{\mathcal{B}'_S}$$

Recalling that:

$$\hat{\mathbf{p}} = \begin{bmatrix} \hat{p}_{+'} = -\frac{\hat{p}_{x'} - i\hat{p}_{y'}}{\sqrt{2}} \\ \hat{p}_{-'} = \frac{\hat{p}_{x'} + i\hat{p}_{y'}}{\sqrt{2}} \\ \hat{p}_{0'} = \hat{p}_{z'} \end{bmatrix}_{\mathcal{B}'_S}$$

and since the hermitian scalar product in invariant in any orthogonal basis change, we deduce:

$$\mathcal{A}_{\mathbf{q},\omega} \cdot \hat{\mathbf{p}} = [\mathcal{A}_{\mathbf{q},\omega}]^\dagger_{\mathcal{B}'_S}[\hat{\mathbf{p}}]_{\mathcal{B}'_S} = (\mathcal{A}_{\mathbf{q},\omega})^*_{+'}\hat{p}_{+'} + (\mathcal{A}_{\mathbf{q},\omega})^*_{-'}\hat{p}_{-'} + (\mathcal{A}_{\mathbf{q},\omega})^*_{0'}\hat{p}_{0'}$$

$$\mathcal{A}_{\mathbf{q},\omega} \cdot \hat{\mathbf{p}} = [\mathcal{A}_{\mathbf{q},\omega}]^\dagger_{\mathcal{B}'_S}[\hat{\mathbf{p}}]_{\mathcal{B}'_S} = \frac{e^{-i\frac{\pi}{4}}}{2}\left(1+\frac{1}{\sqrt{3}}\right)\hat{p}_{+'} - \frac{e^{-i\frac{\pi}{4}}}{2}\left(1-\frac{1}{\sqrt{3}}\right)\hat{p}_{-'} + \frac{e^{-i\frac{\pi}{4}}}{\sqrt{3}}\hat{p}_{0'} \quad (53)$$

In order to specify the optical transitions at the L_1 point, the electronics valence and conductions states symmetry can be obtained for C_{3v} point group in Koster notations [179] in table 1.

Representation	Spin-orbital state at L point	Angular Momentum	Band
L_4^c	$\alpha\|S'\uparrow\rangle + \beta\|Z'\uparrow\rangle$ $\alpha\|S'\downarrow\rangle - \beta\|Z'\downarrow\rangle$	$\|\frac{1}{2},+\frac{1}{2}\rangle_c$ $\|\frac{1}{2},-\frac{1}{2}\rangle_c$	conduction
$L_5^v + L_6^v$	$-\|\frac{X'+iY'}{\sqrt{2}}\uparrow\rangle$ $\|\frac{X'-iY'}{\sqrt{2}}\downarrow\rangle$	$\|\frac{3}{2},+\frac{3}{2}\rangle_v$ $\|\frac{3}{2},-\frac{3}{2}\rangle_v$	heavy-valence
L_4^v	$-\|\frac{X'+iY'}{\sqrt{2}}\uparrow\rangle$ $\|\frac{X'-iY'}{\sqrt{2}}\downarrow\rangle$	$\|\frac{1}{2},+\frac{1}{2}\rangle_c$ $\|\frac{1}{2},-\frac{1}{2}\rangle_c$	spin-orbit valence

Table 1: The L-valley electronic states representation in C_{3v}

$+'$	$\|\frac{X'-iY'}{\sqrt{2}}\downarrow\rangle$	$-\|\frac{X'+iY'}{\sqrt{2}}\uparrow\rangle$	$\|\frac{X'-iY'}{\sqrt{2}}\uparrow\rangle$	$-\|\frac{X'+iY'}{\sqrt{2}}\downarrow\rangle$
$\alpha\|S'\downarrow\rangle - \beta\|Z'\downarrow\rangle$	$-\alpha\prod$	0	0	0
$\alpha\|S'\uparrow\rangle + \beta\|Z'\uparrow\rangle$	0	0	$-\alpha\prod$	0
$-'$ $\sigma^{+'}; \mathbf{q} \parallel [1,1,1]$	$\|\frac{X'-iY'}{\sqrt{2}}\downarrow\rangle$	$-\|\frac{X'+iY'}{\sqrt{2}}\uparrow\rangle$	$\|\frac{X'-iY'}{\sqrt{2}}\uparrow\rangle$	$-\|\frac{X'+iY'}{\sqrt{2}}\downarrow\rangle$
$\alpha\|S'\downarrow\rangle - \beta\|Z'\downarrow\rangle$	0	0	0	$\alpha\prod$
$\alpha\|S'\uparrow\rangle + \beta\|Z'\uparrow\rangle$	0	$\alpha\prod$	0	0

Table 2: The coupling tables of $\hat{p}_{\pm'}$ operators at L point.

Note that the basis vectors of the sum of representation $L_5^v + L_6^v$ are eigenvectors of the hamiltonian since no longitudinal magnetic field is applied here. Here, we have defined the matrix element $\prod \equiv \langle S'|\hat{p}'_x|X'\rangle = \langle S'|\hat{p}'_y|Y'\rangle$. Using this notation, the coupling table with $\hat{p}'_\pm$ operators are easily obtained, and are summarised in the first table. The $\hat{p}_{0'} = \hat{p}_{z'}$ operator does not couple the mentioned conduction and valence states.

Now, we turn back to our excitation configuration with σ^+ photons propagating along [111]. The coupling table obtained from Figure 4.9 is given in the table 2. Using formula (52) and the tables 2 above, we obtain the coupling table 3 below for a $\sigma^+_{[001]}$ photon propagating along the [001] direction. From these tables (1,2) and figure 14, it

$\varepsilon \cdot \hat{p}$ $\sigma^+; \mathbf{q} \parallel [0,0,1]$	$\lvert\frac{X'-iY'}{\sqrt{2}}\downarrow\rangle$	$-\lvert\frac{X'+iY'}{\sqrt{2}}\uparrow\rangle$
$\alpha\lvert S'\downarrow\rangle - \beta\lvert Z'\downarrow\rangle$	$-\frac{e^{+i\frac{\pi}{4}}}{2}\left(1+\frac{1}{\sqrt{3}}\right)\alpha\prod$	0
$\alpha\lvert S'\uparrow\rangle + \beta\lvert Z'\uparrow\rangle$	0	$-\frac{e^{+i\frac{\pi}{4}}}{2}\left(1-\frac{1}{\sqrt{3}}\right)\alpha\prod$
$\varepsilon \cdot \hat{p}$ $\sigma^+; \mathbf{q} \parallel [0,0,1]$	$\lvert\frac{X'-iY'}{\sqrt{2}}\uparrow\rangle$	$-\lvert\frac{X'+iY'}{\sqrt{2}}\downarrow\rangle$
$\alpha\lvert S'\downarrow\rangle - \beta\lvert Z'\downarrow\rangle$	0	$-\frac{e^{+i\frac{\pi}{4}}}{2}\left(1-\frac{1}{\sqrt{3}}\right)\alpha\prod$
$\alpha\lvert S'\uparrow\rangle + \beta\lvert Z'\uparrow\rangle$	$-\frac{e^{+i\frac{\pi}{4}}}{2}\left(1+\frac{1}{\sqrt{3}}\right)\alpha\prod$	0

Table 3: The coupling tables for circularly polarized photons propagating along [001] at L point.

can be inferred that no spin coherences can arise in the conduction band neither with a monochromatic, nor a 2 ps duration laser pulse.

The spin of the population generated by $\sigma^+_{[001]}$ mode is then deduced from (41,42) and table 3, yielding, for excitation energies close to the E_g^L gap:

$$\mathbf{S}_{c,z}|_{gen} = \frac{\hbar}{2}\frac{|\langle u_{c+,k_L}|\varepsilon\cdot\hat{\mathbf{p}}|u_{hh+,k_L}\rangle|^2 - |\langle u_{c-,k_L}|\varepsilon\cdot\hat{\mathbf{p}}|u_{hh-,k_L}\rangle|^2}{|\langle u_{c+,k_L}|\varepsilon\cdot\hat{\mathbf{p}}|u_{hh+,k_L}\rangle|^2 + |\langle u_{c-,k_L}|\varepsilon\cdot\hat{\mathbf{p}}|u_{hh-,k_L}\rangle|^2}$$

$$\mathbf{S}_c^{L_1}|_{gen} = -\frac{\hbar}{2}\frac{\sqrt{3}}{2}\mathbf{e}'_z \tag{54}$$

For the opposite valley $e"_z = -e'_z$, oriented along [–1, –1, –1], it can be easily shown that the generated spin is :

$$\mathbf{S}_c^{L_1}|_{gen} = +\frac{\hbar}{2}\frac{\sqrt{3}}{2}\mathbf{e}"_z = -\frac{\hbar}{2}\frac{\sqrt{3}}{2}\mathbf{e}'_z \tag{55}$$

which is expected, since the valleys in two opposite directions are equivalent.

The spin generated in the other valleys is finally obtained using the invariance of the crystal by rotations around the $\mathbf{e}_z = [001]$ axis. Finally, the total average spin photo-generated from $L_5^v + L_6^v$ valence bands by a σ^+ polarised laser beam propagating along [001] is:

$$\mathbf{S}_c|_{gen} = \frac{1}{4}\sum_{i=1}^{4} S_c^{L_i}|_{gen} = -\frac{\hbar}{2}\frac{\mathbf{e}_z}{2} \tag{56}$$

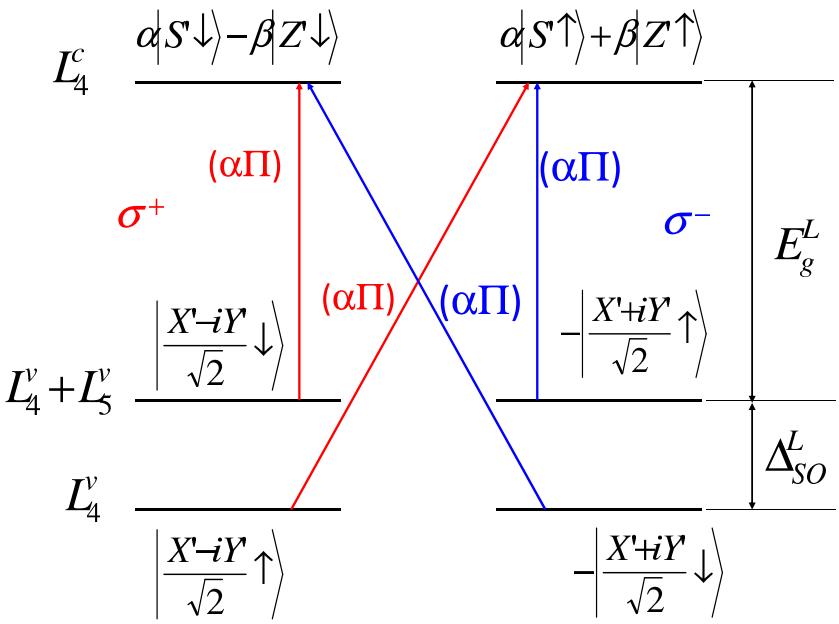

[

]Figure: The optical transitions schele at L point in the GaAs Brillouin zone. The transition amplitudes $(\alpha \prod)$ represents $\langle u_c|e^*_{\pm'}\mathbf{p}_{\pm'}|u_v\rangle$ matrix elements. For the notations, see text and table 1. The transitions amplitudes are taken from table 2 and (52). The $\sigma^{\pm'}$ optical modes propagate along the [1,1,1] direction.

In a similar manner, assuming only the valence band (L_4^v) is excited, and using tables (3), we would arrive for light propagating along [001] direction to the expression opposite to (55): $\mathbf{S}_c|_{gen} = \frac{1}{4}\sum_{i=1}^{4} S_c^{L_i}|_{gen} = +\frac{\hbar}{2}\frac{\mathbf{e}_z}{2}$. However, this cannot be achieved practically without exciting the $L_5^v + L_6^v$ bands simultaneously. In the experimental case, using formula (48), we arrive to the expression:

$$\langle \hat{S}_{c,z}(\Delta t) \approx \frac{\hbar}{2} \frac{\sum\limits_{v=\{L_5+L_6,L_4\}} \mathcal{D}_{v,c}(\hbar\omega)\left(|\langle u_{c_+,k_0}|\mathcal{A}_{\mathbf{q},\omega}\cdot\hat{\mathbf{p}}|u_{v,k_0}\rangle|^2 - |\langle u_{c_-,k_0}|\mathcal{A}_{\mathbf{q},\omega}\cdot\hat{\mathbf{p}}|u_{v,k_0}\rangle|^2\right)}{\sum\limits_{v=\{L_5+L_6,L_4\}} \mathcal{D}_{v,c}(\hbar\omega)\left(|\langle u_{c_+,k_0}|\mathcal{A}_{\mathbf{q},\omega}\cdot\hat{\mathbf{p}}|u_{v,k_0}\rangle|^2 + |\langle u_{c_-,k_0}|\mathcal{A}_{\mathbf{q},\omega}\cdot\hat{\mathbf{p}}|u_{v,k_0}\rangle|^2\right)}$$

$$\langle \hat{S}_{c,z}(\Delta t) \approx \frac{\hbar}{2}\left(-\frac{1}{2}\frac{\mathcal{D}_{L_5+L_6,c}(\hbar\omega) - \mathcal{D}_{L_4,c}(\hbar\omega)}{\mathcal{D}_{L_5+L_6,c}(\hbar\omega) + \mathcal{D}_{L_4,c}(\hbar\omega)}\right) \tag{57}$$

The resulting generated polarisation is expected to be very weak, since the joint density of states $\mathcal{D}_{L_5+L_6,c}(\hbar\omega)$ and $\mathcal{D}_{L_4,c}(\hbar\omega)$ essentially compensate. A more careful examination of the theoretical **k.p** or LDA approaches (see figure 4.7 chapter 4) reveals that when the $L_5^v + L_6^v$ and the L_4^v bands are excited simultaneously, some imbalance occurs between the joint density of state $\mathcal{D}_{L_5+L_6,c}(\hbar\omega)$ and $\mathcal{D}_{L_4,c}(\hbar\omega)$, the former being slightly reduced to the increasing curvature of the conduction band dispersion when moving towards the Γ point. The initial spin will then decay equally in each valleys,

with no spin coherence arising. It will be then transferred to the Γ valley.

Chapter 5

Spin Properties of GaAsBi

5.1 Introduction 139
5.2 TRPL characterization of GaAsBi epilayers 142
5.2.1 Bandgap energy variation and PL linewidth 143
5.2.2 Effect of Rapid Thermal Annealing on carrier lifetime 146
5.3 Spin properties of GaAsBi 148
5.3.1 Experimental determination of g-factor 149
5.3.2 Analysis of spin relaxation time 155
5.4 Conclusions and perspectives 156

In chapter 3, we have described the electrical spin injection into a semiconductor. The spin manipulation is the next step in order to lead to potential applications in the field of spintronics. In this view, new materials with peculiar spin properties, are constantly investigated. In this chapter, we focus on the dilute bismide alloy of GaAs, since a small amount of bismuth to arsenide strongly modifies the electronic and spin properties of GaAs. These remarkable properties make GaAsBi a good candidate for both optoelectronic and spintronic applications.

In this chapter, we describe the recent studies we performed on GaAsBi epilayers. First we introduce the electron properties of this alloy. In a second step, we focus on photoluminescence characterization of these epilayers via the investigation of their bandgap energy dependence upon temperature and photoluminescence excitation power. Finally, we describe the study of their electon spin properties by means of time and polarization resolved photoluminescence. We show that bismuth strongly modifies the spin properties of GaAsBi as compared to GaAs.

5.1 Introduction

There is an increasing interest in the highly mismatched semiconductor alloys $GaBi_xAs_{1-x}$, both from a fundamental perspective [180–183] and also because of its potential device applications [184–187]. When a small fraction of As is replaced by Bi in GaAs, the band gap Eg decreases rapidly, by ∼90 meV when 1% of As is replaced by Bi. In addition, photoreflectance measurements show that the energy separation, Δ_{SO}, between the spin-split-off valence band and the valence band edge also increases rapidly with Bi composition [188]. It has been recently shown [189] that, by increasing the Bi composition in $GaBi_xAs_{1-x}$ to $\sim$ 10%, we enter an Eg $< \Delta_{SO}$ regime in the alloy. This regime is of interest for the design of highly efficient optoelectronic devices since it opens up the possibility of suppression of the nonradiative Auger recombination process involving excitation of holes from the highest valence band into the spin-orbit split-off band, a loss mechanism that plagues the efficiency and dominates the threshold characteristics of GaInAsP and AlGaInAs lasers operating in the telecommunication wavelength range [184,186,189].

The features observed experimentally on GaAsBi alloys strongly remind the ones observed previously in another GaAs diluted alloy: GaAsN. In this ternary alloy, nitrogen cluster states interact strongly with the extended states of the GaAs matrix conduction states, leading to a strong reduction of the band gap energy. This behaviour has been nicely described by a band anticrossing model (BAC), which has shown efficiency to predict band gap reduction of strained or relaxed diluted nitride alloys [190]. However, this oversimplified approach doesn't take into account alloy disorder and underestimates the changes upon electron effective mass or gyromagnetic factor for instance [191]. Tight-binding and pseudopotential calculations have been performed as well [191,192]. They have provided a deeper description of GaAsN alloys, and have confirmed the sufficient reliability of the BAC model to describe the band gap reduction in this material. The strong localization effects observed by photoluminescence experiments [193,194], the large reduction of the band gap energy [195], added to the large bowing of spin-orbit split-off energy [196] have suggested a similar behaviour.

Indeed, a BAC model has been suggested, this time taking into account the inter-

action between bismuth localized states and the extended valence states of the GaAs host matrix [15,16]. Again, this simple model has given satisfactory agreement with experimental determination of the band gap energy and spin-orbit split-off energy, the bismuth related localized states "pushing" up the valence band edge. However, tight-binding calculations carried out on this system by Usman et al. have shown that the experimentally observed strong band gap reduction is only partially explained through the valence band BAC interaction [16]. They find that the conduction band edge energy also decreases with increasing Bi composition, and that both band edge shifts contribute approximately equally at large Bi compositions to the reduction in the band gap energy of unstrained $GaBi_xAs_{1-x}$ alloys. The dependence of the band gap on the Bi composition closely matches with experimental measurements. They also calculated that the band gap and spin-orbit-splitting energies cross each other at 10.5% Bi composition in $GaBi_xAs_{1-x}$, which is consistent with recent experimental measurements [185].

In Figure 5.1 and Figure 5.2 are reported the band gap energies Eg and spin-orbit

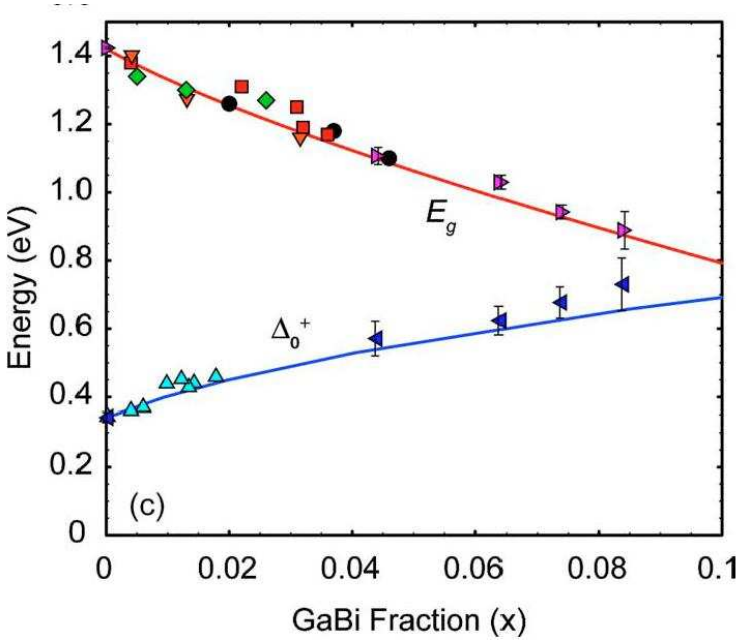

Figure 5.1: Band gap energies and spin-orbit split-off energy calculated using the BAC model [15]

split-off energy calculated using the BAC model (Figure 5.1 [15]) and tight-binding model (Figure 5.2 [16]). One can notice that both model give reasonable agreement as far as Eg and Δ_{SO} are concerned. The major difference remains in the prediction of the conduction band offset, which could be of type I or type II according to the model

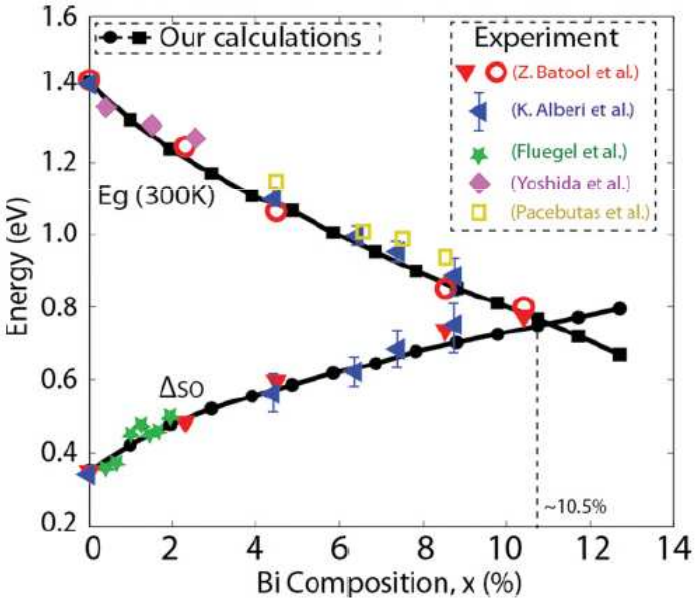

Figure 5.2: band gap energies and spin-orbit split-off energy calculated using tight-binding model [16]

used. Hence, further studies are necessary to understand deeper the GaAsBi electronic properties, so as to refine the models used to predict alloy properties, and be able to use it in optoelectronic devices.

In this chapter, we present rapidly the singular properties of GaAsBi ternary alloy. Then, we present time integrated and time-resolved photoluminescence characterizations of a GaAsBi epilayer containing 2.2% of bismuth, showing the influence of temperature and excitation power density. We discuss the localized character of valence states and the effect of rapid thermal annealing on the improvement of material quality and homogeneity. In a second section, we investigate the spin properties of the alloy as a probe of band structure major changes by time and polarization resolved photoluminescence measurements. We determine the value of the electron gyromagnetic factor and electron spin relaxation time. We show that the experimental values determined here are evidence of the strong modification of host states by bismuth atoms.

5.2 TRPL characterization of GaAsBi epilayers

In this section, we investigate the photoluminescence characteristics of a GaAsBi epilayer as a function of temperature and excitation power density. These experiments are key steps in order to understand the influence of bismuth incorporation upon the matrix states. Moreover, we have performed rapid thermal annealing (RTA) on the studied samples. RTA is well known for improving, under optimised conditions, both the optical quality of the material while reducing the non radiative defect density, and the crystal homogeneity.

First, we present the dependence of the PL linewidth and peak position upon temperature and excitation power density and describe the effect of RTA. In a second step, we investigate the effect of RTA upon carrier lifetime.

The sample investigated in this chapter consists of a bulk undoped 160 nm thick $GaAs_{0.978}Bi_{0.022}$ layer, grown on a 300 nm GaAs buffer layer and a semi-insulating GaAs (100) substrate in a RIBER solid-source MBE system. The substrate temperature was controlled by means of optical bandgap thermometry to be $580°C$ and $380°C$ for the buffer and dilute bismide layers, respectively. The bismide layer was grown at a reduced rate of $0.1\mu mh^{-1}$, and for a stoichiometric As/Ga ratio. The Bi concentration and layer thickness were measured via high-resolution X-ray diffraction, from where it is also evidenced that the GaAsBi layer is elastically strained. Once grown, a part of the GaAsBi sample was subjected to a nitrogen atmosphere during 30s at $750°C$. The sample was capped with a piece of GaAs substrate during the annealing in order to prevent any surface degradation due to arsenic desorption. Moussa et al [197] have shown by varying the annealing temperature for MOVPE-grown $GaAs_{0.96}Bi_{0.04}$ epilayers that the optimization of luminescence efficiency is obtained at around $700°C$. This was also confirmed for MBE-grown samples by Mohmad et al [198]. The temperature used here ($750°C$) is then close to this literature-reported optimal value.

The sample was mounted in a closed He-cooled cycle cryostat, where the temperature varied from 10 to 300 K. Optical excitation was provided by focusing 1.5 ps pulses generated by a mode-locked Ti-Sapphire laser with 80 MHz repetition frequency. The laser wavelength was fixed at $\lambda_{exc} = 795nm$ with 1 mW and 10 mW incident powers, focused on a $50\mu m$ diameter spot at the sample surface. This corresponds to a typical

photon flux of 0.5 and $2.5 \times 10^{13} cm^{-2}$ at the sample surface. The incident angle of the exciting laser beam was perpendicular to the sample surface (along the z axis). Time-integrated and time-resolved PL, measured along the sample growth direction, were recorded using a S1 photocathode Hamamatsu streak camera with an overall time resolution of 8 ps. [199]

5.2.1 Bandgap energy variation and PL linewidth

The investigation of the sample was then carried out as a function of temperature. Figure 5.3 (a) shows the PL peak emission energy versus temperature obtained for the as-grown sample at 1 mW (filled squares) and 10 mW (filled triangles) incident power, and for the $750°C$ annealed sample at 1 mW (open squares) and 10 mW (open triangles). The PL energy values correspond to the expected ones with this Bi concentration [181,195]. At low temperature, the as-grown 1 mW curve departs from the expected Varshni fit [200] by showing the typical S-shape behaviour of disordered semiconductors and already observed in GaAsBi materials [198]. The origin of this deviation is attributed to localized states, alloy disorder, potential fluctuations and cluster localization, induced by Bi incorporation [193,201]. The carrier localization energy at any temperature is given by the difference $E_{loc}(T) = E_{Var}(T) - E_{PL}(T)$, where $E_{Var}(T)$ and $E_{PL}(T)$ are the Varshni theoretical energy value and the temperature dependence of the PL peak energy, respectively [202]. The temperature of the local minimum is around 70 K, and the corresponding maximum localization energy $E_{loc,max}$ is about 8 meV. For the as-grown sample, the S-shape vanishes at higher incident power, due to the expected complete filling of the localized states at high excitation density. The key point is that the S-shape feature disappears as well for the RTA sample. In the latter case, the reason is the improvement of the sample quality through the reduction of the localized defect density. Similar trends were observed for these samples when the full width at half maximum (FWHM) is plotted as a function of temperature (Figure 5.3 (b)), where again the S-shape disappears after annealing. Indeed, for the as-grown sample under 1 mW excitation, the FWHM increases from 60 meV at 10 K to a local maximum of 90 meV at around 100 K, corresponding to the intermediate tempera-

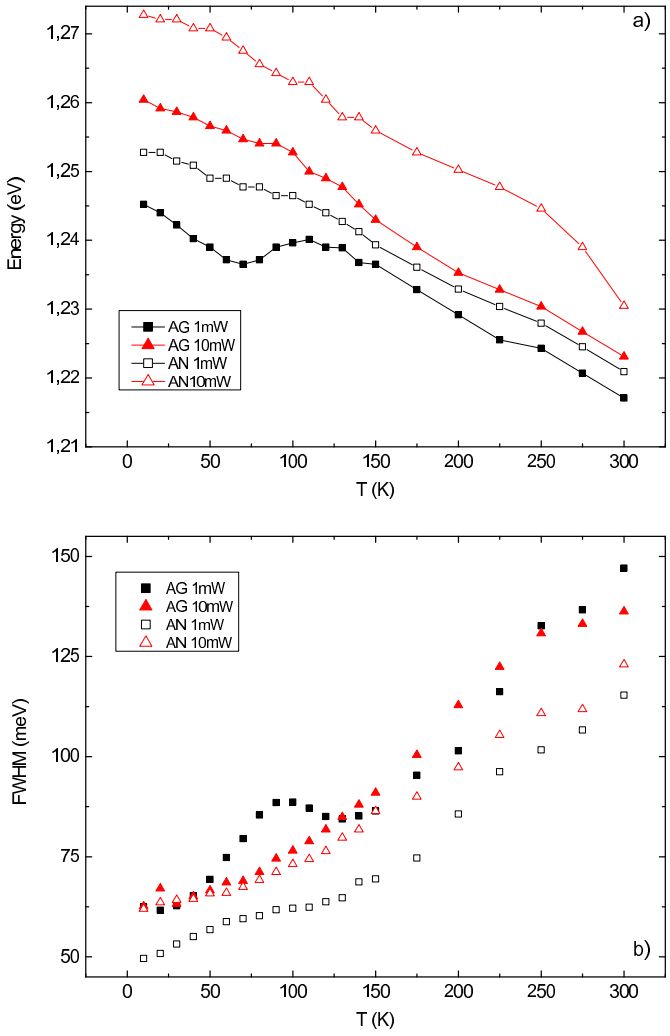

Figure 5.3: PL peak emission energy (a) and FWHM (b) plotted as a function of temperature for the as-grown sample excited at 1 mW (filled squares) and 10 mW (filled triangles), and for the 750°C annealed sample at 1 mW (empty squares) and 10 mW (empty triangles).

ture where carriers are equally separated between localized and valence states. Then, it slightly decreases to 84 meV at 130 K when thermal energy is sufficient to permit de-trapping of holes, and finally it increases again, following the standard temperature dependence feature. The removal of the S-shape behavior by annealing indicates a reduction of the localized states density, and this is further confirmed by the FWHM value, which is smaller for the annealed sample than for the as-grown one whatever the temperature value is. We also observe a slight blue shift of about 5 meV of the GaAsBi bandgap energy induced by annealing.

Figure 5.4 shows the room temperature time-integrated PL spectra measured for the as-grown and the annealed samples. The excitation power was set at 1 mW. The

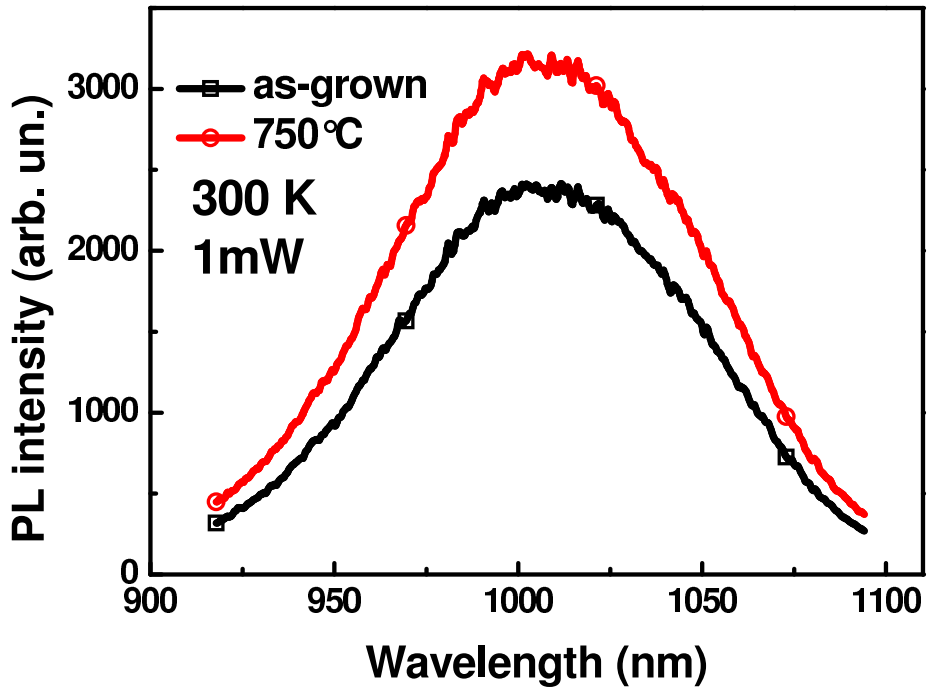

Figure 5.4: Time integrated PL spectra for the as-grown and annealed samples at 750°C, taken at room temperature and 1 mw excitation power

PL intensity is observed to increase by ∼30% after annealing, with almost no change in the emission wavelength.

Another way to characterize the sample quality is to calculate the activation energies of the defects via the evolution of the PL intensity with temperature, using the Arrhenius expression of $log(I_0/I-1)$ versus $1/T$, where I_0 is the PL intensity at 0 K.

Figure 5.5 shows the obtained plots before and after RTA. The plot for the as-grown sample cannot be split into linear components, implying that a continuous range of defect energies from around 5 to 50 meV is present. In contrast, with the annealed sample, the Arrhenius plot can be easily fitted with two single lines, which provides activation energies of around 7 and 30 meV, in the temperature range from 40 to 140 K and from 150 to 300 K, respectively. This confirms that post-growth annealing helps reducing the density and the energy dispersion of defects induced by Bi incorporation.

RTA therefore increases the sample quality by reducing the density of defects, in a similar way as already observed via transmission electron microscopy characterization by Rodrigo et al [16]. In fact, it appears that some types of defects are efficiently cured but only two mainly remain. The corresponding energy values of 7 and 30 meV are similar to those identified by Imhof et al [12, 19] at 11 and 45 meV and which

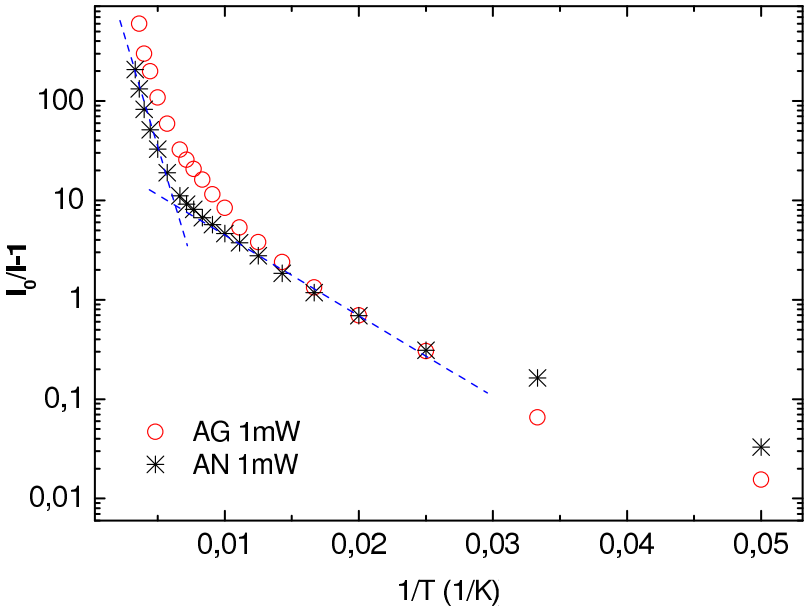

Figure 5.5: Arrhenius plots for the as-grown sample (empty circles) and the annealed (crosses) sample at 1 mW. The dashed lines represent the fitting lines for the calculation of the defects' activation energies in the annealed sample.

were attributed to Bi cluster states and alloy disorder, respectively. Our reduced values might be explained by the lower Bi concentration of our samples. RTA was also demonstrated to influence the carrier dynamics at room temperature. Cechavicius et al [22] also investigated the thermal annealing effect on the GaAsBi carrier dynamics using the optical pump–THz probe technique, but they concluded that RTA is beneficial only on samples with 6% Bi concentration.

5.2.2 Effect of Rapid Thermal Annealing on carrier lifetime

By studying the TRPL decay time at low temperature at low incident power, we found that annealing drastically modifies the photogenerated carrier lifetime. In the as-grown sample, up to about 50 K, the TRPL curve appears almost flat after the laser excitation pulse, and the decay time is longer than our instrumental measurement capability due to the long trapped carrier recombination mechanism. By increasing the temperature above 50 K, the TRPL curve starts showing an exponential decay aspect, due to non-radiative defect thermal activation and band-to-band recombination. This brings the decay time to around 130 ps at room temperature for 1 mW incident power, as represented in Figure 5.6(a). Similar TRPL curves were obtained for the annealed

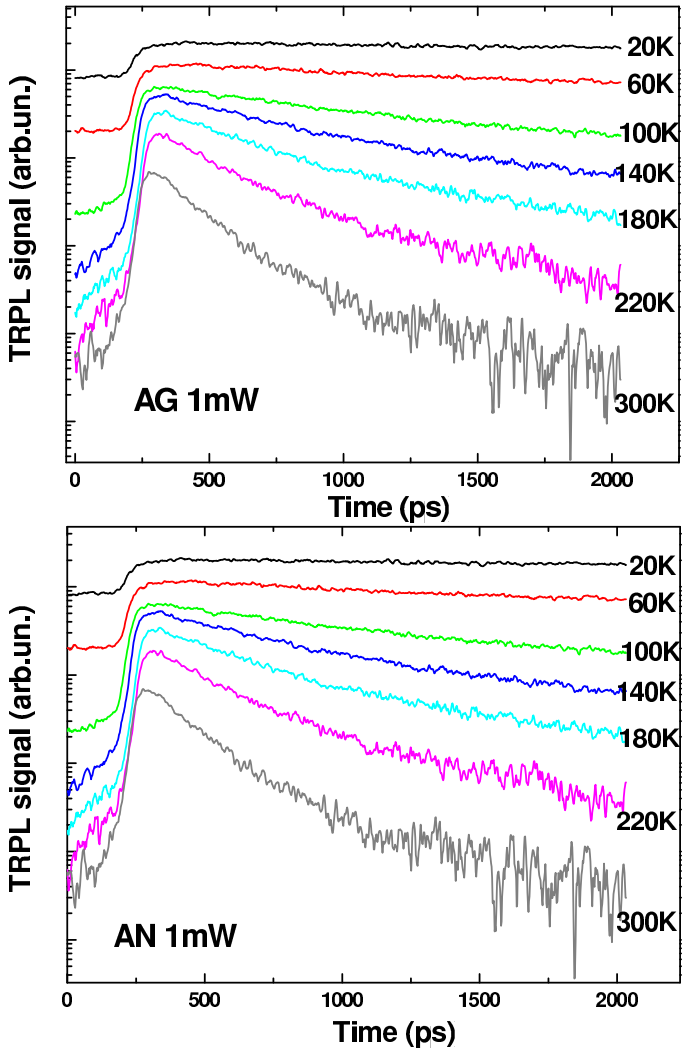

Figure 5.6: TRPL curves for the as-grown sample (a) and the annealed sample (b), taken at 1 mW incident power for a series of increasing temperatures up to 300 K. (NB: The amplitudes of the signals in the two graphs are not comparable as data were taken under different acquisition conditions.) Spectra are shifted for presenting more clearly.

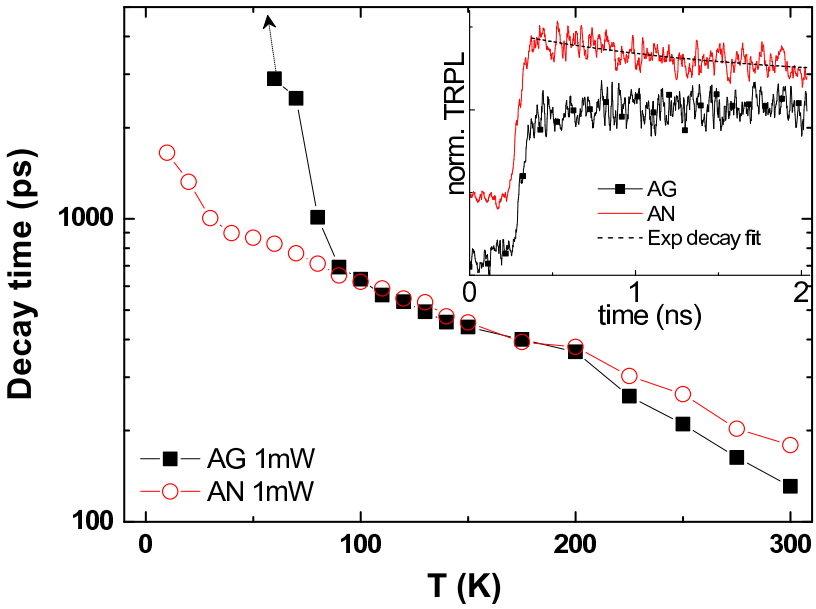

Figure 5.7: Decay time plot versus temperature for the as-grown (filled squares) and $750°C$ annealed samples (empty circles) at 1 mW incident power. The normalized TRPL curves taken at 10 K are shown in the inset (stacked for clarity), together with the exponential fit for the annealed sample.

sample, as shown in Figure 5.6(b). However, when comparing the measured decay time, at low temperature, there is a severe reduction of the carrier lifetime for the RTA sample as compared to the as-grown sample. This is represented in Figure 5.7. At 10 K for example, the decay time of the annealed sample was measured to be equal to 1.65 ns (see the exponential fit in the inset gragh of Figure 5.7). Whereas it is out of the accessible experimental time range for the as-grown sample. This decay time decreases due to the efficient reduction of the defects density and the induced increase of faster delocalized carrier recombination processes. We technically expect this feature to be due to a higher oscillator strength between conduction states and delocalized valence band state. From 90 K, the decay time of the two samples is almost identical, the annealed one marginally higher, because of the slight reduction of the non-radiative defects density after RTA.

5.3 Spin properties of GaAsBi

In this section, we investigate the photoluminescence (PL) polarization dynamics after circularly polarized excitation. The measurement of spin quantum beats in GaAsBi

in transverse magnetic field is used to determine the electron g-factor value. The sign of g is determined by tilting the excitation beam and comparing the outcome to the GaAs polarization dynamics. We also show the dependence of electron spin relaxation dynamics in GaAsBi upon temperature.

5.3.1 Experimental determination of g-factor

Experimental conditions

In the experiment of this chapter, the sample was mounted in Voigt configuration in the TRPL setup (chapter 2). The exciting beam polarization (linear or circular) was set by means of a linear polarizer and a quarter-wave plate. An external continuous magnetic field was applied parallel to the sample layers (along the x axis), with a magnitude up to 0.73 T.

According to the optical selection rules in the bulk material, and assuming fast hole spin relaxation time [81], the degree of electron spin polarization P_e can be obtained from the luminescence circular polarization P_c, by measuring the intensity of the co-polarized (I^+) and counter-polarized (I^-) PL components as compared to the circular excitation polarization:

$$P_c = \frac{I^+ - I^-}{I^+ + I^-} \tag{5.1}$$

The sample and setup we used here for analyzing are the same as in section 5.2. When an external magnetic field B is applied, the precession of the electron spins around B leads to the beating of the photoluminescence polarization dynamics. The polarization quantum beat period yields the value of the electron Landé g-factor.

From previous investigations of the PL peak emission energy versus temperature presented in the section before, a deviation of the obtained values from the expected Varshni fit [200] is expected, especially at low excitation power densities (Figure 5.3(a)). This figure is attributed to localized states due to alloy disorder, cluster formation, and potential fluctuations, induced by Bi incorporation [193,201] and disappears when increasing the incident excitation power density due to the complete filling of the localized states. Above 100 K, band to band recombinations dominate. Hence, all the experiments were performed at 100K under 10 mW excitation and above in order first to eliminate any excitonic effect and second to avoid dominating localized carrier

recombinations.

Experimental measurement of g-factor value

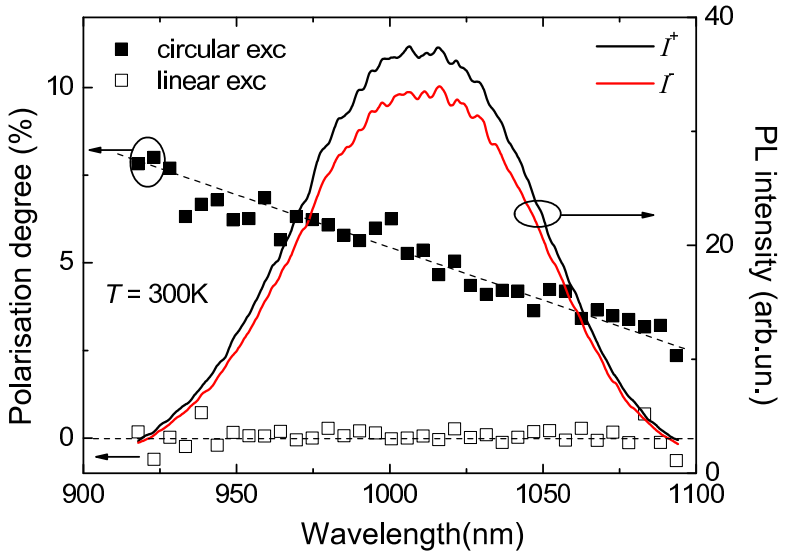

Figure 5.8: Co-polarized I^+ (black line) and counter-polarized I^- (red line) PL components, and related circular polarization degree (P_c) at room temperature under circular (black squares) or linear (hollow squares) excitation; dashed lines are guides to the eye.

Figure 5.8 shows the room temperature time integrated PL spectra measured under circular polarized excitation, in the co- and counter-polarized detection scheme. The excitation beam was incident perpendicular to the sample, with an estimated photogenerated electron density of $2 \times 10^{17} cm^{-3}$ in the GaAsBi layer. The PL peak wavelength is around 1010 nm, demonstrating the clear red-shift of the GaAsBi bandgap energy compared to the one of bulk GaAs. The copolarized PL intensity I^+ is stronger than the counterpolarized component I^-, implying a significantly different population of the spin states in the sample. The corresponding degree of circular polarization, Pc, is also plotted in the same graph [203]. P_c reaches the value of $5 \pm 0.4\%$ at the PL peak, and it increases up to $7 \pm 1.3\%$ in the high energy range of the PL spectrum due to shorter carrier lifetime at high energy. The same trend in the PL spectrum polarization was observed when varying the incident power density. We also obtained a similar degree of polarization when exciting below the GaAs bandgap ($\lambda_{exc} = 892nm$). However, exciting above yields to the light absorption in both GaAs and GaAsBi layers and to a larger photogenerated carrier density inducing a significant increase of the signal/noise ratio for a given photon fluence. In order to confirm that the measured P_c is indeed

related to the carrier spin polarization, we have performed the same experiment using a linear excitation beam. The corresponding polarization degree is also reported in Figure 5.8, where indeed no circular polarization signal is observed, as expected.

In order to make a direct determination of the electron Landé g-factor in the

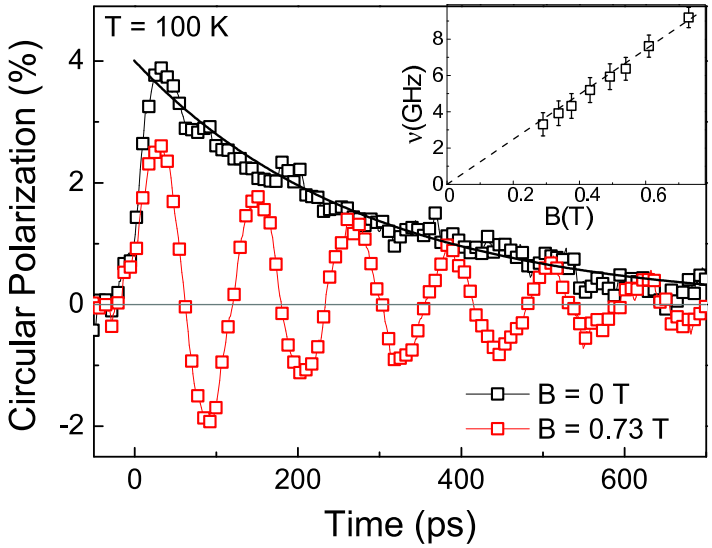

Figure 5.9: Time dependence of the PL circular polarization degree for B=0T (black hollow squares) and B=0.73T (red hollow squares) at T=100 K, the black exponential decay line is a guide to the eye. The inset shows the measured Larmor precession frequency $\mu = \Omega/2\pi$ as a function of the applied magnetic field.

GaAsBi epilayer, we have performed time resolved PL measurements under an external magnetic field. To get an accurate value of g, the measurement was repeated for several values of the applied magnetic field, ranging from 0 to 0.73 T. We have plotted in Figure 5.9 the time dependence of P_c at $T = 100K$ for $B = 0$ and $B = 0.73$ T. The spin relaxation time has been found to be the same whatever the detection wavelength is. Hence, the signal was integrated over the whole PL spectrum in order to increase the signal/noise ratio.

Without magnetic field ($B = 0$ T), we observe an exponential decay of P_c, which is linked to the electron spin relaxation time. The application of a transverse magnetic field adds an oscillating component to the exponential decay, caused by the Larmor precession of the electrons around the applied magnetic field B. The Larmor pulsation of the observed oscillations is simply related to the g-factor through the relation:

$$\Omega = \frac{g\mu_B}{\hbar} B \tag{5.2}$$

where μ_B is the Bohr magneton.

The inset in Figure 5.9 displays the linear variation of the measured precession frequency as a function of B.

The electron GaAsBi g-factor, calculated from the pulsation of the observed os-

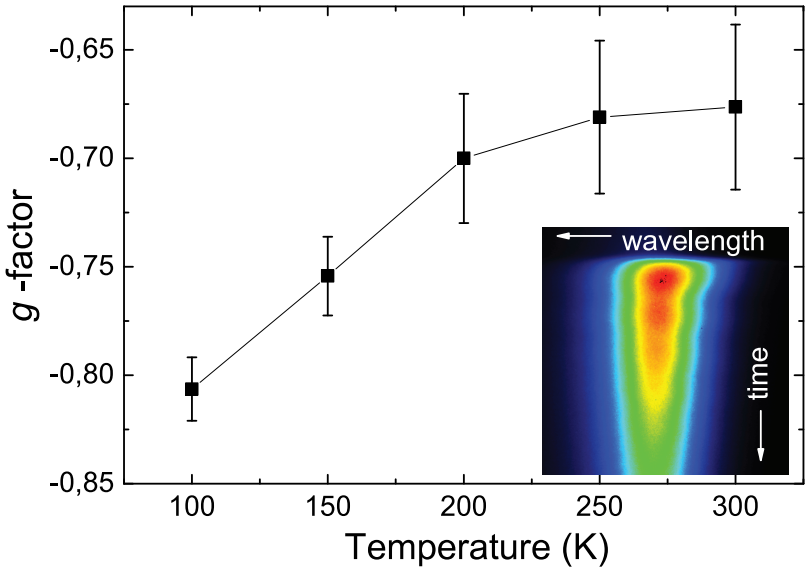

Figure 5.10: Measured electron g-factor in GaAsBi (black squares) as a function of lattice temperature with respective error bars, the line is a guide to the eye. The inset shows an example of acquired TRPL spectrum (I^+ component) with clear intensity oscillations appearing after the application of a transverse magnetic field of 0.73 T.

cillations in the presence of magnetic field using Eq. (5.1), is plotted as function of temperature in Figure 5.10. The choice for the negative sign of g is justified later in the text. An example of a streak camera image is shown in the inset of the same figure, displaying luminescence intensity oscillations after the application of the magnetic field.

Remarkably, the GaAsBi g-factor is almost twice the value of the one in GaAs, decreasing in absolute value from around 0.81 at 100K to 0.68 at room temperature. In order to confirm these results, g was also measured for the GaAs transition observed in the same sample at 100 and 200 K, obtaining 0.41 and 0.36, respectively. These GaAs values fit perfectly with those reported in the literature [204,205].

In a very simple approach, the electron g-factor can be approximated from the following expression [163]:

$$g = 2 - \frac{2}{3}\frac{E_P \Delta_{SO}}{E_g(E_g + \Delta_{SO})} \tag{5.3}$$

where E_P is the Kane energy, E_g the energy bandgap, and Δ_{SO} is the SO splitting energy.

By assuming $\Delta_{SO} = 0.445eV$ for our Bi concentration (compared to $\Delta_{SO} = 0.341eV$ in Bi-free GaAs), as previously reported in the literature [181,206], taking $E_P = 22.7eV$ [207] and extracting E_g from the PL spectrum (1.25 eV), we get $g = -1.18$ at 100K. This calculated value is certainly overestimated compared to the real g (There are two contributions to the temperature change of the optical gap, which are firstly due to lattice dilation arising from the fact that the ionic potential is anharmonic, and secondly the vibrational part. It is well known that the effective mass follows the dilational contribution only, since the vibrations occur on a much slower time scale than the time the electron takes to sample the interband interactions that determine the mass, which are at optical frequency. [204,208]) . However, it is in agreement with our finding that the absolute value of g increases with a small addition of Bi in GaAs, as the result of both increasing the spin-orbit energy and decreasing the bandgap energy.

Determination of the g-factor sign

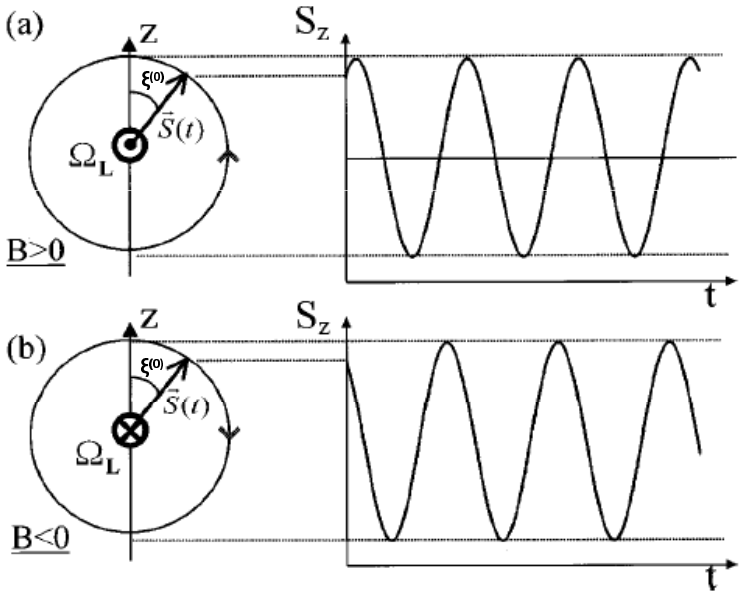

Figure 5.11: The principle of spin quantum-beat dephasing measurements. The sign of the dephasing between the +B and -B experiments allows one to determine the electron transverse Landé g factor sign. [17]

The principle of the experiment is sketched in Figure 5.11. When pumping under oblique incidence, the initial electron spin $\mathbf{S}^{(0)}$ is tilted with respect to the surface axis. The subsequent electron Larmor precession is determined by the rotation vector $\vec{\Omega_L} = g_\perp \mu_B \mathbf{B}/\hbar$, where $g_\perp$ is the transverse electron g factor, μ_B the Bohr magneton,

and **B** the transverse magnetic field, so that the spin projection S_z oscillates with a phase determined by the initial spin angle $\xi^{(0)}$. When the sign of **B** changes, the precession direction is reversed, leading to a phase change in S_z oscillations, inducing a phase shift in the PL polarization.

The measured temporal phase shift Δt between positive (+B) and negative (-B) external field is simply related to $\xi^{(0)}$ by [17]

$$\Delta t = 2\frac{\xi^{(0)}}{g\mu_B B} \tag{5.4}$$

By knowing the sign of g in GaAs [209], a comparison of the sign of Δt for the GaAs and GaAsBi transitions leads to the conclusion that the g-factor of GaAsBi is also negative.

The temporal shift Δt of the PL circular polarization for the GaAs and GaAsBi

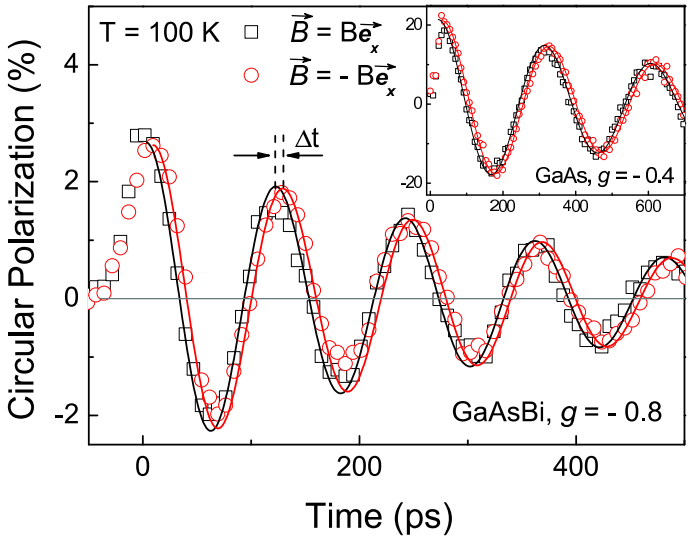

Figure 5.12: Luminescence polarization oscillations at T=100 K for the GaAsBi (main graph) and GaAs (inset) transitions, showing the temporal phase shift Δt between positive ($\mathbf{B}\overrightarrow{e_x}$, black hollow squares) and negative (-$\mathbf{B}\overrightarrow{e_x}$, red hollow circles) external magnetic field.

transitions, measured after changing the polarity of B, is clearly shown in Figure 5.12. The excitation angle was set at 70°, and the detection angle at 20°, leading to 10° internal angle difference. The lattice temperature was fixed at 100K in order to keep sufficiently robust signal for the determination of the polarization dephasing.

5.3.2 Analysis of spin relaxation time

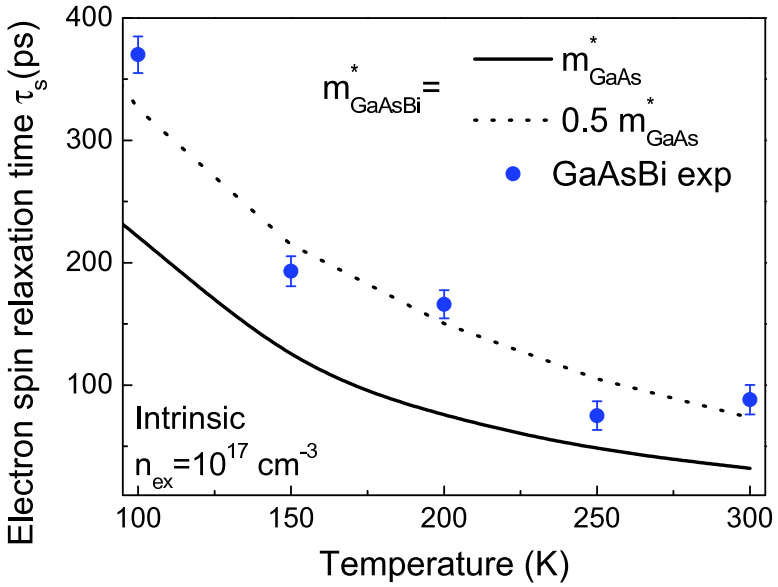

Figure 5.13: Experimentally measured electron spin relaxation time in intrinsic GaAsBi as a function of temperature (blue circles), plotted within the theoretically expected values calculated by Tong et. al. with a photo-electron density of $10^{17} cm^3$.

The electron spin relaxation time τ_s was also investigated as a function of temperature from 100 to 300K with an estimated photo-generated electron density of $2{\times}10^{17} cm^3$; the PL polarization dynamics has been simply fitted with a single exponential decay curve (at B=0T). Since the sample is unintentionally doped, the D'Yakonov-Perel relaxation mechanism [210] is expected to be the dominant mechanism in this temperature range [206], with the spin relaxation time strongly dependent upon the scattering mechanisms in the sample. The measured values of τ_s for GaAsBi are plotted in Figure 5.13 as blue circles. In this temperature range, the spin relaxation time decreased from 370 to 100 ps. At 100 K, we find a product $(g \cdot \tau_s)$ of 300 ps. This value is in good agreement with the value of 180 ps found by Pursley et al. [211] in similar experimental conditions on a $GaAs_{0.992}Bi_{0.008}$ epilayer.

Figure 5.13 shows also the theoretical results obtained by Tong et al. [206] in intrinsic $GaAs_{0.98}Bi_{0.02}$ with a photoelectron density of $10^{17} cm^3$ and assuming the same electron effective mass as GaAs (solid line) and 50% of the effective mass of GaAs (dotted line). Only two groups have investigated the GaAsBi electron effective mass, but they have reported opposite results. From magnetic field-dependent PL, Pettinari et al. [212] found that GaAsBi has a larger mass than GaAs, while Fluegel et al. [213] reported a lower mass in GaAsBi by means of Shubnikov-De Haas technique. Our ex-

perimental results are consistent with the curve corresponding to a Bi content of 2.2% and effective mass smaller than that of GaAs, possibly suggesting a decrease of the electron effective mass in GaAsBi as compared to GaAs. However, even though the experiments were conducted at temperatures and excitation densities at which localization effects should be negligible, the spin relaxation mechanisms can be slowed down by the trapping and detrapping dynamics associated with the localization centers, and may result in a slightly overestimated spin relaxation time as compared to free carriers, and consequently underestimated electron effective mass.

5.4 Conclusions and perspectives

In conclusion, we have investigated the photoluminescence peak position as a function of temperature, for an as-grown and an annealed GaAsBi epilayer containing 2.2% of bismuth. The as-grown sample photoluminescence intensity exhibits a s-shape behaviour when the temperature is raised from 10 K to room temperature. After annealing, while a slight increase of the time integrated photoluminescence intensity was only observed, a clear change in the energy peak position temperature dependence and in the time-resolved photoluminescence characteristics were measured. The s-shape is no longer present, the Arrhenius plot indicates a reduced number of defect types, and the carrier lifetime is shorter in the lower temperature range as compared to the as-grown sample. This shows that rapid thermal annealing leads in the dilute bismide layer to a reduction of the density and dispersion of the defects associated to localized states. On the contrary, the benefit on PL intensity is low, indicating that RTA performed on these MBE grown samples only cures a small density of non radiative defects.

We have also investigated the electron spin dynamics in bulk GaAsBi material, yielding the determination of the electron g-factor and spin relaxation time as function of temperature. We found that the g-factor is negative and almost twice the value in GaAs, ranging from -0.81 to -0.68 from 100 to 300 K. The electron spin relaxation time was also measured; we found that it is also affected by the Bi incorporation, decreasing from 370 to about 100 ps when the temperature is increased from 100 to 300K. These results are in good agreement with previous theoretical and experimental values obtained for similar ternary alloys [206,211]. They demonstrate that the spin properties

of GaAs can be drastically modified with the incorporation of a small percentage of Bi, as a result of increased spin-orbit interaction. This could open up possibilities such as spintronic devices based on Rashba spin-orbit interaction requiring lower modulation electric fields, thanks to the larger spin-orbit interaction as compared to GaAs [214].

Apart from spintronic applications, GaAsBi is of great interest because it allows both a reduction of the band gap energy, and an increase of the spin-orbit split-off energy. GaAsBi based materials, combined for instance to indium or nitrogen incorporation, may have the potential to cover a wide spectral range from near- to mid-infrared with flexible control of the band offsets and spin-orbit splitting. In particular, with a spin-orbit splitting energy larger than the band gap, the design of Auger and leakage free devices for long-wavelength device applications may be possible. However, these potential designs need deeper insights into the material band structure. In this view, we have started a collaboration with E. O'Reilly's group from the Tyndall Institute in Ireland. A refined model of g factor, based on tight-binding calculations, and taking strain into account, is under progress, and will be compared to experimental values determined by TRPL measurements in our group. This joint study should help understanding the nature of valence and conduction states, and give new materials for device modeling.

Conclusion and Perspectives

Among challenges in the field of semiconductor spintronics, one can cite electrical spin injection, transport, spin storage and manipulation, and spin current detection. This thesis is focused on two of these topics: electrical spin injection into III-V semiconductors for spin-optoelectronics applications and exploration of spin properties of the new material GaAsBi in view of manipulation of spin carriers.

Using SpinLEDs based on InGaAs quantum wells, we have analysed the influence of the growth technique (Molecular Beam Epitaxy or Sputtering) of the MgO layer on the efficiency of the spin injection process. Combined analysis of polarization-resolved electroluminescence with time-resolved photoluminescence (TRPL), transmission electron microscopy (TEM) and superconducting quantum interference device (SQUID) measurements, lead to the conclusion that the control of the quality of the CoFeB/MgO interface is more important than the one of the MgO/GaAs interface for an optimal spin injection. A systematic study of the impact of the post-annealing temperature of the injector is also performed for the two types of samples. Both show the same trend: an increase of the EL circular polarization (P_C) when the annealing temperature T_{AN} increases, with an optimized temperature in the range 300-350$°C$. We attribute this behavior mainly to the improvement of the chemical structure at the top CoFeB/MgO interface. The current dependence of the electrical spin injection is also investigated for samples prepared by the two growth techniques. We demonstrate that the electroluminescence circular polarization is very stable as a function of the injected current for sputtered tunnel barriers, whereas this polarization decreases abruptly when the current increases for tunnel barriers grown by Molecular Beam Epitaxy. We attribute this behavior to the MgO/GaAs interface that presents specific characteristics depending on the growth method. It appears that in view of future applications, spinLEDs with sputtered tunnel barriers present the best compromise between high electrolumi-

nescence circular polarization and high electroluminescence intensity. Finally we have demonstrated a very efficient electrical spin injection without any external magnetic field using an ultrathin (a few monolayers) CoFeB injector that presents Perpendicular Magnetic Anisotropy (PMA). The EL circular polarization rate P_C can reach values as large as 20% at 25 K, which is more than six times the values obtained with usual multilayer PMA injectors [35] up to now. A significant P_C ($\sim$8%) is conserved at room temperature. A systematic study of P_C as a function of temperature leads to the conclusion that the injection is stable with temperature and that the variation of P_C are due to variation of the electron lifetime and spin relaxation times within the quantum well.

In the future we plan to include this new injector into the cavity of a Vertical External Cavity Surface Emitting Lasers (VECSELs) to generate coherent circularly polarized light [215], as it was demonstrated in Spin Vertical Cavity Surface Emitting Lasers [28] (where a reduction of the threshold current has been observed). From an optical point of view, these spin VECSELS would present certain advantages compared to Spin VCSELS as high power, high spatial and temporal coherence, wavelength flexibility, and longitudinal multi- or monomode operation. From the point of view of spintronics, it will allow to deposit the ferromagnetic spin injector as close as possible to the emitting quantum well (contrary to spinVCSELS [28]), maximizing the spin polarization degree of the electrically injected electrons. As the magnetic injector has to be embedded inside the optical cavity, the light absorption by the injector becomes a critical point because the corresponding intracavity loss can easily prevent the laser regime. Only an ultrathin injector as we proposed here should be employed, ruling out the use of thick multilayers PMA injectors. In this purpose, let's note that the typical absorption coefficient of Co/Pt (7nm) multilayers integrated in spin-LEDs is about 30% in the infrared spectra [151] which clearly prevents, for instance, any laser operation in cavity VECSELs. On the other hand, the absorption at the same wavelength within a 1.2 nm CoFeB layer has been measured to be less than 3% [151] which is compatible with VECSELs operation.

A second very important functionality would be to be able to electrically switch the helicity of the light. It requires the switching of the electron spin between up and down states by switching the magnetization of the ferromagnetic layer. This could be

accomplished by Spin Transfer Torque (STT) effect with an additional spin polarized control current flowing through the injector. The ultrathin CoFeB PMA layers are now considered as the most promising electrodes for STT operations in MRAM technology, because they satisfy (i) high thermal stability at reduced dimension, (ii) low current induced magnetization switching and (iii) high spin polarization at the same time. Obviously, this type of injector is also the best candidate for electrical control of circularly polarized light via STT for devices operating at room temperature without magnetic field. It constitutes the final target of the French-Chinese ANR-NSFC SISTER (electrical control of Spin Injection in Spin-LEDs via spin TransfER effect without magnetic field) project involving IJL Nancy, UMP-CNRS Thalès Palaiseau, Institute of Physics (IOP) and Institute of Semiconductors (IOS) in Beijing, and LPCNO (Toulouse).

From a fundamental point of view, a deeper understanding of the spin injection process would take benefits from the calculations of density of surface states at CoFeB/MgO and MgO/GaAs interfaces by ab-initio calculations, as it was done for Magnetic Tunnel Junction (MJ) magnetic junction based on Fe/MgO/Fe [10] and CoFe/MgO/CoFe [88]. The question of the existence of the spin filtering effect (that is to say a non equivalent attenuation of the evanescent wavefunctions for the two spin species) across the MgO crystalline tunnel barriers, that was evidenced in these MTJ junctions by theoretical DFT (Density Functional Theory), is still open in Fe (CoFeB)/MgO/(Al)GaAs system, and full calculations have still to be done.

In a second part, we have explored the electron spin properties in the L valleys in GaAs, by polarisation-resolved Photoluminescence Excitation (PLE) spectroscopy in the blue range. These high energy electrons might play an important role in devices based on spin transport (as for example, if one wants to observe the recently predicted spin Gunn effect) as well as in devices where electrical spin injection of high kinetic energy electrons occurs. We demonstrate that a significant fraction of the electron spin memory can be conserved when the electron is scattered from the L to the Γ valley despite an energy relaxation of several hundreds of meV. The dependence of the circular polarization rate measured in Γ as a function of the laser energy is in good agreement with LDA and $k \cdot p$ calculations. Combining high energy photoexcitation experiments under transverse magnetic field (Hanle curves) with time-resolved photoluminescence spectroscopy of Γ valley spin-polarized photogenerated electrons allows

us to deduce a typical L-valley electron spin relaxation time of 200 fs, in agreement with theoretical calculations (large spin splitting of conduction bands responsible for efficient D'Yakonov-Perel mechanism are expected for these valleys).

GaAs that has been widely explored from the point of view of spin properties by optical means due to its direct bandgap can be seen as a model system to explore spin properties in L or X valleys. This work could be a preliminary step in view of future explorations of spin polarizations and spin relaxation times in type IV materials as Silicium where such valleys play a crucial role. On could imagine to excite Silicium at the direct gap with circularly polarized light and try either to detect (and resolve in polarization) the luminescence at the direct gap with CW high sensitivity experiments, either to time (and polarization)-resolve with a triggered streak camera the luminescence emission at the indirect bandgap after the ultra-fast relaxation of carriers from Γ to X valley. In the former case it would give informations on the spin polarization of the photogenerated electrons at the Γ point. In the latter it would allow to measure the electron spin relaxation time in the X valley. These experiment remain very challenging in particular in the former case due to the very fast departure of electrons from Γ to X valley that drastically limits the number of photons emitted at the direct gap (note that the excitation wavelength range is also very restricted in order to perform optical orientation due to the weak spin orbit system in this system).

In the last part, GaAsBi alloy is explored for its potential applications in spintronic, photovoltaic and optical telecommunication fields. In a first step we study the dependence of photoluminescence intensity and decay time upon temperature and excitation power density. GaAsBi shows strong localization effects, due to Bi cluster states and alloy disorder. Optical characterization after rapid thermal annealing evidences that disorder can be partly cured, as well as non radiative recombination processes. In a second step, the spin properties of GaAsBi are explored as their investigation constitutes an interesting way to probe the electronic properties of this material. The introduction of Bismuth into GaAs strongly modifies the band structure, not only in the valence band, but also in the conduction band. The electron spin relaxation time is measured by polarization-resolved TPRL and suggests a diminution of the effective mass of conduction electrons. The measurement of Landé g factor is performed by TRPL under transverse magnetic field by analysing the period of spin quantum beats

as a function of magnetic field. A significant increase of the Lande g factor compared to the one of GaAs is observed, due to the decrease of the bandgap and the increase of the spin–orbit interaction in GaAsBi. Note that large g-factors and strong spin orbit coupling could present an interest for spin manipulation by external magnetic field and electric field respectively. Moreover, both increase of the spin-orbit energy and decrease of bandgap energy are of interest for optoelectronic applications. Indeed, taking advantage of the band gap reduction could allow to reach the 1.3-1.55 μm wavelength range. In addition, the increase of energy separation between the spin-orbit split-off band and the valence band edge could lead to the suppression of IVBA or Auger recombination loss mechanisms. Further investigations of the influence of the composition of Bi in GaAsBi are schedules in order to have a deeper understanding of these modifications, and to be able to tune the optical properties of this material that could present also a potential interest for Photovoltaic and optical telecommunications applications. A collaboration with the group of E. O'Reilly's group from Tyndall Institute, Ireland, has been initiated. A refined model of g factor, based on tight-binding calculations, and taking strain into account, is under progress, and will be compared to experimental values determines by TRPL measurement in our group. This joint study should help understanding the nature of valence and conduction states, and give new material for device modeling.

From a more general point of view, lots of advances have been realized in the field of semiconductor spintronics since the end of the 90's. The electrical spin injection from a ferromagnetic metal into a semiconductor has now been demonstrated by different experimental teams all over the world. In contrast to spin injectors based on diluted magnetic semiconductor, the spin injection is possible at room temperature. One of the main challenges remains to get a full electrical device where both spin injection and spin detection are performed in an electrical way. In this geometry, electrical signal measured are of the order of a few μV up to now [216]. The strategy of non-local geometry, in order to avoid electric parasitic signals due to charge currents instead of spin currents, has been adopted [78,79]. Using this non-local measurement technique, a device called "'field effect spin transistor"' was demonstrated in 2009 at low temperature by M. Johnson and co-workers [217]. The authors have shown that the outpout electrical signal can be modulated by a gate voltage. Their realization is close

to the Datta and Das spin transistor [26], where the electron precession speed due to the Rashba effective magnetic field can be tuned by the applied gate voltage (in the ballistic regime). Moreover, materials with unexplored spin properties have been studied, as for examples single carbon nanotubes in the lateral channel-based geometry devices [218]. Let us mention that spintronics in Silicium and Germanium is nowadays under strong investigation [31,97,152,219,220]. These materials present in particular the advantage to be widely used in the field of conventional microelectronics. In the future, electrical spin injection based on bi-dimensional materials as Graphene [98] or MoS_2 [221], for which the exploration of spin properties has just started [222] could lead to new advances. To finish with, the challenge of detecting a spin polarized photo-generated current (symmetrical to the one encountered in spin-LEDs) has been much less studied than the electrical spin injection problem [107,223–225]. Further investigations (both from theoretical and experimental point of view) are required to get a deeper understanding of the key mechanisms responsible for the spin filtering by the magnetic electrode when electron cross the interface from the semiconductor to the metal). It would help to improve the contrast of photocurrent when the helicity of the light is changed that is still around a few percent.

Bibliography

[1] Gerald Bastard. *Wave mechanics applied to semiconductor heterostructures*. Les Edition de Physique, second edition, 1992.

[2] Johnathan Genest. *Quantum well intermixing controlled by excimer laser for photonic device integration*. PhD thesis, Universite de SherBrooke, 2008.

[3] Jaspit Singh. *Electronic and Optoelectronic Properties of Semiconductor Nanostructures*. Cambridge University Press, 2003.

[4] M. Idrish Miah. Injection and detection of spin current and spin Hall effect in GaAs. *Material Letters*, 60:2863–2866, 2006.

[5] A Fert, J-M George, H Jaffres, and R Mattana. Semiconductors between spin-polarized sources and drains. *Electron Devices, IEEE Transactions on*, 54(5):921–932, 2007.

[6] H. Jaffrès, Electrical spin injection and spin detection, Summer school, Cargèse, June 2005.

[7] A. Fert and H. Jaffrès. Conditions for efficient spin injection from a ferromagnetic metal into a semiconductor. *Phys. Rev. B*, 64:184420, Oct 2001.

[8] S. Liang, private communication.

[9] X. Jiang, R. Wang, R. M. Shelby, R. M. Macfarlane, S. R. Bank, J. S. Harris, and S. S. P. Parkin. Highly Spin-Polarized Room-Temperature Tunnel Injector for Semiconductor Spintronics using MgO(100). *Phys. Rev. Lett.*, 94:056601, Feb 2005.

[10] W. H. Butler, X.-G. Zhang, T. C. Schulthess, and J. M. MacLaren. Spin-dependent tunneling conductance of Fe—MgO—Fe sandwiches. *Phys. Rev. B*, 63:054416, Jan 2001.

[11] Daniel T. Pierce and Felix Meier. Photoemission of spin-polarized electrons from GaAs. *Phys. Rev. B*, 13:5484–5500, Jun 1976.

[12] D. L. Greenaway. Fundamental Reflectivity of GaAs at Low Temperature. *Phys. Rev. Lett.*, 9:97–98, Aug 1962.

[13] A. I. Ekimov and V. I. Safarov. Zh. Eksp. Teor. Fiz. Pisma Red. . *JETP Lett.*, 13:177–179, 1971.

[14] H.-J. Drouhin, C. Hermann, and G. Lampel. Photoemission from activated gallium arsenide. II. Spin polarization versus kinetic energy analysis. *Phys. Rev. B*, 31:3872–3886, Mar 1985.

[15] K. Alberi, J. Wu, W. Walukiewicz, K. M. Yu, O. D. Dubon, S. P. Watkins, C. X. Wang, X. Liu, Y.-J. Cho, and J. Furdyna. Valence-band anticrossing in mismatched III-V semiconductor alloys. *Phys. Rev. B*, 75:045203, Jan 2007.

[16] K. Alberi, O. D. Dubon, W. Walukiewicz, K. M. Yu, K. Bertulis, and A. Krotkus. Valence band anticrossing in $GaBi_xAs_{1-x}$. *Applied Physics Letters*, 91(5):051909, 2007.

[17] X. Marie, T. Amand, J. Barrau, P. Renucci, P. Lejeune, and V. K. Kalevich. Electron-spin quantum-beat dephasing in quantum wells as a probe of the hole band structure. *Phys. Rev. B*, 61:11065–11077, Apr 2000.

[18] Gary A Prinz. Magnetoelectronics. *Science*, 282(5394):1660–1663, 1998.

[19] Mario Norberto Baibich, JM Broto, Albert Fert, F Nguyen Van Dau, F Petroff, P Etienne, G Creuzet, A Friederich, and J Chazelas. Giant magnetoresistance of (001) Fe/(001) Cr magnetic superlattices. *Physical Review Letters*, 61(21):2472, 1988.

[20] Grünberg Binasch, Peter Grünberg, F Saurenbach, and W Zinn. Enhanced magnetoresistance in layered magnetic structures with antiferromagnetic interlayer exchange. *Physical review B*, 39:4828–4830, 1989.

[21] G. Lampel. Nuclear dynamic polarization by optical electronic saturation and optical pumping in semiconductors. *Phys. Rev. Lett.*, 20:491–493, Mar 1968.

[22] F. Meier and B. P. Zakharchenya. *Optical Orientation*. North-Holland Physics Publishing, 1984.

[23] D Hägele, M Oestreich, WW Rühle, N Nestle, and K Eberl. Spin transport in GaAs. *Applied physics letters*, 73(11):1580–1582, 1998.

[24] JM Kikkawa and DD Awschalom. Lateral drag of spin coherence in gallium arsenide. *Nature*, 397(6715):139–141, 1999.

[25] Hideo Ohno. Making nonmagnetic semiconductors ferromagnetic. *science*, 281(5379):951–956, 1998.

[26] Supriyo Datta and Biswajit Das. Electronic analog of the electrooptic modulator. *Applied Physics Letters*, 56(7):665–667, 1990.

[27] R. Fiederling, M. Keim, G. Reuscher, W. Ossau, G. Schmidt, A. Waag, and L. W. Molenkamp. Injection and detection of a spin-polarized current in a light-emitting diode. *Nature*, 402:787–790, 1999.

[28] M. Holub, J. Shin, D. Saha, and P. Bhattacharya. Electrical spin injection and threshold reduction in a semiconductor laser. *Phys. Rev. Lett.*, 98:146603, Apr 2007.

[29] Prashant Sharma. How to create a spin current. *Science*, 307(5709):531–533, 2005.

[30] Daniel Loss and David P DiVincenzo. Quantum computation with quantum dots. *Physical Review A*, 57(1):120, 1998.

[31] Saroj P Dash, Sandeep Sharma, Ram S Patel, Michel P de Jong, and Ron Jansen. Electrical creation of spin polarization in silicon at room temperature. *Nature*, 462(7272):491–494, 2009.

[32] A Jain, J-C Rojas-Sanchez, M Cubukcu, J Peiro, JC Le Breton, E Prestat, C Vergnaud, L Louahadj, C Portemont, C Ducruet, et al. Crossover from spin

accumulation into interface states to spin injection in the germanium conduction band. *Physical review letters*, 109(10):106603, 2012.

[33] H. J. Zhu, M. Ramsteiner, H. Kostial, M. Wassermeier, H.-P. Schönherr, and K. H. Ploog. Room-Temperature Spin Injection from Fe into GaAs. *Phys. Rev. Lett.*, 87:016601, Jun 2001.

[34] A. T. Hanbicki, O. M. J. van 't Erve, R. Magno, G. Kioseoglou, C. H. Li, B. T. Jonker, G. Itskos, R. Mallory, M. Yasar, and A. Petrou. Analysis of the transport process providing spin injection through an Fe/AlGaAs Schottky barrier. *Applied Physics Letters*, 82(23):4092–4094, 2003.

[35] J. Zarpellon, H. Jaffrès, J. Frougier, C. Deranlot, J. M. George, D. H. Mosca, A. Lemaˆ, F. Freimuth, Quang Ha Duong, P. Renucci, and X. Marie. Spin injection at remanence into III-V spin light-emitting diodes using (Co/Pt) ferromagnetic injectors. *Phys. Rev. B*, 86:205314, Nov 2012.

[36] Yunong Qi, Zhi-Gang Yu, and Michael E. Flatté. Spin gunn effect. *Phys. Rev. Lett.*, 96:026602, Jan 2006.

[37] R. Mallory, M. Yasar, G. Itskos, A. Petrou, G. Kioseoglou, A. T. Hanbicki, C. H. Li, O. M. J. van't Erve, B. T. Jonker, M. Shen, and S. Saikin. Phonon-assisted recombination in fe-based spin leds. *Phys. Rev. B*, 73:115308, Mar 2006.

[38] J. M. Jancu, R. Scholz, G. C. La Rocca, E. A. de Andrada e Silva, and P. Voisin. Giant spin splittings in GaSb/AlSb L-valley quantum wells. *Phys. Rev. B*, 70:121306, Sep 2004.

[39] J. M. Luttinger and W. Kohn. Motions of electrons and holes in pertubed periodic fields. *Physical Review*, 97(4):869–883, 1955.

[40] J. M. Luttinger. Quantum theory of cyclotron resonance in semiconductors: General theory. *Physical Review*, 102(4):1030–1041, 1956.

[41] Per-Olov Lowdin. Studies in Pertubation Theory IV: Solution of Eigenvalue Problem by Projection Operator Formalism. *Journal of Mathematical Physics*, 3(5):969–982, 1962.

[42] T. Ando. Hole Subband at GaAs/AlGaAs Heterojunctions and Quantum Wells. *Journal of the Physical Society of Japan*, 54(4):1528–1536, 1985.

[43] Peter Yu and Cardona Manuel. *Fundamentals of Semiconductors: Physics and Materials Properties*. Springer, forth edition, 2010.

[44] QHF Vrehen. Interband magneto-optical absorption in gallium arsenide. *Journal of Physics and Chemistry of Solids*, 29(1):129–141, 1968.

[45] J. Tersoff. Theory of semiconductor heterojunctions : The role of quantum dipoles. *Physical Review B*, 30(8):4874–4877, 1984.

[46] B. R. Nag. *Physics of Quantum Well Devices*. Kluwer Academic Publisher, 2000.

[47] Omar Manasreh. *Semiconductor Heterojunctions and Nanostructures*. McGraw-Hill, 2005.

[48] Benjamin Lax Laura M.Roth and Solomon Zwerdling. Theory of optical magneto-absorption effects in semiconductors. *Physical Review*, 114(1):90–104, 1959.

[49] G.Dresselhaus M.S.Dresselhaus and A.Jorio. *Group Theory : Application for Condensed Matter Physics*. Springer, 2008.

[50] I. Zutic, J. Fabian, and S. Das Sarma. Spintronics: Fundamentals and applications. *Reviews of Modern Physics*, 76:323–410, 2004.

[51] M. I. D'Yakonov and V. I. Perel. Spin orientation of electrons associated with the interband absorption of light in semiconductors. *Soviet Journal of Experimental and Theoretical Physics*, 33:1053, 1971.

[52] G. Dresselhaus. Spin-orbit coupling effects in zinc blende structures. *Phys. Rev.*, 100:580, 1955.

[53] M. I. Dyakonov. Introduction to spin physics in semiconductors. *Physica E-Low-Dimensional Systems Nanostructures*, 35:246–250, 2006.

[54] R. J. Elliott. Theory of the effect of spin-orbit coupling on magnetic resonance in some semiconductors. *Phys. Rev.*, 100:266, 1954.

[55] G. L. Bir, A. G. Aronov, and G. E. Pikus. Spin relaxation of electrons due to scattering by holes. *Sov. Phys. JETP*, 42:705, 1975.

[56] M. J. Maialle, E. A. de Andrada e Silva, and L. J. Sham. Exciton spin dynamics in quantum wells. *Phys. Rev. B*, 47:15776, 1993.

[57] Atsushi Tackeuchi, Shunichi Muto, Tsuguo Inata, and Toshio Fujii. Direct observation of picosecond spin relaxation of excitons in GaAs/AlGaAs quantum wells using spindependent optical nonlinearity. *Applied Physics Letters*, 56(22):2213–2215, 1990.

[58] TC Damen, Juis Vina, JE Cunningham, Jagdeep Shah, and LJ Sham. Subpicosecond spin relaxation dynamics of excitons and free carriers in GaAs quantum wells. *Physical review letters*, 67(24):3432–3435, 1991.

[59] S. Bar-Ad and I. Bar-Joseph. Exciton spin dynamics in GaAs Heterostructures. *Physical Review Letters*, 68(3):349–352, 1992.

[60] L Munoz, E Pérez, L Vina, and K Ploog. Spin relaxation in intrinsic GaAs quantum wells: Influence of excitonic localization. *Physical Review B*, 51(7):4247, 1995.

[61] Y. K. Kato, R. C. Myers, A. C. Gossard, and D. D. Awschalom. Observation of the spin hall effect in semiconductors. *Science*, 306(5703):1910–1913, 2004.

[62] Jean-Christophe Le Breton, Sandeep Sharma, Hidekazu Saito, Shinji Yuasa, and Ron Jansen. Thermal spin current from a ferromagnet to silicon by Seebeck spin tunnelling. *Nature*, 475(7354):82–85, 2011.

[63] K. Ando, S. Takahashi, J. Ieda, H. Kurebayashi, T. Trypiniotis, C. H. W. Barnes, S. Maekawa, and E. Saitoh. Electrically tunable spin injector free from the impedance mismatch problem. *Nature*, 10(9):655–659, 2011.

[64] Y. Ohno, D. K. Young, B. Beschoten, F. Matsukura, H. Ohno, and D. D. Awschalom. Electrical spin injection in a ferromagnetic semiconductor heterostructure. *Nature*, 402:790–792, 1999.

[65] A. T. Hanbicki, B. T. Jonker, G. Itskos, G. Kioseoglou, and A. Petrou. Efficient electrical spin injection from a magnetic metal/tunnel barrier contact into a semiconductor. *Applied Physics Letters*, 80(7):1240–1242, 2002.

[66] Berend T. Jonker, George Kioseoglou, Aubrey T. Hanbicki, Connie H. Li, and Phillip E. Thompson. Electrical spin-injection into silicon from a ferromagnetic metal/tunnel barrier contact. *Nat Phys*, 3:542–546, 2007.

[67] Pol Van Dorpe, Z Liu, Willem Van Roy, VF Motsnyi, M Sawicki, Gustaaf Borghs, and J De Boeck. Very high spin polarization in GaAs by injection from a (Ga, Mn)As Zener diode. *Applied physics letters*, 84(18):3495–3497, 2004.

[68] P. Renucci, H. Jaffrès, J.M. George, T. Amand, X. Marie, Chapter. Electrical spin injection in hybrid ferromagnetic metal/semiconductor structures and in Spin-Light emitting Diodes, in "Spintronic semiconductors" edited by W. Chen and I. Buyanova, Pan Stanford Publishing - World Scientific 2009.

[69] T Valet and A Fert. Theory of the perpendicular magnetoresistance in magnetic multilayers. *Physical Review B*, 48(10):7099, 1993.

[70] G. Schmidt, D. Ferrand, L. W. Molenkamp, A. T. Filip, and B. J. van Wees. Fundamental obstacle for electrical spin injection from a ferromagnetic metal into a diffusive semiconductor. *Phys. Rev. B*, 62:R4790–R4793, Aug 2000.

[71] NF Mott. The resistance and thermoelectric properties of the transition metals. *Proceedings of the Royal Society of London. Series A-Mathematical and Physical Sciences*, 156(888):368–382, 1936.

[72] EI Rashba. Theory of electrical spin injection: Tunnel contacts as a solution of the conductivity mismatch problem. *Physical Review B*, 62(24):R16267, 2000.

[73] D. L. Smith and R. N. Silver. Electrical spin injection into semiconductors. *Phys. Rev. B*, 64:045323, Jul 2001.

[74] V. F. Motsnyi, J. De Boeck, J. Das, W. Van Roy, G. Borghs, E. Goovaerts, and V. I. Safarov. Electrical spin injection in a ferromagnet/tunnel barrier/semiconductor heterostructure. *Applied Physics Letters*, 81(2):265–267, 2002.

[75] OMJ van t Erve, G Kioseoglou, AT Hanbicki, CH Li, BT Jonker, R Mallory, M Yasar, and A Petrou. Comparison of Fe/Schottky and Fe/Al_2O_3 tunnel barrier contacts for electrical spin injection into GaAs. *Applied Physics Letters*, 84(21):4334–4336, 2004.

[76] H. Saito, J. C. Le Breton, V. Zayets, Y. Mineno, S. Yuasa, and K. Ando. Efficient spin injection into semiconductor from an Fe/GaOx tunnel injector. *Applied Physics Letters*, 96(1):–, 2010.

[77] S. A. Crooker, M. Furis, X. Lou, C. Adelmann, D. L. Smith, C. J. Palmstrøm, and P. A. Crowell. Imaging Spin Transport in Lateral Ferromagnet/Semiconductor Structures. *Science*, 309(5744):2191–2195, 2005.

[78] Xiaohua Lou, Christoph Adelmann, Scott A. Crooker, Eric S. Garlid, Jianjie Zhang, K. S. Madhukar Reddy, Soren D. Flexner, Chris J. Palmstrom, and Paul A. Crowell. Electrical detection of spin transport in lateral ferromagnet-semiconductor devices. *Nat Phys*, 3(3):197–202, 2007.

[79] M Tran, H Jaffrès, C Deranlot, J-M George, A Fert, A Miard, and A Lemaître. Enhancement of the spin accumulation at the interface between a spin-polarized tunnel junction and a semiconductor. *Physical review letters*, 102(3):036601, 2009.

[80] AG Aronov and GE Pikus. Spin injection into semiconductors. *Soviet Physics Semiconductors-Ussr*, 10(6):698–700, 1976.

[81] M. Dyakonov. *Spin Physics in Semiconductors*. Springer, New York, 2008.

[82] G. Salis, R. Wang, X. Jiang, R. M. Shelby, S. S. P. Parkin, S. R. Bank, and J. S. Harris. Temperature independence of the spin-injection efficiency of a MgO-based tunnel spin injector. *Applied Physics Letters*, 87(26):262503, 2005.

[83] C. Adelmann, X. Lou, J. Strand, C. J. Palmstrøm, and P. A. Crowell. Spin injection and relaxation in ferromagnet-semiconductor heterostructures. *Phys. Rev. B*, 71:121301, Mar 2005.

[84] M. C. Hickey, C. D. Damsgaard, I. Farrer, S. N. Holmes, A. Husmann, J. B. Hansen, C. S. Jacobsen, D. A. Ritchie, R. F. Lee, G. A. C. Jones, and M. Pepper.

Spin injection between epitaxial $Co_{2.4}Mn_{1.6}Ga$ and an InGaAs quantum well. *Applied Physics Letters*, 86(25):252106, 2005.

[85] E. D. Fraser, S. Hegde, L. Schweidenback, A. H. Russ, A. Petrou, H. Luo, and G. Kioseoglou. Efficient electron spin injection in MnAs-based spin-light-emitting-diodes up to room temperature. *Applied Physics Letters*, 97(4):041103, 2010.

[86] X.-G. Zhang and W. H. Butler. Large magnetoresistance in bcc Co/MgO/Co and FeCo/MgO/FeCo tunnel junctions. *Phys. Rev. B*, 70:172407, Nov 2004.

[87] Stuart S. P. Parkin, Christian Kaiser, Alex Panchula, Philip M. Rice, Brian Hughes, Mahesh Samant, and See-Hun Yang. Giant tunnelling magnetoresistance at room temperature with MgO (100) tunnel barriers. *Nat Mater*, 3(1476-1122):862–867, 2004.

[88] F. Bonell, T. Hauet, S. Andrieu, F. Bertran, P. Le Fèvre, L. Calmels, A. Tejeda, F. Montaigne, B. Warot-Fonrose, B. Belhadji, A. Nicolaou, and A. Taleb-Ibrahimi. Spin-Polarized Electron Tunneling in bcc FeCo/MgO/FeCo (001) Magnetic Tunnel Junctions. *Phys. Rev. Lett.*, 108:176602, Apr 2012.

[89] S. Ikeda, J. Hayakawa, Y. Ashizawa, Y. M. Lee, K. Miura, H. Hasegawa, M. Tsunoda, F. Matsukura, and H. Ohno. Tunnel magnetoresistance of 604% at 300K by suppression of Ta diffusion in CoFeB/MgO/CoFeB pseudo-spin-valves annealed at high temperature. *Applied Physics Letters*, 93(8), 2008.

[90] Y. Lu, V. G. Truong, P. Renucci, M. Tran, H. Jaffrès, C. Deranlot, J.-M. George, A. Lemaître, Y. Zheng, D. Demaille, P.-H. Binh, T. Amand, and X. Marie. Mgo thickness dependence of spin injection efficiency in spin-light emitting diodes. *Applied Physics Letters*, 93(15):152102, 2008.

[91] G Itskos, E Harbord, SK Clowes, E Clarke, LF Cohen, R Murray, Pol Van Dorpe, and W Van Roy. Oblique Hanle measurements of InAs/GaAs quantum dot spin-light emitting diodes. *Applied physics letters*, 88(2):022113–022113, 2006.

[92] L. Lombez, P. Renucci, P. F. Braun, H. Carrère, X. Marie, T. Amand, B. Urbaszek, J. L. Gauffier, P. Gallo, T. Camps, A. Arnoult, C. Fontaine, C. Deranlot,

R. Mattana, H. Jaffrès, J.-M. George, and P. H. Binh. Electrical spin injection into p-doped quantum dots through a tunnel barrier. *Applied Physics Letters*, 90(8):081111, 2007.

[93] W Löffler, M Hetterich, C Mauser, S Li, T Passow, and H Kalt. Parallel preparation of highly spin-polarized electrons in single InAs/GaAs quantum dots. *Applied physics letters*, 90(23):232105, 2007.

[94] V. G. Truong, P.-H. Binh, P. Renucci, M. Tran, Y. Lu, H. Jaffrès, J.-M. George, C. Deranlot, A. Lemaître, T. Amand, and X. Marie. High speed pulsed electrical spin injection in spin-light emitting diode. *Applied Physics Letters*, 94(14):–, 2009.

[95] Pablo Asshoff, Wolfgang Löffler, Jochen Zimmer, Heiko Füser, Harald Flügge, Heinz Kalt, and Michael Hetterich. Spin-polarization dynamics in InGaAs quantum dots during pulsed electrical spin-injection. *Applied Physics Letters*, 95(20):–, 2009.

[96] S. Hövel, N. C. Gerhardt, M. R. Hofmann, F.-Y. Lo, A. Ludwig, D. Reuter, A. D. Wieck, E. Schuster, H. Wende, W. Keune, O. Petracic, and K. Westerholt. Room temperature electrical spin injection in remanence. *Applied Physics Letters*, 93(2):021117, 2008.

[97] L. Grenet, M. Jamet, P. Noé, V. Calvo, J.-M. Hartmann, L. E. Nistor, B. Rodmacq, S. Auffret, P. Warin, and Y. Samson. Spin injection in silicon at zero magnetic field. *Applied Physics Letters*, 94(3):032502, 2009.

[98] OMJ Van't Erve, AL Friedman, E Cobas, CH Li, JT Robinson, and BT Jonker. Low-resistance spin injection into silicon using graphene tunnel barriers. *Nature nanotechnology*, 7(11):737–742, 2012.

[99] En-Shao Liu, Junghyo Nah, Kamran M Varahramyan, and Emanuel Tutuc. Lateral spin injection in germanium nanowires. *Nano letters*, 10(9):3297–3301, 2010.

[100] C. Rullière. *Femtosecond Laser Pulses, Principle and Experiments*. Springer, 1998.

[101] R. Fiederling, M. Keim, G. Reuscher, W. Ossau, G. Schmidt, A. Waag, and L. W. Molenkamp. Injection and detection of a spin-polarized current in a light-emitting diode. *Nature*, 402:787–790, Dec 1999.

[102] C. Adelmann, J. L. Hilton, B. D. Schultz, S. McKernan, C. J. Palmstrøm, X. Lou, H.-S. Chiang, and P. A. Crowell. Spin injection from perpendicular magnetized ferromagnetic δ-MnGa into (Al,Ga)As heterostructures. *Applied Physics Letters*, 89(11):112511, 2006.

[103] R. Wang, X. Jiang, R. M. Shelby, R. M. Macfarlane, S. S. P. Parkin, S. R. Bank, and J. S. Harris. Increase in spin injection efficiency of a CoFe/MgO(100) tunnel spin injector with thermal annealing. *Applied Physics Letters*, 86(5):052901, 2005.

[104] Henning Soldat, Mingyuan Li, Nils C. Gerhardt, Martin R. Hofmann, Arne Ludwig, Astrid Ebbing, Dirk Reuter, Andreas D. Wieck, Frank Stromberg, Werner Keune, and Heiko Wende. Room temperature spin relaxation length in spin light-emitting diodes. *Applied Physics Letters*, 99(5):051102, 2011.

[105] Takashi Manago, Asawin Sinsarp, and Hiro Akinaga. Growth condition dependence of spin-polarized electroluminescence in Fe/MgO/light-emitting diodes. *Journal of Applied Physics*, 102(8):083914, 2007.

[106] Asawin Sinsarp, Takashi Manago, Fumiyoshi Takano, and Hiro Akinaga. Electrical Spin Injection from Out-of-Plane Magnetized FePt/MgO Tunneling Junction into GaAs at Room Temperature. *Japanese Journal of Applied Physics*, 46(1L):L4, 2007.

[107] P. Renucci, V. G. Truong, H. Jaffrès, L. Lombez, P. H. Binh, T. Amand, J. M. George, and X. Marie. Spin-polarized electroluminescence and spin-dependent photocurrent in hybrid semiconductor/ferromagnetic heterostructures: An asymmetric problem. *Phys. Rev. B*, 82:195317, Nov 2010.

[108] C. H. Li, G. Kioseoglou, A. Petrou, M. Korkusinski, P. Hawrylak, and B. T. Jonker. Highly polarized emission from electrical spin injection into an InGaAs quantum well with free carriers. *Applied Physics Letters*, 103(21):212403, 2013.

[109] S. Ikeda, K. Miura, H. Yamamoto, K. Mizunuma, H. D. Gan, M. Endo, S. Kanai, J. Hayakawa, F. Matsukura, and H. Ohno. A perpendicular-anisotropy CoFeB–MgO magnetic tunnel junction. *Nat Mater*, 9:721–724, 09 2010.

[110] B. Baylac, T. Amand, X. Marie, B. Dareys, M. Brousseau, G. Bacquet, and V. Thierry-Mieg. Hole spin relaxation in n-modulation doped quantum wells. *Solid State Communications*, 93(1):57–60, 1995.

[111] Youngman Jang, Chunghee Nam, Ki-Su Lee, B. K. Cho, Y. J. Cho, Kwang-Seok Kim, and K. W. Kim. Variation in the properties of the interface in a cofeb-mgocofeb tunnel junction during thermal annealing. *Applied Physics Letters*, 91(10):102104, 2007.

[112] Y. Lu, B. Lépine, G. Jézéquel, S. Ababou, M. Alnot, J. Lambert, A. Renard, M. Mullet, C. Deranlot, H. Jaffrès, F. Petroff, and J.-M. George. Depth analysis of boron diffusion in MgO/CoFeB bilayer by x-ray photoelectron spectroscopy. *Journal of Applied Physics*, 108(4):043703, 2010.

[113] A. Jain, L. Louahadj, J. Peiro, J. C. Le Breton, C. Vergnaud, A. Barski, C. Beigné, L. Notin, A. Marty, V. Baltz, S. Auffret, E. Augendre, H. Jaffrès, J. M. George, and M. Jamet. Electrical spin injection and detection at Al_2O_3/n-type germanium interface using three terminal geometry. *Applied Physics Letters*, 99(16):162102, 2011.

[114] Pol Van Dorpe, Vasyl F. Motsnyi, Mayke Nijboer, Etienne Goovaerts, Viacheslav I. Safarov, Jo Das, Wim Van Roy, Gustaaf Borghs, and Jo De Boeck. Highly Efficient Room Temperature Spin Injection in a Metal-Insulator-Semiconductor Light-Emitting Diode. *Japanese Journal of Applied Physics*, 42(5B):L502, 2003.

[115] V. F. Motsnyi, P. Van Dorpe, W. Van Roy, E. Goovaerts, V. I. Safarov, G. Borghs, and J. De Boeck. Optical investigation of electrical spin injection into semiconductors. *Phys. Rev. B*, 68:245319, Dec 2003.

[116] G. Kioseoglou, A. T. Hanbicki, B. T. Jonker, and A. Petrou. Bias-controlled hole degeneracy and implications for quantifying spin polarization. *Applied Physics Letters*, 87(12):122503, 2005.

[117] W. Van Roy, P. Van Dorpe, J. De Boeck, and G. Borghs. Spin injection in LED's and in unipolar devices. *Materials Science and Engineering: B*, 126(2–3):155 – 163, 2006. {EMRS} 2005, Symposium B, Spintronics.

[118] M. C. Hickey, S. N. Holmes, T. Meng, I. Farrer, G. A. C. Jones, D. A. Ritchie, and M. Pepper. Strongly bias-dependent spin injection from Fe into n-type GaAs. *Phys. Rev. B*, 75:193204, May 2007.

[119] R. Mallory, M. Yasar, G. Itskos, A. Petrou, G. Kioseoglou, A. T. Hanbicki, C. H. Li, O. M. J. van't Erve, B. T. Jonker, M. Shen, and S. Saikin. Phonon-assisted recombination in Fe-based spin LEDs. *Phys. Rev. B*, 73:115308, Mar 2006.

[120] X. Y. Dong, C. Adelmann, J. Q. Xie, C. J. Palmstrøm, X. Lou, J. Strand, P. A. Crowell, J.-P. Barnes, and A. K. Petford-Long. Spin injection from the Heusler alloy Co_2MnGe into $Al_{0.1}Ga_{0.9}As/GaAs$ heterostructures. *Applied Physics Letters*, 86(10):102107, 2005.

[121] M. I. D'yakonov and V. I. Perel. Soviet Phys. JETP 33 (1971) 1053. *Sov. Phys. Solid State*, 13:3023, May 1972.

[122] MI Dyakonov and V Yu Kachorovskii. Spin relaxation of two-dimensional electrons in noncentrosymmetric semiconductors. *Sov. Phys. Semicond*, 20(1):110–112, 1986.

[123] Note that for samples with a MBE grown MgO/GaAs interaface with a lower density of interface states, the Fermi level pinning should occur closer to the conduction band of GaAs if one compares with the case of spinLEDs with sputtered tunnel barriers. Consequently, the depletion zone in GaAs just after the MgO barrier is smaller and the resistance of the semiconductor part of the device is smaller. That would also lead to a larger voltage drop on the MgO tunnel barrier.

[124] E. Johnston-Halperin, D. Lofgreen, R. K. Kawakami, D. K. Young, L. Coldren, A. C. Gossard, and D. D. Awschalom. Spin-polarized Zener tunneling in (Ga,Mn)As. *Phys. Rev. B*, 65:041306, Jan 2002.

[125] R. Farshchi, M. Ramsteiner, J. Herfort, A. Tahraoui, and H. T. Grahn. Optical communication of spin information between light emitting diodes. *Applied Physics Letters*, 98(16):162508, 2011.

[126] M Holub and P Bhattacharya. Spin-polarized light-emitting diodes and lasers. *Journal of Physics D: Applied Physics*, 40(11):R179, 2007.

[127] Pablo Asshoff, Andreas Merz, Heinz Kalt, and Michael Hetterich. A spintronic source of circularly polarized single photons. *Applied Physics Letters*, 98(11):112106, 2011.

[128] Jian Xu, Akhlesh Lakhtakia, Justin Liou, An Chen, and Ian J. Hodgkinson. Circularly polarized fluorescence from light-emitting microcavities with sculptured-thin-film chiral reflectors. *Optics Communications*, 264(1):235 – 239, 2006.

[129] D. Y. Kim. Potential application of spintronic light-emitting diode to binocular vision for three-dimensional display technology. *Journal of the Korean Physical Society*, 49:S505–S508, 2006.

[130] O. M. J. van 't Erve, G. Kioseoglou, A. T. Hanbicki, C. H. Li, B. T. Jonker, R. Mallory, M. Yasar, and A. Petrou. Comparison of Fe/Schottky and Fe/Al_2O_3 tunnel barrier contacts for electrical spin injection into GaAs. *Applied Physics Letters*, 84(21):4334–4336, 2004.

[131] N. Nishizawa and H. Munekata. Efficient spin injection through a crystalline AlO_x tunnel barrier prepared by the oxidation of an ultra-thin Al epitaxial layer on GaAs. *Journal of Applied Physics*, 114(3):033507, 2013.

[132] O. M. J. van 't Erve, G. Kioseoglou, A. T. Hanbicki, C. H. Li, and B. T. Jonker. Remanent electrical spin injection from Fe into AlGaAs/GaAs light emitting diodes. *Applied Physics Letters*, 89(7):072505, 2006.

[133] N. C. Gerhardt, S. Hövel, C. Brenner, M. R. Hofmann, F.-Y. Lo, D. Reuter, A. D. Wieck, E. Schuster, W. Keune, and K. Westerholt. Electron spin injection into GaAs from ferromagnetic contacts in remanence. *Applied Physics Letters*, 87(3):032502, 2005.

[134] S. Girod, M. Gottwald, S. Andrieu, S. Mangin, J. McCord, Eric E. Fullerton, J.-M. L. Beaujour, B. J. Krishnatreya, and A. D. Kent. Strong perpendicular magnetic anisotropy in Ni/Co(111) single crystal superlattices. *Applied Physics Letters*, 94(26):262504, 2009.

[135] H. X. Yang, M. Chshiev, B. Dieny, J. H. Lee, A. Manchon, and K. H. Shin. First-principles investigation of the very large perpendicular magnetic anisotropy at Fe—MgO and Co—MgO interfaces. *Phys. Rev. B*, 84:054401, Aug 2011.

[136] K. H. Khoo, G. Wu, M. H. Jhon, M. Tran, F. Ernult, K. Eason, H. J. Choi, and C. K. Gan. First-principles study of perpendicular magnetic anisotropy in CoFe/MgO and CoFe/$Mg_3B_2O_6$ interfaces. *Phys. Rev. B*, 87:174403, May 2013.

[137] D. C. Worledge, G. Hu, David W. Abraham, J. Z. Sun, P. L. Trouilloud, J. Nowak, S. Brown, M. C. Gaidis, E. J. O'Sullivan, and R. P. Robertazzi. Spin torque switching of perpendicular Ta/CoFeB/MgO-based magnetic tunnel junctions. *Applied Physics Letters*, 98(2):022501, 2011.

[138] Wei-Gang Wang, Stephen Hageman, Mingen Li, Sunxiang Huang, Xiaoming Kou, Xin Fan, John Q. Xiao, and C. L. Chien. Rapid thermal annealing study of magnetoresistance and perpendicular anisotropy in magnetic tunnel junctions based on MgO and CoFeB. *Applied Physics Letters*, 99(10):102502, 2011.

[139] G. Kresse and J. Hafner. Ab initio molecular dynamics for liquid metals. *Phys. Rev. B*, 47:558–561, Jan 1993.

[140] G. Kresse and J. Furthmüller. Efficient iterative schemes for ab initio total-energy calculations using a plane-wave basis set. *Phys. Rev. B*, 54:11169–11186, Oct 1996.

[141] G. Kresse and J. Furthmüller. Efficiency of ab-initio total energy calculations for metals and semiconductors using a plane-wave basis set. *Computational Materials Science*, 6(1):15 – 50, 1996.

[142] Yue Wang and John P. Perdew. Correlation hole of the spin-polarized electron gas, with exact small-wave-vector and high-density scaling. *Phys. Rev. B*, 44:13298–13307, Dec 1991.

[143] P. E. Blöchl. Projector augmented-wave method. *Phys. Rev. B*, 50:17953–17979, Dec 1994.

[144] G. Kresse and D. Joubert. From ultrasoft pseudopotentials to the projector augmented-wave method. *Phys. Rev. B*, 59:1758–1775, Jan 1999.

[145] H. Meng, W. H. Lum, R. Sbiaa, S. Y H Lua, and H. K. Tan. Annealing effects on cofeb-mgo magnetic tunnel junctions with perpendicular anisotropy. *Journal of Applied Physics*, 110(3):033904–033904–4, 2011.

[146] One cannot totally exclude a contribution of bound exciton at 25K (it can be ruled out at higher temperature). However, this contribution would only results in an artificial diminution of the EL circular polarization compared to the one of the free exciton line.

[147] B. T. Jonker, A. T. Hanbicki, Y. D. Park, G. Itskos, M. Furis, G. Kioseoglou, A. Petrou, and X. Wei. Quantifying electrical spin injection: Component-resolved electroluminescence from spin-polarized light-emitting diodes. *Applied Physics Letters*, 79(19):3098–3100, 2001.

[148] W. R. Mason. *The optical rotation results from A Practical Guide to Magnetic Circular Dichroism Spectroscopy.* John Wiley Sons, Inc., 2007.

[149] D. J. Griffiths. *Introduction to Quantum Mechanics (2nd Edition).* Prentice Hall, 2004.

[150] M. Yamanouchi, A. Jander, P. Dhagat, S. Ikeda, F. Matsukura, and H. Ohno. Domain Structure in CoFeB Thin Films With Perpendicular Magnetic Anisotropy. *Magnetics Letters, IEEE*, 2:3000304–3000304, 2011.

[151] J. Frougier (UMP CNRS-Thales), private communication. .

[152] Berend T. Jonker, George Kioseoglou, Aubrey T. Hanbicki, Connie H. Li, and Phillip E. Thompson. Electrical spin-injection into silicon from a ferromagnetic metal/tunnel barrier contact. *Nat. Phys*, 3:542–546, Aug 2007.

[153] D. Basu, D. Saha, and P. Bhattacharya. Optical polarization modulation and gain anisotropy in an electrically injected spin laser. *Phys. Rev. Lett.*, 102:093904, Mar 2009.

[154] Semion Saikin, Min Shen, and Ming-Cheng Cheng. Spin dynamics in a compound semiconductor spintronic structure with a schottky barrier. *Journal of Physics: Condensed Matter*, 18(5):1535, 2006.

[155] E. A. Barry, A. A. Kiselev, and K. W. Kim. Electron spin relaxation under drift in GaAs. *Appl. Phys. Lett.*, 82(21):3686–3688, 2003.

[156] H. Tong and M. W. Wu. Multivalley spin relaxation in n-type bulk gaas in the presence of high electric fields. *Phys. Rev. B*, 85:075203, Feb 2012.

[157] J. B. Gunn. Microwave oscillations of current in III-V semiconductors. *Solid State Comm.*, 1(4):88–91, 1963.

[158] B. K. Ridley and T. B. Watkins. The possibility of negative resistance effects in semiconductors. *Proceedings of the Physical Society*, 78(2):293, 1961.

[159] D. N. Mirlin, I. Ja. Karlik, L. P. Nikitin, I. I. Reshina, and V. F. Sapega. Hot electron photoluminescence in GaAs crystals. *Solid State Comm.*, 37(9):757 – 760, 1981.

[160] Jun-Wei Luo, Gabriel Bester, and Alex Zunger. Full-zone spin splitting for electrons and holes in bulk GaAs and GaSb. *Phys. Rev. Lett.*, 102:056405, Feb 2009.

[161] M. W. Wu, Jiang J. H., and M. Q. Weng. Spin dynamics in semiconductors. *Physics Reports*, 493(2-4):61 – 236, 2010.

[162] P. Pfeffer and W. Zawadzki. Conduction electrons in gaas: Five-level $k \cdot p$ theory and polaron effects. *Phys. Rev. B*, 41:1561–1576, Jan 1990.

[163] E. L. Ivchenko and G. E. Pikus. *Superlattices and Other Heterostructures*. Springer-Verlag, Berlin, 1995.

[164] JY Fu, MQ Weng, and MW Wu. Spin–orbit coupling in bulk GaAs. *Physica E: Low-dimensional Systems and Nanostructures*, 40(9):2890–2893, 2008.

[165] G. Borghs, K. Bhattacharyya, K. Deneffe, P. Van Mieghem, and R. Mertens. Band-gap narrowing in highly doped n- and p-type GaAs studied by photoluminescence spectroscopy. *J. Appl. Phys.*, 66(9):4381–4386, 1989.

[166] F. Nastos, J. Rioux, M. Strimas-Mackey, Bernardo S. Mendoza, and J. E. Sipe. Full band structure LDA and $\mathbf{k} \cdot \mathbf{p}$ calculations of optical spin-injection. *Phys. Rev. B*, 76:205113, Nov 2007.

[167] D. J. Chadi. Spin-orbit splitting in crystalline and compositionally disordered semiconductors. *Phys. Rev. B*, 16:790–796, Jul 1977.

[168] Fred H. Pollak and Manuel Cardona. Piezo-Electroreflectance in Ge, GaAs, and Si. *Phys. Rev.*, 172:816–837, Aug 1968.

[169] K. Zerrouati, F. Fabre, G. Bacquet, J. Bandet, J. Frandon, G. Lampel, and D. Paget. Spin-lattice relaxation in p-type gallium arsenide single crystals. *Phys. Rev. B*, 37:1334–1341, Jan 1988.

[170] D. Z. Garbuzov, A. I. Ekimov, and V. I. Safarov. Measurement of the lifetime and of the spin-relaxation time of electrons in semiconductors by the optical-orientation method. *JETP Lett.*, 13:24, 1971.

[171] A. G. Aronov, G. E. Pikus, and A. N. Titkov. Spin relaxation of conduction electrons in p-type III-V compounds. *JETP*, 57:680, Mar 1983.

[172] D. Rosen, A. G. Doukas, Y. Budansky, A. Katz, and R. R. Alfano. Time resolved luminescence of photoexcited p-type gallium arsenide by population mixing. *Appl. Phys. Lett.*, 39(12):935–937, 1981.

[173] Jagdeep Shah, Benoit Deveaud, T. C. Damen, W. T. Tsang, A. C. Gossard, and P. Lugli. Determination of intervalley scattering rates in GaAs by subpicosecond luminescence spectroscopy. *Phys. Rev. Lett.*, 59:2222–2225, Nov 1987.

[174] C. J. Stanton and D. W. Bailey. Rate equations for the study of femtosecond intervalley scattering in compound semiconductors. *Phys. Rev. B*, 45:8369–8377, Apr 1992.

[175] Note that the ΓL transfer time is $\sim$100 fs, much shorter than the $L\Gamma$ one because of the smaller density of states in the valley linked to the very different effective electron masses : $m_\Gamma = 0.067 m_0$ and $m_L = 0.23 m_0$, with m_0 representing the free electron mass.

[176] F. Pezzoli, F. Bottegoni, D. Trivedi, F. Ciccacci, A. Giorgioni, P. Li, S. Cecchi, E. Grilli, Y. Song, M. Guzzi, Dery H., and G. Isella. Optical Spin Injection and Spin Lifetime in Ge Heterostructures. *Phys. Rev. Lett.*, 108:156603, Apr 2012.

[177] A. Abragam. *Principles of Nuclear magnetism, International series of monographs on Physics, vol. 32*. Oxford Science Publication, 1983.

[178] A. Messiah. *Quantum Mechanics*. Dover publications, 1999.

[179] G. F. Koster, R. G. Wheeler, J. O. Dimmock, and H. Statz. *Properties of the thirty-two point groups*. MIT Press, 1963.

[180] Hui-Xiong Deng, Jingbo Li, Shu-Shen Li, Haowei Peng, Jian-Bai Xia, Lin-Wang Wang, and Su-Huai Wei. Band crossing in isovalent semiconductor alloys with large size mismatch: First-principles calculations of the electronic structure of Bi and N incorporated GaAs. *Physical Review B*, 82(19):193204, 2010.

[181] Muhammad Usman, Christopher A. Broderick, Andrew Lindsay, and Eoin P. O'Reilly. Tight-binding analysis of the electronic structure of dilute bismide alloys of GaP and GaAs. *Phys. Rev. B*, 84:245202, Dec 2011.

[182] P Ludewig, N Knaub, W Stolz, and K Volz. MOVPE growth of Ga (AsBi)/GaAs multi quantum well structures. *Journal of Crystal Growth*, 370:186–190, 2013.

[183] K Bertulis, A Krotkus, G Aleksejenko, V Pacebutas, R Adomavicius, G Molis, and Saulius Marcinkevicius. GaBiAs: A material for optoelectronic terahertz devices. *Applied physics letters*, 88(20):201112–201112, 2006.

[184] S. J. Sweeney, Z. Batool, K. Hild, S. R. Jin, and T. J. C. Hosea. The potential role of bismide alloys in future photonic devices. In *13th International Conference on Transparent Optical Networks(ICTON)*, pages 1–4, Stockholm, 2011. IEEE.

[185] S. J. Sweeney and S. R. Jin. Bismide-nitride alloys: Promising for efficient light emitting devices in the near- and mid-infrared. *Journal of Applied Physics*, 113(4):043110, 2013.

[186] Christopher A Broderick, Muhammad Usman, Stephen J Sweeney, and Eoin P O'Reilly. Band engineering in dilute nitride and bismide semiconductor lasers. *Semiconductor Science and Technology*, 27(9):094011, 2012.

[187] Yu I Mazur, VG Dorogan, M Schmidbauer, GG Tarasov, SR Johnson, X Lu, SQ Yu, Zh M Wang, T Tiedje, and GJ Salamo. Optical evidence of a quantum well channel in low temperature molecular beam epitaxy grown Ga (AsBi)/GaAs nanostructure. *Nanotechnology*, 22(37):375703, 2011.

[188] Z. Batool, K. Hild, T. J. C. Hosea, X. Lu, T. Tiedje, and S. J. Sweeney. The electronic band structure of GaBiAs/GaAs layers: Influence of strain and band anti-crossing. *Journal of Applied Physics*, 111(11):113108, 2012.

[189] S. J. Sweeney, Patent No. WO2010149978, 2010.

[190] W Shan, W Walukiewicz, JW Ager III, EE Haller, JF Geisz, DJ Friedman, JM Olson, and Sarah R Kurtz. Band anticrossing in gainnas alloys. *Physical Review Letters*, 82(6):1221, 1999.

[191] EP O'Reilly, A Lindsay, PJ Klar, A Polimeni, and M Capizzi. Trends in the electronic structure of dilute nitride alloys. *Semiconductor Science and Technology*, 24(3):033001, 2009.

[192] PRC Kent and Alex Zunger. Theory of electronic structure evolution in GaAsN and GaPN alloys. *Physical review B*, 64(11):115208, 2001.

[193] Sebastian Imhof, Angela Thränhardt, Alexej Chernikov, Martin Koch, Niko S. Köster, Kolja Kolata, Sangam Chatterjee, Stephan W. Koch, Xianfeng Lu, Shane R. Johnson, Dan A. Beaton, Thomas Tiedje, and Oleg Rubel. Clustering effects in Ga(AsBi). *Applied Physics Letters*, 96(13):131115, 2010.

[194] E.-M. Pavelescu, T. Jouhti, M. Dumitrescu, P. J. Klar, S. Karirinne, Y. Fedorenko, and M. Pessa. Growth-temperature-dependent (self-)annealing-induced blueshift of photoluminescence from 1.3 μm GaInNAs/GaAs quantum wells. *Applied Physics Letters*, 83(8):1497–1499, 2003.

[195] S. Francoeur, M.-J. Seong, A. Mascarenhas, S. Tixier, M. Adamcyk, and T. Tiedje. Band gap of $GaAs_{1-x}Bi_x$, $0 < x < 3.6\%$. *Applied Physics Letters*, 82(22):3874–3876, 2003.

[196] B. Fluegel, S. Francoeur, A. Mascarenhas, S. Tixier, E. C. Young, and T. Tiedje. Giant Spin-Orbit Bowing in $GaAs_{1-x}Bi_x$. *Phys. Rev. Lett.*, 97:067205, Aug 2006.

[197] I. Moussa, H. Fitouri, Z. Chine, A. Rebey, and B. El Jani. Effect of thermal annealing on structural and optical properties of the $GaAs_{0.963}Bi_{0.037}alloy$. $SemiconductorScienceandTechnology$, 23(12) : 125034, 2008.

[198] A. R. Mohmad, F. Bastiman, C. J. Hunter, J. S. Ng, S. J. Sweeney, and J. P. R. David. The effect of Bi composition to the optical quality of $GaAs_{1-x}Bi_x$. *Applied Physics Letters*, 99(4):042107, 2011.

[199] S. Mazzucato, P. Boonpeng, H. Carrère, D. Lagarde, A. Arnoult, G. Lacoste, T. Zhang, A. Balocchi, T. Amand, X. Marie, and C. Fontaine. Reduction of defect density by rapid thermal annealing in GaAsBi studied by time-resolved photoluminescence. *Semiconductor Science and Technology*, 28(2):022001, 2013.

[200] Y. P. Varshni. Temperature dependence of the energy gap in semiconductors. *Physica*, 34(1):149 – 154, 1967.

[201] Sebastian Imhof, Christian Wagner, Angela Thränhardt, Alexej Chernikov, Martin Koch, Niko S. Köster, Sangam Chatterjee, Stephan W. Koch, Oleg Rubel, Xianfeng Lu, Shane R. Johnson, Daniel A. Beaton, and Thomas Tiedje. Luminescence dynamics in ga(asbi). *Applied Physics Letters*, 98(16):161104, 2011.

[202] R. J. Potter and N. Balkan. Optical properties of GaNAs and GaInAsN quantum wells. *Journal of Physics: Condensed Matter*, 16(31):S3387, 2004.

[203] When increasing the temperature from 100 to 300 K, both electron spin lifetime τ_s and PL decay time τ_{lum} decrease. However, τ_{lum} decreases faster than τ_s. Hence, the time integrated PL degree of polarization is stronger at 300 K (Figure 2) than at 100 K (Figure 3).

[204] M. Oestreich and W. W. Rühle. Temperature Dependence of the Electron Landé g Factor in GaAs. *Phys. Rev. Lett.*, 74:2315–2318, Mar 1995.

[205] W. Zawadzki, P. Pfeffer, R. Bratschitsch, Z. Chen, S. T. Cundiff, B. N. Murdin, and C. R. Pidgeon. Temperature dependence of the electron spin g factor in GaAs. *Phys. Rev. B*, 78:245203, Dec 2008.

[206] H. Tong, X. Marie, and M. W. Wu. Electron spin relaxation in $GaAs_{1-x}Bi_x$: Effects of spin-orbit tuning by Bi incorporation. *Journal of Applied Physics*, 112(6):063701, 2012.

[207] G. Bastard. *Wave Mechanics Applied to Semiconductor Heterostructures*. EDP sciences, Paris, 1992.

[208] K. L. Litvinenko, L. Nikzad, C. R. Pidgeon, J. Allam, L. F. Cohen, T. Ashley, M. Emeny, W. Zawadzki, and B. N. Murdin. Temperature dependence of the electron Landé g factor in InSb and GaAs. *Phys. Rev. B*, 77:033204, Jan 2008.

[209] A.M. White, I. Hinchliffe, P.J. Dean, and P.D. Greene. Zeeman spectra of the principal bound exciton in Sn-doped gallium arsenide . *Solid State Communications*, 10(6):497 – 500, 1972.

[210] M.I. D'yakonov and V.I. Perel. Spin relaxation of conduction electrons in noncentrosymmetric semiconductors. *Sov. Phys. Solid State*, 13(12):3023–3026, 1972.

[211] Brennan Pursley, M. Luengo-Kovac, G. Vardar, R. S. Goldman, and V. Sih. Spin lifetime measurements in GaAsBi thin films. *Applied Physics Letters*, 102(2):022420, 2013.

[212] G. Pettinari, A. Polimeni, M. Capizzi, J. H. Blokland, P. C. M. Christianen, J. C. Maan, E. C. Young, and T. Tiedje. Influence of bismuth incorporation on the valence and conduction band edges of $GaAs_{1-x}Bi_x$. *Applied Physics Letters*, 92(26):262105, 2008.

[213] B. Fluegel, R. N. Kini, A. J. Ptak, D. Beaton, K. Alberi, and A. Mascarenhas. Shubnikov-de Haas measurement of electron effective mass in $GaAs_{1-x}Bi_x$. *Applied Physics Letters*, 99(16):162108, 2011.

[214] Yu A. Bychkov and E. I. Rashba. Oscillatory effects and the magnetic susceptibility of carriers in inversion layers. *Journal of Physics C: Solid State Physics*, 17(33):6039, 1984.

[215] J Frougier, G Baili, M Alouini, I Sagnes, H Jaffres, A Garnache, C Deranlot, D Dolfi, and J-M George. Control of light polarization using optically spin-

injected vertical external cavity surface emitting lasers. *Applied Physics Letters*, 103(25):252402, 2013.

[216] X Lou, C Adelmann, M Furis, SA Crooker, CJ Palmstrøm, and PA Crowell. Electrical detection of spin accumulation at a ferromagnet-semiconductor interface. *Physical review letters*, 96(17):176603, 2006.

[217] Hyun Cheol Koo, Jae Hyun Kwon, Jonghwa Eom, Joonyeon Chang, Suk Hee Han, and Mark Johnson. Control of spin precession in a spin-injected field effect transistor. *Science*, 325(5947):1515–1518, 2009.

[218] Luis E Hueso, Jose M Pruneda, Valeria Ferrari, Gavin Burnell, Jose P Valdes-Herrera, Benjamin D Simons, Peter B Littlewood, Emilio Artacho, Albert Fert, and Neil D Mathur. Transformation of spin information into large electrical signals using carbon nanotubes. *Nature*, 445(7126):410–413, 2007.

[219] Ron Jansen. Silicon spintronics. *Nature Materials*, 11(3293):400–408, 2012.

[220] André Dankert, Ravi S Dulal, and Saroj P Dash. Efficient spin injection into silicon and the role of the schottky barrier. *Scientific reports*, 3, 2013.

[221] Jen-Ru Chen, Patrick M. Odenthal, Adrian G. Swartz, George Charles Floyd, Hua Wen, Yunqiu Kelly Luo, and Roland K. Kawakami. Control of Schottky Barriers in Single Layer MoS2 Transistors with Ferromagnetic Contacts. *Nano Lett.*, 13(7):3106–3110, 2013.

[222] G Sallen, L Bouet, X Marie, G Wang, CR Zhu, WP Han, Y Lu, PH Tan, T Amand, BL Liu, et al. Robust optical emission polarization in MoS_2 monolayers through selective valley excitation. *Physical Review B*, 86(8):081301, 2012.

[223] Christian Rinaldi, Matteo Cantoni, Daniela Petti, Andrea Sottocorno, Marco Leone, Nuala M Caffrey, Stefano Sanvito, and Riccardo Bertacco. Ge-based spin-photodiodes for room-temperature integrated detection of photon helicity. *Advanced Materials*, 24(22):3037–3041, 2012.

[224] Bernhard Endres, Mariusz Ciorga, Maximilian Schmid, Martin Utz, Dominique Bougeard, Dieter Weiss, Günther Bayreuther, and CH Back. Demonstration of the spin solar cell and spin photodiode effect. *Nature communications*, 4, 2013.

[225] Ron Jansen. Spintronics: solar spin devices see the light. *Nature materials*, 12(9):779–780, 2013.

Résume de la thèse en français

Introduction

L'électronique de spin ou spintronique dans les semiconducteurs vise à utiliser le spin de l'électron comme degré de liberté supplémentaire (en plus de la charge électrique) afin de véhiculer l'information. Cela permettrait la mise au point de composants plus performants (faible consommation d'énergie, vitesse plus rapide) intégrant de nouvelles fonctionnalités (Spin transistor, Diodes électroluminescentes polarisées en spin (Spin-LEDs), Spin lasers). Cependant, avant d'envisager le développement de dispositifs reposant sur les propriétés de spin des porteurs, plusieurs verrous doivent être levés. Dans un premier temps, il est nécessaire de pouvoir injecter électriquement le spin dans les semiconducteurs. La nature et la qualité des interfaces entre les injecteurs et le dispositif semiconducteur sont la première barrière à lever. Il faut ensuite s'assurer que, malgré une injection des porteurs à très haute énergie, le spin des porteurs sera conservé. Enfin, il convient de trouver des matériaux qui permettraient de moduler les propriétés de spin au sein des dispositifs. Ce travail de thèse porte sur deux étapes importantes qui doivent être maîtrisées: l'injection électrique de porteurs polarisés en spin dans les semiconducteurs III-V, et la manipulation du spin de l'électron par champ magnétique dans ces matériaux.

L'exposé de nos travaux est divisé en 5 chapitres. Dans le premier chapitre, nous présentons l'état de l'art de la discipline, les règles de sélection qui régissent les interactions entre le spin des porteurs et les recombinaisons optiques que nous détectons, ainsi que les mécanismes de relaxation de spin des porteurs. Dans le second chapitre, nous présentons les équipements expérimentaux utilisés et les techniques nouvelles que nous avons dû développer notamment dans le but d'étudier les processus de relaxation de spin lorsque les électrons sont injectés à haute énergie dans les vallées L du

GaAs. Le troisième chapitre est consacré à l'injection électrique de spin dans le semi-conducteur. Nous présentons les résultats de caractérisation par électroluminescence obtenus sur des spin-LEDs dont nous avons fait varier la nature de l'injecteur. Dans le quatrième chapitre, nous étudions l'effet de l'injection optique dans les vallées L du GaAs, les mécanismes de relaxation de spin sont modélisés et comparés aux résultats expérimentaux. Enfin, le cinquième chapitre porte sur l'exploration des propriétés électroniques et de spin du matériau GaAsBi afin d'en déterminer ses potentialités pour les applications spintroniques.

Chapitre 1

Propriétés électroniques des semiconducteurs III-V zinc-blende

Ce premier chapitre décrit d'abord la structure de bande des semiconducteurs III-V de type GaAs. Les bases de la théorie de la fonction enveloppe sont présentées. Cette dernière permet de calculer les états électroniques dans les hétérostructures, en particulier dans les puits quantiques de type InGaAs/GaAs. Les règles de sélections optiques (Figure 1) lors de l'interaction lumière-matière, qui repose sur l'interaction dipolaire électrique, sont énoncées dans le cas de matériaux volumiques et des puits quantiques semiconducteurs où le confinement et la contrainte (dans le cas des puits InGaAs/GaAs) lèvent la dégénérescence entre trous lourds et trous légers dans la bande de valence.

Ensuite, les principaux mécanismes de relaxation de spin sont détaillés. Il s'agit

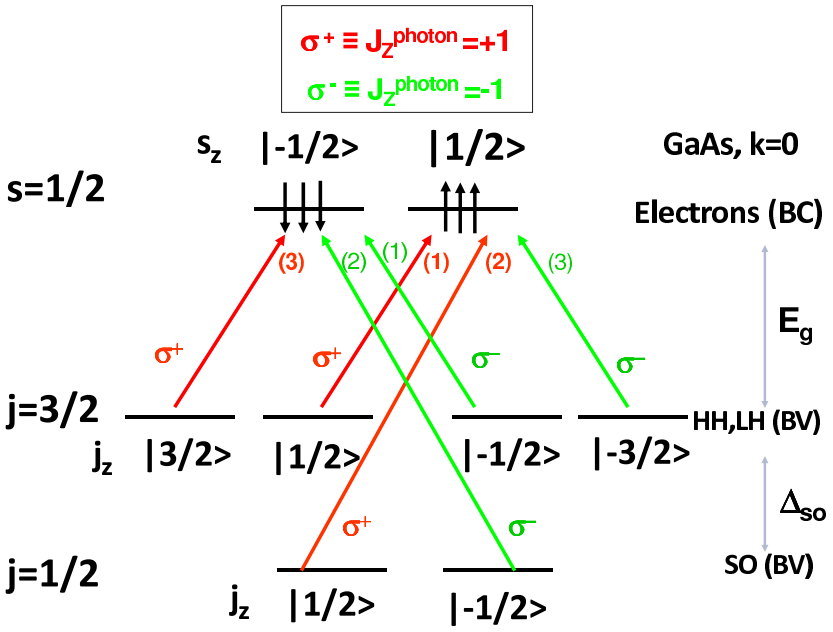

[

]Figure 1: Règles de sélection optiques pour les puits quantiques III-V.

des mécanismes de D'Yakonov-Perel et Eliott-Yaffet (basés sur le couplage spin-orbite dans la bande de conduction), du mécanisme de Bir-Aronov-Pikus (qui repose sur l'interaction d'échange électron-trou), et du mécanisme reposant sur l'interaction hyperfine entre le spin de l'électron et le spin des noyaux environnants. Le mécanisme de relaxation de spin de la paire électron-trou en bloc au sein de l'exciton est également

présenté. Enfin, la problématique de l'injection électrique de spin dans les semiconducteurs est développée. La technique la plus efficace pour réaliser une injection de spin à température ambiante consiste à injecter les électrons à partir d'un métal ferromagnétique (CoFeB dans notre cas). Le principal obstacle à l'injection de spin dans le régime diffusif réside dans la très grande différence de conductivité entre le métal et le semiconducteur. La solution consiste à insérer une fine barrière tunnel (à base de MgO dans cette thèse) afin de travailler en régime tunnel et de restaurer une injection de spin efficace à l'interface Métal/Semiconducteur.

Chapitre 2

Dispositifs experimentaux

Les techniques expérimentales utilisées sont l'Electroluminescence (EL) stationnaire résolue en polarisation, la Photoluminescence résolue en temps (TRPL) et en polarisation, et l'excitation de la photoluminescence (PLE) résolue en polarisation.

Spectroscopie d'électroluminescence résolue en polarisation

Pour réaliser les mesures de rendement d'injection de spin dans les diodes électroluminescentes polarisées en spin (Spin-LEDs), nous avons utilisé un dispositif d'électroluminescence stationnaire, basé sur une camera CCD à très bas bruit optimisé pour le proche infra-rouge. Les échantillons sont excités par des créneaux de tension de durée 5 microsecondes (séparés de 15 microsecondes) afin de ne pas chauffer l'échantillon. La durée des créneaux est très longue comparée aux temps caractéristiques du système (temps de relaxation de spin, temps de vie de spin), de sorte que l'on travaille en régime quasi-stationnaire. L'amplitude en tension des créneaux est variable. Un champ magnétique longitudinal variant de 0 à 0.8T est appliqué à la spin-LED via un électroaimant.

Spectroscopie de Photoluminescence résolue en temps

Pour les études de spectroscopie de photoluminescence présentées dans ce mémoire, nous avons utilisé une chaîne constituée d'un laser solide qui sert de pompe à un oscillateur Titane-Saphir (Ti:Sa) impulsionnel.

Le laser Titane-Saphir à modes bloqués

Ce laser est un oscillateur Titane-Saphir impulsionnel dont le milieu amplificateur solide est un cristal de saphir dopé au titane (Al_2O_3:Ti). Nous pouvons l'accorder en longueur d'onde sur un domaine spectral allant de 680 nm jusqu'à 990 nm en mode impulsionnel et nous pouvons le faire fonctionner dans deux configurations différentes qui génèrent des impulsions limitées par transformée de Fourier respectivement picosecondes ($\sim$ 1.5 ps) et sub-picosecondes ($\sim$ 100 fs). Au cours de ma thèse, seul le mode picoseconde a été utilisé pour l'étude des dynamiques de spin dans les puits quantiques

d'InGaAs/GaAs et GaAsBi. La fréquence de répétition du laser Ti:Sa est de 80 Mhz et sa puissance moyenne suivant la longueur d'onde varie dans la gamme 0,4-2 Watt (ce qui correspond à une énergie dans l'impulsion de 5 à 25 nJ).

La caméra à balayage de fente

Le dispositif expérimental d'étude de photoluminescence résolue en temps exposé dans cette thèse se base sur une caméra à balayage de fente (≪ streak camera ≫ en anglais) en mode synchronisé, à photocathode S2 refroidie (Hamamatsu).

Le principe du dispositif expérimental est très simple: l'échantillon est excité par des impulsions issues du laser Ti:Sa, et le signal de photoluminescence est dispersé dans un monochromateur puis envoyé dans la caméra à balayage de fente.

La lumière à analyser entre dans la caméra et arrive sur une photocathode, générant ainsi un flux d'électrons qui va être ensuite accéléré par un champ électrique dans un tube sous vide. Dans ce tube, les électrons sont déviés par une paire d'électrodes à laquelle est appliquée une tension sinusoïdale calée en phase par rapport au laser Ti:Sa (une photodiode rapide détectant les impulsions périodiques du laser Ti:Sa est employée à cet usage). Le flux d'électrons arrive ensuite sur une galette à micro-canaux où il est amplifié avant de frapper un écran de phosphore. L'image de l'écran de phosphore est collectée et intégrée par une caméra CCD. Les images collectées sont corrigées par le bruit de la photocathode et par sa sensibilité. La caméra étant précédée par un monochromateur qui disperse la lumière horizontalement, les images obtenues sont donc en deux dimensions: horizontalement nous avons la dépendance de l'intensité de la photoluminescence en fonction de la longueur d'onde et verticalement sa dépendance en fonction du temps. Un code des couleurs représente l'intensité de la photoluminescence.

Mesures de la polarisation de la lumière

Afin d'analyser les propriétés de spin des porteurs dans nos structures, nous utilisons la polarisation de la lumière, que ce soit lors des expériences d'électroluminescence ou de photoluminescence résolue en temps. Dans un premier temps, il faut pourvoir faire exciter l'échantillon avec de la lumière polarisée circulairement (dans le cas de la TRPL). Pour ce faire nous utilisons un polariseur et une lame quart-d'onde. Réciproquement,

pour étudier la polarisation circulaire de la photoluminescence, nous disposons d'une lame quart-d'onde rotative et d'un analyseur (cube séparateur de polarisation dans notre montage). Le taux de polarisation circulaire se définit ainsi:

$$P_{circ} = \frac{I^+ - I^-}{I^+ + I^-}$$

Avec I^+ et I^- les intensités des deux composantes de la lumière polarisées circulairement droite et gauche.

Spectroscopie d'excitation de la photoluminescence (PLE) résolue en polarisation.

Afin de mesurer la polarisation de spin et le temps de relaxation de spin de l'électron

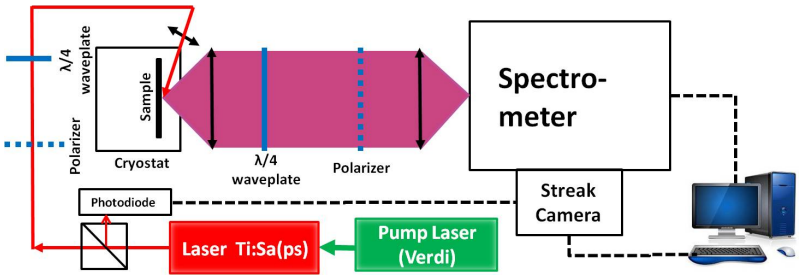

Figure 2: Schéma du dispositif d'excitation de la photoluminescence (PLE) résolu en polarisation basé sur une double modulation de l'intensité et de l'hélicité de la lumière.

dans les vallées L, nous avons développé un banc de mesure spécifique (Figure 2). D'abord, la longueur d'onde d'excitation doit être étendue vers le bleu dans le domaine 2.8-3.2 eV afin de photogénérer des électrons dans les vallées L. Nous avons donc utilisé un doubleur de fréquence (Spectra GWU) basé sur un cristal non linéaire de LBO. Ensuite, nous devons être capable détecter des taux de polarisation circulaire de l'ordre du pourcent. Nous avons donc utilisé une technique de double modulation. L'intensité du faisceau laser est modulée par un hacheur à quelques centaines de Hertz, tandis que l'hélicité de la lumière est modulée à 50kHz à l'aide d'un modulateur photoélastique. La photoluminescence est dispersée par un monochromateur, détectée par une photodiode au Silicium, puis filtrée par deux détections synchrones. La sensibilité de ce dispositif ($\sim$0.1%) est bien meilleure que celle ($\sim$1%) obtenue par rotation d'une lame quart-d'onde (technique qui est utilisée dans les expériences d'électroluminescence et de photoluminescence résolues en polarisation).

Chapitre 3

Injection électrique de spin dans une spin-LED

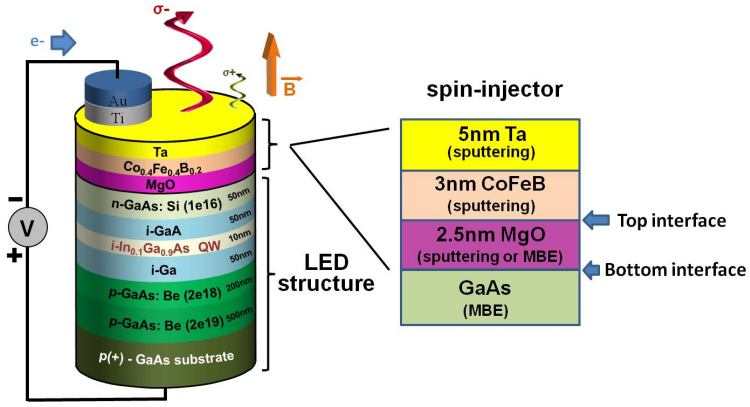

Figure 3: Schéma de principe d'une Spin-LED.

La détection de la polarisation de spin injectée à l'interface Métal/Semiconducteur se fait via l'analyse du taux de polarisation circulaire de l'électroluminescence de dispositifs spécifiques élaborés à cet effet appelés Spin-LEDs (Figure 3). Ces composants comportent un ou plusieurs puits quantiques dans la zone intrinsèque de la jonction P-I-N de la diode électroluminescente. La lumière est détectée dans la direction de l'axe de croissance des structures, et la polarisation de spin des électrons injectée est déduite de la polarisation circulaire de l'électroluminescence grâce aux règles de sélection optiques qui gouvernent l'émission des puits quantiques semiconducteurs. L'insertion de barrières tunnel de MgO texturées à l'interface entre métal et semiconducteur est la méthode qui donne à l'heure actuelle les résultats les plus remarquables dans le cadre de l'injection électrique de spin dans les semiconducteurs de type III-V. Des taux de polarisation circulaire de l'électroluminescence de l'ordre 50% ont ainsi été détectés à 100 K sur des Spin-LEDs à base de CoFe/MgO/AlGaAs. Une polarisation élevée de l'ordre de 32% est maintenue jusqu'à 300 K dans ces systèmes. Ces forts taux de polarisation pourraient être dus à une atténuation différente des fonctions d'onde évanescentes à travers la barrière tunnel pour les deux populations de spin (filtrage de spin). Nous nous concentrons dans ce chapitre sur l'injection électrique de spin à partir d'une électrode ferromagnétique de $Co_{0.4}Fe_{0.4}B_{0.2}$ dans des puits quantiques $In_{0.1}Ga_{0.9}As$/GaAs à travers une barrière de MgO. Le matériau CoFeB présente l'intérêt de pouvoir être épitaxié grain à grain en phase cristalline cubique centrée sur MgO après recuit, ce qui

pourrait favoriser l'effet de filtrage de spin. De plus le champ magnétique longitudinal à appliquer pour saturer l'aimantion de la couche ferromagnétique est inférieur à celui du CoFe (typiquement de 1.3 T au lieu de 2.2 T). Trois points principaux sont abordés. D'abord, lors d'une étude comparative entre des spin-LEDs comportant une barrière tunnel fabriquée soit par épitaxie par jets moléculaires, soit par pulvérisation cathodique, nous avons établi que l'interface CoFeB/MgO joue un rôle prépondérant dans le processus d'injection de spin. Dans un deuxième temps, nous avons étudié sur ces mêmes échantillons l'influence du courant injecté dans les spin-LEDs sur le rendement d'injection de spin. Nous montrons que le taux de polarisation circulaire est nettement plus stable en fonction du courant dans le cas où la barrière tunnel de MgO est fabriquée par pulvérisation cathodique. Enfin nous démontrons la possibilité d'injecter très efficacement des électrons polarisés en spin sans champ magnétique appliqué, en utilisant une électrode ultrafine de CoFeB présentant une aimantation rémanente perpendiculaire au plan des couches.

Comparaison entre Spin-LEDs comportant une barrière tunnel de MgO fabriquée par Epitaxie par Jets Moléculaires (MBE) et par pulvérisation cathodique.

Deux types de spin-LEDs sont fabriquées: la partie semiconductrice est identique et est élaborée par MBE. La jonction P-I-N comporte l'empilement de couches suivant: substrat p+-GaAs (001) /500nm p-GaAs (p=21019cm-3) /200 nm GaAs ($p = 2 \times 10^{18} cm^{-3}$)/50 nm GaAs non dopé /10 nm $In_{0.1}Ga_{0.9}As$ non dopé/ 50 nm GaAs non dopé/ 50 nm n-GaAs ($n = 1 \times 10^{16} cm^{-3}$). Cette jonction est recouverte d'une couche d'Arsenic afin de la protéger. Cette couche est désorbée dans la chambre MBE. L'élaboration de la partie métal ferromagnétique/oxyde est alors réalisée selon deux protocoles différents. Concernant les échantillons dits $\ll$ MBE $\gg$, le MgO (2.5 nm) est déposé dans le bâti MBE. L'échantillon est ensuite transféré via un sas (le processus prend plusieurs minutes sous une pression de 10^{-7} torr) dans le bâti de pulvérisation cathodique où la couche de CoFeB (3 nm) est élaborée. Concernant les échantillons dont la barrière tunnel est élaborée par pulvérisation cathodique, l'échantillon est d'abord transféré via le sas dans le bâti de pulvérisation cathodique où sont alors élaborées les couches de MgO et de CoFeB. Toutes les couches ont la

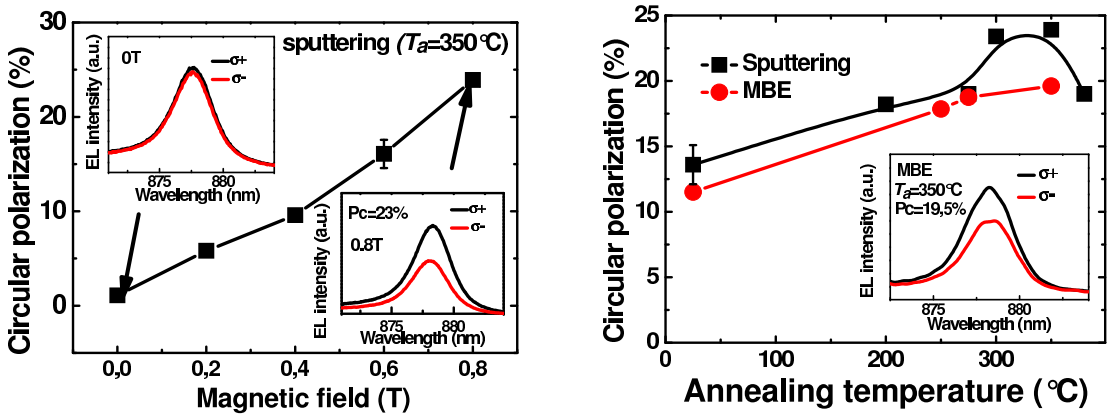

Figure 4: (a) échantillon avec barrière tunnel fabriquée par pulvérisation cathodique recuit à 350 °C. Polarisation circulaire de l'électroluminescence en fonction du champ magnétique appliqué. Insert supérieur: Spectre des composantes σ^+ et σ^- de l'électroluminescence à champ magnétique nul. Insert inférieur: même quantités sous B=0.8 T. (b) Polarisation circulaire de l'électroluminescence en fonction de la température de recuit pour les deux types d'échantillons. Insert: échantillon avec barrière tunnel fabriquée par MBE recuit à 350 °C. Spectre des composantes σ^+ et σ^- de l'électroluminescence sous B=0.8 T

même épaisseur quelque soit la technique de croissance. On s'attend donc à ce que l'interface MgO/GaAs soit d'une qualité supérieure pour les échantillons MBE. Au contraire, l'interface CoFeB/MgO est de meilleure qualité pour les échantillons dont la barrière tunnel est élaborée par pulvérisation cathodique. Ces deux types d'échantillons vont nous permettre de tester quelle est l'interface qui joue un rôle prépondérant dans l'injection électrique de spin. Nous observons que le recuit rapide (3 mn) en température permet d'améliorer sensiblement le taux de polarisation circulaire mesuré, et ce pour les deux types d'échantillons (Figure 4). Les valeurs optimales de la polarisation circulaire sont comparables avec les deux types de croissances. Les températures de recuit optimales TAN se situent dans la gamme 300-350°C. Des taux de polarisation circulaire de P_C ∼23% à 0.8 T correspondant à ∼40% à saturation sont mesurés, démontrant clairement l'efficacité de ces injecteurs. Des mesures de photoluminescence résolues en temps et en polarisation permettent de montrer que l'amélioration de P_C observée avec l'augmentation de la température de recuit n'est pas due à une modification du ratio entre le temps de vie des électrons et leur temps de relaxation de spin dans les puits quantiques.

Des mesures d'aimantation par SQUID (Superconducting Quantum Interference Device) avec champ magnétique appliqué perpendiculairement au plan des couches per-

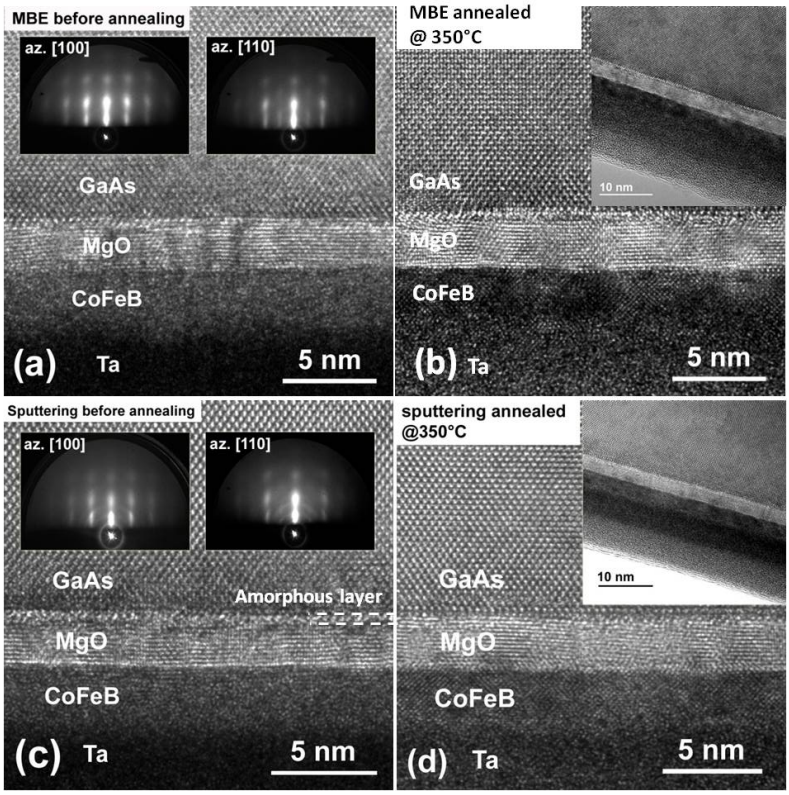

Figure 5: (a) Echantillon avec barrière tunnel élaborée par MBE avant recuit. Image HRTEM. Insert de gauche: RHEED sur MgO dans la direction [100]. Insert de droite: RHEED sur MgO dans la direction [110]. (b) Echantillon après recuit à 350 $°C$ avec barrière tunnel élaborée par MBE. Image HRTEM. Insert: coupe TEM à faible grandissement. (c) Echantillon avant recuit avec barrière tunnel élaborée par pulvérisation cathodique. Insert de gauche: RHEED sur MgO dans la direction [100]. Insert de droite: RHEED sur MgO dans la direction [110]. (d) Echantillon après recuit à 350 $°C$ avec barrière tunnel élaborée par pulvérisation cathodique. Image HRTEM. Insert: coupe TEM à faible grandissement.

mettent de montrer que cette augmentation de P_C avec TAN n'est pas due à une variation du champ magnétique de saturation (notons que le champ appliqué de 0.8 T dans nos expériences n'est jamais suffisant pour saturer l'aimantation). Des études couplées de mesures d'aimantation par SQUID, de microscopie à transmission à haute résolution (HRTEM voir Figure 5) et de diffraction d'électrons (RHEED Reflexion Hight Energy Electrons Diffraction) permettent de déterminer l'interface cruciale pour l'injection de spin. Dans le cas des échantillons MBE, la polarisation circulaire augmente nettement avec le recuit, alors que dans le même temps aucun changement notable de l'interface MgO/GaAs n'est observable dans les images TEM. Au contraire, l'interface CoFeB/MgO est fortement modifiée comme le montre la cristallisation complète de la couche après le recuit à 350 $°C$. Cette observation semble indiquer que l'interface cruciale pour l'injection de spin est l'interface supérieure CoFeB/MgO. De plus, si l'on compare la polarisation circulaire mesurée sur les échantillons non recuit, il apparait que P_C est légèrement supérieure pour la structure comportant une barrière tunnel fabriquée par pulvérisation cathodique, alors que pourtant l'interface MgO/GaAs est clairement de moins bonne qualité (une fine couche amorphe est observée par HRTEM). C'est donc plutôt l'interface CoFeB/MgO qui joue un rôle clé dans l'injection de spin. Une amélioration chimique de cette interface est induite par le recuit, qui provoque également une cristallisation du CoFeB au-delà de 300 $°C$, comme le montrent les mesures par SQUID des champs coercitifs en fonction de la température de recuit lorsque le champ magnétique est appliqué dans le plan des couches.

Dépendance de l'injection de spin vis-à-vis du courant injecté dans la spin-LED

Nous avons ensuite étudié sur ces mêmes échantillons l'influence du courant injecté dans les spin-LEDs sur les taux de polarisation circulaire mesurés. Nous avons concentré nos efforts sur les échantillons recuits à 300 $°C$, mais nous avons vérifié que les tendances sont les mêmes quelque soit le recuit. Il apparait que P_C reste très stable lorsque le courant augmente pour l'échantillon dont la barrière tunnel est élaborée par pulvérisation cathodique (Figure 6). Au contraire, P_C décroit rapidement dans le cas de l'échantillon MBE. La tendance est la même lorsque l'on trace P_C en fonction de ΔV, $\Delta V = V - V_{th}$ avec V la tension appliquée sur l'échantillon et Vth la tension

de seuil nécessaire pour obtenir le phénomène d'électroluminescence. Nous attribuons cet effet à une nature d'interface MgO/GaAs très différente selon les deux techniques de croissance. Dans le cas de l'échantillon présentant une barrière tunnel élaborée par pulvérisation cathodique, la densité d'états d'interface est certainement supérieure. Un courant de fuite, partant du niveau de Fermi du CoFeB vers la bande de valence de GaAs via ces états, est favorisé. Ceci peut être modélisé comme une résistance de fuite à travers la barrière tunnel. La tension s'applique donc moins efficacement sur la barrière tunnel.

Les porteurs sont injectés avec une énergie cinétique moindre et le mécanisme

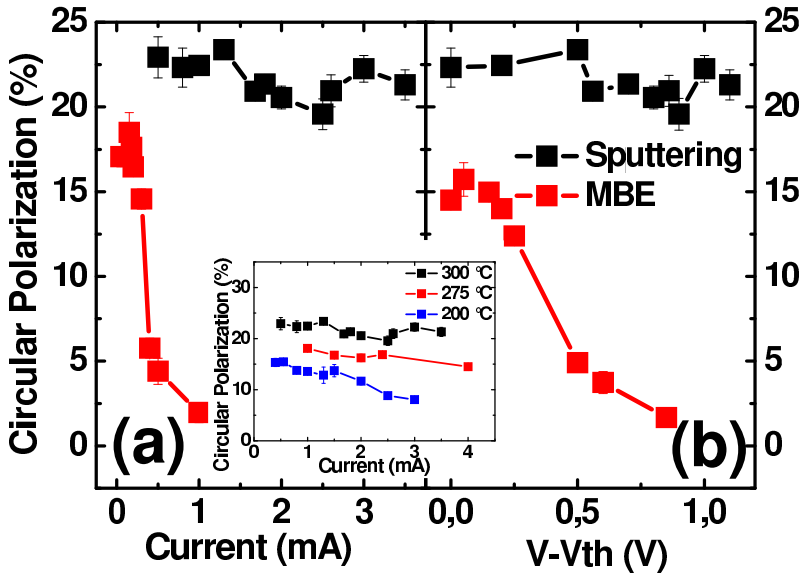

Figure 6: (a) Polarisation circulaire en fonction du courant injecté dans la spin-LED pour l'échantillon présentant une barrière tunnel de MgO fabriquée par pulvérisation cathodique et pour l'échantillon MBE recuits à 300 $°C$. Insert: P_C en fonction du courant pour différentes températures de recuit (échantillon sputtering). (b) Polarisation circulaire en fonction de ΔV pour les même échantillons.

de relaxation de type D'Yakonov-Perel est donc moins efficace. Notons que dans ce cas le courant total traversant la spin-LED est pour partie constitué du courant de fuite. Dans le régime des faibles courants, le courant de seuil afin d'obtenir le phénomène d'électroluminescence est supérieur et l'intensité d'électroluminescence est donc plus faible (si on compare avec les données obtenues pour la spin-LED avec barrière tunnel élaborée par MBE). De manière complémentaire, la tension appliquée à la partie semiconductrice du système est plus importante pour les échantillons avec une barrière tunnel élaborée par pulvérisation cathodique. Comme aucun décalage de

Stark n'est observé sur les longueurs d'onde d'émission lorsque la tension appliquée sur la structure varie, il est possible que cette tension se reporte principalement dans la partie semiconductrice juste après la barrière de MgO. Cela faciliterait le transit des électrons vers le puits quantique, et expliquerait qu'aux valeurs de courant plus élevées, l'électroluminescence devienne comparable et même légèrement supérieure à celle obtenue pour les échantillons MBE. Finalement, il apparait que les échantillons dont la barrière tunnel est élaborée par pulvérisation cathodique présentent le meilleur compromis Forte polarisation circulaire/Forte intensité, ce qui pourrait être important dans de futures applications.

Spin-LED avec injecteur à aimantation verticale rémanente

En vue de la mise au point futurs dispositifs, il est capital de pouvoir s'affranchir de l'application d'un champ magnétique externe appliqué. Nous avons donc travaillé sur un nouveau type d'injecteur présentant de l'anisotropie magnétique perpendiculaire (PMA) qui induit une aimantation rémanente perpendiculaire au plan des couches. Nous avons étudié un injecteur ultrafin original de CoFeB (quelques plans atomiques). Cet injecteur permet de limiter très fortement l'absorption optique si on le compare aux injecteurs multicouches présentant de la PMA utilisés jusqu'à présent. Ceci pourrait s'avérer important pour la mise au point de lasers VCSELs (Lasers à cavité verticale) ou VECSELs (VECSEL à cavité externe) polarisés en spin, qui nécessitent de très faibles pertes dans la cavité laser. De plus, cet injecteur présente de bonnes propriétés de commutation de son aimantation par injection d'un courant de spin polarisé en spin (effet spintorque), comme cela a été montré dans les jonctions tunnel magnétiques. Des mesures SQUID avec champ magnétique appliqué perpendiculairement aux couches ont permis de montrer que la réduction de l'épaisseur t de la couche de CoFeB de 1.7 nm à 1.1 nm permet l'apparition de la PMA pour t= 1.2 nm car l'anisotropie d'interface prend le pas sur l'anisotropie de forme (qui tend à aligner l'aimantation dans le plan des couches). Cette épaisseur t sera donc choisie pour l'échantillon optimal. La température de recuit rapide (3 mn) optimale est de 250 $°C$. Le recuit permet d'améliorer la qualité chimique de l'interface (élimine la sur(ou sous)-oxygénation qui dégrade la PMA). Au-delà de 250 $°C$, le Tantale surmontant la couche de CoFeB commence à diffuser à travers cette couche vers l'interface CoFeB/MgO et occasionne

une perte de PMA. L'origine microscopique de la PMA est expliqué par le transfert d'électron des orbitales du Fe(Co) pointant le long de la direction de croissance vers les atomes d'Oxygènes situés en regard à l'interface. A l'interface, l'occupation des orbitales dans le plan du métal ferromagnétique est donc supérieure à l'occupation des orbitales hors du plan. Il en résulte un moment orbital perpendiculaire au plan des couches. En prenant en compte l'interaction spin-orbite, ceci mène finalement à une aimantation perpendiculaire au plan des couches. Des calculs ab-initio menés en utilisant le simulateur Vienna (VASP) viennent renforcer cette interprétation. Grâce à des mesures d'électroluminescence, un taux de polarisation circulaire de P_C=13% (à 25 K) est observé en l'absence de champ magnétique appliqué (Figure 7).

En jouant sur la tension appliqué, cette valeur peut atteindre jusqu'à 20%. C'est

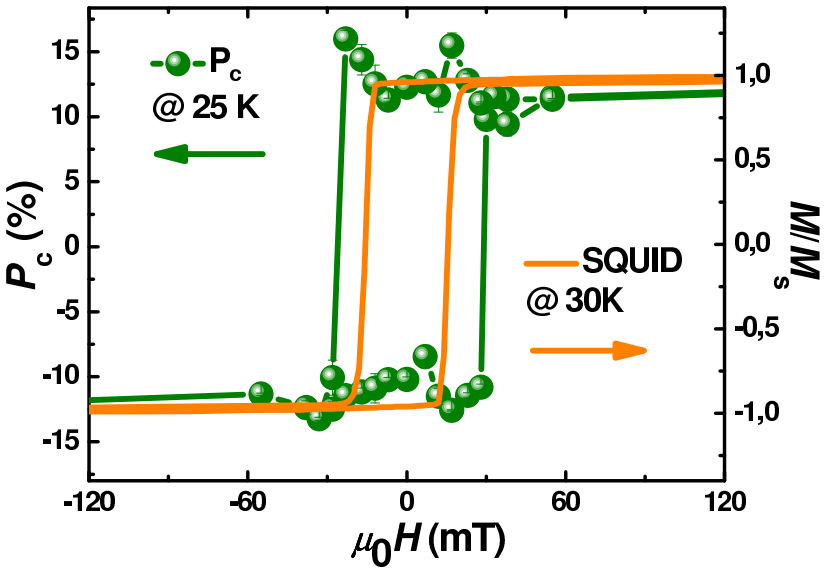

Figure 7: Polarisation circulaire P_C de l'électroluminescence en fonction du champ magnétique appliqué à 30 K. En pointillé, cycle d'hystérésis de la couche de CoFeB mesurée par SQUID à 30 K.

la première fois que la possibilité d'injecter des électrons polarisés en spin sans champ magnétique est observée avec une telle efficacité (6 fois plus que les meilleurs résultats de l'état de l'art). Cette polarisation reste conséquente à température ambiante (P_C=8% à 300 K voir Figure 8). L'électroluminescence reste détectable à 300 K grâce à la présence de 3 puits quantiques d'$In_{0.1}Ga_{0.9}As/GaAs$ dans la zone intrinsèque de la P-I-N. Une étude systématique est réalisée en fonction de la température avec et sans champ magnétique longitudinal appliqué. Dans les deux cas, le taux de polarisation

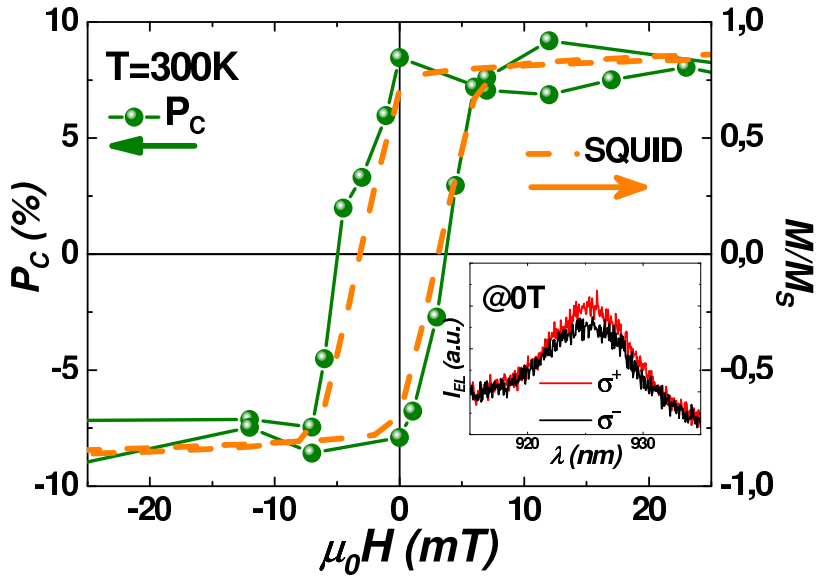

Figure 8: Polarisation circulaire P_C de l'électroluminescence en fonction du champ magnétique appliqué à 300 K. En pointillé, cycle d'hystérésis de la couche de CoFeB mesurée par SQUID à 300 K. Insert: Spectres d'électroluminescence mesurés pour les deux hélicités de la lumière en l'absence de champ magnétique appliqué.

circulaire de l'électroluminescence décroit jusqu'à 100 K, puis reste relativement stable jusqu'à 300 K. Il semble donc que cette décroissance soit liée à la partie semiconductrice du dispositif plutôt qu'aux propriétés de l'injecteur. Pour vérifier ceci, nous avons mesuré de manière systématique le temps de vie des porteurs τ et leur temps de relaxation de spin τ_s dans les puits quantiques via la technique de photoluminescence résolue en temps et en polarisation. Nous confirmons ainsi que le comportement en température de la polarisation circulaire de l'électroluminescence est lié à la dépendance en température de τ et τ_s.

Chapitre 4

Mécanismes de relaxation de spin dans les vallées L du GaAs

Dans ce chapitre nous étudions la dynamique de relaxation de spin lors de la relaxation énergétique des porteurs vers les états de la vallée Γ. Nous présentons les règles de sélection optiques qui régissent la photogénération de porteurs polarisés lors de l'excitation dans la bande L, nous modélisons les mécanismes de relaxation de spin et nous montrons expérimentalement que malgré une injection de spin des porteurs à haute énergie, une fraction de la mémoire de spin est conservée.

Motivations

La dynamique de spin des électrons a été particulièrement étudié ces cinquante dernières années dans les matériaux semiconducteurs III-V, et plus particulièrement dans GaAs. Cependant, toutes les études expérimentales qui ont été menées ont été faites à des énergies d'excitation proches de l'énergie de bande interdite, typiquement dans la gamme 1,5-2 eV, menant à la photogénération de porteurs dans la vallée Γ. Au-delà de son aspect fondamental, la compréhension des mécanismes de relaxation de spin dans les vallées de plus haute énergie est cruciale pour le développement potentiel de dispositifs basés sur l'injection électrique de spin. En effet, dans les composants tels que les lasers ou les diodes électroluminescentes polarisées en spin, les électrons injectés électriquement peuplent à la fois la vallée Γ mais aussi les vallées satellites X et L. La contribution des mécanismes de relaxation de spin dans ces vallées à l'efficacité d'injection globale doit donc être prise en compte. Elle est aussi primordiale pour l'observation de la génération spontanée de courant polarisé en spin ou effet spin Gunn, comme cela a été récemment décrit. En effet, les électrons qui peuplent les vallées Γ et L sont soumis à des couplages spin-orbites très différents, et les valeurs attendues en L sont plus élevées que celles observées en Γ. Ainsi, on s'attend à ce que le spin des électrons de la vallée L soit d'avantage soumis au mécanisme de relaxation de D'Yakonov-Perel.

Le faible nombre d'études ayant porté sur la polarisation de spin des électrons de la vallée L ont été réalisées par spectroscopie de photoémission dans GaAs. Dans ces expériences, les traitements de surface des échantillons peuvent avoir modifié la polar-

isation de spin des électrons lors de la photoémission. De plus, l'énergie cinétique des électrons émis n'a pas été mesurée, ce qui ne permet pas de déterminer avec certitude si ces électrons étaient émis depuis la bande L seulement, ou si une contribution de la bande Γ était présente. Afin de sonder la polarisation de spin des électrons peuplant la vallée L, nous avons réalisé des expériences d'orientation optique de spin à l'aide d'excitations laser dans la gamme 2,8-3,2 eV et nous avons mesuré le taux de polarisation de la luminescence en détectant la transition au niveau de l'énergie de bande interdite de GaAs à $\sim$1,5 eV.

Détails expérimentaux

L'échantillon étudié dans ces expériences est une couche de 1 μm de GaAs de type p dopé au béryllium ($p_0 = 10^{18} cm^{-3}$), réalisé au LAAS par épitaxie par jets moléculaires. Les résultats présentés ici ont été obtenus à une température de 10 K. Des expériences d'excitation de la photoluminescence dans la gamme 2,8-3,2 eV et de photoluminescence résolue en temps proche de l'énergie de bande interdite ont été réalisées afin de sonder la dynamique de polarisation de spin dans les vallées Γ et L. Le détail des techniques expérimentales développées pour réaliser ces mesures est donnée dans le chapitre 2.

Polarisation de spin dans les vallées L, règles de sélection

Lorsque les porteurs sont photogénérés par une énergie d'excitation de 2,987 eV, plusieurs transitions sont possibles. Trois d'entre elles vont peupler la bande de conduction au voisinage du point Γ, impliquant les transitions depuis les bandes de trous lourds, légers, et spin-orbite (transitions représentées en pointillés dans la figure 9), conférant aux électrons de conduction une énergie cinétique de l'ordre de 1 eV. Une forte absorption se produit également au voisinage des vallées L (transition $L_{4,5} \rightarrow L_6$, indiquée en noir dans la figure 9). En raison de l'espace étendu sur lequel les bandes $L_{4,5}$ et L_6 sont parallèles, et des masses effectives plus élevées dans cette région qu'en Γ, la transition $L_{4,5} \rightarrow L_6$ est prédominante dans cette gamme d'excitation. Nous avons reporté dans l'insert de la figure 10 le spectre de photoluminescence intégrée en temps obtenue pour cette énergie d'excitation et une polarisation σ^+ (courbe noire). Le taux

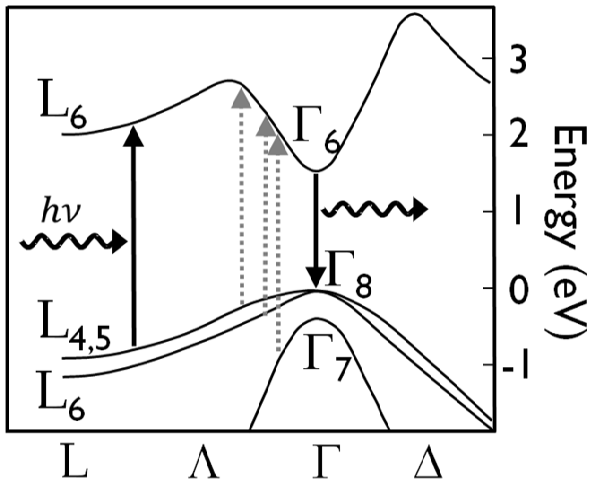

Figure 9: structure de bandes de GaAs, les flèches représentent les transitions (excitation et détection) impliquées dans les études de PL et PLE.

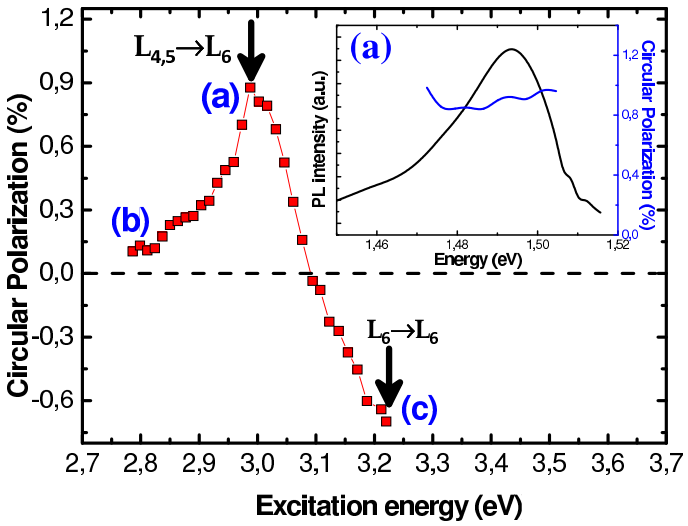

Figure 10: polarisation de la PLE détectée à 1.494 eV à 10 K en fonction de l'énergie d'excitation. Insert: spectre de PL intégré en temps (courbe noire) et taux de polarisation circulaire (courbe bleu).

de polarisation circulaire est également reporté (courbe bleue) et présente une valeur au pic de l'ordre de 0,9% que nous attribuons à la conservation du spin des électrons photogénérés en L. La figure 10 présente le taux de polarisation détecté au pic de photoluminescence en fonction de l'énergie d'excitation. Le maximum de polarisation est atteint sans ambigüité pour une énergie d'excitation correspondant à la transition $L_{4,5} \rightarrow L_6$. Pour des énergies d'excitation inférieures à 2,8 eV, où seules les transitions en Γ sont possibles, le taux de polarisation détecté est proche de zéro, en raison du fort couplage spin-orbite auquel les électrons de grand vecteur d'onde k sont soumis, induisant de très courts temps de relaxation de spin. Enfin, à plus haute énergie, lorsque la transition $L_6 \rightarrow L_6$ est impliquée, le taux de polarisation circulaire devient négatif, pour atteindre une valeur de l'ordre de -0,6%.

Les valeurs expérimentales sont en bon accord avec les valeurs prévues par différentes

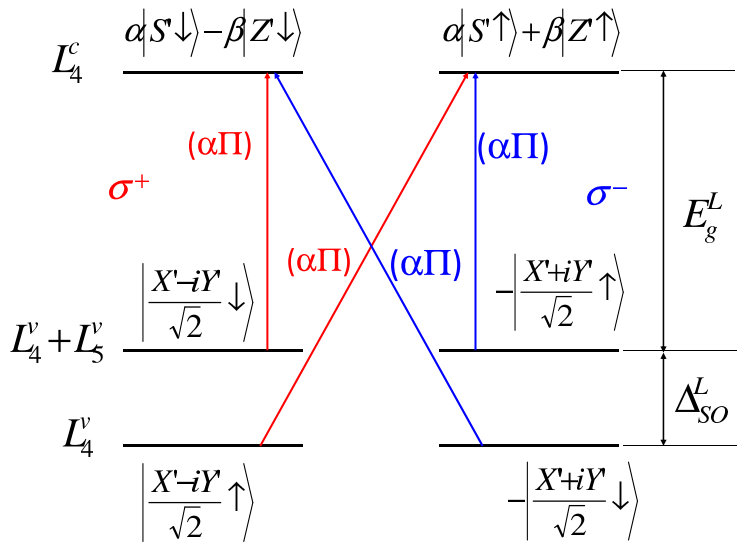

Figure 11: règles de sélection pour les transitions $L_(4,5) \rightarrow L_6$ et $L_6 \rightarrow L_6$ pour une excitation laser σ^+ se propageant selon la direction [111].

méthodes de calcul (LDA et k.p), qui prévoient des taux de polarisation initiale P_0 de 30% et -5% pour les transitions $L_{4,5} \rightarrow L_6$ et $L_6 \rightarrow L_6$, respectivement, et de 10% pour la transition en Γ. Les règles de sélection calculées pour les transitions en L, pour une direction de propagation selon [111] sont reportées dans la figure 11. Dans le cas d'une excitation laser polarisée σ^+ elles prévoient un taux de polarisation de 100% pour la transition $L_{4,5} \rightarrow L_6$ et de -100% pour la transition $L_6 \rightarrow L_6$, ce qui devrait aboutir à un taux de polarisation initial P_0 de 0% quand les deux transitions sont impliquées à poids égal. Cependant, dans les mesures réalisées ici, la direction

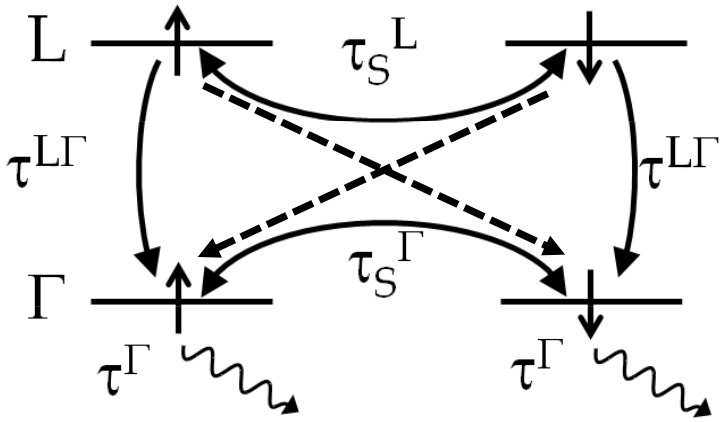

Figure 12: représentation schématique du modèle à deux niveaux faisant intervenir les temps de relaxation de spin des électrons dans les vallées L et Γ (^L_s et $^\Gamma_s$), le temps de relaxation des vallées L vers Γ ($^{L\Gamma}$) et le temps de vie des électrons dans la vallée Γ ($^\Gamma$).

de propagation est selon l'axe de croissance [001], et en prenant en compte les orientations des 8 vallées L, le calcul aboutit à un taux de polarisation initiale P_0 de 50% pour la transition $L_4, 5 \rightarrow L_6$. Cette valeur est en accord raisonnable avec les 30% prévus par les calcules de LDA et $k \cdot p$ qui incluent une contribution des électrons chauds photogénérés en Γ. Le taux maximum de polarisation de la luminescence attendu, sans tenir compte des effets de relaxation de spin des porteurs, est donc de 25%.

Temps de vie de spin dans les vallées L

Afin de déterminer le temps de vie de spin des électrons dans les vallées L, nous avons schématisé l'évolution du système par un modèle à deux niveaux (voir figure 12):

$$\begin{cases} \dfrac{dn^L_{+(-)}}{dt} &= -\dfrac{n^L_{+(-)} - n^L_{-(+)}}{2\tau^L_S} - \dfrac{n^L_{+(-)}}{\tau^{L\Gamma}} - \dfrac{n^L_{+(-)}}{\tau^{L\Gamma}_S} \\ \dfrac{dn^\Gamma_{+(-)}}{dt} &= \dfrac{n^\Gamma_{+(-)} - n^\Gamma_{-(+)}}{2\tau^\Gamma_S} - \dfrac{n^\Gamma_{+(-)}}{\tau^\Gamma} + \dfrac{n^L_{+(-)}}{\tau^{L\Gamma}} + \dfrac{n^L_{-(+)}}{\tau^{L\Gamma}_S} \end{cases}$$

où $n^L_{+(-)}$ et $n^\Gamma_{+(-)}$ sont les densités d'électrons de spins up ou down dans les vallées L et Γ, respectivement. En régime stationnaire, la résolution de ce système conduit à une expression de la polarisation circulaire de la luminescence P_C:

$$P_C^{\Gamma,0} = \frac{P_0^L}{2} \frac{1}{\left(1 + \frac{\tau^\Gamma}{\tau^\Gamma_S}\right)\left(1 + \frac{\tau^{L\Gamma}}{\tau^L_S}\right)}$$

Nous avons mesuré de manière indépendante un temps de relaxation de spin des électrons en Γ de 200 ps par des expériences de photoluminescence résolue en temps. En considérant un taux initial P_0^L de 30% et un temps de transfert $\tau^{L\Gamma}$ de 2 ps, nous estimons un temps de relaxation de spin des électrons en L de 200 fs. Ce résultat est en accord avec avec des calculs récents qui prévoient des temps de relaxation de spin de l'ordre de 100 fs à cause du fort coulage spin-orbite auquel sont soumis les électrons des vallées L. Ainsi, nous avons pu montrer expérimentalement que les temps de relaxation de spin dans les vallées L sont de plusieurs ordres de grandeur inférieurs à ceux de la vallée Γ et qu'ils sont également beaucoup plus courts que ceux de matériaux centrosymétriques présentant un plus faible couplage spin-orbite comme le silicium ou le germanium.

Chapitre 5

Propriétés de spin des alliages GaAsBi

Depuis une dizaine d'années, les alliages GaAsBi ont suscité un intérêt croissant dans les domaines des télécommunications optiques et des applications photovoltaïques, mais également auprès d'équipes se focalisant sur les propriétés plus fondamentales de ce matériau. En effet, l'incorporation d'atomes de bismuth dans une matrice de GaAs induit une forte perturbation des états hôtes, provocant une augmentation significative du couplage spin-orbite ainsi qu'une diminution de l'énergie de bande interdite. Ces propriétés singulières ont amené une réflexion quant aux potentielles applications de cet alliages dans des dispositifs spintroniques mais au-delà des ces objectifs, sonder les propriétés de spin des porteurs pourrait permettre de mieux comprendre la modification des états de valence. Dans ce chapitre, nous déterminons, via la mesure directe du facteur de Landé des états de conduction, l'impact de la modification des états de valence sur les propriétés de spin des électrons.

GaAsBi: un alliage perturbé

L'échantillon étudié dans ces travaux de thèse a été réalisé au LAAS par épitaxie par

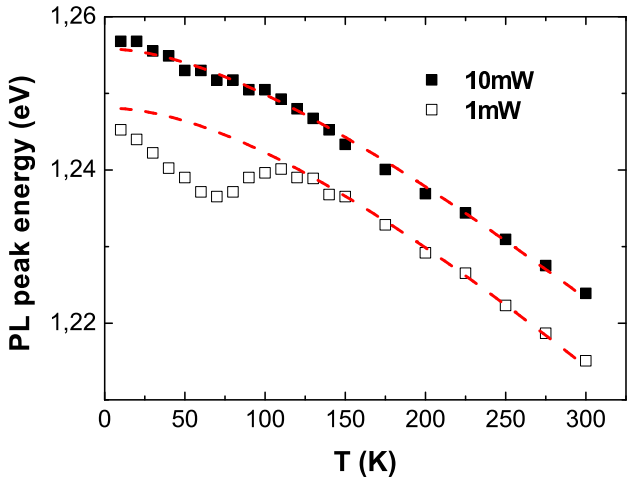

Figure 13: position du pic de photoluminescence en fonction de la température pour des puissances d'excitation de 1 mW et 10 mW.

jets moléculaires à une température de 380 $°C$. La concentration de Bi est de 2.2% et l'épaisseur de l'échantillon, non relaxé, est de 160 nm. La figure 13 met en évidence des effets de localisation liés à la présence d'agrégats de bismuth et au désordre d'alliage.

A basse température et faible puissance d'excitation (carrés blancs), la recombinaison radiative implique les états localisés, situés en-dessous du minimum de bande. Lorsque la température augmente (T¿60 K), l'énergie thermique permet une délocalisation des porteurs vers le minimum de bande, expliquant la déviation du pic de PL vers des énergies plus élevées, puis la diminution de l'énergie de PL avec la température suit la tendance classique des alliages semiconducteurs décrite par Varshni. Une augmentation de la puissance d'excitation permet de saturer les états localisés et de peupler le minimum de bande. Ainsi, la contribution des états délocalisés devient prépondérante et la transition observée ne montre plus de forme 's-shape' liée au mécanisme de délocalisation. Notons qu'un traitement par recuit thermique rapide après croissance permet d'améliorer non seulement la qualité optique mais également l'homogénéité du matériau, faisant disparaître la tendance de 's-chape' décrite ci-dessus.

Ces propriétés ne sont pas sans rappeler celles observées sur GaAsN, alliage dans

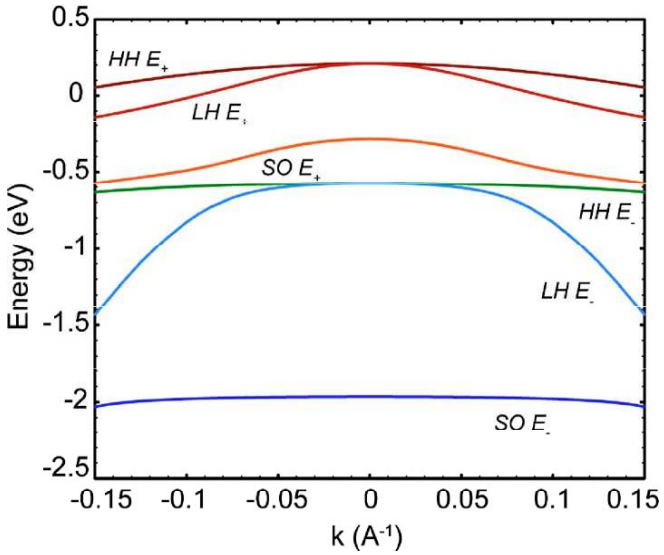

Figure 14: structure de bande de valence de GaAsBi d'après le modèle de BAC [15].

lequel se forment des agrégats d'azote dont les niveaux d'énergie interagissent avec les états de conduction de la matrice. Un modèle simple décrivant cette interaction comme un anti-croisement de bande (BAC) entre les états localisés des niveaux d'azote et les état étendus de la bande de conduction a permis de donner une description correcte de la diminution de l'énergie de bande interdite lorsque la concentration d'azote augmente. De la même manière, une telle description a été proposée pour l'alliage GaAsBi, les niveaux liés au bismuth interagissant avec les états de valence du GaAs. Par ailleurs, des calculs de liaisons fortes, ayant abouti à des résultats comparables,

ont montré la validité de cette approche simple pour prédire la diminution de l'énergie de bande interdite et la modification des états de valence. Une représentation de la structure de bande de valence obtenue à partir du modèle de BAC est reporté dans la figure 14 pour une couche de GaAsBi relaxé contenant 4% de bismuth. Pour cette concentration, l'énergie de splitting spin-orbite Δ_{SO} est de l'ordre de 500 meV, alors qu'elle vaut 340 meV dans GaAs.

Dynamique de relaxation de spin des électrons

Nous avons mené des expériences de photoluminescence résolue en temps et en po-

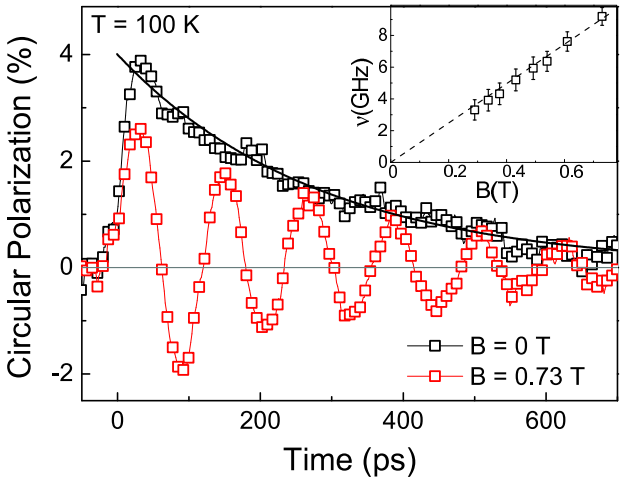

Figure 15: dynamique de la polarisation circulaire de la photoluminescence avec (rouge) et sans (noir) champ magnétique. Insert: fréquence des oscillations en fonction du champ magnétique appliqué.

larisation sur l'échantillon décrit plus haut. La température a été fixée à 100 K afin de minimiser la contribution des porteurs localisés et des effets excitoniques. En l'absence de champ magnétique, le déclin de la polarisation de la luminescence montre une allure monoexponentielle (courbe noire de la figure 15), le temps de relaxation de spin des électrons est de l'ordre de $_s$=360 ps. Lorsqu'un champ magnétique $\vec{B}$ transverse est appliqué, selon la direction ($\vec{e_x}$), la précession des spins des électrons selon $\vec{B}$ conduit à des oscillations de la polarisation de la luminescence (courbe rouge de la figure 3). La mesure de la pulsation Ω de ces oscillations permet de déterminer la valeur absolue du facteur de Landé g selon:

$$\Omega = \frac{g\mu_B}{\hbar}B$$

Les mesures répétées pour différentes valeurs de champ magnétique ont permis de

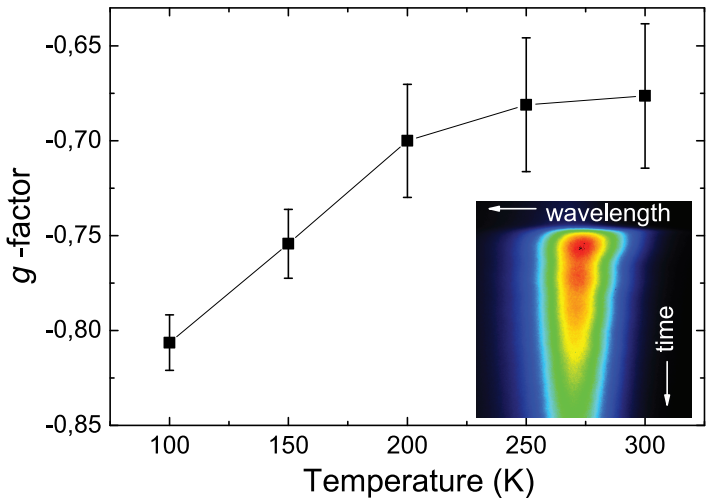

Figure 16: valeurs du facteur de Landé g en fonction de la température. Insert: image de la photoluminescence co-polarisée avec l'excitation mettant en évidence les oscillations de la polarisation

déterminer un facteur de Landé de l'ordre de g=0.81. Nous avons également réalisé ces mesures en faisant varier la température (figure 16), on observe une diminution de la valeur absolue de g lorsque la température augmente, passant de 0,82 à 100 K à 0,68 à 300 K. Nous avons également déterminé que le facteur de Landé de GaAsBi est du même signe que celui de GaAs. De manière remarquable, on constate que le facteur de Landé dans l'alliage de GaAsBi contenant 2,2% de bismuth est le double de celui de GaAs. Cette augmentation significative témoigne de la modification de la structure de bande de l'alliage. En effet, si l'on utilise un modèle simple faisant intervenir l'énergie de bande interdite et l'énergie de splitting spin-orbite, g peut s'exprimer:

$$g = 2 - \frac{2}{3}\frac{E_P \Delta_{SO}}{E_g(E_g + \Delta_{SO})}$$

où E_P est l'énergie de Kane (22,7 eV dans GaAs). Dans cette approximation, si l'on considère Δ_{SO}=0,445 eV (correspondant aux valeurs reportées dans la littérature), E_g=1,25 eV (obtenu d'après les mesures de photoluminescence), on trouve une valeur théorique de g de -1,18. Cette valeur est largement surestimée mais l'augmentation attendue due à la fois à la diminution de E_g et à l'augmentation de Δ_{SO} est observée expérimentalement. Une collaboration avec l'institut Tyndall de l'Université de Cork, qui fait suite à ces travaux, est en cours afin de donner une modélisation plus précise des états de valence.

Enfin, nous avons également étudié le temps de relaxation de spin τ_s des électrons.

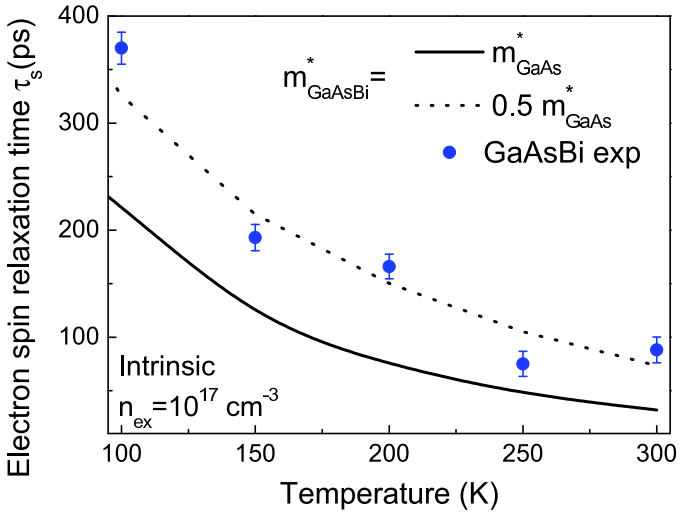

Figure 17: Temps de relaxation de spin en fonction de la température. Cercles bleus: valeurs expérimentales; trait plein: valeurs théoriques considérant une masse effective égale à celle de GaAs; trait pointillé: valeurs théoriques considérant une masse deux fois inférieure.

Les résultats obtenus lorsque la température augmente sont reportés dans la figure 17.

Nous les avons comparés à des valeurs théoriques prenant en compte la possibilité d'une masse effective plus faible dans l'alliage GaAsBi que dans GaAs. Les valeurs expérimentales sont en bon accord avec une masse effective des électrons deux fois plus faible que celle dans GaAs. Les résultats expérimentaux de mesure de masse effective obtenus dans la littérature divergent, cependant la tendance observée dans nos expériences est en bon accord avec des mesures de Shubnikov-De Haas reportées antérieurement.

Conclusions

Afin de sonder les propriétés électroniques de l'alliage GaAsBi, nous avons étudié la dynamique de relaxation de spin avec et sans champ magnétique. La mesure du temps de relaxation de spin des électrons suggère une diminution de la masse effective des électrons de conduction. Par ailleurs, la mesure du facteur de Landé g montre une augmentation significative de sa valeur en comparaison à celle de GaAs, liée à la fois à la diminution de l'énergie de bande interdite et à l'augmentation de l'interaction spin-orbite. L'ensemble de ces résultats suggère que l'introduction de bismuth dans GaAs induit une modification profonde de la structure de bandes, de manière évidente dans

la bande de valence, mais aussi dans la bande de conduction. Ces travaux nous ont permis d'avoir une première image des propriétés électroniques de cet alliage et seront approfondis, afin de déterminer les potentialités de cet alliage pour les applications diverses où il pourrait présenter un intérêt telles que les télécommunications optiques ou le photovoltaïque.

Conclusions et perspectives

Dans le cadre de cette thèse, nous avons dans un premier temps étudié le processus d'injection électrique de spin d'une électrode de CoFeB vers des puits quantiques d'InGaAs/GaAs à travers des barrières cristallines de MgO. Trois points principaux sont abordés. D'abord, lors d'une étude comparative entre des spin-LEDs comportant une barrière tunnel fabriquée soit par épitaxie par jets moléculaires, soit par pulvérisation cathodique, nous avons établi que l'interface CoFeB/MgO joue un rôle prépondérant dans le processus d'injection de spin. Nous montrons en outre que le recuit permet une amélioration significative de l'injection de spin. La température optimale de recuit se situe dans la fenêtre 300-350 $°C$. Dans un deuxième temps, nous avons étudié sur ces mêmes échantillons l'influence du courant injecté dans les spin-LEDs sur le rendement d'injection de spin. Nous montrons que le taux de polarisation circulaire est nettement plus stable en fonction du courant dans le cas où la barrière tunnel de MgO est fabriquée par pulvérisation cathodique. Nous attribuons cet effet à une densité d'états d'interface plus importante à l'interface MgO/GaAs pour ce type d'échantillons. Enfin nous démontrons la possibilité d'injecter très efficacement des électrons polarisés en spin sans champ magnétique appliqué, en utilisant une électrode ultrafine de CoFeB (d'une épaisseur de quelques plans atomiques) présentant une aimantation rémanente perpendiculaire au plan des couches. Un prolongement de ce travail consistera dans le futur à utiliser ce type d'injecteur dans des structures plus complexes où un courant auxiliaire polarisé en spin permettrait de commuter l'aimantation de la couche de CoFeB à la demande, par effet spin torque. Ce type de système pourrait ensuite être inséré dans des systèmes de types VCSEL (lasers à cavité verticale) et VECSELs (lasers à cavité verticale à cavité externe) en vue de produire une émission cohérente polarisée circulairement d'hélicité pilotable électriquement. De plus, des expériences de photocourant résolu en spin ainsi que des calculs ab-initio sur l'interface CoFeB/MgO/GaAs pourraient aider dans le futur à mieux comprendre le rôle des états d'interface dans le processus d'injection électrique de spin. Nous avons ensuite étudié les mécanismes de relaxation de spin des électrons injectés à haute énergie dans les vallées satellites L du GaAs. En effet, la compréhension de ces mécanismes est primordiale afin de pouvoir prévoir les effets de l'injection électrique des porteurs

qui transitent par ces états d'énergie élevée. Nous avons photogénéré des électrons polarisés vers les vallées L du GaAs et observé un taux de polarisation de la luminescence significatif (0,9%). Nous avons également observé les variations du taux de polarisation en fonction de l'énergie d'excitation. Ces résultats sont en bon accord avec des calculs de LDA et $k \cdot p$ réalisés précédemment par d'autres groupes, et ont été également corroborés par les calculs des règles de sélection optiques dans les vallées L que nous avons développés dans le cadre de cette thèse. Enfin, nous avons développé un modèle à deux niveaux faisant intervenir les temps de vie et les temps de vie de spin des porteurs dans les vallées L et Γ. Combiné à des mesures directes de temps de vie de spin en Γ, ceci nous a permis de déterminer un temps de vie de spin des électrons en L de 200 fs, mettant en évidence l'augmentation attendue des effets du couplage spin-orbite dans les vallées L. Enfin, nous avons étudié les propriétés de spin de GaAsBi. Ce matériau présente des propriétés électroniques singulières qui en font un très bon candidat pour les applications dans les domaines du photovoltaïque et des télécommunications optiques. La mesure du temps de relaxation de spin des électrons suggère une diminution de la masse effective des électrons de conduction. Par ailleurs, la mesure du facteur de Landé g montre une augmentation significative de sa valeur en comparaison à celle de GaAs, liée à la fois à la diminution de l'énergie de bande interdite et à l'augmentation de l'interaction spin-orbite. L'ensemble de ces résultats suggère que l'introduction de bismuth dans GaAs induit une modification profonde de la structure de bandes, de manière évidente dans la bande de valence, mais aussi dans la bande de conduction. Les travaux futurs, portant sur l'influence de la composition en bismuth des alliages de GaAsBi permettront de déterminer plus précisément les propriétés des états de valence et de conduction afin d'en déterminer les avantages pour les applications pour lesquelles ils sont pressentis.